TECHNISCHE UNIVERSITÄT
MÜNCHEN

Lehrstuhl für Flugsystemdynamik

Impact of Aeroelasticity on Flight Dynamics and Handling Qualities of Novel Aircraft Configurations

Klaus Seywald

Vollständiger Abdruck der von der Fakultät für Maschinenwesen der Technischen Universität München zur Erlangung des akademischen Grades eines

Doktor-Ingenieurs

genehmigten Dissertation.

Vorsitzender:		apl. Prof. Dr.-Ing. habil. Christian Breitsamter
Prüfer der Dissertation:	1.	Prof. Dr.-Ing. Florian Holzapfel
	2.	Prof. Dr.-Ing. Horst Baier

Die Dissertation wurde am 20.04.2016 bei der Technischen Universität München eingereicht und durch die Fakultät für Maschinenwesen am 26.09.2016 angenommen.

Acknowledgments

The following work has been created during my time as a Research Engineer at Airbus Group Innovations Germany in cooperation with the Institute of Flight System Dynamics at the Technische Universität München. At this point would like to thank all parties who made this work possible.

First of all I owe my deepest gratitude to my supervisor Professor Dr.-Ing. Florian Holzapfel. Without his continuous support, enthusiasm and guidance this thesis would not have been possible. His insightful feedback and the productive discussions significantly contributed to the success of this work.

I also express my warmest gratitude to Dr.-Ing. Andreas Wildschek for making this work possible through his continuous support and encouragement to pursue my ideas. Thanks for always having open ears and taking the time for fruitful discussions.

I would also like to thank Prof. Dr.-Ing. Horst Baier and apl. Prof. Dr.-Ing. habil. Christian Breitsamter for offering to chair the examination.

Many thanks also go out to my colleague, Fabian Hellmundt for always making time and offering support, whenever his expertise in flight control law design was required. Furthermore I want to especially thank my successor Simon Binder, who already supported me as part of his Diploma Thesis and now continues to work on this project.

I also want to thank all my other colleagues at Airbus, particularly crowd in the student room, who made these past three and a half years so much fun. I will miss the extended coffee and lunch breaks and fun conversations.

However most of all, I would like to thank my parents and my family. Without your support, neither my studies, my semesters abroad, nor my doctorate studies would have been possible.

Abstract

The trend in innovative aircraft configurations is moving towards extended wingspans and unconventional wing shapes aiming at the minimization of fuel consumption. This trend leads to an increasing flexibility of the aircraft structure which might end up in tremendous problems in the design processes. So far aeroelasticity has been considered only very limited in conceptual aircraft design and generally the link between aeroelasticity and flight dynamics is not taken into account at all. Consequentially, difficulties resulting from these interdependencies are often only recognized in more mature design stages leading to additional design iterations as well as delays and increased cost. This work presents a generic method for the modeling and assessment of unconventional aircraft configurations in conceptual design. The analysis specifically focuses on flight dynamics and handling qualities considering aeroelasticity as well as the couplings of flight dynamics and aeroelasticity. In particular certification requirements with respect to handling qualities are evaluated, allowing a preliminary statement on the certifiability of a new aircraft concept. The study compares a classical aircraft configuration and an unconventional configuration with respect to handling qualities and flight dynamics taking into account the impact of aeroelasticity. The hypothesis of a significantly increased impact of aeroelasticity for the unconventional configuration has been confirmed.

Kurzfassung

Innovative Flugzeugkonfigurationen zeigen deutliche Trends zu größeren Spannweiten und ungewöhnlichen Flügelformen mit dem Ziel den Kraftstoffverbrauch zu minimieren. Diese Entwicklung führt zu einer zunehmenden Flexibilität der Flugzeugstruktur, welche zu erheblichen Problemen im Flugzeugdesign führen kann. Bisher wird die Aeroelastik im Flugzeugvorentwurf nur sehr limitiert berücksichtigt und grundsätzlich die Kopplung der Aeroelastik mit der Flugdynamik nicht berücksichtigt. Dies führt dazu, dass Probleme die aus diesen Kopplungen entstehen oft erst in späteren Entwurfsphasen erkannt werden, was zu zusätzlichen Iterationen führt und den Designprozess verlangsamt und verteuert. Diese Arbeit stellt eine generische Methodik zur Modellierung und Bewertung von ungewöhnlichen Flugzeugkonfigurationen auf Vorentwurfslevel unter Berücksichtigung der Aeroelastik sowie der Kopplung zwischen Flugdynamik und Aeroelastik vor. Insbesondere werden Zulassungsanforderungen hinsichtlich Flugeigenschaftskriterien berücksichtigt und ausgewertet, was eine Aussage zur Realisierbarkeit und Komplexität einer möglichen Zertifizierung eines Flugzeugkonzeptes ermöglicht. In der Arbeit wird eine klassische Flugzeugkonfiguration mit einer ungewöhnlichen Konfiguration hinsichtlich ihrer Flugeigenschaften und des Einflusses der Aeroelastik auf die Flugdynamik verglichen. Die Hypothese eines signifikant erhöhten Einflusses der Flugzeugelastizität bei der ungewöhnlichen Konfiguration wurde bestätigt.

Contents

List of Figures

List of Tables

Acronyms

Notation	**Description**	**Page List**
A/C	Aircraft	10
CAP	Control Anticipation Parameter	82, 85
CC	Classical Configuration	69, 70, 75, 98, 110, 135, 140
CFD	Computational Fluid Dynamics	9, 43
CRM	Common Research Model	9
DLM	Doublet Lattice Method	8, 29, 135
DoF	Degree of Freedom	15, 22, 48
FCS	Flight Control System	61
FE	Finite Element	8, 9, 11, 41, 46
FSI	Fluid Structure Interaction	47
GAF	Generalized Aerodynamic Forces	140
HARW	High Aspect Ratio Wing	2, 6
HOS	High Order System	80–82
HQ	Handling Qualities	10
LOES	Low Order Equivalent System	80–85, 99–102, 113
MTOW	Maximum Takeoff Weight	26
MUAD	Maximum Unnoticable Additional Dynamics	81
OEI	One Engine Inoperative	58, 109
OWE	Operating Weight Empty	26
PIO	Pilot Induced Oscillations	81, 92, 96, 99

Notation	Description	Page List
RFA	Rational Function Approximation	8, 52, 53, 56
SFC	Specific Fuel Consumption	1
SSM	State Space Model	140
TPR	Transient Peak Ratio	98
UCC	Unconventional Configuration	69, 70, 75, 85, 87, 92, 93, 98, 109
UVLM	Unsteady Vortex Lattice Method	9, 31, 35, 51, 115
VLM	Vortex Lattice Method	32, 35

Latin Symbols

Notation	**Description**	**Page List**
$\bar{0}$	3x3 Zero Matrix	38
A	RFA Approximation Coefficient	51–56
A	Area	24, 25, 34
$\mathbf{A}$	System Matrix	53, 55
A	Aerodynamic Influence Coefficient Matrix	31, 32
a	Aerodynamic Influence Coefficient	30
$\mathbf{B}$	System Input Matrix	53–56
b_{Ref}	Reference Span	48, 53, 55
C	Damping Matrix in Local Coordinates	53, 54
C	Aerodynamic Coefficient	48, 134
$\mathbf{C}$	System Output Matrix	53, 54, 56
c_{Ref}	Reference Span	48, 54
cg	Center of Gravity Vector	42
c_p	Pressure Coefficient	34
D	MS Approximation Coefficient Matrix	52, 54, 55
E	MS Approximation Coefficient Matrix	52, 54–56
E	Energy	41, 42
E	Young's Modulus	24
$\boldsymbol{f}$	Force Vector in Global Coordinates	39, 40, 46, 47
f	Force Vector in Local Coordinates	21, 22, 24, 31, 33, 34, 40, 43, 45, 47–51, 53, 56
G	Shear Modulus	24

Notation	**Description**	**Page List**
G	Transfer Function	64, 80, 82, 87, 93, 110
g	Gravitational Acceleration	1
$\hat{\mathbf{I}}$	Stacked Identity Matrix	39–43, 45, 48, 52
$\boldsymbol{I}$	Identity Matrix	53–55
$\bar{I}$	3x3 Identity Matrix	38
$\mathbf{I}$	Inertia Tensor	42, 43, 45, 48
I	Second Moment of Area	24
$\boldsymbol{K}$	Stiffness Matrix in Global Coordinates	39, 40
K	Stiffness Matrix in Local Coordinates	22, 24, 40, 43, 45, 47, 52–56
k	Gain	80–82, 87, 90, 93
k	Reduced Frequency	51
$\underline{\boldsymbol{K}}$	Stiffness Matrix of Free Flying System	43
l	Length	25
$\mathbf{L}$	Lemma Variable	38, 39
$\boldsymbol{M}$	Mass Matrix in Global Coordinates	39–43, 45, 48
M	Mass Matrix in Local Coordinates	22, 24, 39, 40, 42, 43, 45, 47, 52–55
m	Moment Vector in Global Coordinates	53, 56
$\mathbf{m}$	Mass Tensor	42, 43, 45, 48
m	Mass	25, 48
Ma	Mach number	35, 48, 51
$\underline{\boldsymbol{M}}$	Mass Matrix of Free Flying System	42, 43
$\vec{n}$	Normal Vector	34
n	Number of	42, 51
n	Nodal Index	37
n_{nodes}	Number of Structural Nodes	39
n_p	Number of Panels	34

Notation	**Description**	**Page List**
n_z	Load Factor	49
P	Propagation Matrix	32
p	Root of Rational Function Approximation	51–53
$\mathbf{p}$	Roll Rate	18, 31, 32, 44, 48, 57, 107, 134
PG	Prandtl-Glauert Correction Factor	35
Q	Generalized Aerodynamic Coefficient	50–52, 56
q_∞	Dynamic Pressure	18, 48, 51–53, 55, 56
$\mathbf{q}$	Pitch Rate	18, 31, 32, 44, 48, 57, 82, 85, 93, 96, 98, 134
R	Root Matrix for Minimum State Approximation	52, 55
$\bar{\mathbf{R}}$	Total Rotation Matrix	39–43, 45, 48, 52
R	3x3 Rotation Matrix	16, 18, 36–38
$\mathbf{R}$	Nodal Rotation Matrix	38, 39
$\hat{\tilde{\mathbf{r}}}$	Stacked Global Skew Symmetric Matrix	39–43, 45, 48, 52
$\hat{\mathbf{r}}$	Stacked Coordinates of Deformed Aircraft relative to Aircraft Reference Point	38–41, 43, 45, 48
$\mathbf{r}$	Nodal Position / Orientation Vector	38, 39, 41
$\widetilde{\mathbf{r}}$	Skew Symmetric Matrix of Nodal Coordinate and Orientation, deformed a/c	38, 39
r	Position Vector	15, 36–41, 43, 45, 46, 48
$\mathbf{r}$	Yaw Rate	18, 31, 32, 48, 57, 133, 134
$\widetilde{r}$	Skew Symmetric Matrix of Nodal Coordinate, Deformed Aircraft	38
S_{Ref}	Reference Area	48, 54
s'	Nondimensionalized Laplace Variable	51, 52

Notation	**Description**	**Page List**
s	Laplace Variable	52, 53, 55, 64, 82, 99
T	Transformation Matrix	21
$T_{\Theta 2}$	Longitudinal Dynamics Time Constant	82
u	Velocity in x-Direction given in Body-Fixed Frame	17, 18
$\mathbf{v}$	Velocity Vector	17
V	Velocity Norm	1, 53–55
v	Velocity in y-Direction given in Body-Fixed Frame	17, 18
w	Downwash Velocity	30
w	Velocity in z-Direction given in Body-Fixed Frame	17, 18
$\mathbf{X}$	x Position relative to E	17
x	State Vector	46, 53, 55, 56
$\mathbf{Y}$	y Position relative to E	17
$\mathbf{Z}$	z Position relative to E	17
z	Modal Coordinate	42, 43, 45, 48, 51–53, 55–57

Greek Symbols

Notation	**Description**	**Page List**
α	Angle of Attack	18, 31, 32, 48, 57, 85, 133, 134
β	Sideslip Angle	18, 31, 32, 48, 57, 71, 134
δ	Displacement	36, 37
δ_T	Thrust Control	61
$\boldsymbol{\delta}$	Global Deformation	39–42
δ	Local Deformation	22, 24, 26, 31, 32, 39–42
ε	Nodal Orientation of the Undeformed Aircraft relative to the Aircraft Reference Point	37, 41
η	Pitch Control Stick Input	61, 62, 82, 87
Γ	Vorticity	30–34
λ	Eigenvalue	24
$\mathbf{\Phi}$	Velocity Potential	29
$\mathit{\Phi}$	Roll Angle	17, 18, 57, 109, 110
$\mathit{\Phi}$	Phase Offset	34
$\mathit{\Psi}$	Yaw Angle	17, 57
ψ	Eigenshape Matrix	24, 42, 43, 45, 48, 52
ρ	Density	24, 25, 31, 34, 54

Notation	**Description**	**Page List**
τ	Time Constant	82, 87, 90, 99, 100
Θ	Pitch Angle	17, 18, 57, 87
$\tilde{\Omega}$	Skew Symmetric Angular Rate Tensor	37, 38
$\bar{\tilde{\boldsymbol{\Omega}}}$	Stacked Rotation Tensor	39–41
$\tilde{\boldsymbol{\Omega}}$	Rotation Tensor	38, 39
ω	Angular Rate	18, 37–43, 45, 46, 48, 64, 65, 80
ξ	Roll Control Stick Input	61, 62, 64, 99, 107, 110
ζ	Yaw Control Pedal Input	61, 62
ζ	Actuator Damping	64

Subscripts

Notation	Description	Page List
0	0th Order (constant)	50–52, 54–56
1	1st Order	51, 52, 54–56
2	2nd Order	51, 52, 54–56
A	Aerostructural Frame	15, 16, 18, 36–43, 45, 46, 48
A	Amplitude	34
Aer	Aerodynamic	21, 48–50
air	Air	31, 34
as	Related to Aerodynamic Surface	25
B	Body Fixed Frame	16, 18
b	Bound	32
BC	Boundary Condition	41
BW	Bandwidth	87
const	Constant	34
c	Control	48, 50–56
cmd	Command	64
dyn	Dynamic Component	56
el	Element	25, 42
e	Elastic	49–56
encl	Wingbox Enclosed Area that Contains Fuel	25
fuel	Fuel	25
fus	Related to Fuselage	25
g	Gravity	48, 51

Notation	**Description**	**Page List**
Kin	Kinetic	41, 42
L	Lag State	53, 55, 56
l	Moment about Body-Fixed x Direction	48
lc	Load Carrying	25
M	Mean Axis Frame	16
m	Moment about Body-Fixed y Direction	48
m	Modal	43, 45, 47, 51, 52, 54–56
ms	Minimum State Method	55, 56
N'	Nodal Fixed Frame in Undeformed State	36–39
N	Nodal Fixed Frame	36–39, 42
n	Moment about Body-Fixed z Direction	48
n	Nodal	15, 36–39, 41
N	nth Order	52, 56
P	Pilot	87, 90
p	Aerodynamic Panel	31, 33, 34
pld	Related to Payload	25
ps	Primary Structure	25
qs	Quasi-Steady Component	56
Ref	Reference	18, 42
R	Rogers Method	53, 54
R	Roll Motion	99, 100, 104
r	Rigid	49–56
S	Spiral Motion	99
sec	Secondary Mass Components	25
SP	Short Period	65, 82, 85
ss	Steady State Value	96, 98
st	Steady Component	33, 34
Str	Given in Structural Environment/Solver	21
T	Thrust	48, 51

Notation	**Description**	**Page List**
t	Translation	36–39, 41
us	Unsteady Component	33, 34
w	Wake	32, 33
x	Component in x-Direction	15, 36–38, 42, 48
y	Component in y-Direction	15, 36–38, 42, 48
z	Component in z-Direction	15, 36–38, 42, 48

Superscripts

Notation	Description	Page List
E	Earth Fixed Frame	15–18, 36–43, 45, 46, 48
T	Matrix Transpose	15, 16

1. Introduction

The strong competition among airlines is driving the demand for increasingly fuel efficient aircraft. The Advisory Council for Aeronautics Research in Europe (ACARE) has also set ambitious goals aiming at a significant reduction of the environmental impact caused by civil air transportation [6] [102]. The competition for aircraft manufacturers is getting harder due to a rising number of companies that can design and manufacture airliners. Thus well established aircraft companies are looking at new aircraft configurations that promise a huge step of improvement, especially in terms of fuel efficiency and emissions, in order to maintain their head start. The main factors contributing to the overall aircraft fuel efficiency can be identified quantitatively by investigating the Breguet Range equation [125]:

$$A/C \text{ Range} = \frac{V}{g}\frac{1}{\text{SFC}}\frac{L}{D}ln\left(1+\frac{W_{\text{Fuel}}}{W_{\text{Payload}}+W_0}\right). \tag{1.1}$$

Eq. 1.1 describes an aircraft's range as a function of the lift to drag ratio L/D, the structural airframe weight W_0 and the Specific Fuel Consumption (SFC) of the propulsion system. The factors W_{Fuel} and W_{Payload} represent the weight of the fuel and the weight of the payload, is the aircraft velocity, and g is the gravitational acceleration. The lift to drag ratio L/D is subject to aerodynamic design and optimization, whereas W_0 is impacted by the structural design and component weights, while the SFC is determined by the propulsion system. Leaving the propulsion system out of consideration, the required fuel for a given flight mission can for this reason be reduced by improving aerodynamics and by decreasing the aircraft structural weight. The improvement of the lift to drag ratio L/D, and the reduction of the airframe weight W_0, usually pose a compromise, as improving one of the factors will negatively impact the other. Multidisciplinary considerations in the aircraft design process are thus of great importance to find the optimal trade-off for the most efficient design.

Since the beginning of air transport nearly all transport aircraft are classic wing-tube configurations with a vertical, and a horizontal stabilizer at the rear end of the fuselage. This convergence in configurations unfortunately has limited the potential for significant improvements in the aerodynamic aspects of the design. In order enable an improvement of aerodynamics beyond the limits of what is possible through incremental changes in existing designs, novel unconventional configurations are investigated increasingly [27]. The most obvious measures to improve the aerodynamic efficiency are on the one hand the increase of the wing aspect ratio, and on the other hand the introduction of non-planar wings, which reduce the induced drag [71] [95]. Additionally taking into account the structural weight, the aerostructurally optimal spans increase as the material properties improve,

Figure 1.1. – Examples for Unconventional A/C Configurations, Illustration Credits see Appendix D

both for metallic and for composite material wings [65]. This explains the evolution of passenger transport aircraft towards higher aspect ratio wings and the increasing activities in the investigation of unconventional novel configurations (UCC) for future airliners. Among these novel configurations are the blended wing body configuration [75] [80], High Aspect Ratio Wing (HARW) configurations such as the Boeing SUGAR truss braced wing [27] or the D8 transport configuration [35], but also forward swept wing concepts aiming at an improvement of laminar flow capabilities as for example the DLR Project LamAiR [113] and others such as box-wing configurations investigated by NASA and Lockheed Martin [76] or the C-wing concept [58] [82] [95], all shown in Figure 1.1. These efforts to increase fuel efficiency via aerodynamic and structural design lead to higher aspect ratios or non-planarities which increase airframe elasticity.

1.1. Motivation

The design of new conventional wing-tube configurations by incremental design changes comes at a comparably low and well assessable risk. This is for the reason that the properties of this configuration are well understood and the necessary design tools in combination with a lot of experience are available. The design, development, and certification of a new unconventional aircraft type however poses a huge economic risk since this task requires enormous capital expenditures. Moreover, in the case of unconventional configurations the designer cannot draw on previous experience, as many aircraft properties might be significantly differing from the standard wing-tube configuration, and possibly unanticipated aircraft behavior may be discovered in late design phases. Furthermore not all the necessary tools are available or applicable for non-standard configurations.

The aircraft design process is essentially divided into three main design stages, the conceptual design, the preliminary design and the detailed design phase. As most of the life-cycle cost of an aircraft is incurred during the first out of the three design stages [25] it is essential for an economic design process to develop an excellent understanding of a new unconventional configuration before proceeding to stage two. Redesigns and corrections in the later design phases are very costly and can lead to significant program delays. Thus the associated risk for a new design can be reduced significantly by increasing this early design knowledge.

The investigation of unconventional and high aspect ratio configurations in conceptual design poses new challenges. Especially aeroelasticity and flight dynamics, as well as their interaction have to be considered in greater detail, because an increasing impact thereof is expected. Liebeck e.g. [75] identified the flight mechanics to be critical for the blended wing body configuration. The consideration of aeroelasticity in the conceptual design phase is required for two major reasons. Firstly in order to achieve a design close to the optimum efficiency, the aerodynamic design and the structural design can not be performed independently. These two disciplines are significantly interdependent, since aerodynamic loads pose the sizing loadcases for a large fraction of the airframe structure. In turn structural deformations influence aerodynamic loads and aerodynamic efficiency. These interdependencies impact the structural weight as well as the aerodynamic properties and hence the performance. Secondly aeroelasticity impacts stability and control characteristics in multiple ways. On the one hand classic aeroelastic instabilities such as divergence, control reversal, or flutter can occur, which were indeed found to be prevalent for the SUGAR configuration shown earlier [112]. On the other hand interactions with flight dynamics can have a significant influence, one example being that the deformation of the wing shifts the neutral point of the aircraft and thus impacts the static stability margin.

One major driver for the success of a commercial transport aircraft in the current market environment is the fuel or energy efficiency, which makes the previously mentioned UCCs very attractive. However, many other design and certification requirements have to be met for an aircraft configuration in order to reach market readiness. The overall goal of the aircraft design process is to find an optimal design that both increases efficiency and complies with all other requirements and regulations. In order to certify an aircraft for commercial purposes, airworthiness requirements according to EASA CS-25 [37], which ensure the safe operation of the vehicle over the entire operational envelope have to be fulfilled. These among others include aircraft stability, controllability and handling qualities. The detailed investigation of certification requirements is becoming increasingly important in the early design phase for novel designs, as aircraft properties can not be anticipated as well as for the conventional configuration. Certification requirements may also significantly drive the design and potentially interfere with other design goals. Therefore their consideration during the concept selection and conceptual design investigations is important.

The consideration of aeroelasticity as a separate discipline is however insufficient as aircraft designs evolve. Due to the increasing flexibility of the aircraft, which is a result of optimization towards higher fuel efficiency, the structural mode frequencies move closer to the rigid body aircraft dynamics. This leads to an increasing impact of elastic deformations on the flight dynamics, which can in many cases also play a major role for airworthiness requirements. Wazak et. al. [132] showed that there may be a severe detrimental impact on the desired aircraft behavior such as stability and handling qualities. Therefore using the common simplification of a rigid body for flight dynamic and control investigations may no longer be valid. It is therefore necessary to model aeroelasticity and flight dynamic aeroelastic coupling effects in the early conceptual design process to consider it's impact before the design is evolved to a certain detail and maturity, where design changes become more costly. This can be achieved by introducing more advanced methods and models into conceptual design providing a better insight into potential issues and problems.

1.2. Objectives

As explained in Section 1.1 an improved fidelity in conceptual design is becoming increasingly important as aircraft flexibility increases and configurations change to less conventional ones. The aim of this dissertation is to perform a step towards the enhancement and refinement of conceptual design methods, improving the overall aircraft concept assessment capabilities and assessment accuracy for unconventional and high aspect ratio wing aircraft designs. It is highly desirable for the aircraft designer to assess potential risks as early as possible in the design phase and to correctly analyze properties which were previously unforeseeable. Specifically this work aims at the concept assessment with respect to flight dynamics and aircraft handling qualities of the flexible aircraft, which is addressing a major challenge arising with the increasing flexibility of future transport aircraft. The main objectives are thus:

- The design and implementation of a highly automated process for the preliminary assessment of unconventional aircraft designs with respect to airworthiness requirements including stability, controllability as well as handling and flying qualities considering aircraft flexibility.
- The derivation of a method which is not limited to a certain configuration but open for the application on different unconventional designs and furthermore allowing an arbitrary control surface layout.
- An implementation of the method which is computationally efficient enough to allow the assessment of multiple concepts within a short amount of time.
- The implementation of a process chain in an object oriented fashion ensuring generality as well as the ability to easily exchange and update methods and subroutines.
- The demonstration of the process on the example of an unconventional aircraft, comparing the results to a conventional design, and the rigid aircraft respectively.

In order to meet the objectives, a multidisciplinary integration of the disciplines of aeroelasticity, flight dynamics and structural sizing, applied to conceptual aircraft design

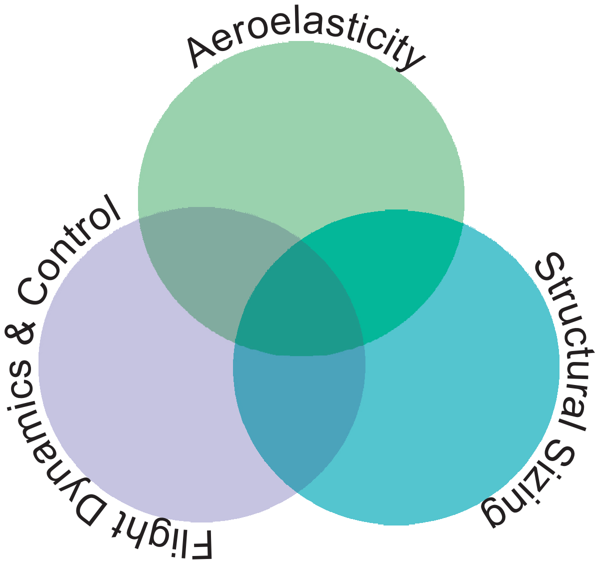

Figure 1.2. – Overlapping of Research Areas Emerging from Increased Flexibility

is required as depicted in Figure 1.2. The process for the aircraft concept assessment can be divided into three major steps as depicted in Figure 1.3. The first step is the rapid generation of an elastic aircraft model. Then the aeroelastic model is combined with the flight dynamic equations of motion to form an integrated flight dynamic aeroelastic model. Finally the airworthiness of the flexible aircraft requirement is assessed. The three main steps are detailed in the following:

- *The rapid generation of an elastic aircraft model*
  A conceptual design level aeroelastic model has to be generated in a rapid and automated process for an arbitrary aircraft configuration, at the same time being able to cope with the low amount of known parameters in the conceptual design phase. These parameters are typically the geometry as well as payload, weights and material definitions. The model shall be based mostly on physical methods instead of empirical methods to avoid applicability issues for unconventional configurations and to improve reliability.

- *The integration of the aeroelastic model with the flight dynamic equations of motion*
  The aeroelastic aircraft model has to be integrated with the flight dynamic equations of motion in order to allow the simulation of the properties of the free-flying flexible aircraft. A reduced order, and fast time capable flight simulation model is generated automatically for efficient aircraft assessment, and to facilitate pilot in the loop simulations for further investigations. This requires the rapid prototyping of flight control laws to further assess the closed loop aircraft behavior.

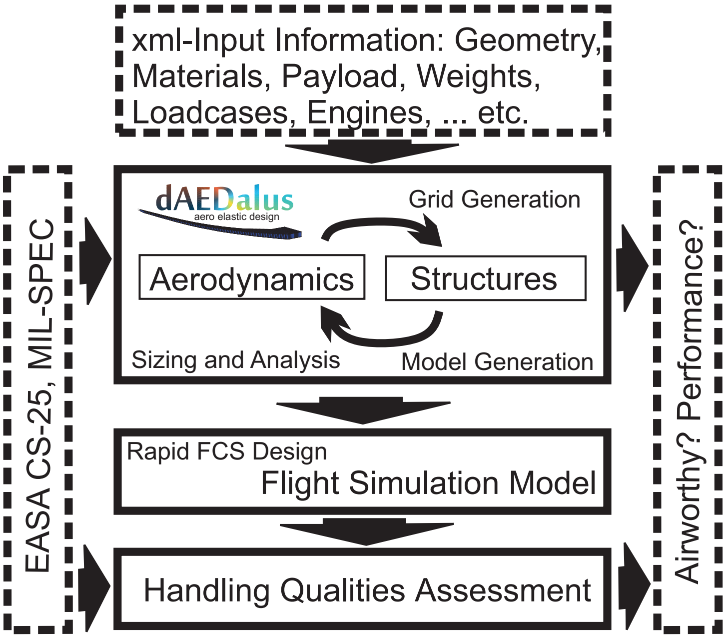

Figure 1.3. – Process for A/C Concept Assessment

- *Airworthiness requirement assessment*
  The flight simulation model is then applied for the assessment of aircraft stability, controllability and handling qualities considering EASA CS-25 requirements [37] as well as additional requirements such as the military specifications for the flying qualities of piloted aircraft [129] issued by the U.S. Department of the Defense.

1.3. State of the Art and Literature Survey

This section presents the state-of-the-art for conceptual aircraft design methods and tools as well as the relevant disciplines required for this work, which include the structural design, aeroelasticity as well as flight dynamics, control, and aircraft handling qualities. The literature survey first addresses conceptual aircraft design and then step by step sums up the additional disciplines required to cover the objectives of this work. The results of this thesis were already partly published in [115], [116] and [117] by the author.

1.3.1. Conceptual Aircraft Design

Traditionally conceptual aircraft design is performed mostly relying on handbook methods based on semi empirical relations and data, such as found in [101] or [123]. The prediction of weights, which is an important part in conceptual design, is commonly performed relying on statistical-based approaches. A more detailed knowledge of the aircraft structure is thus basically absent until the preliminary design phase. Statistical based methods are however unreliable for unconventional configurations and HARW designs, since they are not based on actual physical loads, and do not take into consideration the unique properties of a certain configuration [25], [26]. The wing weight estimation was improved compared to statistical based approaces for wings using predictions based on actual aircraft loading see [7], [17], [26], [95] and [114]. A wing weight estimation method for the strut-braced-wing was developed by Chiozzotto [100] considering aeroelastic effects. The research project SimSAC (simulating aircraft stability and control characteristics for use in conceptual design) funded by the European Community under Framework 6 focused on enhancing the conceptual design and early preliminary design processes by developing an integrated digital design and decision-making environment, called CEASIOM (computerized environment for aircraft synthesis and integrated optimization methods) in which for any given aircraft configuration, the specific information for weight prediction, aeroelastic analysis, performance, stability, and control assessment can be computed at a specific user-defined fidelity level. Recently an open source conceptual design framework called SUAVE (Stanford University Aerospace Vehicle Environment) was published [20], [79] which presents the latest state-of-the-art in conceptual design. As aircraft become more and more flexible, there is a strong interest to consider aeroelastic effects right from the beginning, since redesign during the preliminary design phase is very expensive. Furthermore the predicted weight differs compared to a rigid sizing procedure [64]. In order to consider aeroelastic requirements a sufficiently detailed structural model must be available. The necessity to include a more elaborate aeroelastic model in conceptual design was noted by Ricci and Cavagna [26] who made significant contributions in that field. The developed tool NeoCASS (Next generation Conceptual Aero Structural Sizing) enables the aeroelastic assessment of preliminary concepts with some restrictions. NeoCass is providing a simplified stick model with automated sizing and aeroelastic analysis capabilities. The sizing of the stick model in NeoCass is based on rigid aircraft VLM loads. Other recent literature contributions improve the applicability of handbook methods to future concepts such as nonplanar wings [124], but still rely on empirical data.

1.3.2. Flexible Aircraft Flight Dynamics

In the beginning of aeronautical research, the fields of flight mechanics and aeroelasticity have been studied as separate disciplines for a long period of time. This was a good approximation for most early aircraft designs, but for many recent designs a significant coupling of these disciplines occurs, such as for large transport aircraft with low frequency structural modes or high agility aircraft. The motion of the elastic aircraft was among others addressed by Waszak and Schmidt [133], Waszak and Butril [131] and Bisplinghoff [18] or Schwanz [111] assuming the aircraft structure to be a continuous elastic body. Many methods dealing with flight dynamics of elastic aircraft rely on the inertial decoupling of rigid body motion and elastic deformation, applying the so called "mean-axis" approach introduced by Milne [88]. The mean axis reference frame is a free floating reference frame positioned at the instantaneous center of gravity of the body, and thereby decoupling the rigid body motion and elastic body motion. This mean axis approach neglecting inertial coupling was questioned by Meirovitch and Tuzcu [84] arguing that a fixed point reference frame is better suited and provides better accuracy for the analysis of free flying elastic vehicles. They suggest a different approach [85], [127] based on a Lagrangian formulation and quasi coordinates for an aircraft with a continuous structural model. Reschke [103], [104] formulates the equations of motion for the elastic aircraft using a Lagrangian approach considering inertial coupling. The approach is tailored towards the incorporation of Finite Element (FE) models of the aircraft structure. The proposed method is suitable for loads computation and flight dynamic investigations. Li [73], [74] and Abbasi [4] investigated differences between the mean-axis and a fixed-axis approach finding moderate differences, however leaving certain interesting points open for further investigation. As the fixed-axes equations consider the effect of elastic deformation on the 1^{st} and 2^{nd} mass moments of inertia they have the potential to produce more accurate results. Nikravesh [94] provided a comprehensive comparison of the mean-axis and fixed-axis equations.

The application of integrated aeroelastic flight dynamic models reaches from flight dynamic investigations, flight simulation and control systems design to flight loads computation. Models for flight dynamic investigations, flight simulation and control systems are often aiming at the elastification of existing rigid body or quasi steady flight dynamic models. Schuler [110] developed an integrated aeroelastic, flight dynamics model and applied the model to the design of control laws for active structural damping. This model is extended by Hanel [45] for a wider range of the flight envelope who then develops control laws for integrated aeroelastic flight control [44], as structural and flight dynamic modes are not clearly separated. Different variations of this approach were further developed by Schuler and König [70] (KS-approach) as well as Winther [135], also aiming at the elastification of existing rigid body or quasi steady flight dynamic models. The method by Winther was extended by Looye [77] for the application on a quasi steady nonlinear flight mechanics model, using an elastic force feedback into the rigid equations of motion based on the state output, further referred to as the minimum residual approach (MS-approach). Reschke [105] compared the KS, and the MS-approach finding both providing very similar results. Both are efficient in terms of computation power requirements, however finding the MS-approach more flexible since the consideration of the dynamic pressure dependency is possible. Silvestre [118] presented another approach for the continuous flight simulation of an elastic aircraft over the entire flight envelope, based on Waszak and Schmidt and applying strip theory to determine the unsteady aerodynamic forces. A method for the generation of purely linear aeroservoelastic models is suggested by Baldelli [10] who further corrects computational aerodynamic data with wind tunnel measurements to better represent the flight dynamics. The decoupling of the rigid- and flexible-body equations of motion, with the exception of aerodynamic forces, is commonly assumed in above methods. Methods for loads computation were presented by Kier [66], [67] and Hofstee et. al. [53]. The methods mentioned so far mostly rely on linear finite element beam models and Doublet Lattice Method (DLM) aerodynamics, which has become a quasi standard for industrial applications. The frequency domain potential flow generalized aerodynamic coefficients determined by the DLM are commonly approximated by means of the Rational Function Approximation (RFA) using the method of Rogers [107] or Karpel [60] and then transformed into the time domain. The generalized aerodynamic coefficients are computed using the free-free elastic modes, which are a result from the mean-axis approximation and automatically ensure that the mean-axis conditions are met. A different model for loads prediction in wake vortices based on the Unsteady Vortex Lattice Method (UVLM) was developed by Mauermann [81]. High fidelity integrated aeroelastic flight dynamic methods are mostly intended for loads computation where a better accuracy is required. An integrated aeroelastic flight dynamics time domain model, incorporating Computational Fluid Dynamics (CFD), extracting the unconstrained free-free vibration modes from a FE model was developed by Ritter [106]. Wellmer [134] developed a free flying elastic model in the time domain by coupling a CFD solver, a FE solver and the flight dynamics equations via a general coupling approach. All above methods presume linear elastic structural properties. Models for the simulation of free flying aircraft with nonlinear structural deflections are subject of more recent and current research especially driven by Cesnik and Palacios [98], [99]. Furthermore structurally nonlinear flight dynamic aeroelastic models were developed and investigated by Simpson and Palacios [119], Murua et. al. [91], Hesse and Palacios [49] and Drela [34].

1.3.3. Structural Sizing

The automated structural sizing of aircraft structures and airframe parts has gained popularity since the increasing computational speed and resources enable the use of more advanced models earlier in the design. For conceptual design the tool NeoCass Smartcad was created [26], which allows the overall sizing of an aircraft structure but does not involve an iterative aeroelastic sizing process. The author [114] designed a tool for the iterative aeroelastic sizing of conventional and unconventional wings for the purpose of wingbox mass estimation in conceptual design. Hürlimann [56] created a high fidelity model for the wingbox mass prediction of transport aircraft considering aeroelasticity. Other state-of-the-art tools for the structural sizing and MDO of aircraft configurations are PRADO (Preliminary Aircraft Design and Optimisation Program) originally developed by Heinze [46], the tool FAME (Fast and Advanced Mass Estimation) developed by Airbus Germany [130] and MDCAD by QinetiQ. Klimmek [68] set up a parametric model for the FERMAT configuration used for multidisciplinary design optimization applying an automated sizing algorithm. This model is however generated on a much higher fidelity level as required for this work and is restricted to the FERMAT configuration. A similar approach in structural sizing however is used in this work. The geometry of the FERMAT configuration is based on the NASA Common Research Model (CRM) which represents a long-range, wide-body transonic transport aircraft. High-fidelity MDO investigations based on the CRM were recently performed by [23] and [24].

1.3.4. Handling Qualities

The fundamentals of handling qualities are laid out e.g. by Hodkinson [51] and Abzug [5]. Handling qualities can introduce critical issues during the development of future aircraft. Waszak [132] showed that flexibility can alter the handling qualities of aircraft. Andrews

[8] investigated the impact of flexibility and active loads control on the handling qualities of a large transport aircraft. Mitchell et. al. [89] summarized the evolution and challenges of handling qualities. Hodginkson [52] outlines the history of the use of Low Order Equivalent systems, used for higher order aircraft systems, where standard Handling Qualities (HQ) requirements, such as the short period frequency cannot be applied directly. Berger et. al. apply advanced HQ criteria to control law design for the longitudial [14] and lateral [13] motion. Damveld [29] developed a method to assess the longitudinal handling qualities of an elastic aircraft using a cybernetic approach.

1.4. Contribution

Current conceptual design methods do not allow a sufficiently thorough assessment of the aircraft with respect to aeroelastic and flight dynamic properties, which play an increasingly important role for future concepts. The developed method introduces the coupled analysis of flight dynamics and aeroelasticity in the conceptual design process, allowing the investigation of the behavior of the free-flying flexible aircraft for arbitrary novel and classic configurations. This leads to an improvement of the fidelity level in conceptual design. In particular the following contributions were achieved:

- A method for the flight dynamics and handling quality assessment for arbitrary aircraft configurations in the conceptual design phase was developed and implemented, only requiring basic geometry, weights and materials definition for the analysis.

- A generic flight dynamic model considering aeroelasticity was introduced in the conceptual design phase. Given the state-of-the art, flight dynamic investigations are only made based on a rigid aircraft model, and aeroelastic investigations such as in [26] do not consider flight mechanics. The interaction between aeroelastictiy and flight dynamics was not considered before at a conceptual design level. Additionally this method provides the freedom for the investigation of arbitrary configurations. Most of the state-of-the-art work is dedicated to simulating the behavior of a specific given configuration, such as [8], while this thesis focuses on generality and applicability on a wide range of possible Aircraft (A/C) configurations. However [19] meanwhile generated a similar flight simulation model based on the aeroelastic model generated by NeoCass.

- Following the generation of a generic flight dynamic aeroelastic model, a problem first addressed by the author [116], is a more detailed investigation of a wide range of flight dynamic airworthiness requirements out of the EASA-CS 25 [37] and the Military Specifications for flying qualities of piloted aircraft [128] in the conceptual aircraft design stage. The investigations are based on the free-flying flexible aircraft behavior including control laws, and allow for fast time as well as pilot in the loop simulations.

- The generation and sizing of a structural model for conceptual design was refined, considering the redistribution of loads due to aeroelasticity for the overall aircraft [115], which was previously only available for wing sizing [114]. Other state-of-the-art methods [26] which perform an overall aircraft sizing, do not consider the redistribution of the aerodynamic loads due to flexibility but instead are based on the rigid aircraft loads. This can have a significant impact on loads, and hence on the structural mass estimate of high aspect ratio wings and unconventional concepts. The conceptual sizing of the structure based on actual physical loads improves the overall reliability of the structural component weight estimates. The structural model generation is furthermore more general, and allows the modeling e.g. of C-shaped nonplanar wings, or box-wings, which is not possible with the method in [26].

- The integration of a structural sizing model with a free-flying elastic aircraft simulation model is unique. All existing work on flexible flight dynamic simulation mentioned in the previous section requires a readily existing FE model, e.g. a known stiffness and mass distribution of the aircraft which is usually not available at the design stage considered here.

- The method is applied to an innovative C-wing concept plane. A C-wing aircraft promises improved aerodynamic efficiency [116] in cruise but poses significant challenges with respect to control and stability. The flight dynamics and the aeroelastic behavior of such a configuration have never been investigated more closely before.

- As part of this work a number of modeling approaches for the free flying elastic aircraft were investigated. The different implementations allow a direct comparison of the direct, and the indirect simulation of the flexible aircraft. Different integrated methods were derived and compared, based on a consistent model, allowing to compare the impact of different simplifications and approximations.

The developed process chain is on the one hand unique with respect to the ability to quickly model unconventional configurations, including C-wings, box wings or other wing systems, with a large degree of automation. Furthermore, in this work a structural model is generated as part of the process using quasi steady and dynamic loads obtained from the free flying elastic aircraft simulation. The presented highly automated process is speeding up the design process and increasing the design knowledge in early design phases and allows a better understanding of the behavior of unconventional concepts. The method is highly modular allowing an easy exchange and extension of applied methods. The presented code was built from scratch only drawing on the finite element code for wing structures developed by the author [114], which was however further refined in this work. The tool developed during this project is called dAEDalusNXT. Figure 1.4 is comparing the tool developed during this work to other state-of-the-art design tools. Especially the conceptual design tool CEASIOM developed as part of an European Union funded research project already covers a wide range of multidisciplinary considerations. It can be seen that there were however some gaps which were closed in this presented work. These gaps in particular included the aeroelastic sizing, as well as the flight dynamic and handling qualities investigation in conceptual design, taking into account the aircraft elasticity.

1.5. Structure of the Thesis

Chapter 2 outlines the modeling of the elastic airframe. At first important notations and definitions are introduced. Then the geometric modeling is outlined along with the aeroelastic coupling. Subsequently the structural, and the aerodynamic modeling of the airframe is detailed. Next the equations of motion for the free-flying elastic aircraft are derived in a discrete form, tailored for the integration of a structural finite element model with six degrees of freedom per node. These equations are then simplified to derive the reduced equations used in many common and industry applied methods for the flight simulation of an elastic aircraft. The different methods are compared on the example of a flexible aircraft configuration in order to show the impact of the respective simplifications. The derived equations are valid independently of the respective finite element model or aerodynamic model. In Chapter 3 the generation of the generic flight simulation system is presented. Chapter 4 presents the certification criteria which are investigated and shows the assessment of an unconventional configuration with respect to handling qualities and compares the results to a classical configuration benchmark aircraft. The results are shown for the rigid and the elastic case. Chapter 5 provides a summary and an outlook.

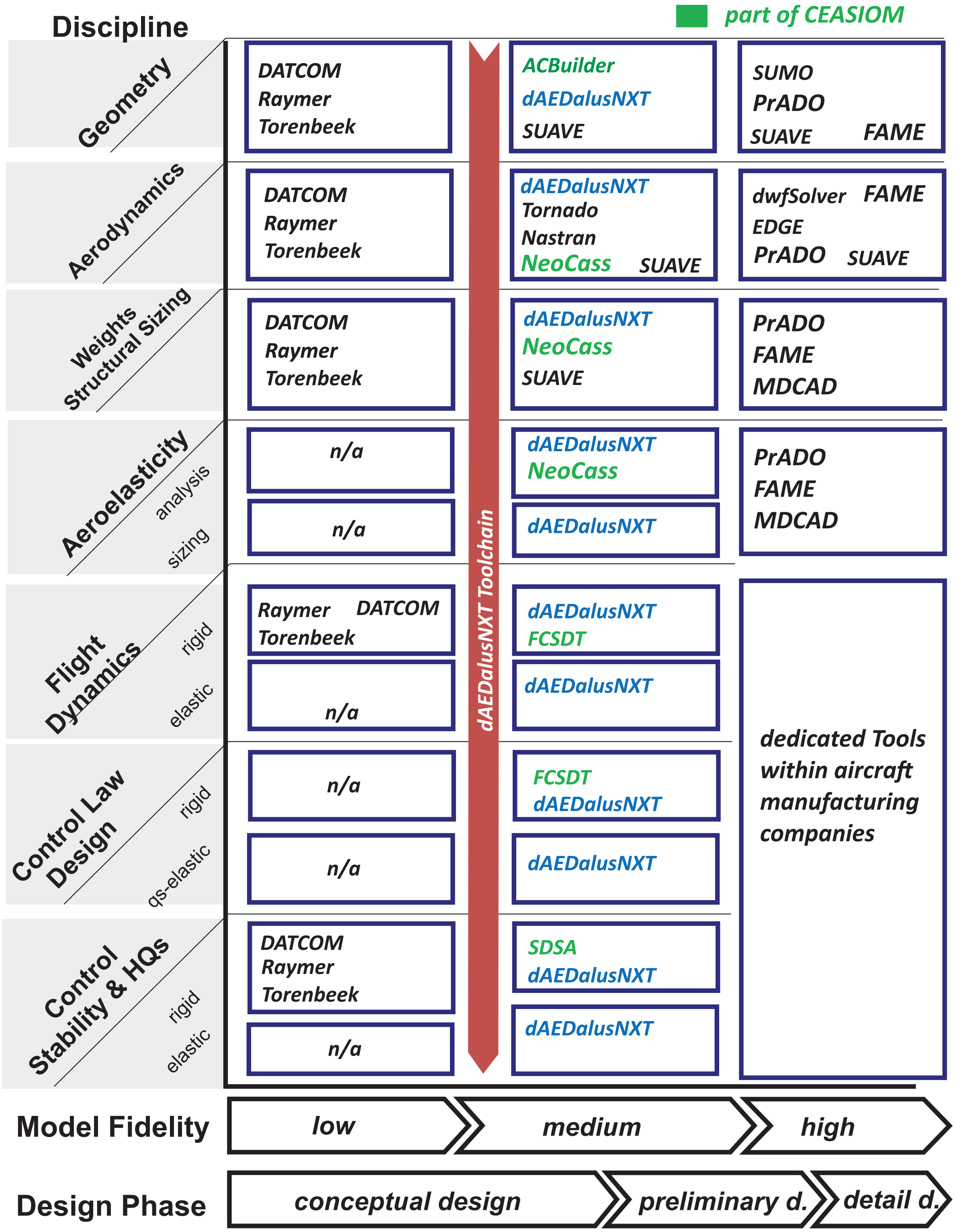

Figure 1.4. – Conceptual Design Tool Landscape (non-exhaustive)

2. Elastic Airframe Modeling

This chapter outlines the modeling of the free flying elastic airframe. The multiple objectives of this work, including the aircraft conceptual sizing, and the fast time flight simulation, require different models which are tailored for their respective purpose. Firstly, an integrated nonlinear flight dynamics, aeroelastic time domain aircraft model is developed, in order to simulate the aircraft dynamic response, as well as static and dynamic loads, required for the structural sizing of the airframe. A similar model for loads prediction due to wake vortices was developed by Mauermann [81]. Secondly, a fast and efficient flight simulation model is required for fast time flight simulations. Furthermore, linearized flight dynamic-aeroservoelastic models are required for the control system design throughout the flight envelope.
At first, coordinate systems and notations are introduced, and the geometry model is presented including the aeroelastic coupling method. Subsequently, the structural modeling of the airframe is outlined, which includes an automated structural design procedure. Next, the implemented aerodynamic models are presented. Then the equations of motion for the free flying elastic aircraft are derived, which are tailored for the implementation of a six Degree of Freedom (DoF) per node finite element model. These equations of motion are simplified in order to obtain a fast reduced order model, which is similar to most models widely used throughout research and industry e.g. by [45], [70], [78] and [135]. The different modeling approaches for the free flying flexible aircraft are compared and discussed. It is highlighted that the main purpose of the resulting free flying aeroelastic model serves the conceptual investigation of conventional and unconventional elastic aircraft behavior.

2.1. Coordinate Systems and Notations

In order to allow the reader a better understanding of the following derivations and equations, the applied vector and matrix notations and coordinate systems are introduced initially.

2.1.1. Vectors and Matrices

Vectors Vectors are always written in lower case letters, where all four corners of the vector may have index notations, such as

$${}^{E}_{n}r^{T}_{EA} = {}^{E}_{n}\begin{pmatrix} r_x \\ r_y \\ r_z \end{pmatrix}^{T}_{EA} . \tag{2.1}$$

The upper left index states the system in which the vector is noted, while the lower left index may indicate the size of the vector. The upper right index is reserved for mathematical operation symbols and the lower right index indicates the start and end point of the vector.

Matrices Matrices are written in upper case letters, such as

$$^{EA}M_A^T. \tag{2.2}$$

A matrix with upper left index indicates a transformation or rotation matrix, where in this case the indices note the system transformation from the A system into the E system. The upper right index is again reserved for mathematical operation symbols. The lower right index indicates the system in which the matrix is formulated. A $\hat{M}$ indicates that the matrix is stacked for multiple nodes, a $\bar{M}$ indicates an expanded matrix.

2.1.2. Coordinate Systems

Four different major coordinate systems are utilized for the definition of the problem. These are depicted in Figure 2.1. The first coordinate system, denoted by the subscript E, serves as the inertial reference frame which e.g. is required for the derivation of the equations of motion based on Newtons first law. In this application the earth fixed frame is considered sufficiently inertial. The structural model is formulated relative to a coordinate system which is fixed to a specific node on the aircraft structural mesh. The aerodynamic mesh is utilizing the same reference frame, resulting in a common reference frame for aerodynamics and structures which is fixed to the aircraft. This aircraft fixed aero-structural system is noted by subscript A. However many approaches for the computation and simulation of elastic aircraft rely on a so-called "mean-axis" system, introduced here noted by subscript M. This reference frame is a free floating coordinate system remaining at the instantaneous center of mass, independent of the deformation, thereby minimizing the inertial coupling between rigid body motion and elastic deformation [106]. Flight mechanic states are defined in the body fixed frame B. The origin of B may be either a physical structural node, such as the origin of the A frame or attached to the free-floating M frame, depending on the desired information. Specifically for handling qualities investigations the pilot seat location may be used as reference, as these are the state variables perceived by the pilot. The transformation between the body-fixed frame B and the respective reference frame is given by the transformation matrix

$$^{BA}R = \begin{pmatrix} -1 & 0 & 0 \\ 0 & 1 & 0 \\ 0 & 0 & -1 \end{pmatrix}. \tag{2.3}$$

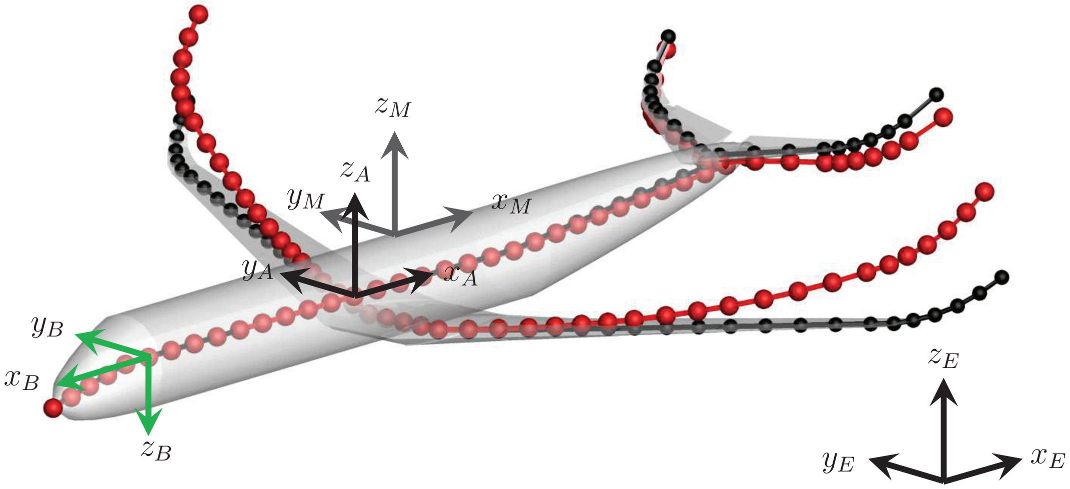

Figure 2.1. – Coordinate Systems

2.1.3. Flight Dynamic States

The flight dynamic state is defined by position, orientation, velocities and rotation rates of the aircraft reference point.

Position The position of the body-fixed frame reference point relative to the earth fixed system origin E is denoted by $\mathbf{X}$, $\mathbf{Y}$, $\mathbf{Z}$.

Orientation The orientation of the body-fixed frame relative to the earth fixed inertial system E is given by the Euler angles

$$\begin{pmatrix} \varPhi \\ \varTheta \\ \varPsi \end{pmatrix} \tag{2.4}$$

where $\varPhi$ is the bank angle, $\varTheta$ is the pitch angle and $\varPsi$ is the heading.

Velocity The velocity vector is denoted by

$$\mathbf{v} = \begin{pmatrix} u \\ v \\ w \end{pmatrix} \tag{2.5}$$

Rotation The rotation rates of the body-fixed frame are given by **p**, **q**, **r** are obtained from the rotation rates relative to the inertial frame using the equation

$$\begin{pmatrix} \mathbf{p} \\ \mathbf{q} \\ \mathbf{r} \end{pmatrix} = {}^{BA}R \begin{pmatrix} 1 & \sin\Phi \tan\Theta & \cos\Phi \tan\Theta \\ 0 & \cos\Phi & -\sin\Phi \\ 0 & \frac{\sin\Phi}{\cos\Theta} & \frac{\cos\Phi}{\cos\Theta} \end{pmatrix}^{-1} {}^{E}\omega_{AE}. \tag{2.6}$$

2.1.4. Aerodynamic States

The aerodynamic angle of attack is defined by

$$\alpha = \tan^{-1}\frac{w}{u} \tag{2.7}$$

The aerodynamic sideslip angle is given by

$$\beta = \tan^{-1}\frac{v}{u} \tag{2.8}$$

The dynamic pressure is determined by

$$q_\infty = \frac{1}{2}\rho V^2 S_{\text{Ref}} \tag{2.9}$$

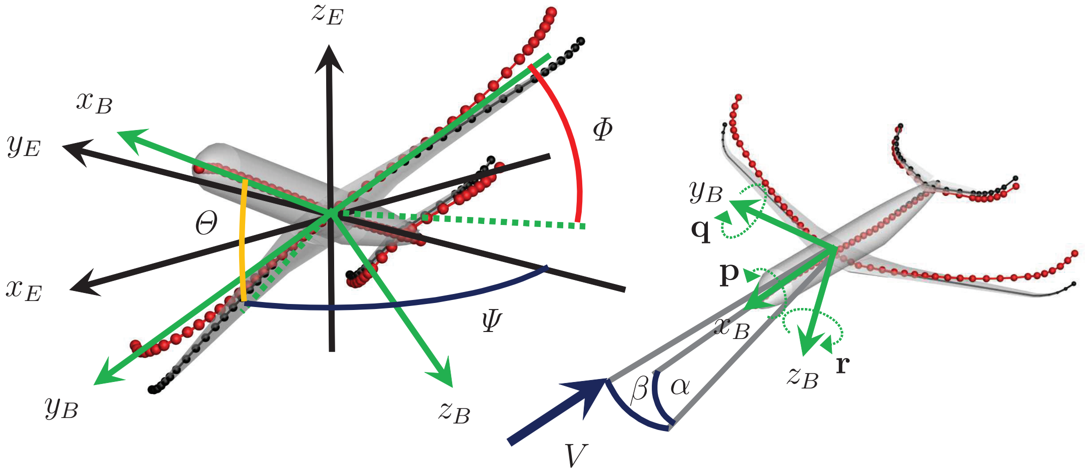

Figure 2.2. – Flight Dynamic and Aerodynamic States

2.2. Geometric Model

One of the objectives of this work stated in Section 1.2 is the fast generation of an integrated flight dynamic aeroelastic model for different aircraft concepts. This means that the process must be able to quickly adapt to changing geometries without manual adjustments. In order to obtain this goal a parametrized geometric master model is generated which allows to automatically produce the meshes for the respective structural and aerodynamic model. The geometric master model is defined using an XML based geometry definition file. The aircraft is described broken down into its components e.g. the main wing, the fuselage, the stabilizer and the engines. Each of the components requires a set of parameters to be defined. The required parameters and the XML format are described in more detail in Appendix E. The geometry model contains the three dimensional geometry of the aircraft including details like the sectional span profiles of the wing and the wing twist. This geometry model is then individually discretized to meet the requirements for the aerodynamic and the structural model, as depicted in Figure 2.3.

The aerodynamic model requires two different geometric representations, as shown in Section 2.4. At first a mean camber representation of all aerodynamic surfaces is produced which is applied for the implemented steady and unsteady vortex lattice method. Furthermore the fully three dimensional aircraft is discretized to allow a skin friction drag estimate based on the wetted surface area. The methods will be described in more detail in Section 2.4. The aircraft structure in this case is represented by beam models. Thus on the one hand the grid of the finite element beam needs to be generated, but furthermore the crosssections of the load carrying structure are required for the presented sizing method, which will be described in more detail in Section 2.3.

2.2.1. Control Surfaces

The geometry model also requires the definition of control surfaces used for longitudinal and lateral control. The deflection is set on the master model and respectively linked to the aerodynamic grid. Control surfaces can be defined on the leading and trailing edge of each aerodynamic surface, more details can be found in Appendix E.

2.2.2. Aeroelastic Coupling

The geometric model also implements the aeroelastic coupling method, transferring structural deformations and aerodynamic loads between the meshes. Due to the different nature of the aerodynamic and structural mesh, transformation rules must be defined. On the one hand the aerodynamic loads from the three dimensional surface mesh must be transformed onto the structural mesh, which in this case is a beam. On the other hand the aerodynamic mesh must deform according to the structural deformations computed by the structural solver. The aeroelastic coupling is performed using a splining method closely following the procedure presented in [21].

Load Transfer The load transfer method assigns a volume perpendicular to the beam axis to each beam element, as shown in Figure 2.4 for a wing with multiple cranks. Within this volume all aerodynamic panel areas are assigned either to this beam element or in case of overlaps, split up and partly assigned to more beam elements using an interpolation.

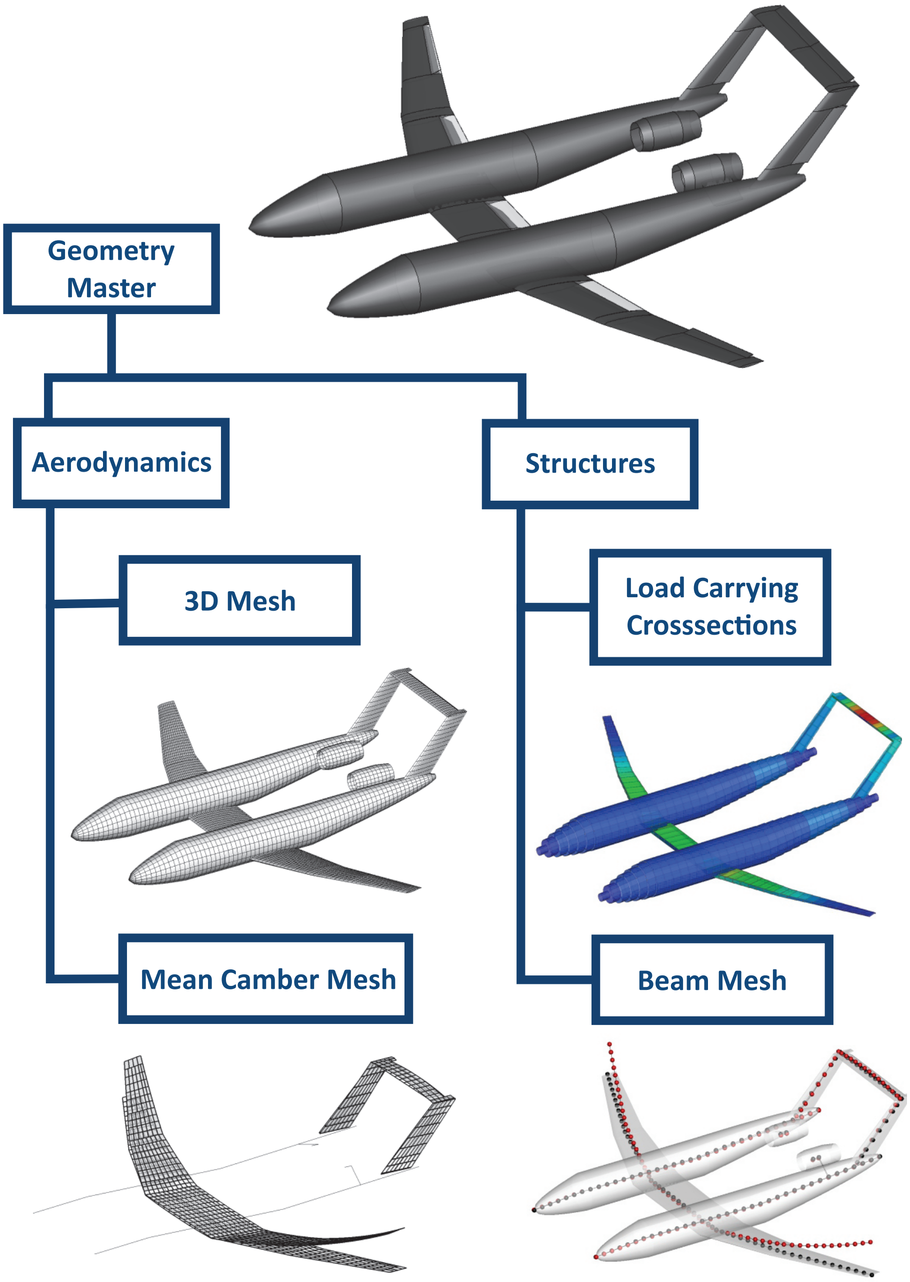

Figure 2.3. – Geometry Model

In a crank some panels may be fully or partly unassigned (see Figure 2.4), where the respective forces are then assigned to the closest structural node. A force transformation matrix is determined in the non-deflected state which performs the transformation from the panel force vector to a beam force vector.

$$f_{\text{Str}} = {}^{\text{StrAer}}T f_{\text{Aer}} \tag{2.10}$$

The method ensures a conservative transformation, meaning that the sum of the forces in a specific direction before and after the transformation are exactly equal. This is validated and shown in Appendix C.4.1.

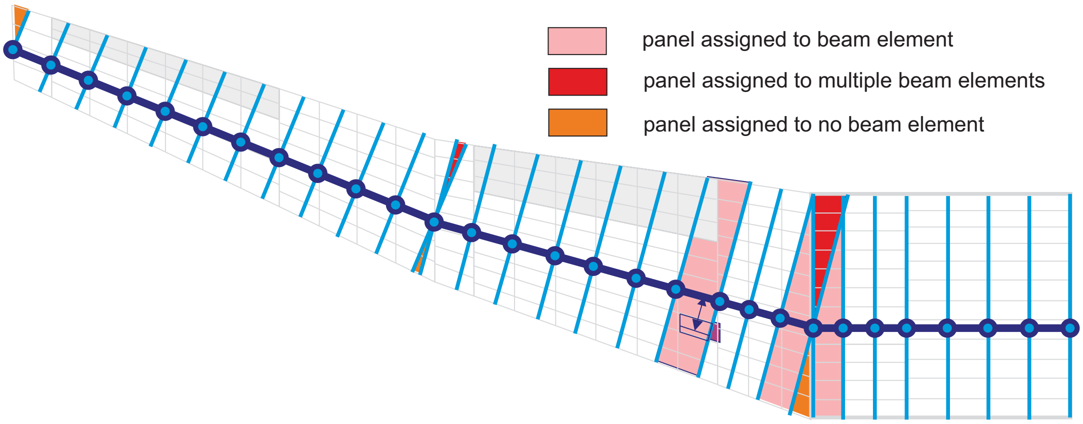

Figure 2.4. – Load Coupling

Deformation Coupling The computed structural deformations are linked to the aerodynamic mesh using geometric relations. In order to project the rotations from the beam elements, stiff elements oriented perpendicular to each beam element between the wing leading and trailing edge are introduced (see Figure 2.5) which are used for the interpolation of aerodynamic mesh grid-point deformations. A validation of the aeroelastic coupling algorithm is found in Appendix C.4.

2.3. Structural Modeling

The structure of most transport aircraft as well as many other aircraft types such as UAVs is composed of high aspect ratio components such as the wing, the fuselage and the tail. For this type of structure, beam models are well capable of representing desired characteristics and are therefore frequently used for modeling elastic airframes, especially in the early design phases [53]. In the presented process beam models are applied to represent the airframe structure. For this purpose the airframe is separated into its main components which are individually modeled as beams. This breakdown is shown in Figure 2.6 in more detail for the example of an unconventional configuration.

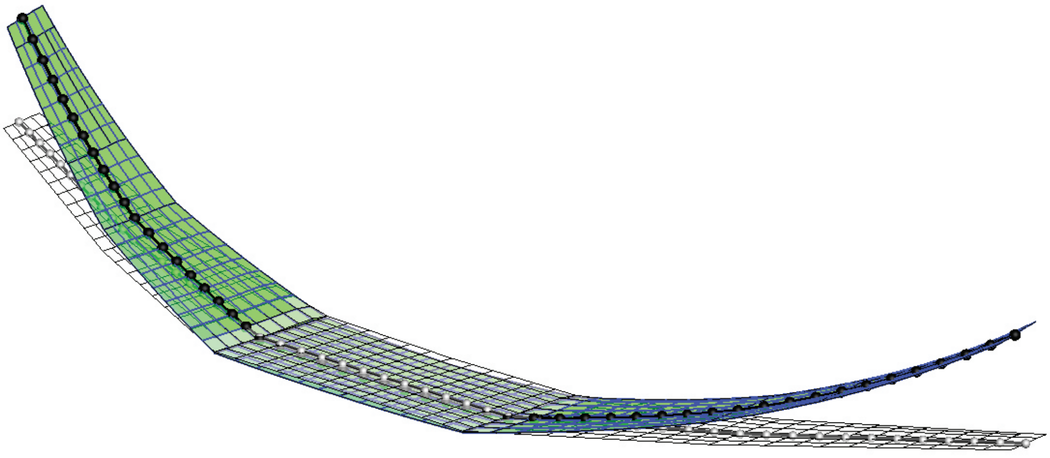

Figure 2.5. – Deformation Coupling

2.3.1. Finite Element Method

The airframe structure is discretized by means of a Finite Element Method (FEM) implemented as a classical stiffness method. The airframe components, which are simplified as beam structures, are represented by means of three dimensional beam elements with six degrees of freedom per node (DoF), three translational and three rotational DoF. The beam grid is positioned along the elastic axis of the respective component. The beam element stiffness and mass matrices are derived from the weak form of the differential Euler-Bernoulli beam equation. The element governing equations for the beam can be found summarized in the Appendix A.1 and are also described in more detail in references [83] or [137]. The individual element stiffness and mass matrices are compiled into a single global stiffness matrix K and mass matrix M which govern the behavior of the entire structure. The different airframe components are connected using coupling conditions.

Quasisteady Analysis For static analysis the nodal forces and nodal displacements are related through the stiffness matrix K via the following relation

$$K\delta = f \tag{2.11}$$

where δ are the nodal displacements and f are the external forces. In order to allow the solution of this equation with respect to δ, boundary conditions must be imposed, since K has a rank deficiency of six. These boundary conditions can either be set by restraining each degree of freedom at least once, or in order to obtain a solution for an unrestrained structure by transforming the system into modal coordinates and removing the rigid body modes. The quasi steady nodal deformations of the structure are given by the following equation

$$\delta = K^{-1}f \tag{2.12}$$

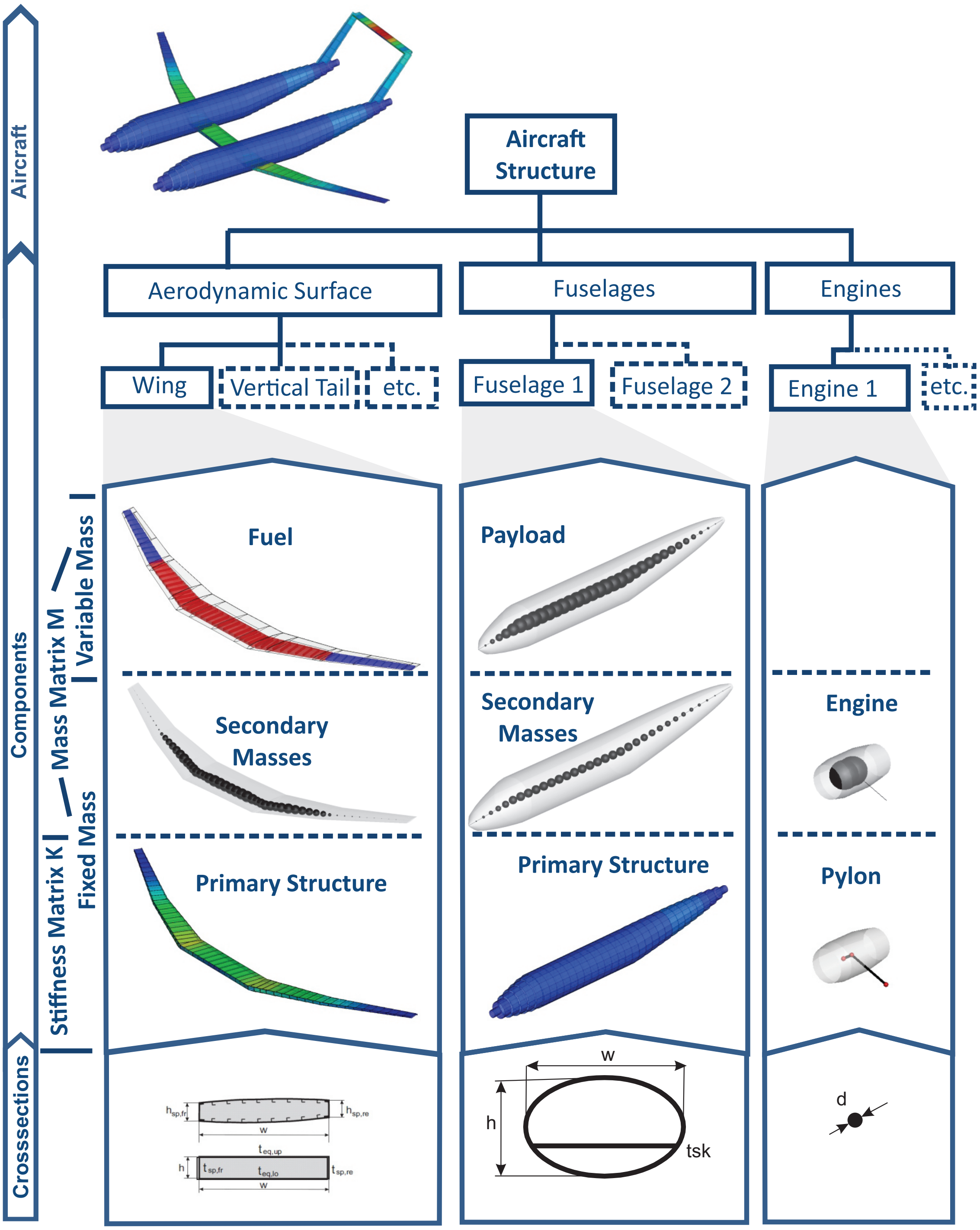

Figure 2.6. – Structural Model Breakdown

A validation of the implemented finite element solver for a quasi steady solution of the implemented finite element method is shown in Appendix C.2.

Dynamic Analysis The discretized equation of motion of an undamped system is given by

$$M\ddot{\delta} - K\delta = f(t) \tag{2.13}$$

where f are the external forces acting on the structure. The solution of this equation requires a numerical time integration scheme such as the Newmark-Beta method described in Section 2.5.6.

Modal Analysis The dynamic behavior of a structure is characterized by its natural modeshapes and frequencies. These natural modes and frequencies are found by so called modal analysis. Solving Equation 2.13 with the Ansatz $\delta(t) = \delta e^{\lambda t}$ leads to the eigenvalue problem

$$\psi = \mathrm{eig}(K, M) \tag{2.14}$$

where the eigenvalues and eigenshapes represent the natural frequencies and modeshapes. For an unrestrained structure in addition to elastic modes, six rigid body movements are found in the solution, which are characterized by a natural frequency of zero. A validation of the modal solution of the implemented finite element method is shown in Appendix C.2.

2.3.2. Component Modeling

The individual beam element stiffness and mass properties are derived from characteristic cross-sections for the respective airframe parts and their material properties. The parameters required for the construction of the element stiffness matrix are the cross-sectional area A, the second moments of area I_{xx}, I_{zz} and I_{zx} as well as the torsional constant I_p. The required material properties are the young's modulus E, the shear modulus G and the material density ρ. The element mass matrix is constructed given the element masses and positions, composed of the mass for the primary load-carrying structure and secondary variable and fixed mass components, where e.g. fuel and payload would be considered a variable mass and fixed secondary masses account for systems (e.g. landing gear, controls, APU), non-loadcarrying structure and other additional masses such as paint, interior etc. (see Figure 2.6). The cross-sectional modeling for the most important airframe components is detailed in the following.

Aerodynamic Surfaces All aerodynamic surfaces, such as wings and stabilizers assume a wingbox-type cross-section as load carrying component. This wingbox is simplified using a thin walled, equivalent thickness approximation as shown in [114] and in Figure 2.6. The respective wingbox skin thicknesses are determined using a sizing algorithm presented in Section 2.3.3 applying different critical loadcases. This model on the one hand provides a stiffness and mass distribution for the wing to allow aeroelastic analysis and on the other hand provides a mass prediction for the respective wing. This mass estimate may be significantly better than the mass estimates provided by traditional conceptual design methods especially for unconventional wings. Similar methods for estimating the wing mass have been applied e.g. by [7] or [17]. Dorbath [33] studied beam and shell models for preliminary wing design and weight prediction and found that beam models are sufficiently accurate and provide almost equivalent accuracy compared to shell elements. The element mass of an aerodynamic surface element $m_{\mathrm{el,as}}$ is determined as the sum of the primary structural weight and the fuel mass and other secondary masses m_{sec}, estimated using the methods presented in [2] and [3].

$$m_{\mathrm{el,as}} = A_{\mathrm{lc}} \rho_{\mathrm{ps}} l_{\mathrm{el}} + A_{\mathrm{encl}} \rho_{\mathrm{fuel}} l_{\mathrm{el}} + m_{\mathrm{sec}} \tag{2.15}$$

where A_{lc} is the area of the load-carrying cross-section, ρ_{ps} is the material density of the primary structure, A_{encl} is the cross-section enclosed by the wingbox determining available space for fuel, ρ_{fuel} is the fuel density and l_{el} is the element length.

Fuselage The fuselage structural model adopts a Z-stiffened elliptical cylindrical shell with longitudinal frames. This structure is again is represented by a simplified thin-walled circular beam in which the structural members (skin, stringers and frames) are considered as an equivalent isotropic thickness, equally distributed along the beam element length and circumference. This modeling resembles the one presented in [9]. Similar fuselage beam models are also used in [93]. The fuselage structure is sized for loadcases defined in the sizing algorithm described in 2.3.3, additionally taking into account the requirements for pressurized compartment loads. The respective skin thicknesses are a result from the sizing procedure and again provide a stiffness as well as a mass distribution of the fuselage. The mass per fuselage element $m_{\mathrm{el,fus}}$ of the given cross-section is again the sum of the mass for the primary load-carrying structure, m_{pld} accounting for payloads such as passengers and cargo and secondary mass components m_{sec} estimated using methods provided in [2] and [3].

$$m_{\mathrm{el,fus}} = A_{\mathrm{lc}} \rho_{\mathrm{ps}} l_{\mathrm{el}} + m_{\mathrm{pld}} + m_{\mathrm{sec}} \tag{2.16}$$

Engines The engine is modeled as concentrated mass connected to the respective airframe component with a pylon which is modeled by means of stiff beam elements. The engine loads resulting from thrust and weight are considered in the airframe sizing by default if defined in the input XML. Any additional masses not covered by the mass estimation methods can be added manually.

2.3.3. Structural Sizing

The structure is sized in an iterative procedure considering the redistribution of loads due to deformations, until an equilibrium is reached. The algorithm is similar to the one presented in [114]. For the structural sizing process the ultimate tensile yield strength needs to be defined as a fully stressed sizing approach is used. Figure 2.7 shows the structural sizing procedure. In the first iteration (i=1) the loads for the rigid aircraft are computed. Using these loads all elements are sized and masses are estimated. After the first iteration the elastic loads can be computed and the process is repeated until convergence is obtained. The convergence criterion applied in this case requires that the change of deformations from the previous step δ_{prv} to the current step δ is smaller than a defined limit for the error Err given by

$$\text{Err} = \frac{\sum_{i=1}^{n}(\delta_i - \delta_{i,\text{prv}})^2}{\sum_{i=1}^{n}\delta_i^2} \tag{2.17}$$

The standard value set for the convergence tolerance is Err $< 0.1\%$. The loadcases to be considered can be defined by the user. The standard loadcases considered from the EASA CS-25 [37] include

- 2.5g pull-up maneuver (CS 25.331)
- 1.67g turn maneuver (CS 25.349)
- discrete gusts (CS 25.341 (a))
- sideslip maneuver (CS 25.351)

Additionally dynamic loadcases can be defined

- vertical dynamic gust profiles
- lateral dynamic gust profiles

Figure 2.8 shows an aircraft beam model with the respective cross-sections and resulting skin thicknesses for an example case.

Figure 2.9 depicts an example for the external aerodynamic and inertial loads acting on the beam model for a trimmed cruise case with forward center of gravity. Inertial relief from the engine mass, the fuel mass, payloads and eigenmass of the aircraft can be identified clearly. Figure 2.10 shows the resulting mass distribution for Maximum Takeoff Weight (MTOW) and Operating Weight Empty (OWE) of the aircraft. The mass distribution and the differentiation between fixed and variable masses as shown in Figure 2.6 allows the computation of a worst case weight and balance diagram. This is done by enabling and disabling the variable mass component for each individual finite element for all possible combinations and then computing the respective total aircraft mass and position of the center of gravity. The resulting weight and balance diagram is a worst case, since unrealistic combinations are considered as well due to the automated algorithm, e.g. all passengers only sitting in the front part of the fuselage. The verification of the structural model and the structural sizing is shown in Appendix C.5.

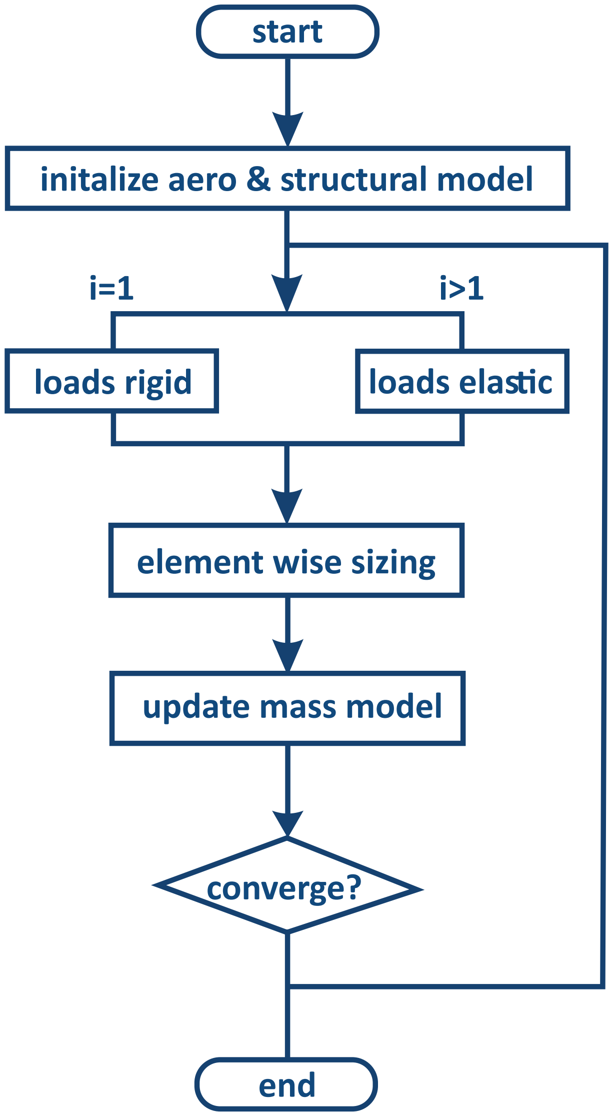

Figure 2.7. – Structural Sizing

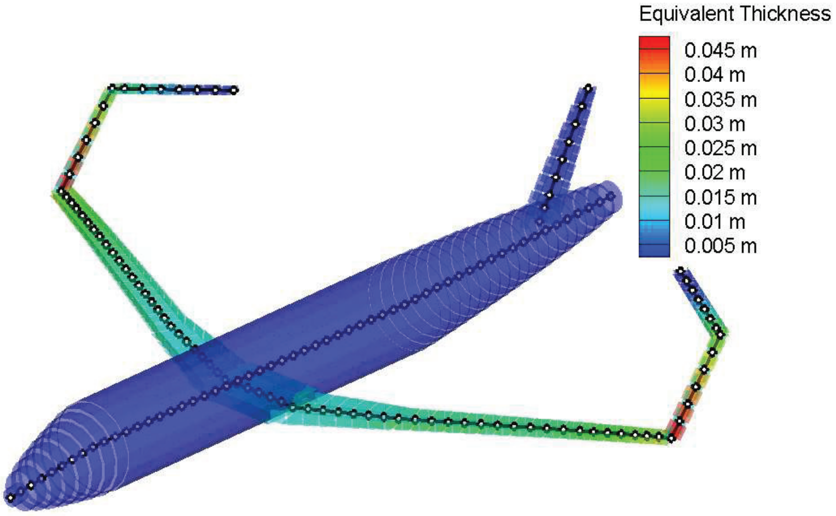

Figure 2.8. – Structural Model

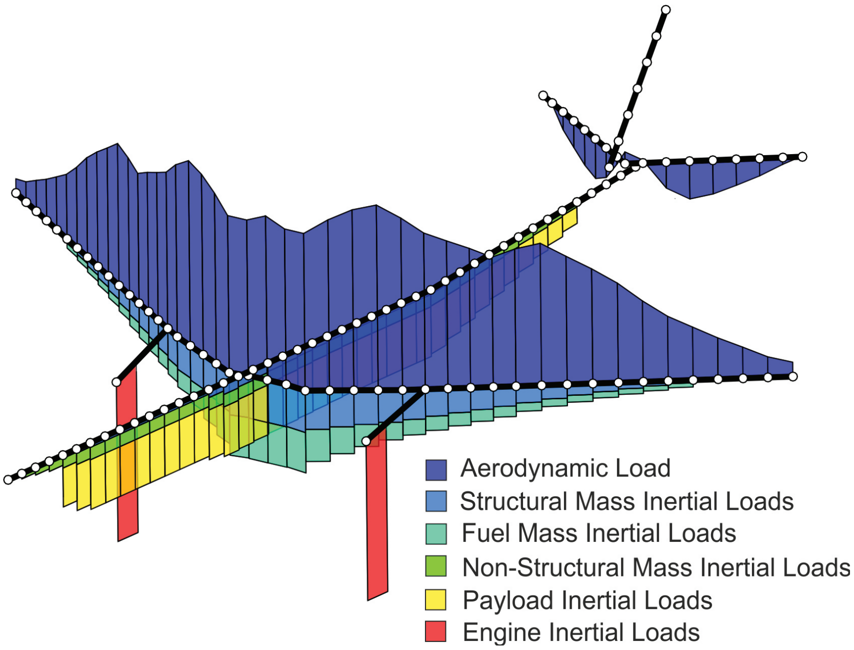

Figure 2.9. – External Loads on Structure for 1g Cruise

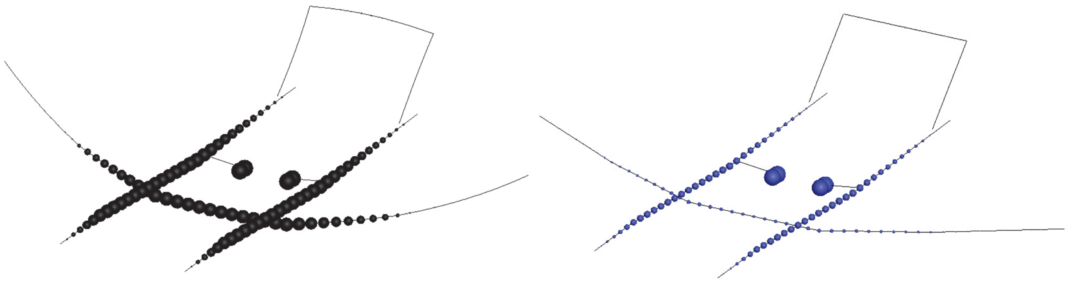

Figure 2.10. – Mass Distribution of the Airframe for MTOW and OWE

2.4. Aerodynamic Modeling

The aerodynamic model must be computationally efficient but at the same time reasonably accurate. Overall trends must be represented correctly in order to allow a reliable assessment of an aircraft concept. Furthermore the local aerodynamic load distribution is required for the computation of sizing loads and the direct simulation of the free flying elastic aircraft. The consideration of unsteady aerodynamic forces and structural flexibility is also essential as these effects may considerably alter the aircraft dynamics and loads [8]. The simulation of arbitrarily maneuvering aircraft taking into account unsteady aerodynamic effects require a time-domain representation of the aerodynamic forces. Panel methods, which are based on potential flow theory, meet these requirements and are utilized to model the steady and unsteady aerodynamic forces in this work. They are well suited for conceptual and preliminary design purposes since they provide good accuracy results within their range of applicability [87] and are computationally efficient. Furthermore the geometry is not required to be known in great detail, which suits the purpose for conceptual design. Specifically the Vortex Lattice Method (VLM) and the Unsteady Vortex Lattice Method (UVLM) are implemented for this process. However most commonly the unsteady aerodynamic coefficients and forces are computed using the DLM applying an acceleration potential. The DLM is written in the frequency domain and hence only allows the indirect simulation of the time dependent unsteady aerodynamic forces, using solutions for small out-of-plane harmonic motions, which are only valid about the considered reference geometry. The UVLM is a time domain method considering unsteady wake effects using a time dependent free wake discretization. This allows the computation of any excitation and motion, simultaneously considering the steady and unsteady aerodynamic loads and not restricted to a reference shape. In contrast to the DLM it is furthermore straightforward to compute the unsteady induced drag [63]. Both the VLM and the UVLM require a paneling of the mean surface where only the camber and no thickness is considered. Correction methods are applied to improve the drag computation through estimating the surface friction drag and to account for Mach number influences.

2.4.1. Potential Flow Theory

Potential flow theory states that the velocity field of an inviscid, irrotational flow can be described as the gradient of a scalar function following the equation

$$w = \nabla \mathbf{\Phi}, \tag{2.18}$$

where w is the velocity field and Φ is the velocity potential. This Laplace equation can be solved by discretizing the problem and applying elementary solutions. Both implemented aerodynamic methods use the potential vortex as elementary solution.

2.4.2. Biot-Savart Law

The Biot-Savart law describes the induced velocity by a finite potential vortex filament. The induced velocity w_{ind} at an arbitrary point is given by

$$w_{\mathrm{ind}} = \frac{\Gamma}{4\pi} \frac{r_1 \times r_2}{\mid r_1 \times r_2 \mid^2 + \mid {r_0}^2 \mid^2} \left(r_0 \frac{r_1}{\mid r_1 \mid} - r_0 \frac{r_2}{\mid r_2 \mid} \right), \tag{2.19}$$

where Γ is the vorticity of the vortex filament, r_1 and r_2 are the vectors pointing from the arbitrary point to the start and end point of the vortex filament and r_0 points from the start point to the end point of the vortex filament. The induced velocity of a horseshoe vortex or vortex ring is computed by applying the Biot-Savart law on each vortex element of the horseshoe vortex or vortex ring.

2.4.3. Vortex Lattice Method

The vortex lattice method is a widely used method within aircraft design, for a detailed understanding it is referred to [63]. The vortex lattice method divides a lifting surface into separate panels. On each of these panels a horseshoe vortex is attached to the quarter-chordline. There are different options for the arrangement of the horseshoe vortex, discussed in more detail in [86] or [114] and shown in Figure 2.11. The vortex filaments of the horseshoe induce a velocity on the panels, which is computed using the Biot-Savart law. The induced velocity is computed at a collocation point placed three quarters from the panel front. The induced velocities are represented in an influence coefficient matrix, containing the influence of each horseshoe vortex with a unit vorticity on all other panel collocation points. In order to determine the vorticities of the horseshoe vortices a kinematic boundary condition is applied which forces the normal velocity w, to be zero at the collocation point of each panel, the so called no penetration boundary condition. The normal vector for a wing with symmetric airfoils is found by computing the panel normal vector, whereas for the consideration of a non-symmetric airfoil the normal vector on the

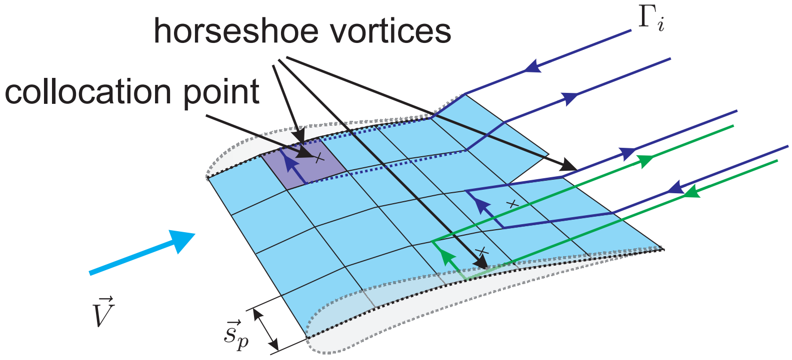

Figure 2.11. – Modeling for the Vortex Lattice Method

curvature of the airfoil skeleton line at the collocation points has to be determined. The linear equation system for the VLM is given by

$$\begin{pmatrix} a_{11} & a_{12} & \dots & a_{1n} \\ a_{21} & a_{22} & \dots & a_{2n} \\ \vdots & & & \\ a_{n1} & a_{n2} & \dots & a_{nn} \end{pmatrix} \begin{pmatrix} \Gamma_1 \\ \Gamma_2 \\ \vdots \\ \Gamma_n \end{pmatrix} = \begin{pmatrix} w_1 \\ w_2 \\ \vdots \\ w_n \end{pmatrix} \tag{2.20}$$

where a represent the influence coefficients, Γ denotes the vorticity, and w denotes the induced velocity at each individual panel collocation point. The induced velocities w are determined from the external flow conditions given by the velocity V, the angle of attack α, the sideslip angle β as well as the body fixed rotation rates $\mathbf{p}$, $\mathbf{q}$ and $\mathbf{r}$ and the instantaneous deformations δ as well as the instantaneous deformation velocities $\dot{\delta}$. The system is solved for the vorticities Γ. The application of the Kutta-Joukowski theorem [11] then allows the computation of the panel forces from the vorticities Γ. The induced drag is computed via a Trefftz plane analysis, see e.g. in [36].

Computation of Forces and Coefficients The panel forces f_p are computed using the Kutta-Joukowski theorem via the following equation

$$f_p = \rho_{\text{air}} \Gamma_p (\vec{V} \times \vec{s_p}) \tag{2.21}$$

where ρ_{air} is the air density, $\vec{V}$ is the inflow velocity vector and $\vec{s_p}$ denotes the vector along the quarter-chordline of the individual panel p.

2.4.4. Unsteady Vortex Lattice Method

The UVLM presents a low to medium fidelity method for the computation of steady and unsteady aerodynamic forces, directly solving the time-dependent governing equations of the flow field. The UVLM represents an unsteady extension of the VLM and is described comprehensively in [63], [81] and [91]. This method applies vortex rings instead

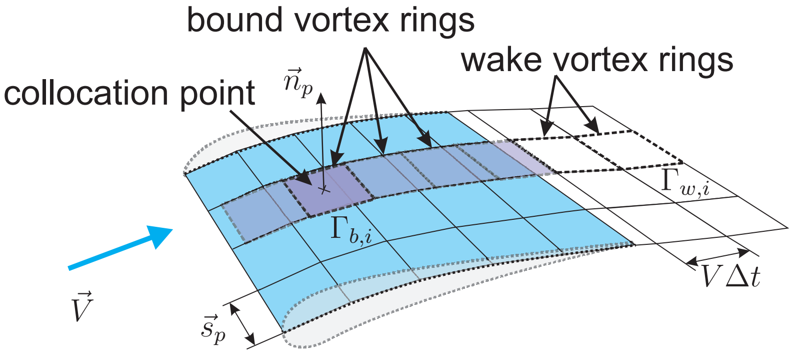

Figure 2.12. – Modeling for the Unsteady Vortex Lattice Method

of horseshoe vortices. This additionally allows to model bodies [81], which is however not pursued within the scope of this work. Similar to the VLM a panel discretization of the aerodynamic surfaces is required for the modeling. The vortex ring is placed at the quarter chordline of the panel, and the collocation point is located three quarters from the panel front (see Figure 2.12). The unsteady aerodynamics are introduced by generating a wake behind the aerodynamic surfaces. For each timestep the trailing edge vortex rings are propagated into the wake satisfying the Kelvin-condition [63], which states that the circulation around a closed curve moving through a fluid remains constant with time. The induced velocity for each vortex ring is computed using the Biot-Savart law. Influence coefficient matrices A are composed, which contain the induced downwash w_p at each panel collocation point from a unit vorticity on a given vortex ring. The influence coefficient matrices are separated into an influence coefficient matrix A_{bb} accounting for the self-induced velocities from the aerodynamic surfaces, and an influence coefficient matrix A_{bw} accounting for the induced velocities from the wake on the aerodynamic surfaces. In case a free-wake model (see e.g. [81]) is used for the simulation, the influence coefficient matrices for the computation of the induced velocities on the wake panels A_{wb} and A_{ww} have to be determined additionally. Given these influence coefficient matrices the bound vortex strength $\Gamma_{b,t+1}$ for the following timestep $t+1$ can be computed

$$\Gamma_{b,t+1} = A_{bb}^{-1}(-w_t - A_{bw}\Gamma_{w,t}), \tag{2.22}$$

where Γ_b denote the vorticities of the aerodynamic surface panels, $\Gamma_{w,t}$ denote the vorticities of the wake panels and w_t denotes the downwash at time t. The downwash w_t is composed of a component from the rigid body movement of the aircraft w_{rgd}, a component from the elastic deformation velocities w_{δ} and a component from atmospheric disturbances w_{gust} resulting in

$$w_t = w_{\text{rgd}} + w_{\dot{\delta}} + w_{\text{gust}}. \tag{2.23}$$

Equivalent to the Vortex Lattice Method (VLM) a no penetration boundary condition at the collocation points is implemented. Thus the determination of the boundary conditions again requires the velocity V, the angle of attack α, the sideslip angle β as well as the body fixed rotation rates $\mathbf{p}$, $\mathbf{q}$ and $\mathbf{r}$ and the instantaneous deformations δ as well as the

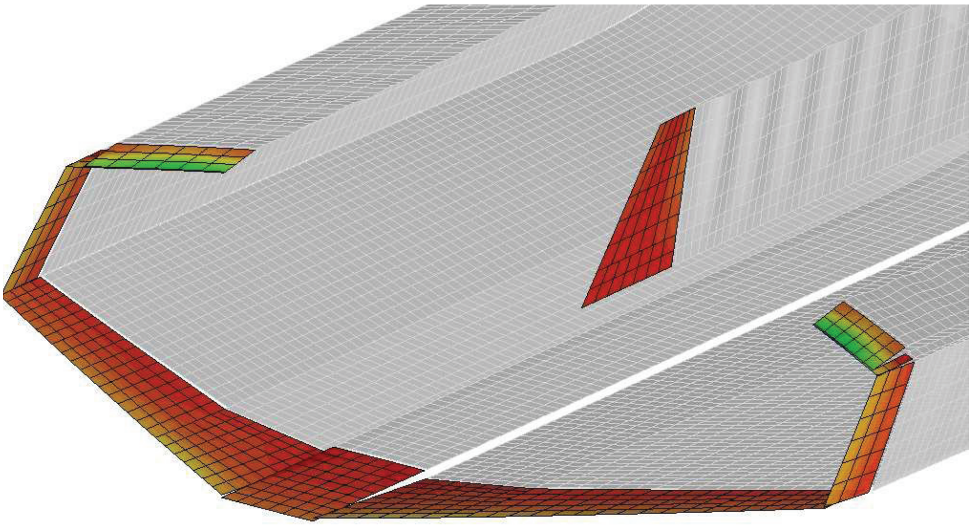

Figure 2.13. – UVLM Aerodynamic Model for a C-Wing Configuration

instantaneous deformation velocities $\dot{\delta}$. The wake vortex strength for the next timestep $t+1$ is computed using the propagation matrix P_{bb}, which is a binary matrix shifting the trailing edge vortices into the wake towards the free stream velocity, and P_{bw}, which also is a binary matrix shifting all vortices in the wake downstream by one timestep,

$$\Gamma_{w,t+1} = P_{bb}\Gamma_{b,t} + P_{bw}\Gamma_{w,t}. \tag{2.24}$$

P_{bw} is, depending on the wake discretization, a potentially very large but sparsely populated matrix, merely serving the purpose of shifting the wake vorticities downstream by one panel. Arranging the wake vortex vector $\Gamma_{w,t}$ in spanwise direction this can be simplified to the following equation resulting in increased computational efficiency,

$$\Gamma_{w,t+1} = C_{bb}\Gamma_{b,t} + \begin{pmatrix} 0 \\ \vdots \\ 0_{n_{te}} \\ \Gamma_{w,t_1} \\ \vdots \\ \vdots \\ \Gamma_{w,t_{n_w-n_{te}}} \end{pmatrix}, \tag{2.25}$$

where n_w is the number of wake panels and n_{te} is the number of trailing edge panels. There are different ways for the modeling of the wake [81]. In this case the rigid wake model was chosen since the force free wake method did not result in noticeable changes in the result. An example for a UVLM model of a C-Wing configuration including the wake model can be seen in Figure 2.13.

Computation of Forces and Coefficients Given the vorticities of the vortex ring elements the aerodynamic forces can be computed. In this implementation of the UVLM, the method commonly referred to as the Joukowski method [120] is implemented. The forces are summed up from a steady and an unsteady component

$$f_p = f_{p,\mathrm{st}} + f_{p,\mathrm{us}}. \tag{2.26}$$

The steady part is given by

$$f_{p,\mathrm{st}} = \rho_{\mathrm{air}} \Gamma_p (\vec{V} \times \vec{s_p}) \tag{2.27}$$

The unsteady part is given by

$$f_{p,\mathrm{us}} = \rho_{\mathrm{air}} \frac{\partial \Gamma}{\partial t} \vec{n}_p \tag{2.28}$$

where $\vec{n}_p$ is the panel normal vector. The Joukowski method automatically determines the unsteady induced drag and leading edge suction effects, which is simply the force component in x direction. Simpson et. al. [120] has shown that the Joukowski method shows better convergence for coarser grids compared to other methods for the determination of the unsteady induced drag, and therefore is chosen for this application. A validation of the unsteady induced drag computation comparing to analytical solutions based on Theodorsen and Garrick is shown in Appendix C.3.2.1.

Computation of the Generalized Aerodynamic Forces Especially for fast time applications the direct simulation of the time-dependent governing equations of the flow field is too computationally expensive. Therefore indirect methods are commonly used for many aeroelastic applications, constructing the time response from existing solutions for oscillatory, step or impulse type of motion [81]. These solutions for oscillatory motion are called generalized aerodynamic forces (GAF), and are the aerodynamic forces computed for a modal oscillation written in modal coordinates. Given the harmonic pressure distribution $c_p(t)$ the generalized aerodynamic coefficient is determined by following relation

$$\mathrm{GAF}(t) = \sum_{i=1}^{n_p} c_{p,i}(t)(\vec{n}_{x,i}\delta_{x,i} + \vec{n}_{y,i}\delta_{y,i} + \vec{n}_{z,i}\delta_{z,i})A_{p,i} \tag{2.29}$$

where $\vec{n}_x$, $\vec{n}_y$ and $\vec{n}_z$ are the components of the panel normal vector in x, y and z direction, and δ_x, δ_y and δ_z are the deformations of each panel for the respective investigated mode-shape. Commonly the GAF are written in the frequency domain as complex coefficients, representing amplitude and phase information. In order to obtain the complex GAF matrix a Fourier transformation of the time domain GAF is performed. The time domain response which is of the form

$$\mathrm{GAF}(t) = \mathrm{GAF}_A \cos(\omega t + \mathit{\Phi}) + GAF_{\mathrm{const}} \tag{2.30}$$

allows the identification of the amplitude GAF_A, the phase delay Φ and the constant offset $\mathrm{GAF}_{\mathrm{const}}$ using a straightforward curve fit. The complex GAF coefficients are then determined by

$$\mathrm{GAF} = Re(\mathrm{GAF}_A e^{i(\Phi-\pi/2)}) + Im(\mathrm{GAF}_A e^{i(\Phi-\pi/2)}). \tag{2.31}$$

The GAFs computed with quasi-linear assumptions on the UVLM are compared to results from analytical solutions and the DLM method from MSC Nastran for rigid body modes, elastic modes and control surface modes. The results are shown in Appendix C.3.2.

2.4.5. Correction Methods

In order to improve the accuracy of the implemented aerodynamic models some correction methods are applied. First the friction drag is modeled, as it can not be considered directly with potential flow methods. Furthermore a compressibility correction is introduced to improve the validity of the results for higher Mach numbers.

Drag Model The implemented method additionally performs a friction and pressure drag estimation using the methods from Kroo [72]. The friction drag for the wings is computed as a function of the runlength Reynolds number of the respective wing segment, a form factor based on the sweep and the wetted surface area. Additionally control surface gap drag components are considered. The fuselage friction and pressure drag is computed based on the wetted surface, a friction coefficient and a form factor based on the slenderness of the fuselage.

Mach Number Correction A Prandtl-Glauert transformation is applied to account for compressibility. The Prandtl-Glauert factor is determined by

$$\mathrm{PG} = \frac{1}{\sqrt{1-\mathrm{Ma}^2}} \tag{2.32}$$

and used for the scaling of the geometry and pressure coefficients. The Prandtl-Glauert correction is applied both for the VLM and for the quasi-steady part of the forces from UVLM. The application of the Prandtl-Glauert factor in the UVLM is however only an approximation, since the derivation of the of the Prandtl-Glauert method is based on a steady potential flow equation. O. Soviero and Hernandes [97] developed a compressible UVLM for the arbitrary two dimensional motion of thin profiles. A compressible UVLM for the three dimensional case has not yet been addressed in the literature. Appendix C.3.2 shows that this approximation is relatively good for low reduced frequencies k and shows increasing discrepancies compared to the DLM with increasing Mach number and increasing reduced frequencies. Since the main objective of this work is the investigation of aircraft maneuvering dynamics, where usually low reduced frequencies are present and only a small contribution from the unsteady aerodynamics is expected this approximation is considered sufficient. The correction is approximately only valid for Mach numbers up to $Ma = 0.7$, which is considered sufficient for the conceptual design level.

2.5. Equations of Motion for the Free Flying Elastic Aircraft

In the following, the equations of motion for the elastic aircraft are derived based on the general formulation for moving deformable bodies closely following Nikravesh [94], however extending these equations by rotational degrees of freedom and thereby allowing for the direct incorporation of a finite element model with six nodal DoFs. Fixed axis and mean axis boundary conditions are implemented in these general equations to allow the solution of the equation system. Subsequently the mean axis equations are simplified and modified further, finally obtaining the commonly used formulations for flight simulation and control of flexible aircraft, similar to [110].

Kinematics It is assumed that the elastic aircraft is discretized as depicted in Figure 2.14 and each node n has three translational and three rotational degrees of freedom. The aerostructural frame A is translating and rotating relative to the earth fixed frame E. A node n is therefore fully determined by three positions and three orientation angles relative to the inertial reference frame E. The instantaneous position of each node is determined

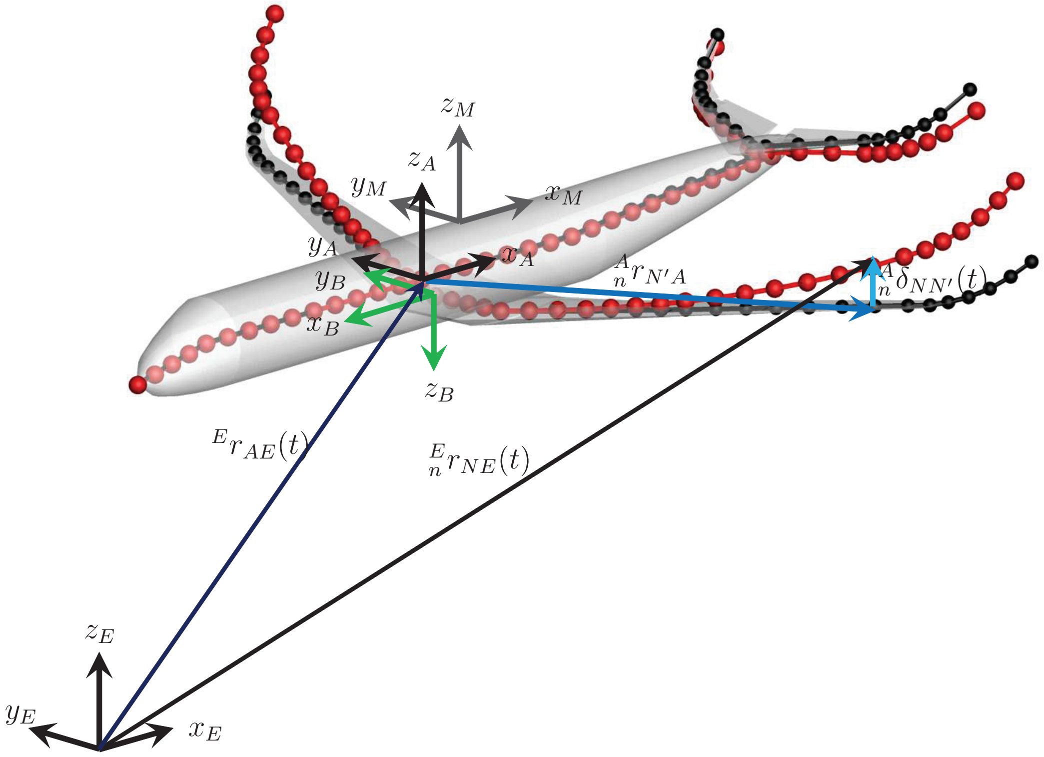

Figure 2.14. – Discrete Aircraft Model

by

$$
{}^{E}_{n}\begin{pmatrix} r_x \\ r_y \\ r_z \end{pmatrix}_{NE} = {}^{E}\begin{pmatrix} r_x \\ r_y \\ r_z \end{pmatrix}_{AE} + {}^{EA}R\left[{}^{A}_{n}\begin{pmatrix} r_x \\ r_y \\ r_z \end{pmatrix}_{N'A} + {}^{A}_{n}\begin{pmatrix} \delta_{t,x} \\ \delta_{t,y} \\ \delta_{t,z} \end{pmatrix}_{NN'} \right], \tag{2.33}
$$

or similarly in vector notation by

$$
{}^{E}_{n}r_{NE}(t) = {}^{E}r_{AE}(t) + {}^{EA}R\left[{}^{A}_{n}r_{N'A} + {}^{A}_{n}\delta_{t,NN'}(t)\right]. \tag{2.34}
$$

The vector ${}^{E}_{n}r_{NE}$ points from the E frame origin to the respective node n. The vector ${}^{E}_{n}r_{AE}$ points from the origin of E to the origin of the aerostructural frame A, where its components are given in the E system. The vector ${}^{A}_{n}r_{N'A}$ and the instantaneous displacement ${}^{A}_{n}\delta_{t,NN'}$ are given in the aerostructural system. The rotation matrix ${}^{EA}R$ transforms from the A frame into the inertial frame E.
In order to improve readability ${}^{A}_{n}r_{NA}(t)$ is defined as the vector from the origin of A to the displaced node n

$$
{}^{A}_{n}r_{NA}(t) = {}^{A}_{n}r_{N'A} + {}^{A}_{n}\delta_{t,NN'}(t) \tag{2.35}
$$

The absolute velocity of node n with respect to the inertial system E is determined by the first time derivative of Equation 2.34. This yields

$$
{}^{E}_{n}\dot{r}_{NE}(t) = {}^{E}\dot{r}_{AE}(t) + {}^{E}\widetilde{\Omega}_{AE}{}^{EA}R^{A}_{n}r_{NA}(t) + {}^{EA}R^{A}_{n}\dot{\delta}_{t,NN'}(t) \tag{2.36}
$$

using the well known formula for the time derivative of a rotation matrix from [43],

$$
\frac{d^{EA}R}{dt} = {}^{E}\widetilde{\Omega}_{AE}{}^{EA}R, \tag{2.37}
$$

where

$$
{}^{E}\widetilde{\Omega}_{AE} = \begin{pmatrix} 0 & -{}^{E}\omega_{AE,z} & {}^{E}\omega_{AE,y} \\ {}^{E}\omega_{AE,z} & 0 & -{}^{E}\omega_{AE,x} \\ -{}^{E}\omega_{AE,y} & {}^{E}\omega_{AE,x} & 0 \end{pmatrix} \tag{2.38}
$$

is the skew symmetric angular rate Tensor. The instantaneous nodal acceleration is determined by the second time derivative of Equation 2.34 leading to

$$
\begin{aligned}
{}^{E}_{n}\ddot{r}_{NE}(t) = {}^{E}\ddot{r}_{AE}(t) &+ {}^{E}\dot{\widetilde{\Omega}}_{AE}{}^{EA}R^{A}_{n}r_{NA}(t) + {}^{E}\widetilde{\Omega}_{AE}{}^{E}\widetilde{\Omega}_{AE}{}^{EA}R^{A}_{n}r_{NA}(t) \\
&+ 2{}^{E}\widetilde{\Omega}_{AE}{}^{EA}R^{A}_{n}\dot{\delta}_{t,NN'}(t) + {}^{EA}R^{A}_{n}\ddot{\delta}_{t,NN'}(t).
\end{aligned} \tag{2.39}
$$

Additionally the orientation of the coordinate system of node n is defined relative to the inertial system E. The instantaneous orientation of each nodal coordinate system is given by the rotation matrix

$$
{}^{EN}R = {}^{EA}R^{AN}R \tag{2.40}
$$

The angular rate ${}^{E}\omega_{NE}$ of the N frame relative to the inertial frame E is derived using the Poisson Equation [136, p. 45 ff.] on Equation 2.40 which results in

$$ {}^{E}_{n}\omega_{NE} = {}^{E}\omega_{AE} + {}^{EA}R^{A}_{n}\dot{\delta}_{\varepsilon,NA}. \tag{2.41}$$

The inertial angular nodal acceleration given by the second time derivative is

$$ {}^{E}_{n}\dot{\omega}_{NE} = {}^{E}\dot{\omega}_{AE} + {}^{EA}R^{A}_{n}\ddot{\delta}_{\varepsilon,NA} + {}^{E}\widetilde{\Omega}_{AE}{}^{EA}R^{A}_{n}\dot{\delta}_{\varepsilon,NA}. \tag{2.42}$$

In the next step Equation 2.36 and 2.41 are stacked to receive one equation for the nodal translational velocity and angular rate

$$ {}^{E}_{n}\begin{pmatrix}\dot{r}\\ \omega\end{pmatrix}_{NE} = \begin{pmatrix}\bar{I}\\ \bar{0}\end{pmatrix} {}^{E}_{n}\dot{\begin{pmatrix}r_x\\ r_y\\ r_z\end{pmatrix}}_{AE} + \begin{pmatrix}-{}^{E}_{n}\widetilde{r}\\ \bar{I}\end{pmatrix} {}^{E}_{n}\begin{pmatrix}\omega_x\\ \omega_y\\ \omega_z\end{pmatrix}_{AE} + \begin{pmatrix}{}^{EA}R & \bar{0}\\ \bar{0} & {}^{EA}R\end{pmatrix} {}^{A}_{n}\dot{\begin{pmatrix}\delta_t\\ \delta_\varepsilon\end{pmatrix}}_{NN'} \tag{2.43}$$

where $\bar{I}$ is a three by three identity matrix, $\bar{0}$ is a three by three zero matrix, furthermore ${}^{E}_{n}\widetilde{r}$ is the skew symmetric matrix

$$ {}^{E}_{n}\widetilde{r} = {}^{EA}R \begin{pmatrix} 0 & -{}^{A}_{n}r_{NA,z} & {}^{A}_{n}r_{NA,y}\\ {}^{A}_{n}r_{NA,z} & 0 & -{}^{A}_{n}r_{NA,x}\\ -{}^{A}_{n}r_{NA,y} & {}^{A}_{n}r_{NA,x} & 0 \end{pmatrix}. \tag{2.44}$$

Applying the equivalent stacking procedure on equation 2.39 and 2.42 the nodal inertial acceleration in matrix form is derived as follows

$$ \begin{aligned} {}^{E}_{n}\begin{pmatrix}\ddot{r}\\ \dot{\omega}\end{pmatrix}_{NE} = \begin{pmatrix}\bar{I}\\ \bar{0}\end{pmatrix} {}^{E}\ddot{\begin{pmatrix}r_x\\ r_y\\ r_z\end{pmatrix}}_{AE} + \begin{pmatrix}-{}^{E}_{n}\widetilde{r}\\ \bar{I}\end{pmatrix} {}^{E}\dot{\begin{pmatrix}\omega_x\\ \omega_y\\ \omega_z\end{pmatrix}}_{AE} + \\ \begin{pmatrix}{}^{E}\widetilde{\Omega}_{AE} & \bar{0}\\ \bar{0} & \frac{1}{2}{}^{E}\widetilde{\Omega}_{AE}\end{pmatrix} \begin{pmatrix}{}^{E}\widetilde{\Omega}_{AE} & \bar{0}\\ \bar{0} & \frac{1}{2}{}^{E}\widetilde{\Omega}_{AE}\end{pmatrix} \begin{pmatrix}{}^{E}_{n}r_{NA}\\ {}_{3x1}0\end{pmatrix} + \\ 2\begin{pmatrix}{}^{E}\widetilde{\Omega}_{AE} & \bar{0}\\ \bar{0} & \frac{1}{2}{}^{E}\widetilde{\Omega}_{AE}\end{pmatrix} \begin{pmatrix}{}^{EA}R & \bar{0}\\ \bar{0} & {}^{EA}R\end{pmatrix} {}^{A}_{n}\dot{\begin{pmatrix}\delta_t\\ \delta_\varepsilon\end{pmatrix}} + \begin{pmatrix}{}^{EA}R & \bar{0}\\ \bar{0} & {}^{EA}R\end{pmatrix} {}^{A}_{n}\ddot{\begin{pmatrix}\delta_t\\ \delta_\varepsilon\end{pmatrix}}_{NN'} \end{aligned} \tag{2.45}$$

In order to improve readability the following definitions are introduced

$$ \mathbf{L} = \begin{pmatrix}\bar{I}\\ \bar{0}\end{pmatrix} \tag{2.46}$$

$$ \widetilde{\mathbf{r}} = \begin{pmatrix}-{}^{E}_{n}\widetilde{r}\\ \bar{I}\end{pmatrix}, \tag{2.47}$$

$$ \hat{\mathbf{r}} = \begin{pmatrix}{}^{E}_{n}r_{NA}\\ {}_{3x1}0\end{pmatrix}, \tag{2.48}$$

$$\widetilde{\boldsymbol{\Omega}} = \begin{pmatrix} {}^{E}\widetilde{\Omega}_{AE} & \bar{0} \\ \bar{0} & \frac{1}{2}{}^{E}\widetilde{\Omega}_{AE} \end{pmatrix}, \tag{2.49}$$

$$\mathbf{R} = \begin{pmatrix} {}^{EA}R & \bar{0} \\ \bar{0} & {}^{EA}R \end{pmatrix}, \tag{2.50}$$

$$\dot{\mathbf{r}} = {}^{E}_{n}\begin{pmatrix} \dot{r} \\ \omega \end{pmatrix}_{NE}, \tag{2.51}$$

and

$${}_{n}\dot{\delta} = {}^{A}_{n}\begin{pmatrix} \dot{\delta}_t \\ \dot{\delta}_\varepsilon \end{pmatrix}_{NN'}. \tag{2.52}$$

Rewriting equations 2.43 and 2.45 leads to

$${}_{n}\dot{\mathbf{r}} = \mathbf{L}^{E}\dot{r}_{AE} + \widetilde{\mathbf{r}}^{E}\omega_{AE} + \mathbf{R}_{n}\dot{\delta} \tag{2.53}$$

for the nodal velocity and

$${}_{n}\ddot{\mathbf{r}} = \mathbf{L}^{E}\ddot{r}_{AE} + \widetilde{\mathbf{r}}^{E}\dot{\omega}_{AE} + \widetilde{\boldsymbol{\Omega}}\widetilde{\boldsymbol{\Omega}}\hat{\mathbf{r}} + 2\widetilde{\boldsymbol{\Omega}}\mathbf{R}_{n}\dot{\delta} + \mathbf{R}_{n}\ddot{\delta} \tag{2.54}$$

for the nodal acceleration. Equation 2.53 and 2.54 are valid for each single node n. Stacking these equations for each node leads to an equation system for the entire deformable structure. For this purpose the matrices $\mathbf{L}$, $\widetilde{\mathbf{r}}$ need to be stacked and $\widetilde{\boldsymbol{\Omega}}$, $\mathbf{R}$ need to be extended leading to the equation for the discrete velocity field

$$\dot{\mathbf{r}} = \hat{\mathbf{I}}^{E}\dot{r}_{AE} + \hat{\tilde{\mathbf{r}}}^{E}\omega_{AE} + \bar{\mathbf{R}}\dot{\delta} = \begin{pmatrix} \hat{\mathbf{I}} & \hat{\tilde{\mathbf{r}}} & \bar{\mathbf{R}} \end{pmatrix} \begin{pmatrix} {}^{E}\dot{r}_{AE} \\ {}^{E}\omega_{AE} \\ \dot{\delta} \end{pmatrix} \tag{2.55}$$

and derived similarly the acceleration field equation is given by

$$\begin{gathered} \ddot{\mathbf{r}} = \hat{\mathbf{I}}^{E}\ddot{r}_{AE} + \hat{\tilde{\mathbf{r}}}^{E}\dot{\omega}_{AE} + \bar{\tilde{\boldsymbol{\Omega}}}\bar{\tilde{\boldsymbol{\Omega}}}\hat{\mathbf{r}} + 2\bar{\tilde{\boldsymbol{\Omega}}}\bar{\mathbf{R}}\dot{\delta} + \bar{\mathbf{R}}\ddot{\delta} = \\ \begin{pmatrix} \hat{\mathbf{I}} & \hat{\tilde{\mathbf{r}}} & \bar{\mathbf{R}} \end{pmatrix} \begin{pmatrix} {}^{E}\ddot{r}_{AE} \\ {}^{E}\dot{\omega}_{AE} \\ \ddot{\delta} \end{pmatrix} + \bar{\tilde{\boldsymbol{\Omega}}}\bar{\tilde{\boldsymbol{\Omega}}}\hat{\mathbf{r}} + 2\bar{\tilde{\boldsymbol{\Omega}}}\bar{\mathbf{R}}\dot{\delta} \end{gathered} \tag{2.56}$$

Equations 2.55 and 2.56 have $6 \cdot (n_{\text{nodes}} + 1)$ degrees of freedom, including six degrees of freedom for each node and additionally the six degrees of freedom for a free flying object.

Kinetics A deformable body discretized by means of a finite element method is characterized by a stiffness matrix K and a mass matrix M. These matrices are defined in the global coordinate system of the structural solver and are described in more detail in Section 2.3 and Appendix A.1 of this thesis. The general equation of motion for a structure Eq. 2.13 is only valid in an inertial system. Hence for a free flying deformable body this equation must be written in the inertial system, using the previously derived inertial acceleration of Eq. 2.56, leading to

$$\boldsymbol{M}\ddot{\mathbf{r}} + \boldsymbol{K}^{E}\boldsymbol{\delta} = \boldsymbol{f} \tag{2.57}$$

where the transformation matrix $\bar{\mathbf{R}}$ transforms the finite element mass and stiffness matrix from the aerostructural system into the inertial system, leading to

$$\boldsymbol{M} = \bar{\mathbf{R}}M\bar{\mathbf{R}}^{T} \tag{2.58}$$

and respectively

$$\boldsymbol{K} = \bar{\mathbf{R}}K\bar{\mathbf{R}}^{T}. \tag{2.59}$$

Similarly the externally applied forces and the displacements are transformed into the inertial system E given by

$$\boldsymbol{f} = \bar{\mathbf{R}}f \tag{2.60}$$

and

$$^{E}\boldsymbol{\delta} = \bar{\mathbf{R}}^{A}\delta. \tag{2.61}$$

Inserting Eq. 2.56 into Eq. 2.57 results in

$$\boldsymbol{M}\left[\begin{pmatrix}\hat{\mathbf{I}} & \hat{\tilde{\mathbf{r}}} & \bar{\mathbf{R}}\end{pmatrix}\begin{pmatrix}^{E}\ddot{r}_{AE} \\ ^{E}\dot{\omega}_{AE} \\ \ddot{\delta}\end{pmatrix} + \bar{\tilde{\boldsymbol{\Omega}}}\bar{\tilde{\boldsymbol{\Omega}}}\hat{\mathbf{r}} + 2\bar{\tilde{\boldsymbol{\Omega}}}\bar{\mathbf{R}}^{A}\dot{\delta}\right] + \boldsymbol{K}\bar{\mathbf{R}}^{A}\delta = \bar{\mathbf{R}}f \tag{2.62}$$

The deflections δ and the forces f remain in the A system to be compatible with the structural and aerodynamic solver. Extending this Equation 2.62 by

$$\begin{pmatrix}\hat{\mathbf{I}}^{T} \\ \hat{\tilde{\mathbf{r}}}^{T} \\ \bar{\mathbf{R}}^{T}\end{pmatrix} \tag{2.63}$$

and rearranging some expressions yields the general equation of motion for the elastic aircraft given by

$$\underline{\mathbf{M}}\begin{pmatrix}^{E}\ddot{r}_{AE} \\ ^{E}\dot{\omega}_{AE} \\ \ddot{\delta}\end{pmatrix} + \underline{\mathbf{K}}\delta = \underline{\mathbf{f}}_{\mathbf{EXT}} - \underline{\mathbf{f}}_{\mathbf{ACC}}, \tag{2.64}$$

where the matrix $\underline{\mathbf{M}}$ is given by

$$\underline{\mathbf{M}} = \begin{pmatrix}\hat{\mathbf{I}}^{\mathbf{T}}\boldsymbol{M}\hat{\mathbf{I}} & \hat{\mathbf{I}}^{\mathbf{T}}\boldsymbol{M}\hat{\tilde{\mathbf{r}}} & \hat{\mathbf{I}}^{\mathbf{T}}\bar{\mathbf{R}}M \\ \hat{\tilde{\mathbf{r}}}^{\mathbf{T}}\boldsymbol{M}\hat{\mathbf{I}} & \hat{\tilde{\mathbf{r}}}^{\mathbf{T}}\boldsymbol{M}\hat{\tilde{\mathbf{r}}} & \hat{\tilde{\mathbf{r}}}^{\mathbf{T}}\bar{\mathbf{R}}M \\ M\bar{\mathbf{R}}^{T}\hat{\mathbf{I}} & M\bar{\mathbf{R}}^{T}\hat{\tilde{\mathbf{r}}} & M\end{pmatrix} \tag{2.65}$$

and the matrix $\underline{\underline{\mathbf{K}}}$ results in

$$\underline{\underline{\mathbf{K}}} = \begin{pmatrix} {}_{6x1}0 \\ K \end{pmatrix}, \tag{2.66}$$

considering that the terms $\hat{\mathbf{I}}^{\mathbf{T}}\bar{\mathbf{R}}K$ and $\hat{\bar{\mathbf{r}}}^{\mathbf{T}}\bar{\mathbf{R}}K$ result in zero as found by expansion. The force vector is split up the external forces

$$\underline{\mathbf{f}}_{\mathbf{EXT}} = \begin{pmatrix} \hat{\mathbf{I}}^{\mathbf{T}}\bar{\mathbf{R}}f \\ \hat{\bar{\mathbf{r}}}^{\mathbf{T}}\bar{\mathbf{R}}f \\ f \end{pmatrix} \tag{2.67}$$

and the inertial acceleration forces given by

$$\underline{\mathbf{f}}_{\mathbf{ACC}} = \begin{pmatrix} \hat{\mathbf{I}}^{\mathbf{T}}\boldsymbol{M} \\ \hat{\bar{\mathbf{r}}}^{\mathbf{T}}\boldsymbol{M} \\ \bar{\mathbf{R}}^{T}\boldsymbol{M} \end{pmatrix} \left(\bar{\tilde{\bar{\boldsymbol{\Omega}}}}\bar{\tilde{\bar{\boldsymbol{\Omega}}}}\hat{\mathbf{r}} + 2\bar{\tilde{\bar{\boldsymbol{\Omega}}}}\bar{\mathbf{R}}\dot{\delta}\right) \tag{2.68}$$

The derived equations have a rank deficiency of six since the performed mathematical operations expanded the original FE matrices by six. In order to be able to solve the equations boundary conditions must be imposed. In a classical finite element problem these boundary conditions are found by restraining each degree of freedom at least once on a support, however for a free flying body a support is non existent, and a different way of imposing boundary conditions must be used. Two different ways are presented in the following.

2.5.1. Equations of Motion with Fixed-Axis

In the fixed axis approach these boundary conditions are applied by fixing the moving coordinate system A to one of the nodes on the finite element model. In other words this means that the deformations δ at the boundary condition node n_{BC} will always remain zero at any instant of time. To ensure this condition three translational DoFs δ_t and three rotational DoF δ_ε are set to zero by removing the respective rows and columns from the mass matrix of Eq. 2.65 and the stiffness matrix of Equation 2.66 as well as removing the respective lines from the force vectors in Equations 2.68 and 2.67. The system is now of full rank and solvable using an appropriate numerical integration scheme such as the Newmark-Beta method described in Section 2.5.6.

2.5.2. Equations of Motion with Mean-Axis

Another way to solve Equation 2.64 is the incooperation of mean axis boundary conditions. The mean axis approach uses a floating reference system in order to minimize the inertial coupling between the rigid body movement and elastic deformations, in other words it is the location where the kinetic energy due to deformation is a minimum. The kinetic energy is expressed by

$$E_{\text{Kin}} = \frac{1}{2}\dot{\boldsymbol{\delta}}^T \boldsymbol{M} \dot{\boldsymbol{\delta}} \tag{2.69}$$

utilizing Equation 2.55 this writes as

$$E_{\text{Kin}} = \frac{1}{2}(\dot{\mathbf{r}} - \hat{\mathbf{I}}^E \dot{r}_{AE} - \hat{\hat{\mathbf{r}}}^E \omega_{AE})^T \boldsymbol{M} (\dot{\mathbf{r}} - \hat{\mathbf{I}}^E \dot{r}_{AE} - \hat{\hat{\mathbf{r}}}^E \omega_{AE}) \tag{2.70}$$

The derivative with respect to ${}^E\dot{r}_{AE}$ results in

$$\frac{dE_{\text{Kin}}}{{}^E\dot{r}_{AE}} = \dot{\boldsymbol{\delta}}^T \boldsymbol{M} \hat{\mathbf{I}} \tag{2.71}$$

and the derivative with respect to ${}^E\omega_{AE}$ gives

$$\frac{dE_{\text{Kin}}}{{}^E\omega_{AE}} = \dot{\boldsymbol{\delta}}^T \boldsymbol{M} \hat{\hat{\mathbf{r}}}. \tag{2.72}$$

These energy derivatives are set to zero according to the assumption. By expanding and rearranging these results and additionally incooperating the assumption that the initial origin of the mean-axis frame located at the center of mass the mass matrix of Eq. 2.65 simplifies to

$$\underline{\boldsymbol{M}} = \begin{pmatrix} \hat{\mathbf{I}}^{\mathbf{T}} \boldsymbol{M} \hat{\mathbf{I}} & 0 & 0 \\ 0 & \hat{\hat{\mathbf{r}}}^{\mathbf{T}} \boldsymbol{M} \hat{\hat{\mathbf{r}}} & 0 \\ M \bar{\mathbf{R}}^{\mathbf{T}} \hat{\mathbf{I}} & M \bar{\mathbf{R}}^{\mathbf{T}} \hat{\hat{\mathbf{r}}} & M \end{pmatrix}. \tag{2.73}$$

For details it is referred to [94]. It can be seen that now the only coupling terms between the elastic motion and the rigid body motion are $M\bar{\mathbf{R}}^{\mathbf{T}}\hat{\mathbf{I}}$ and $M\bar{\mathbf{R}}^{\mathbf{T}}\hat{\hat{\mathbf{r}}}$. Furthermore it can be found that

$$\hat{\mathbf{I}}^{\mathbf{T}} \mathbf{M}_{\mathbf{I}} \hat{\mathbf{I}} = \begin{pmatrix} m & 0 & 0 \\ 0 & m & 0 \\ 0 & 0 & m \end{pmatrix} = \mathbf{m} \tag{2.74}$$

is the mass tensor and

$$\hat{\hat{\mathbf{r}}}^{\mathbf{T}} \boldsymbol{M} \hat{\hat{\mathbf{r}}} = \begin{pmatrix} I_{xx} & I_{xy} & I_{xz} \\ I_{yx} & I_{yy} & I_{yz} \\ I_{zx} & I_{zy} & I_{zz} \end{pmatrix} = \mathbf{I} \tag{2.75}$$

is the inertia tensor. The stiffness and mass matrices remain as given in Equations 2.66, 2.67 and 2.68. The center of mass is found by applying the following equation

$$\begin{pmatrix} \text{cg}_x \\ \text{cg}_y \\ \text{cg}_z \end{pmatrix} = \begin{pmatrix} \sum_1^{n_{\text{el}}} r^i_{\text{Ref}Nx} m_i \\ \sum_1^{n_{\text{el}}} r^i_{\text{Ref}Ny} m_i \\ \sum_1^{n_{\text{el}}} r^i_{\text{Ref}Nz} m_i \end{pmatrix} \frac{1}{\sum_1^{n_{\text{el}}} m_i} \tag{2.76}$$

which determines the position of the center of gravity cg relative to an arbitrary reference location. $r^i_{\mathrm{Ref}N}$ is the vector from the reference to the respective node, and m_i is the condensed mass at the respective node.

2.5.3. Modal Transformation

Under the prerequisite of a linear elastic structure, e.g. the stiffness matrix is independent of deformation, a modal transformation can be applied to the mean axis equations. For this purpose the modeshape matrix found by modal analysis (see Section 2.3) is used for the transformation from the physical coordinates δ into the modal coordinates z

$$\delta = \psi z \tag{2.77}$$

Replacing the nodal coordinates by generalized coordinates and multiplying the last row of $\underline{\boldsymbol{M}}$, $\underline{\boldsymbol{K}}$ with ψ one receives

$$\underline{\mathbf{M}} \begin{pmatrix} {}^E\ddot{r}_{AE} \\ {}^E\dot{\omega}_{AE} \\ \ddot{z} \end{pmatrix} + \underline{\mathbf{K}}\psi z = \underline{\mathbf{f}}_{\mathbf{EXT}} - \underline{\mathbf{f}}_{\mathbf{ACC}}, \tag{2.78}$$

where

$$\underline{\mathbf{M}}_{\mathbf{m}} = \begin{pmatrix} \mathbf{m} & 0 & 0 \\ 0 & \mathbf{I} & 0 \\ \psi^T M \bar{\mathbf{R}}^{\mathbf{T}} \hat{\mathbf{I}} & \psi^T M \bar{\mathbf{R}}^{\mathbf{T}} \hat{\tilde{\mathbf{r}}} & M_m \end{pmatrix} \tag{2.79}$$

and the resulting stiffness matrix is

$$\underline{\mathbf{K}}_{\mathbf{m}} = \begin{pmatrix} 0 \\ 0 \\ K_m \end{pmatrix} \tag{2.80}$$

with

$$M_m = \psi^T M \psi, \tag{2.81}$$

and

$$K_m = \psi^T K \psi \tag{2.82}$$

defined as the generalized mass and stiffness matrix. The force vectors are given by

$$f_m = \psi^T f, \tag{2.83}$$

$$\underline{\mathbf{f}}_{\mathbf{EXT,m}} = \begin{pmatrix} \hat{\mathbf{I}}^{\mathbf{T}} \bar{\mathbf{R}} f \\ \hat{\tilde{\mathbf{r}}}^{\mathbf{T}} \bar{\mathbf{R}} f \\ f_m \end{pmatrix} \tag{2.84}$$

and

$$\underline{\mathbf{f}}_{\mathbf{ACC,m}} = \begin{pmatrix} \hat{\mathbf{I}}^{\mathbf{T}} \boldsymbol{M} \\ \hat{\hat{\mathbf{r}}}^{\mathbf{T}} \boldsymbol{M} \\ \psi^T \bar{\mathbf{R}}^T \boldsymbol{M} \end{pmatrix} \left(\widetilde{\mathbf{\Omega}} \widetilde{\mathbf{\Omega}} \hat{\mathbf{r}} + 2 \widetilde{\mathbf{\Omega}} \psi z \right) . \tag{2.85}$$

2.5.4. Modal Reduction

In certain applications, e.g. the generation of linearized state space models for control systems design it is required to reduce the number of structural modes for the aeroelastic model in order to limit the system order to enable the synthesis of a low order control law. Furthermore when using CFD methods or other time domain aerodynamic methods, the computation of the generalized aerodynamic forces is computationally significantly more expensive compared to the doublet lattice method. The standard approach here used e.g. by [8] or [110] is a classical modal truncation, disregarding all modes above a certain number or frequency. The applied modal reduction technique therefore aims at the reduction of the required structural modes for accurate response simulation, without prior consideration of special input/output variables to match. The structural mass and stiffness matrix may be transformed into modal space using the unrestrained free-free modeshapes. It is assumed that the deformation of the maneuvering aircraft can be reproduced well using a relatively low amount of modes. These modes are identified by weighing the modal deformations for different characteristic loadcases. An example is shown in Figure 2.15. It can be seen that the deformation for the 1g cruise case is reproduced well by just considering the main wing and horizontal stabilizer bending modes. This weighing is averaged for a number of characteristic loadcases which are available since they are considered for the structural sizing process such as the 2.5g pull maneuver or the sideslip maneuver. The modes are then ordered according to their contribution to the overall deformation and the modes accounting for 99% of the characteristic loadcase deformations are kept, whereas the rest is truncated. For the benchmark aircraft this was achieved with only 24 modes. This loadcase selective truncation (LST) shows good results for response investigations. This can also be seen in Appendix C.4.4, where the response on the pitch rate $\mathbf{q}$ and the roll rate $\mathbf{p}$ to an elevator and an aileron doublet input are compared. The direct time domain model for the unreduced case and the LST model match very closely while the difference is slightly larger using the classic modal truncation.

2.5.5. Partitioned Approach

The partitioned approach as used e.g. by [134] decouples the rigid and elastic motion, and solves the rigid body movements separately from the elastic motion. This is useful and necessary if there is no access to the finite element stiffness and mass matrices, which is the case e.g. for commercial codes. In this case the structural solver is only used to compute the deflections due to external loads. Since the presented method should be modular and easily extendable this approach allows the simple implementation of other finite element codes. The partitioned method and the following methods implement simplifications such

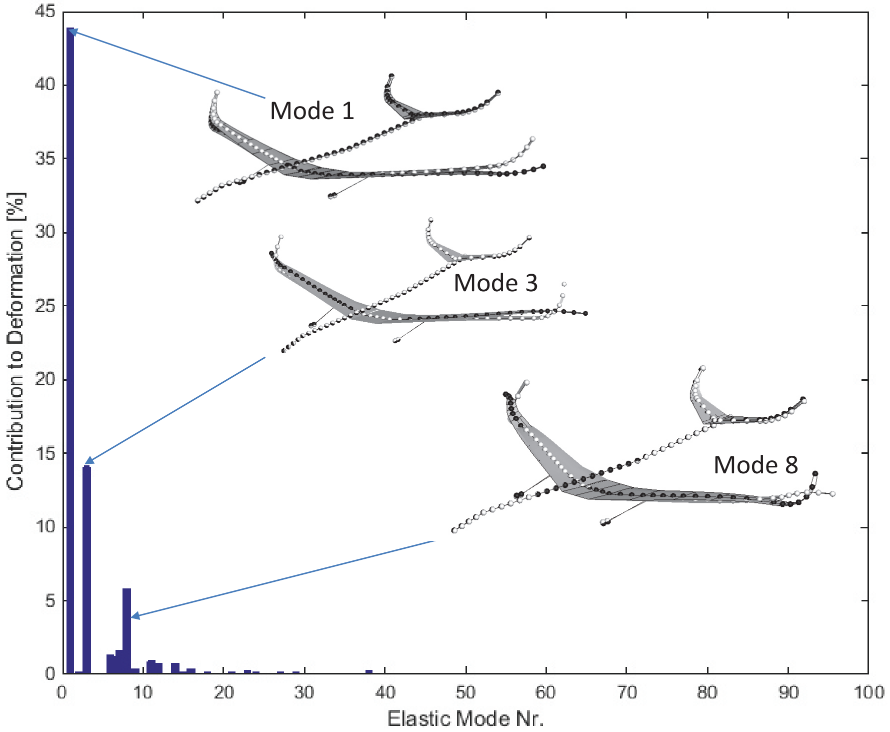

Figure 2.15. – Modal Reduction

as the removal of the inertial coupling, which may not be valid for certain configurations. Before using simplified models, reference computations with the fixed-axis model have to be carried out, to verify the validity of simplified approaches. Investigating Equations 2.79 it can be seen that by neglecting the terms $\psi^T M\bar{\mathbf{R}}^{\mathbf{T}}\hat{\mathbf{I}}$ and $\psi^T M\bar{\mathbf{R}}^{\mathbf{T}}\hat{\tilde{\mathbf{r}}}$ the system mass matrix becomes

$$\underline{\mathbf{M}}_{\mathbf{m}} = \begin{pmatrix} \mathbf{m} & 0 & 0 \\ 0 & \mathbf{I} & 0 \\ 0 & 0 & M_m \end{pmatrix} \tag{2.86}$$

and is inertially decoupled. This inertial decoupling is the assumption used in most applications for the simulation of an elastic aircraft. Equation 2.78 can now be separated into the 6DoF equations of motion used for the rigid body motion

$$\begin{pmatrix} \mathbf{m} & 0 \\ 0 & \mathbf{I} \end{pmatrix} \begin{pmatrix} {}^E\ddot{r}_{AE} \\ {}^E\dot{\omega}_{AE} \end{pmatrix} = \begin{pmatrix} \hat{\mathbf{I}}^{\mathbf{T}}\bar{\mathbf{R}} f({}^E\dot{r}_{AE}, {}^E\omega_{AE}, z, \dot{z}) \\ \hat{\tilde{\mathbf{r}}}^{\mathbf{T}}\bar{\mathbf{R}} f({}^E\dot{r}_{AE}, {}^E\omega_{AE}, z, \dot{z}) \end{pmatrix} + \begin{pmatrix} \hat{\mathbf{I}}^{\mathbf{T}}\boldsymbol{M} \\ \hat{\tilde{\mathbf{r}}}^{\mathbf{T}}\boldsymbol{M} \end{pmatrix} \left(\tilde{\boldsymbol{\Omega}}\tilde{\boldsymbol{\Omega}}\hat{\mathbf{r}} + 2\tilde{\boldsymbol{\Omega}}\psi z\right) \tag{2.87}$$

and the equations of motion for the elastic system

$$M_m\ddot{z} + K_m z = \psi^T f({}^E\dot{r}_{AE}, {}^E\omega_{AE}, z, \dot{z}) + \psi\bar{\mathbf{R}}^T\boldsymbol{M}\left(\tilde{\boldsymbol{\Omega}}\tilde{\boldsymbol{\Omega}}\hat{\mathbf{r}} + 2\tilde{\boldsymbol{\Omega}}\psi\dot{z}\right). \tag{2.88}$$

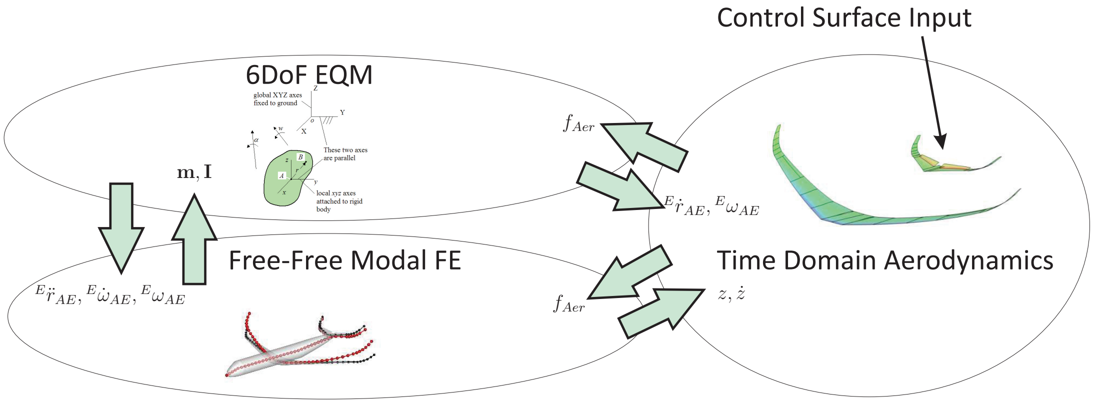

Figure 2.16. – Solution Scheme for Partitioned Approach

It can be assumed that the deformation induced due centrifugal and coriolis acceleration $\left(\widetilde{\mathbf{\Omega}}\widetilde{\mathbf{\Omega}}\hat{\mathbf{r}} + 2\widetilde{\mathbf{\Omega}}\psi\dot{z}\right)$ is very small compared to the aerodynamic forces, since the rotation rates and deformation rates are relatively low and hence can be neglected. Equation 2.88 then simplifies to

$$M_m\ddot{z} + K_m z = f_m, \tag{2.89}$$

where f_m is the sum of all external forces in modal coordinates. This formulation is similar to the equation found in [10] or [78]. The 6DoF rigid equations of motion are solved separately from the elastic structural equations of motion. The finite element system is transformed into modal coordinates system using the free-free modeshapes and applying the aerodynamic and inertial loads to obtain the instantaneous deformation. This procedure is depicted in Figure 2.16. The force vector f is composed of all external loads such as aerodynamic forces, gravitational loads and engine forces. Equation 2.87 and Equation 2.88 are only coupled via the aerodynamic forces which are obtained as a function of the inflow boundary conditions given by the rigid body states ${}^E\dot{r}_{AE}$ and ${}^E\omega_{AE}$ and the instantaneous modal deformation z and modal deformation velocity $\dot{z}$ projected from the structural mesh onto the aerodynamic mesh.

2.5.6. Numerical Solution

The solution of the equations of motion for a structural FE system requires an implicit time integration scheme. In this work the Newmark-Beta method first introduced in [92] is implemented, for details of the derivation also see [92]. The state vector x for the elastic system is given by

$$x = \begin{pmatrix} {}^E\ddot{r}_{AE} \\ {}^E\dot{\omega}_{AE} \\ \ddot{\delta} \end{pmatrix} \tag{2.90}$$

containing the rigid body states and the elastic deformations. The state vector for time $t+1$ is given by

$$\begin{aligned} x_{t+1} = (\underline{\mathbf{M}} + \beta_{\mathrm{NM}}\Delta t^2\underline{\mathbf{K}} + \gamma_{\mathrm{NM}}\Delta t\underline{\mathbf{C}})^{-1}(\beta_{\mathrm{NM}}\Delta t^2\boldsymbol{f} + \underline{\mathbf{M}}x_t + \Delta t\underline{\mathbf{M}}\dot{x}_t + \Delta t^2\underline{\mathbf{M}}(\frac{1}{2} - \beta_{\mathrm{NM}})\ddot{x}_t \\ + \underline{\mathbf{C}}\beta_{\mathrm{NM}}\Delta t^2\frac{\gamma_{\mathrm{NM}}}{\beta_{\mathrm{NM}}\Delta t}x_t + (\frac{\gamma_{\mathrm{NM}}}{\beta_{\mathrm{NM}}} - 1)\dot{x}_t + \frac{1}{2}\Delta t(\frac{\gamma_{\mathrm{NM}}}{\beta_{\mathrm{NM}}} - 2)\ddot{x}_t \end{aligned}. \tag{2.91}$$

The derivative of the state vector is given by

$$\ddot{x}_{t+1} = \frac{1}{\beta_{\mathrm{NM}}\Delta t^2}(x_{t+1} - x_t - \Delta t\dot{x}_t - \Delta t^2(\frac{1}{2} - \beta_{\mathrm{NM}})\ddot{x}_t), \tag{2.92}$$

and the acceleration of the state vector is given by

$$\dot{x}_{t+1} = \dot{x}_t + \Delta t((1 - \gamma_{\mathrm{NM}})\ddot{x}_t + \gamma_{\mathrm{NM}}\ddot{x}_{t+1}). \tag{2.93}$$

The parameters are set to $\beta_{NM} = \frac{1}{4}$ and $\gamma_{\mathrm{NM}} = \frac{1}{2}$ which is equivalent with assuming constant acceleration between two timesteps. Note that unless analyzing a restrained finite element model the matrices $\underline{\mathbf{M}}$, $\underline{\mathbf{K}}$ and $\boldsymbol{f}$ vary in time and hence have to be recomputed for each timestep. Using the partitioned approach the Newmark-Beta scheme can also be applied using the matrices M_m, K_m and the force vector f_m where no re-computation of the matrices per timestep is required. For the damping matrix $\underline{\mathbf{C}}$ a very small Rayleigh Damping is introduced to suppress numerical noise.

2.5.7. Dynamic Coupling

Dynamic aeroelastic time domain computations require the coupling of aerodynamic and structural equations. Here a partitioned Fluid Structure Interaction (FSI) approach is implemented. The time marching UVLM is loosely coupled to the transient beam model (see Figure 2.17). For each time step the aerodynamic forces are computed and mapped onto the structural model where the deformations and body movements are computed and transformed to the aerodynamic grid and boundary conditions for the next time step. The analysis can be performed on the restrained or free flying aircraft. The free flying aircraft can be trimmed initially using the trim computation described in Section 2.9.

2.6. Fast Time Flight Simulation Model

The direct simulation of the free flying elastic aircraft is in some cases computationally too expensive for the efficient evaluation of aircraft flight dynamics and handling qualities. Therefore a fast time simulation model is generated from the existing models. The fast time method is based on the partitioned method, solving the rigid body equations of motion separately from the elastic equations of motion.

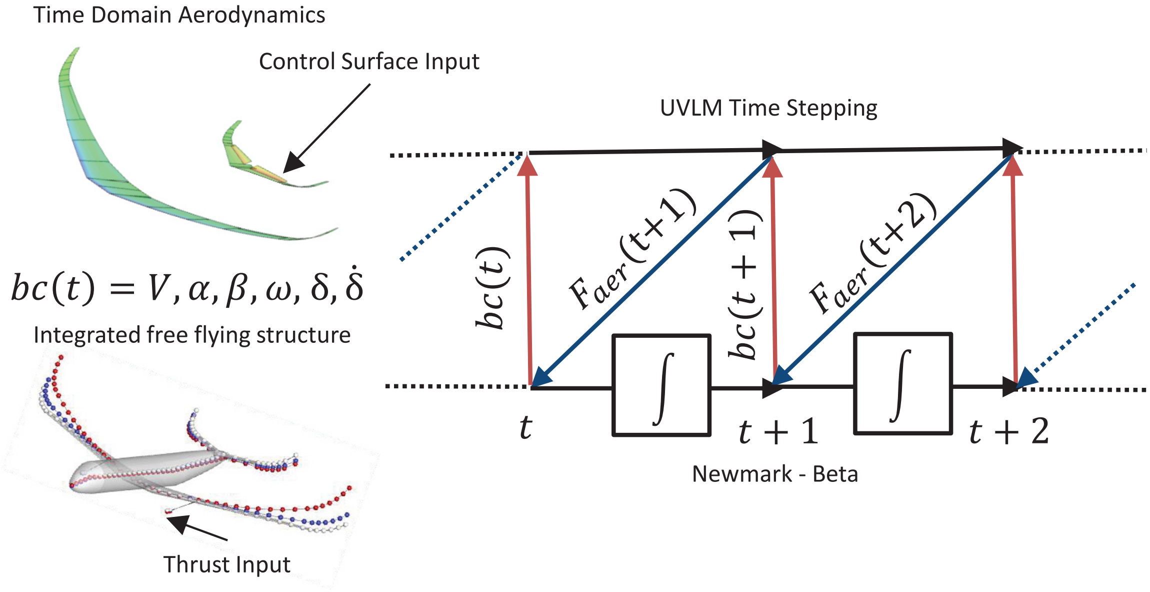

Figure 2.17. – Direct Simulation Flowchart

2.6.1. Rigid Body Equations of Motion

Investigating the six DoF rigid equation of motion, Equation 2.87 it can be seen that the terms $\hat{\mathbf{I}}^T\bar{\mathbf{R}}f$ and $\hat{\tilde{\mathbf{r}}}^{\mathbf{T}}\bar{\mathbf{R}}f$ represent the sum of all external forces and moments about the mean axis reference point, given in the X, Y, Z direction of the E frame. In order to solve the rigid body equations of motion the local force distribution in the structural system, given by the vector f is not of interest. The movement of the body is only depending on the sum of all external forces. Therefore the terms $\hat{\mathbf{I}}^T\bar{\mathbf{R}}f$ and $\hat{\tilde{\mathbf{r}}}^{\mathbf{T}}\bar{\mathbf{R}}f$ of Equation 2.87 can be rewritten as the sum of the total aerodynamic, engine and gravitational forces and moments about the mean axis reference point, resulting in

$$\begin{pmatrix}\hat{\mathbf{I}}^{\mathbf{T}}\bar{\mathbf{R}}f\\ \hat{\tilde{\mathbf{r}}}^{\mathbf{T}}\bar{\mathbf{R}}f\end{pmatrix} = q_\infty S_{\text{Ref}} \begin{pmatrix} C_x(\alpha,\beta,\text{Ma},\mathbf{p},\mathbf{q},\mathbf{r},z,\dot{z},z_c)\\ C_y(\alpha,\beta,\text{Ma},\mathbf{p},\mathbf{q},\mathbf{r},z,\dot{z},z_c)\\ C_z(\alpha,\beta,\text{Ma},\mathbf{p},\mathbf{q},\mathbf{r},z,\dot{z},z_c)\\ b_{\text{Ref}}C_l(\alpha,\beta,\text{Ma},\mathbf{p},\mathbf{q},\mathbf{r},z,\dot{z},z_c)\\ c_{\text{Ref}}C_m(\alpha,\beta,\text{Ma},\mathbf{p},\mathbf{q},\mathbf{r},z,\dot{z},z_c)\\ b_{\text{Ref}}C_n(\alpha,\beta,\text{Ma},\mathbf{p},\mathbf{q},\mathbf{r},z,\dot{z},z_c)\end{pmatrix} + \begin{pmatrix} f_{T,x}\\ f_{T,y}\\ f_{T,z}\\ m_{T,x}\\ m_{T,y}\\ m_{T,z}\end{pmatrix} + m\begin{pmatrix}0\\0\\g\\0\\0\\0\end{pmatrix} = f_{\text{Aer}} + f_T + f_g. \tag{2.94}$$

This leads to the rigid body equations of motion in the E system

$$\begin{pmatrix}\mathbf{m} & 0\\ 0 & \mathbf{I}\end{pmatrix}\begin{pmatrix}{}^E\ddot{r}_{AE}\\ {}^E\dot{\omega}_{AE}\end{pmatrix} = f_{\text{Aer}} + f_T + f_g + \begin{pmatrix}\hat{\mathbf{I}}^{\mathbf{T}}\boldsymbol{M}\\ \hat{\tilde{\mathbf{r}}}^{\mathbf{T}}\boldsymbol{M}\end{pmatrix}\left(\tilde{\boldsymbol{\Omega}}\tilde{\boldsymbol{\Omega}}\hat{\mathbf{r}} + 2\tilde{\boldsymbol{\Omega}}\psi z\right) \tag{2.95}$$

The most time consuming part of the solution procedure is the computation of the aerodynamic forces f_{Aer} for each time step. In order to reduce the computational requirements for flight simulations, aerodynamic datasets are usually obtained initially and stored in

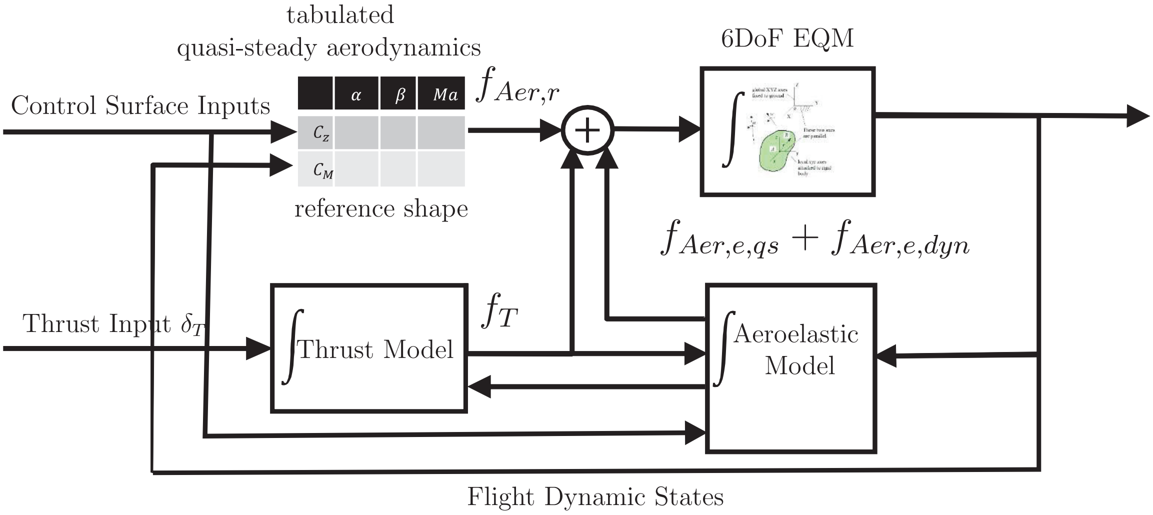

Figure 2.18. – Structure of the Fast Time Simulation Model

large tables. These aerodynamic coefficients are then interpolated during a simulation for the current flight state as a function of $\alpha, \beta, \mathrm{Ma}, \mathbf{p}, \mathbf{q}, \mathbf{r}$ and the control inputs z_c as shown in Figure 2.18. In aeroelasticity it is common practice to define the control deflections as an additional set of modes, hence the notation z_c, which denote the control surfaces deflections. Current practice is to generate these coefficient tables by means of handbook methods, low and high fidelity CFD methods, windtunnel experiments and finally correct them with flight test data. These aerodynamic tables can be generated relatively straightforward for a rigid aircraft using high or low fidelity CFD computations or windtunnel measurements [40]. In case of an elastic aircraft obtaining aerodynamic coefficients is more elaborate. Windtunnel testing is a challenge due to scalability issues of aeroelastic properties. Similarly obtaining high fidelity computational aerodynamic data via Euler or RANS for an elastic vehicle requires coupled CSD/CFD simulations which require a large computational effort compared to a rigid aircraft. In order to overcome that problem, it is assumed that the overall aerodynamic force coefficient can be separated into a rigid component $f_{Aer,r}$ and an elastic, deformation induced component $f_{Aer,e}$ leading to

$$f_{\mathrm{Aer}} = f_{\mathrm{Aer},r} + f_{\mathrm{Aer},e}. \tag{2.96}$$

The rigid aerodynamic forces $f_{\mathrm{Aer},r}$ are determined from an interpolation of rigid aerodynamic coefficient tables depending on the control surface inputs as well as the current flight state. The deformation induced contribution to the aerodynamic force $f_{\mathrm{Aer},e}$ is determined by solving the elastic equation of motion (Equation 2.88). The deformation induced part from 2.95 can be generally separated into a quasi-steady component $f_{\mathrm{Aer},e,qs}$ and into an unsteady component $f_{\mathrm{Aer},e,dyn}$ [78]. The quasi-steady part of the deformation induced force is often already integrated in the tabulated dataset by means of so-called flex factors which may be a function of flight dynamic states (e.g. load factor n_z) and control inputs. The flex factor may be obtained by CFD computations and eventually be corrected by flight test data. However in the given early design state no flex factor corrected aerdynamic dataset is available. The given method however should not be restricted towards the later application of more accurate and flex factor corrected aero tables, therefore the quasi steady and unsteady part are considered separately in the model. The method for the separation of the quasi-steady and unsteady aeroelastic increments is detailed in Section 2.6.3. Figure 2.18 shows the structure of the fast time flight simulation model. The external forces are summed up from the rigid aerodynamic forces, the elastic aerodynamic forces, the gravitational forces and the thrust forces. Landing gear forces are considered as well upon ground contact but are not shown in the graph. The thrust model is described in Section 2.8.1.

2.6.2. First Order Linear Aeroelastic Model

The quasi-steady and the dynamic elastic forces $f_{\mathrm{Aer},e}$ are found by solving the elastic equation of motion Eq. 2.89. These are influenced by the flight state, the control surface deflections as well as the thrust forces. The solution of Eq. 2.89 for a fast time application utilizes an indirect method for the computation of the elastic aerodynamic forces. Indirect methods construct the time-response of a direct method using oscillatory, step or impulse responses. In this case oscillatory responses are used generating the generalized aerodynamic forces, as described in Section 2.4. The UVLM has the significant advantage that the constant part Q_0 can be determined simultaneously while the DLM is not able of capturing the constant contribution. A generalized aerodynamic coefficient matrix including the rigid body modes and control modes is of the form

$$Q = \left(\begin{array}{c|c|c} Q_{rr} & Q_{re} & Q_{rc} \\ \hline Q_{er} & Q_{ee} & Q_{ec} \\ \hline Q_{cr} & Q_{ce} & Q_{cc} \end{array}\right) + Q_0 \tag{2.97}$$

where Q_{rr} represents the influence coefficients of the rigid body movements on the aerodynamic rigid body coefficients, Q_{re} represents the impact of elastic modal displacements on the rigid body coefficients, Q_{er} describes the impact of rigid body movements on modal elastic forces, and Q_{ee} describes the elastic-elastic interaction. The control surface movements are considered as a separate set of modes where Q_{ec} represents the impact of a control surface deflection on the elastic deformation. The free-free modal analysis leads to six zero frequency modes which are rigid body modes. These rigid body modes are solved in principal axis, which are not matching the B frame. Therefore these modes are replaced by the six rigid body modes z_r , which are unit translations and unit rotations in the B frame (similar to [105]) as shown in Figure 2.19, before the GAF's are computed. This results in body referenced aerodynamic coefficients making further transformations obsolete, as suggested in [78, p77. ff]. This simplifies the later integration into the flight dynamic model. The parts Q_{rr} and Q_{rc} are accounted for in the rigid nonlinear tabulated data, and are therefore not required in the further analysis. Furthermore Q_{cr}, Q_{ce} and Q_{cc} are small compared to other influences and are not considered in the further modeling.

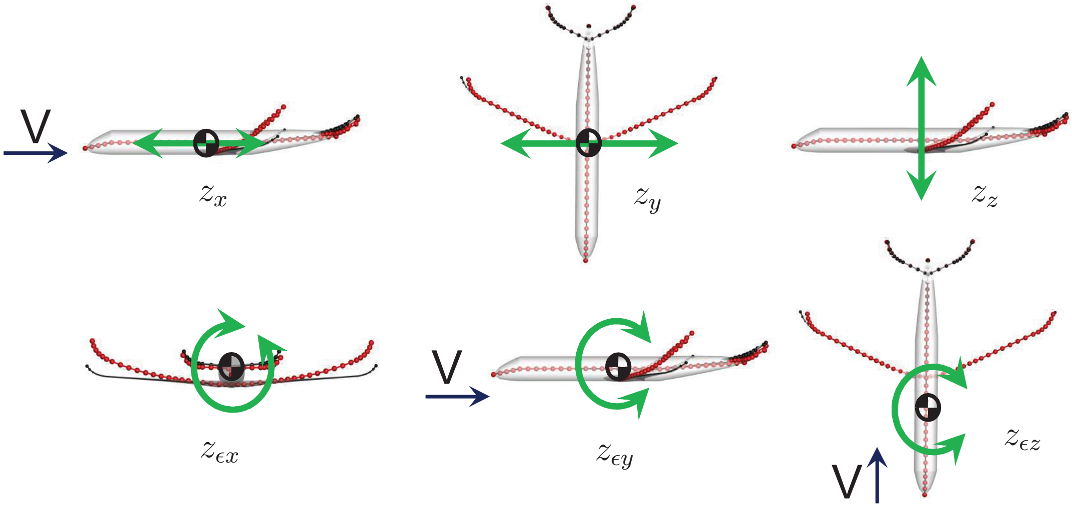

Figure 2.19. – Rigid Body Modes in Body Coordinates

Note that Q only represents linear increments about a reference geometry. The constant force coefficients resulting while all modal deflections are at zero are given in the matrix Q_0. The generalized aerodynamic coefficient matrix Q in the presented toolchain is obtained using the UVLM. The coefficients are computed for a number of reduced frequencies k defined by

$$k = \frac{\omega c_{Ref}}{2V} \tag{2.98}$$

and Mach Numbers Ma resulting in a tabulated set of $Q(k, \mathrm{Ma})$ which is transformed into the frequency domain to allow the further application of a Rational Function Approximation as described in the next paragraph. Q may also depend on other flight parameters such as n_z which reflects the shape. The external force f_m can be written as

$$f_m = q_\infty Q_{ee}(s) z_e + q_\infty Q_{er}(s) z_r + q_\infty Q_{ec}(s) z_c + q_\infty Q_{0,e} + f_T + f_g \tag{2.99}$$

and the deformation induced force on the rigid equations of motion is determined by following equation

$$f_{re} = q_\infty Q_{re} z_e \tag{2.100}$$

Rational Function Approximation The aerodynamic forces are approximated in the Laplace domain using the method of Roger as outlined in [122], [107] and the methods of Karpel as outlined [61], [62]. These methods are frequently applied for flight simulation and flight control of elastic aircraft. The method of Rogers performs an approximation of the form

$$Q(s') = \left(A_0 + A_1 s' + A_2 s'^2 + \sum_{i=3}^{n} \frac{A_i s'}{s' + p_i} \right) z + Q_0, \tag{2.101}$$

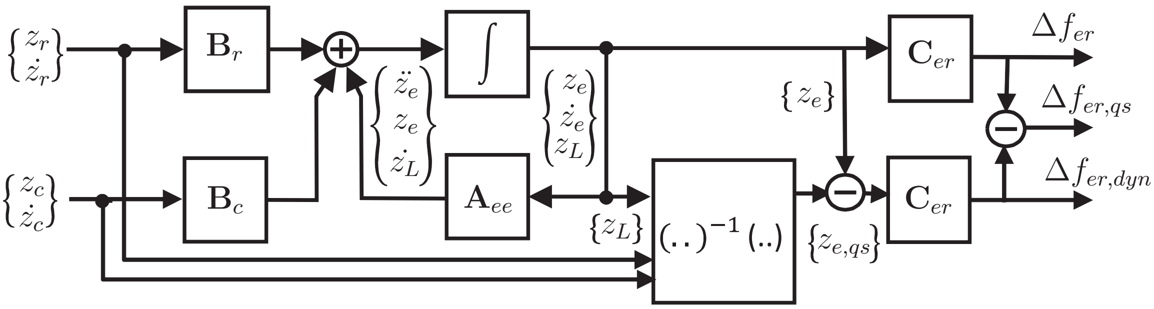

Figure 2.20. – Structure of First Order Linear Aeroelastic State Space System

where s' is the nondimensionalized Laplace variable given by

$$s' = \frac{s c_{Ref}}{2V}. \tag{2.102}$$

A are the coefficients of the approximated function and p are the roots of the rational function. In Rogers method each coefficient is approximated by a separate rational function, which leads to a large amount of augmented aerodynamic lag states when transforming the equation into the time domain. Karpel [60] developed a method minimizing the number of augmented aerodynamic states, by using the same set of lag states for all coefficients, leading to an approximation of the aerodynamic coefficients of the following form

$$Q(s') = \left(A_0 + A_1 s' + A_2 s'^2 + D(s'I - R)^{-1} E s'\right) z + Q_0. \tag{2.103}$$

It is convenient to perform the rational function approximation on the whole set of generalized aerodynamic coefficients of Eq. 2.97 and separate the system later to obtain the forces in Equations 2.99 and 2.100. Applying a RFA on the generalized aerodynamic coefficient matrix allows a significant reduction of the computational requirements compared to the direct time domain computation of the aerodynamic forces.

Derivation of the State-Space System using Rogers Approximation The matrices A_0, A_1, A_2 and A_N result from a least squares fit on a tabulated set of $Q(s)$ and result in the same form as given in Equation 2.97. Inserting Equation 2.99 into the Laplace transformed version of Equation 2.89 results in

$$M_m s^2 z + K_m z = q_\infty Q_{ee} z_e + q_\infty Q_{er} z_r + q_\infty Q_{ec} z_c + q_\infty Q_0. \tag{2.104}$$

Note that at this point the the gyroscopic coupling terms $\psi^T M \bar{\mathbf{R}}^{\mathbf{T}} \hat{\mathbf{I}}$ and $\psi^T M \bar{\mathbf{R}}^{\mathbf{T}} \hat{\hat{\mathbf{r}}}$ neglected in Section 2.5.5 may be incorporated into the equation. Furthermore the mass coupling between the control and the structural modes may be incorporated at this point. In order to keep the equations reasonably simple this exercise is left to the reader, as it does not lead to additional insights. In the next step Q is replaced by the approximated set of coefficients yielding in

$$\begin{aligned} M_m s^2 z_e + K_m z_e = q_\infty &\left(A_{0,ee} + A_{1,ee} s + A_{2,ee} s^2 + \sum \frac{A_{i,e} s}{s + p_i} \right) z_e + \\ q_\infty &\left(A_{0,er} + A_{1,er} s + A_{2,er} s^2 + \sum \frac{A_{i,e} s}{s + p_i} \right) z_r + \\ q_\infty &\left(A_{0,ec} + A_{1,ec} s + A_{2,ec} s^2 + \sum \frac{A_{i,e} s}{s + p_i} \right) z_c + q_\infty Q_0 \end{aligned} \tag{2.105}$$

and the elastic force increment due to deformation is then given by

$$f_{re} = q_\infty \left(A_{0,er} + A_{1,er} s + A_{2,er} s^2 + \sum \frac{A_N s}{s + p} \right) z_e. \tag{2.106}$$

Transforming Equation 2.105 back into the time domain yields a first-order, linear, aeroservoelastic mathematical model of the form

$$\begin{pmatrix} \dot{z}_e \\ \ddot{z}_e \\ \dot{x}_{L,e} \\ \dot{x}_{L,r} \\ \dot{x}_{L,c} \end{pmatrix} = \mathbf{A} \begin{pmatrix} z_e \\ \dot{z}_e \\ x_{L,e} \\ x_{L,r} \\ x_{L,c} \end{pmatrix} + \mathbf{B}_r \begin{pmatrix} z_r \\ \dot{z}_r \\ \ddot{z}_r \end{pmatrix} + \mathbf{B}_c \begin{pmatrix} z_c \\ \dot{z}_c \\ \ddot{z}_c \end{pmatrix} \tag{2.107}$$

and

$$\begin{pmatrix} \Delta f_e \\ \Delta m_e \end{pmatrix} = \mathbf{C} \begin{pmatrix} z_e \\ \dot{z}_e \\ \ddot{z}_e \\ x_{L,e} \end{pmatrix} \tag{2.108}$$

where $\mathbf{A}$ is the system matrix, $\mathbf{B}_r$ is the input matrix for the rigid states, $\mathbf{B}_c$ is the input matrix for the control states and $\mathbf{C}$ is an output matrix determining the elastic force increments. This state space system is depicted in Figure 2.20. The matrices $\mathbf{B}$ and $\mathbf{C}$ are found by separating the system resulting from the RFA of the generalized aerodynamic forces. The transformation into the time domain requires additional state variables, the lag states, or augmented aerodynamic states, which are to be separated into elastic, rigid and control contributions. This is for the reason that only the elastic lag states should impact the aeroelastic aerodynamic increments, as the rigid aerodynamics are already considered in the data tables. They are defined as

$$x_{L,e} = \frac{s}{s + p} z_e \tag{2.109}$$

for the elastic states,

$$x_{L,r} = \frac{s}{s + p} z_r \tag{2.110}$$

for the rigid states and

$$x_{L,c} = \frac{s}{s+p} z_c \tag{2.111}$$

for the control states. The system matrix results in

$$\mathbf{A}_R = \begin{pmatrix} 0 & \boldsymbol{I} & 0 & 0 & 0 \\ -M_{ee}^{-1}K_{ee} & -M_{ee}^{-1}C_{ee} & M_{ee}^{-1}A_{i,ee} & M_{ee}^{-1}A_{i,er} & M_{ee}^{-1}A_{i,ec} \\ 0 & \boldsymbol{I} & \frac{V}{b_{\mathrm{Ref}}}\boldsymbol{I}p & 0 & 0 \\ 0 & 0 & 0 & \frac{V}{b_{\mathrm{Ref}}}\boldsymbol{I}p & 0 \\ 0 & 0 & 0 & 0 & \frac{V}{b_{\mathrm{Ref}}}\boldsymbol{I}p \end{pmatrix} \tag{2.112}$$

also shown in [77] and [78] where

$$K_{ee} = -\frac{1}{2} S_{\mathrm{Ref}} \rho V^2 A_{0,ee} + K_m \tag{2.113}$$

is the aeroelastic stiffness matrix,

$$C_{ee} = -\frac{1}{2} S_{\mathrm{Ref}} \rho V \frac{c_{\mathrm{Ref}}}{2} A_{1,ee} \tag{2.114}$$

is the aeroelastic damping matrix and

$$M_{ee} = -\frac{1}{2} S_{\mathrm{Ref}} \rho \frac{c_{\mathrm{Ref}}}{2} A_{2,ee} + M_m \tag{2.115}$$

is the equivalent aeroelastic mass matrix. The input matrix for the rigid states is given by

$$\mathbf{B}_{R,r} = \begin{pmatrix} 0 & 0 & 0 \\ M_{ee}^{-1}K_{er} & M_{ee}^{-1}C_{er} & M_{ee}^{-1}M_{er} \\ 0 & 0 & 0 \\ 0 & \boldsymbol{I} & 0 \\ 0 & 0 & 0 \end{pmatrix}. \tag{2.116}$$

The input matrix for the control states is given by

$$\mathbf{B}_{R,c} = \begin{pmatrix} 0 & 0 & 0 \\ M_{ee}^{-1}K_{ec} & M_{ee}^{-1}C_{ec} & M_{ee}^{-1}M_{ec} \\ 0 & 0 & 0 \\ 0 & 0 & 0 \\ 0 & \boldsymbol{I} & 0 \end{pmatrix} \tag{2.117}$$

The output matrix **C** is determined as

$$\mathbf{C}_R = \begin{pmatrix} K_{er} & C_{er} & M_{er} & A_{er,lag} \end{pmatrix} \tag{2.118}$$

where

$$K_{er} = \frac{1}{2} S_{\mathrm{Ref}} \rho V^2 A_{0,er}, \tag{2.119}$$

$$C_{er} = \frac{1}{2} S_{\mathrm{Ref}} \rho V \frac{c_{\mathrm{Ref}}}{2} A_{1,er} \tag{2.120}$$

and

$$M_{er} = \frac{1}{2} S_{\mathrm{Ref}} \rho \frac{c_{\mathrm{Ref}}}{2} A_{2,er}. \tag{2.121}$$

Derivation of the State-Space System using Karpels Minimum State Approximation
When applying Karpel's method an iterative approximation procedure determines the approximated matrices A, E and D for Eq. 2.103. The procedure for the generation of the state space model is very similar for Rogers and for Karpels method, however the lag states cannot be separated in the same way. Starting again by inserting Equation 2.99 into the Laplace transformed version of Equation 2.89 this yields

$$\begin{aligned} M_m s^2 z_e + K_m z_e = q_\infty \left(A_{0,ee} + A_{1,ee} s + A_{2,ee} s^2 + D_e (s\boldsymbol{I} - R)^{-1} E_e s \right) z_e + \\ q_\infty \left(A_{1,er} s + A_{2,er} s^2 + D_e (s\boldsymbol{I} - R)^{-1} E_r s \right) z_r + \\ q_\infty \left(A_{0,ec} + A_{1,ec} s + A_{2,ec} s^2 + D_e (s\boldsymbol{I} - R)^{-1} E_c s \right) z_c \end{aligned} \tag{2.122}$$

and

$$f_{re} = q_\infty \left(A_{0,er} + A_{1,er} s + A_{2,er} s^2 + D_r (s\boldsymbol{I} - R)^{-1} E_e s \right) z_e \tag{2.123}$$

for the output equation. Again at this point the gyroscopic coupling terms and the mass coupling between the control surface modes and the elastic modes may be incorporated. The system matrix results in

$$\mathbf{A}_{\mathrm{ms}} = \begin{pmatrix} 0 & \boldsymbol{I} & 0 & 0 & 0 \\ -M_s^{-1} K_s & -M_s^{-1} B_s & M_s^{-1} D_e & M_s^{-1} D_e & M_s^{-1} D_e \\ 0 & E_e & \frac{V}{b_{\mathrm{Ref}}} R & 0 & 0 \\ 0 & 0 & 0 & \frac{V}{b_{\mathrm{Ref}}} R & 0 \\ 0 & 0 & 0 & 0 & \frac{V}{b_{\mathrm{Ref}}} R \end{pmatrix} \tag{2.124}$$

with the augmented states defined as

$$x_{L,e} = (sI - R)^{-1} E_e s z_e \tag{2.125}$$

for the elastic states,

$$x_{L,r} = (sI - R)^{-1} E_r s z_r \tag{2.126}$$

for the rigid states and

$$x_{L,c} = (sI - R)^{-1} E_c s z_c \tag{2.127}$$

for the control states. The rigid body state input matrix is

$$\mathbf{B}_{\mathrm{ms},r} = \begin{pmatrix} 0 & 0 & 0 \\ M_s^{-1}K_{sc} & M_s^{-1}B_{sc} & M_s^{-1}M_{sc} \\ 0 & 0 & 0 \\ 0 & E_r & 0 \\ 0 & 0 & 0 \end{pmatrix} \tag{2.128}$$

and the control input matrix is

$$\mathbf{B}_{\mathrm{ms},c} = \begin{pmatrix} 0 & 0 & 0 \\ M_s^{-1}K_{sc} & M_s^{-1}B_{sc} & M_s^{-1}M_{sc} \\ 0 & 0 & 0 \\ 0 & 0 & 0 \\ 0 & E_c & 0 \end{pmatrix}. \tag{2.129}$$

The output matrix, similar to Roger's method, is of the form

$$\mathbf{C}_{\mathrm{ms}} = \begin{pmatrix} K_{er} & C_{er} & M_{er} & D_{er} \end{pmatrix} \tag{2.130}$$

Using Karpels method a good approximation with a relatively low number of aerodynamic augmented states per desired accuracy is achieved. [61] and [62] investigate different possibilities for weighting the errors for the approximation of the generalized aerodynamic forces. Since the RFA cannot be performed without an approximation error the simulation accuracy of the fully nonlinear time domain model cannot be achieved even in the proximity of the linearization point. These linear models are however a good approximation in many cases and important for frequency domain analysis as well as controller design.

2.6.3. Separation of Quasi-Static and Dynamic Aeroelastic Increments

The incremental elastic forces can be separated into a dynamic and a quasi steady part. The quasi steady modal state can be determined by setting the elastic modal state derivatives to zero. This yields the equation for the quasi steady part of the modal state

$$\begin{aligned} z_{e,\mathrm{qs}} = q_\infty \left(K_m - q_\infty A_{0,ee}\right)^{-1} (A_{1,er}\dot{z}_r + A_{2,er}\ddot{z}_r + A_{N,e}x_{L,r} \\ A_{0,ec}z_c + A_{1,ec}\dot{z}_c + A_{2,ec}\ddot{z}_c + A_{Nr}x_{L,c} + q_\infty Q_0 \end{aligned}. \tag{2.131}$$

The unsteady part of the elastically induced aerodynamic force is then given by

$$\begin{pmatrix} \Delta f_{e,\mathrm{dyn}} \\ \Delta m_{e,\mathrm{dyn}} \end{pmatrix} = \mathbf{C} \begin{pmatrix} z_e - z_{e,\mathrm{qs}} \\ \dot{z}_e \\ \ddot{z}_e \\ x_{L,e} \end{pmatrix} \tag{2.132}$$

and the quasi steady part of the elastic increment is obtained by

$$\begin{pmatrix} \Delta f_{e,\text{qs}} \\ \Delta m_{e,\text{qs}} \end{pmatrix} = \mathbf{C} \begin{pmatrix} z_{e,\text{qs}} \\ 0 \\ 0 \\ 0 \end{pmatrix} . \tag{2.133}$$

This method is also referred to as the minimum residual method (MS-method) [78]. This separation allows to separately model the quasi steady contribution, where more elaborate methods can be used as the design process proceeds to more mature phases. In the conceptual aircraft design phase considered in this work, the fidelity level of the presented model is however sufficient.

2.6.4. Transformation of the Flight Dynamic States to Rigid Body Modes

The rigid body modal coordinates have to be determined from the flight dynamic states to integrate the aeroelastic state-space model into the fast time flight simulation. The generalized aerodynamic coefficients are computed in body axes relative to the reference inflow conditions. Therefore the position of the aircraft and the absolute orientation of the aircraft (Φ Θ Ψ) do not play any role for the aircraft elastic deformation. Similarly the translational modes r_x, r_y and r_z may remain zero since the aeroelastic coefficients should be independent of the position. Only considering the aerodynamic inflow angles α and β and the rotation rates $\mathbf{p}$, $\mathbf{q}$ and $\mathbf{r}$ determined by the transformation

$$\begin{pmatrix} z_x \\ z_y \\ z_z \\ z_{\epsilon x} \\ z_{\epsilon y} \\ z_{\epsilon z} \\ \dot{z}_x \\ \dot{z}_y \\ \dot{z}_z \\ \dot{z}_{\epsilon x} \\ \dot{z}_{\epsilon y} \\ \dot{z}_{\epsilon z} \end{pmatrix} = \begin{pmatrix} 0 & 0 & 0 & 0 & 0 \\ 0 & 0 & 0 & 0 & 0 \\ 0 & 0 & 0 & 0 & 0 \\ 0 & 0 & 0 & 0 & 0 \\ 1 & 0 & 0 & 0 & 0 \\ 0 & 1 & 0 & 0 & 0 \\ 0 & 0 & 0 & 0 & 0 \\ 0 & 0 & 0 & 0 & 0 \\ 0 & 0 & 0 & 0 & 0 \\ 0 & 0 & 1 & 0 & 0 \\ 0 & 0 & 0 & 1 & 0 \\ 0 & 0 & 0 & 0 & 1 \end{pmatrix} \begin{pmatrix} \alpha \\ \beta \\ \mathbf{p} \\ \mathbf{q} \\ \mathbf{r} \end{pmatrix} \tag{2.134}$$

represents an excellent approximation in most cases. A validation of the linear aeroelastic state-space model is presented in Appendix C.4.3.1 by comparing the gust response for a restrained model. Furthermore a validation of the full fast time simulation model can be found in Appendix C.4.5 comparing a pitch maneuver response to the direct time domain approach.

2.7. Atmosphere Model

The flight simulation requires the modeling of atmospheric properties. The atmosphere is modeled using an ISA standard atmosphere, which provides pressure, density and the speed of sound depending on the altitude [57].

2.8. Other External Forces

This section presents the modeling of other external forces on the aircraft such as the thrust forces and the landing gear forces.

2.8.1. Engine Model

An engine is represented by a first-order system with dimensionless heuristic lookup tables for thrust, thrust specific fuel consumption (TSFC), and the engine time constant. For the lookup table data, thrust is a function of throttle position and the Mach number Ma. TSFC is a function of thrust and the Mach number Ma, and the engine time constant is a function of thrust. The dimensionless lookup table outputs are corrected for altitude using the relative pressure ratio and the relative temperature ratio. The lookup tables are scaled by the maximum sea level static thrust, fastest engine time constant at sea level, the specific fuel consumption at sea level, and the ratio of installed thrust to uninstalled thrust [1], [101].

2.8.2. Landing Gear Model

A simple landing gear model is required for a number of criteria to be investigated as part of this work. The effect of lateral forces on the main landing gear was neglected since the implementation of a landing gear model which is sufficiently accurate for a reliable prediction of the aircraft behavior on the runway in case of One Engine Inoperative (OEI) was considered out of scope for this project. The main use for the landing gear model in the presented toolchain is the determination of take-off and landing performance which only requires ground contact forces and friction forces. The landing gear is modeled by means of a simple spring damper system for each of the gears and a friction model as shown in Figure 2.21.

2.9. Trimming

In order to perform any simulation, the model has to be trimmed initially. For this purpose the VLM and the beam model are coupled and an iterative solution is performed until an equilibrium between structural deformation and aerodynamic forces is reached. Deflections and aerodynamic forces can be computed for any given flight state. Figure 2.22 shows the trimming procedure. Initially the rigid aerodynamic forces are computed, which leads to

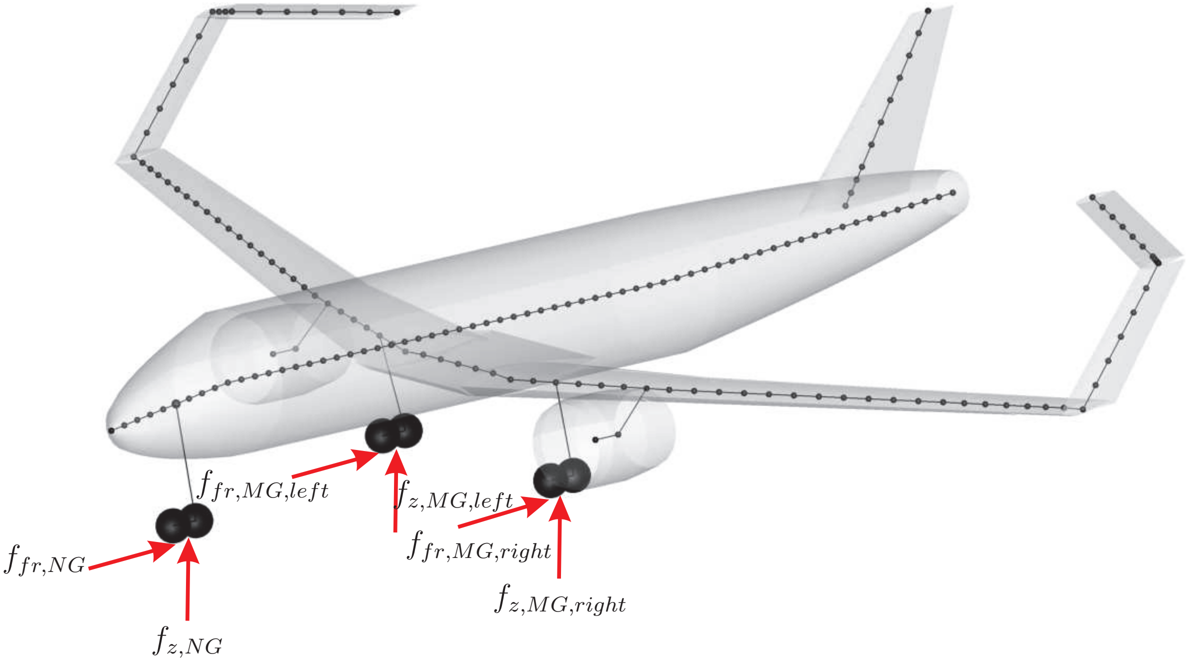

Figure 2.21. – Landing Gear Model

the initial deformation of the aircraft. After that, the new center of gravity is computed, which may have changed due to deformations. Then the new set of aerodynamic forces is computed for the deformed aircraft. This procedure is repeated until the deformation change from one step to the next is below a defined convergence limit.

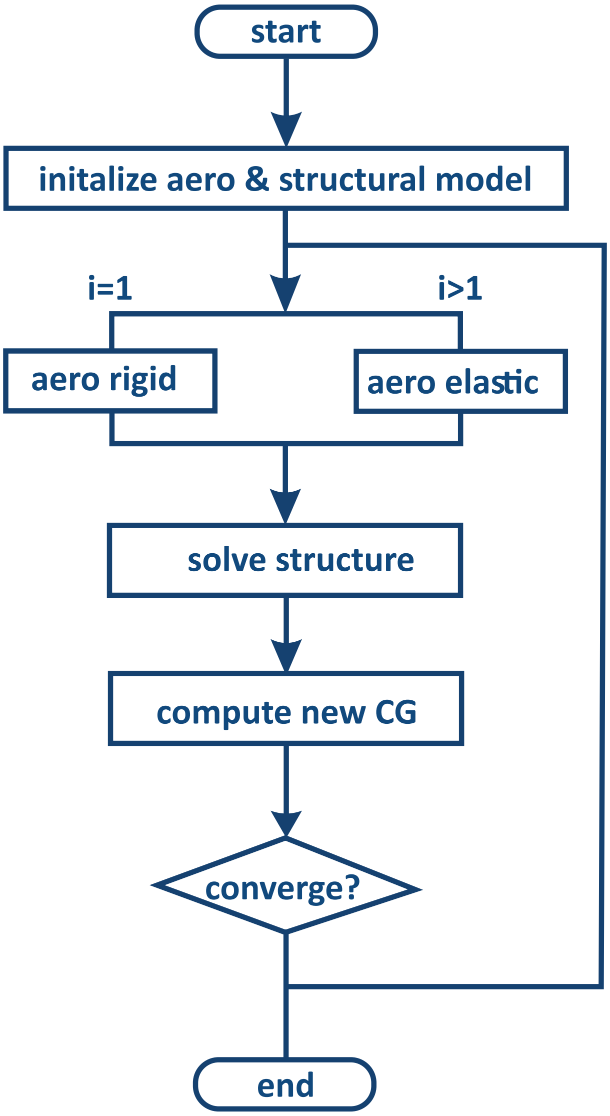

Figure 2.22. – Trim Loop

3. Generic Flight Simulation System

In Chapter 2 the modeling of the parametrized elastic airframe was presented, allowing the generation of arbitrary elastic airframe models for classic and novel configurations. In order to obtain a functional flight simulation model for flight dynamics and handling qualities analysis additional steps are required, which are detailed in this Chapter. Furthermore the example aircraft configurations investigated in further Chapters are presented.

3.1. Flight Simulation Model Generation

The additional steps required to generate a fully functional flight simulation model from the elastic aircraft model include the control allocation, the actuator modeling, the sensor modeling and the design of a Flight Control System (FCS). The FCS is representative of a digital fly-by-wire flight control system found on modern, civil transport aircraft. Figure 3.1 shows the structure of the flight simulation model for the elastic aircraft. The pilot signals are fed to the controller, which determines the desired virtual control deflections each mainly contributing to one axis i.e. pitch, roll or yaw. These virtual pitch, roll and yaw motion command signals are transformed into actuator command signals using the control allocation. After being split up into portions corresponding to real control surfaces, the command signals are fed to the actuator models, which provide the actual control surface deflection to the aircraft model. The outputs of the aircraft model are forwarded from the aircraft model to the sensor model. The sensor signals are finally fed back to the control law, which closes the loop. Each of the components is described in more detail in the following subsection.

3.1.1. Control Allocation

The aircraft is assumed to be controlled by four virtual inputs, the pitch control command η, the roll control command ξ, the yaw control command ζ and the thrust lever command δ_T. In order to allow the design of a standard flight control system, all control surfaces of the aircraft have to be allocated to a respective control task, either about the pitch, the yaw or the roll axis or multiple functions. The pitch control command η, the roll control

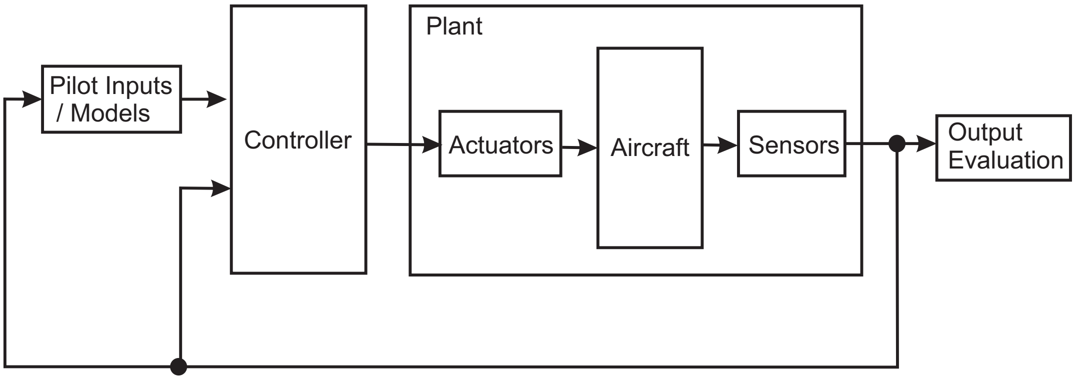

Figure 3.1. – Closed Loop Model for HQ Assessment

command ξ and the yaw control command ζ are assigned to the respective control surfaces via a control allocation matrix $\mathbf{G}$,

$$\begin{pmatrix} \delta_{aileron,left} \\ \delta_{aileron,right} \\ \delta_{rudder,left} \\ \delta_{elevator} \\ \cdots \end{pmatrix} = \mathbf{G} \begin{pmatrix} \eta \\ \xi \\ \zeta \end{pmatrix} . \tag{3.1}$$

The optimal allocation of control surfaces can be subject of more detailed investigations such as performed in [31], but is not considered more closely in this work.

3.2. Controller

The flight control system is designed using state of the art methods as e.g. presented in [22] and implemented in [47]. The controller provides two main operational modes, which are Normal Law and Direct Law. Normal Law is the mode active during normal operation of the aircraft and serves the purpose to translate pilot commands to respective actuator commands, adjusting the aircraft dynamics using the feedback loop to ensure good handling qualities as presented in Section 4 and furthermore to ensure that stability requirements as presented are met. Direct Law directly translates the pilot inputs to control surface commands and is active on ground, and partially during takeoff and landing. During a system failure Direct Law may also be active in flight operation.
The longitudinal control law structure is depicted in Figure 3.2. The controller uses a C^* command system. The concept of C^* is described in more detail in Section 4.2.3. The gains k_I, k_{n_Z} and $k_{\dot{\Theta}}$ are determined using an Eigenstructure Assignment. The feedforward gain h_η is determined such that a transmission zero is placed on the exact position of the pole corresponding to the C^* error integration. By means of this choice the integrator dynamics are invisible to the pilot command, whereas still compensate for

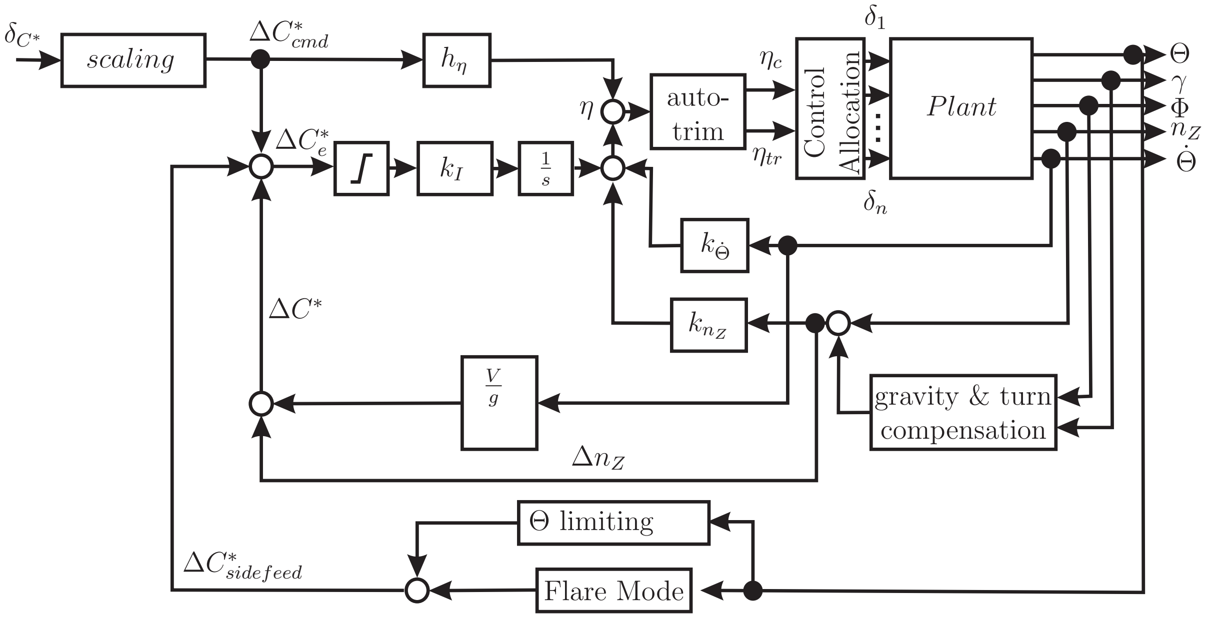

Figure 3.2. – Structure of Longitudinal Controller

disturbances. A turn compensation generates a compensating $\Delta n_{Z,turn}$ in order to track the commanded ΔC^*_{cmd} also precisely during turn maneuvers. Furthermore for take-off and landing simulations a flare mode and an attitude angle limitation is implemented. The auto-trim is only active if the simulated aircraft type has separate control surfaces for trimming and longitudinal control. For more details it is referred to [47]. A more detailed description of the Eigenstructure Assignment is e.g. found in [48] and [55]. The lateral controller depicted in Figure 3.3 implements a bank angle and sideslip angle command system. The feedback gains are also determined using an Eigenstructure Assignment, for more details it is again referred to [47].

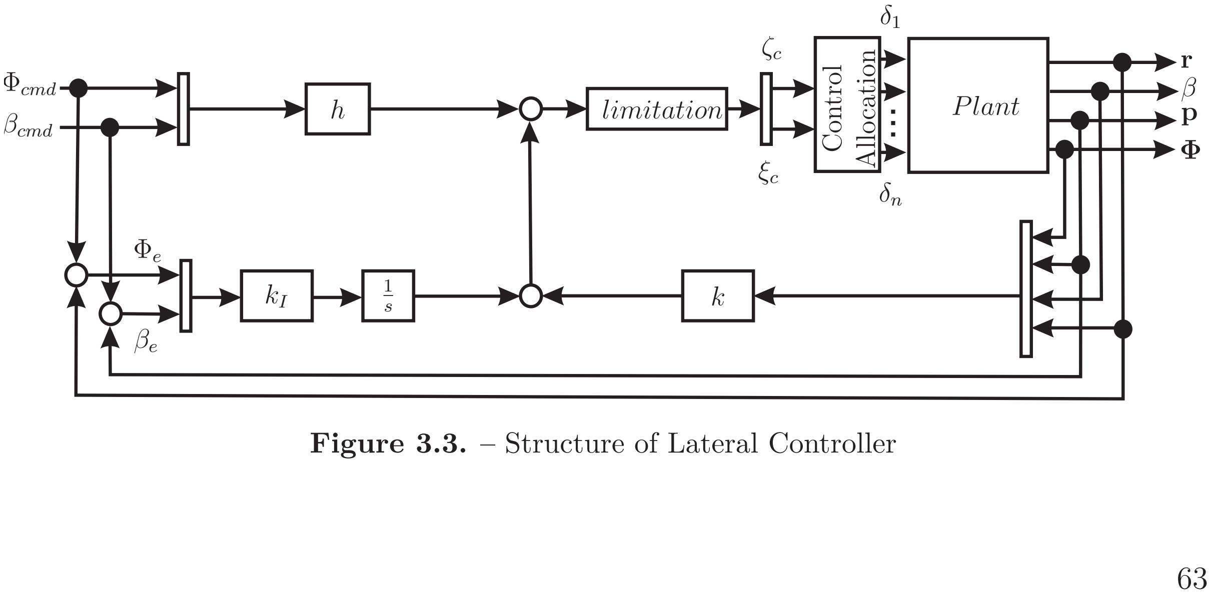

Figure 3.3. – Structure of Lateral Controller

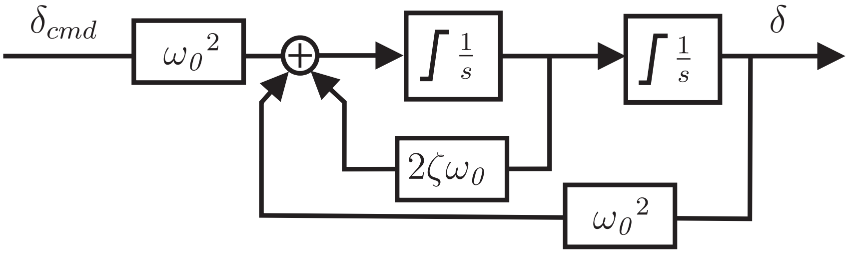

Figure 3.4. – Actuator Model

3.2.1. Actuators

A command by the pilot or controller will not affect the control surface instantaneously. The dynamics of actuators generally exhibit low pass behavior which is accounted for in the actuator model. All actuators are modeled by means of a second order low pass filter. The transfer function of a second order low pass filter is given by

$$G(s) = \frac{\omega^2}{1 + 2\zeta\omega s + \omega^2 s^2}. \tag{3.2}$$

Figure 3.4 exemplary shows the signal flow diagram of an actuator element, where ξ_{cmd} is the commanded control surface deflection and ξ is the resulting control surface deflection. All actuators implement a rate limit and deflection limit, depending on the control surface and the aircraft type. The deflection limit for a standard control surface unless specified otherwise assumes a range of $\delta_{max} = \pm 25°$. The standard rate limit assumes a value of $\dot{\delta}_{max} = \pm 40°/s$.

3.2.2. Sensors

Aircraft states are measured by sensors which cause delays and measure values with a measurement error. These effects are modeled in the sensor model. In the present model only a time delay is modeled. Measurement uncertainties are left out of consideration. This simple sensor model contains a representative delay of $160ms$. Thereof $20ms$ are the average delay between a measured physical event and the next sample, and $40ms$ result from a one-sample delay, based on a 25Hz sampling rate. This delay can actually be regarded as part of the control system and not of the sensor itself.

3.2.3. Rapid Controller Prototyping

The design of a flight control system requires linearized flight dynamic state space models which are generated for the entire flight envelope exemplary shown in Figure 3.5, for a range of different masses, CG's, Mach numbers and dynamic pressures. A longitudinal and a lateral gain scheduled controller is designed using an automatic design method described in [47]. The gains are determined using a pole placement algorithm, placing the respective poles at the desirable frequency and damping using Military Specifications

[129]. Hence a part of the required closed loop handling qualities is already implemented in the design of the control laws. The longitudinal control anticipation parameter (CAP) as defined in Section 4.2.1.2 is set to 1 determining the closed loop short period frequency. For the design of the control system, aeroelasticity is merely considered applying flex factors (quasi-steady aeroelasticity), hence assuming quasi steady aeroelasticity, which is valid if the short period frequency, ω_{SP} (see Section 4.2.1.1) is sufficiently separated from the lowest structural modes. An integrated approach for control design such as shown by [44] is required if the rigid and elastic modes are not clearly separated. The primary scope of this work however is the investigation of configurations, not the design of aeroelastic control methods. Hence in this work, the pole placement approach is used for all investigated concepts, which will already reveal in the conceptual design phase whether a classic control method can be used to design the control law of an aircraft or whether an advanced method is required to cope with aeroelastic effects.

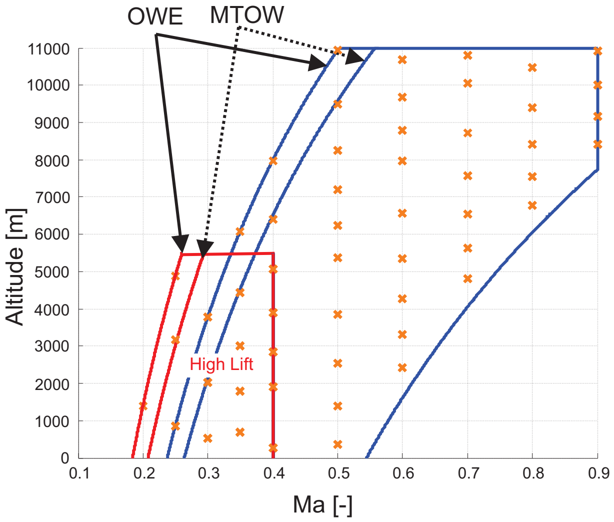

Figure 3.5. – Flight Envelope

3.3. Investigated Example Configurations

The process chain is used to evaluate two different aircraft configurations. The first configuration represents a classical aircraft (CC) which is used as a reference, and the second model represents a highly unconventional configuration (UCC).

3.3.1. Reference Benchmark Aircraft

The classical configuration shown in Figure 3.6 is a short to mid range aircraft with a capacity for 150 passengers. The aircraft is powered by two turbofan engines with a thrust of 120kN at sea-level. Basic aircraft data is presented in Table 3.1. Control is obtained by two independent outboard ailerons for roll control, a trimmable tailplane

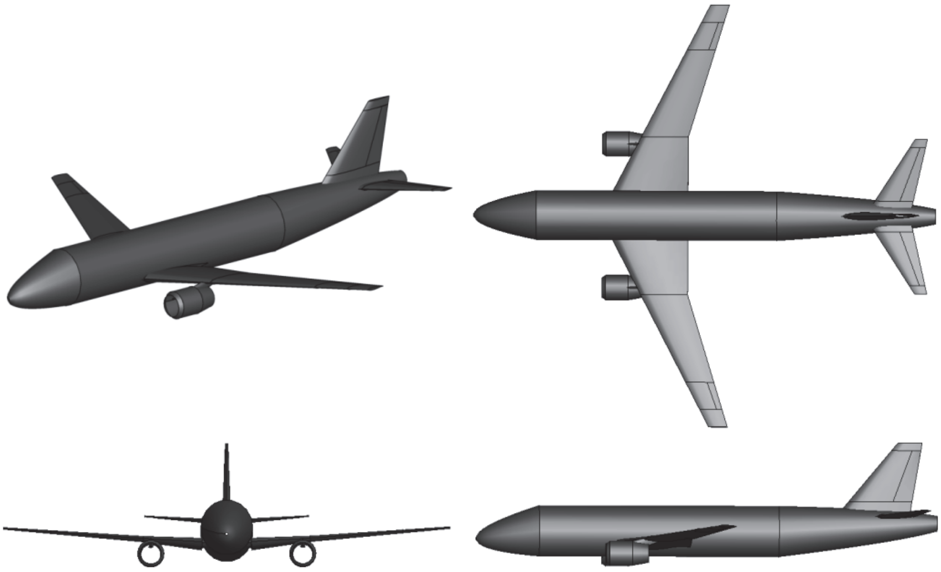

Figure 3.6. – Geometry of Benchmark Aircraft

for longitudinal trimming and elevators for pitch control, and a rudder for control in the yaw-axis. Important for the aeroelastic behavior are the frequencies and modeshapes of the structure. The first modes are shown in Figure 3.7 and their frequencies presented in Table 3.2, both for the fully fueled wing and empty state.

Table 3.1. – Basic Aircraft Data: Benchmark Aircraft

Parameter	Value	Unit
Service Altitude	11000	m
PAX	150	
Fuel Capacity	20	t
OWE	55	t
MTOW	78t	t

Table 3.2. – Eigenmode Frequencies of Benchmark Aircraft

Mode	Fuel Empty	Fuel Full	symmetry
1	2.53Hz	1.60Hz	symmetric
2	3.54Hz	2.39Hz	antisymmetic
3	4.67Hz	3.73Hz	symmetric
4	5.45Hz	4.06Hz	antisymmetic
5	6.8Hz	5.32Hz	symmetric

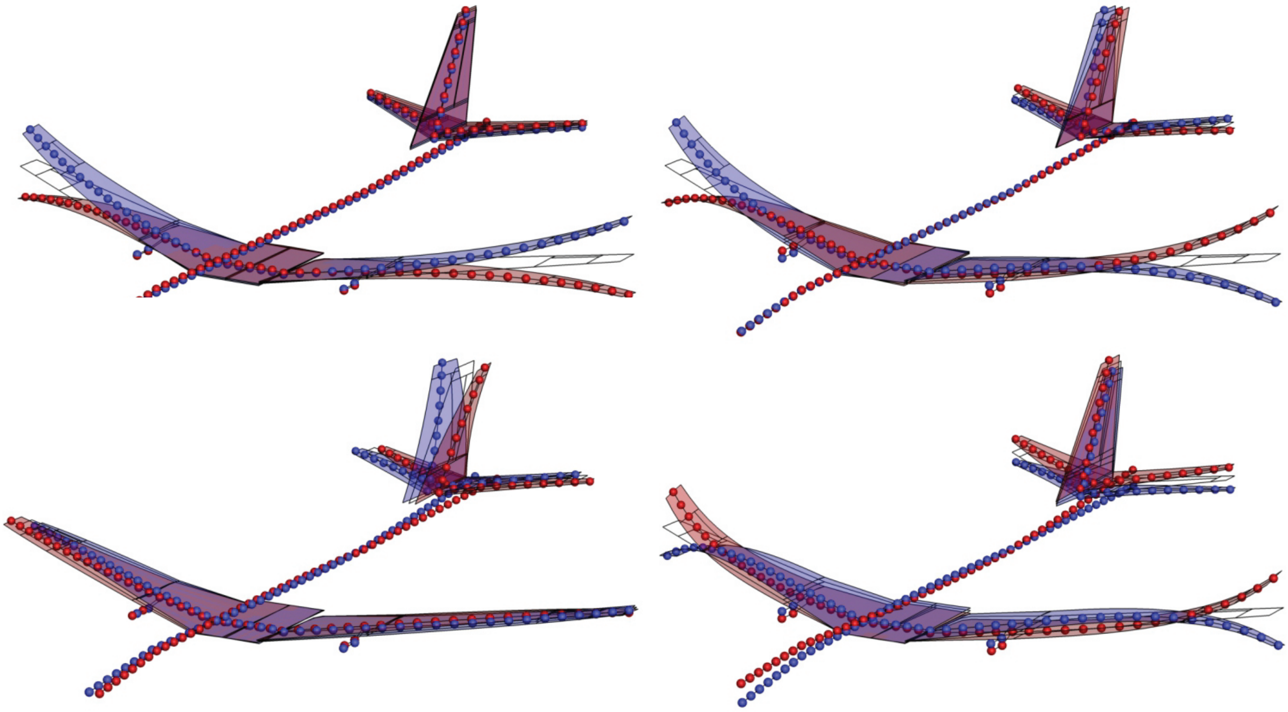

Figure 3.7. – Characteristic Modeshapes of the Classical Configuration

3.3.2. Unconventional Configuration

The investigated unconventional concept is a C-wing configuration shown in Figure 3.8. A C-shaped wingtip can be exploited to unify several advantages. It was shown that the theoretical induced drag reduction is close to the achievable optimum which can be obtained by a closed biplane, at the same time not increasing the wingspan [71]. This is a significant advantage considering airport parking size limitations. The predicted induced drag reductions are based on potential flow theory investigations but have been shown to hold for high fidelity Euler computations as well [108]. Transport aircraft designs involving a C-wing were shown in [58] and [82] suggesting to replace the horizontal stabilizer by using the top wing for pitch trimming and control. This is further investigated in [69] and [126] showing that trimming is possible for high altitude and high speed cases. Other multidisciplinary investigations of C-shaped wingtips were made in [59] and [96], however not considering the possibility of pitch trimming and control. Overall benefits considering multidisciplinary aspects of the C-wing were also predicted in [16].

The payload is equivalent to the classic configuration. Comparing to a classical configuration the horizontal stabilizer was removed, instead the top wing is applied for pitch control. It is assumed that all control surfaces can deflect by ±25° assuming attached flow under all conditions. Basic aircraft data is presented in Table 3.3.

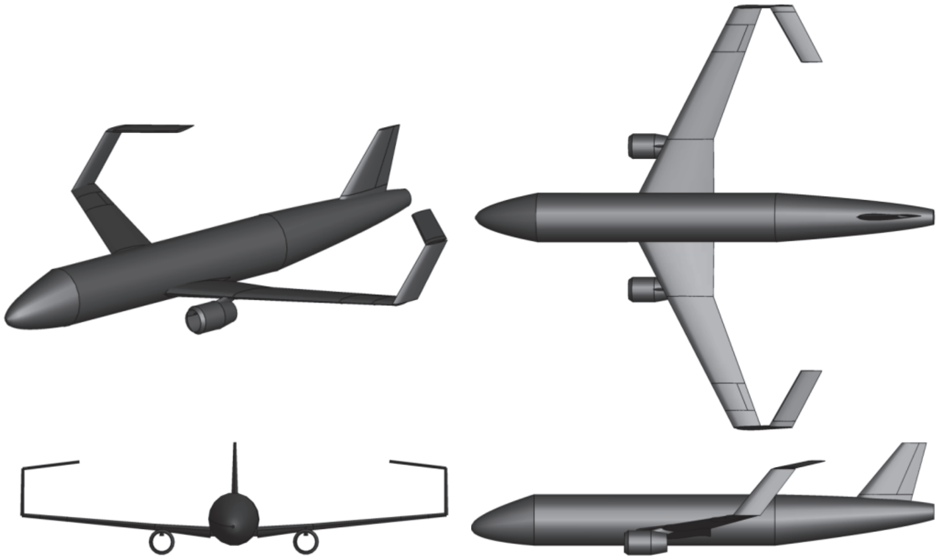

Figure 3.8. – Concept 1 Geometry

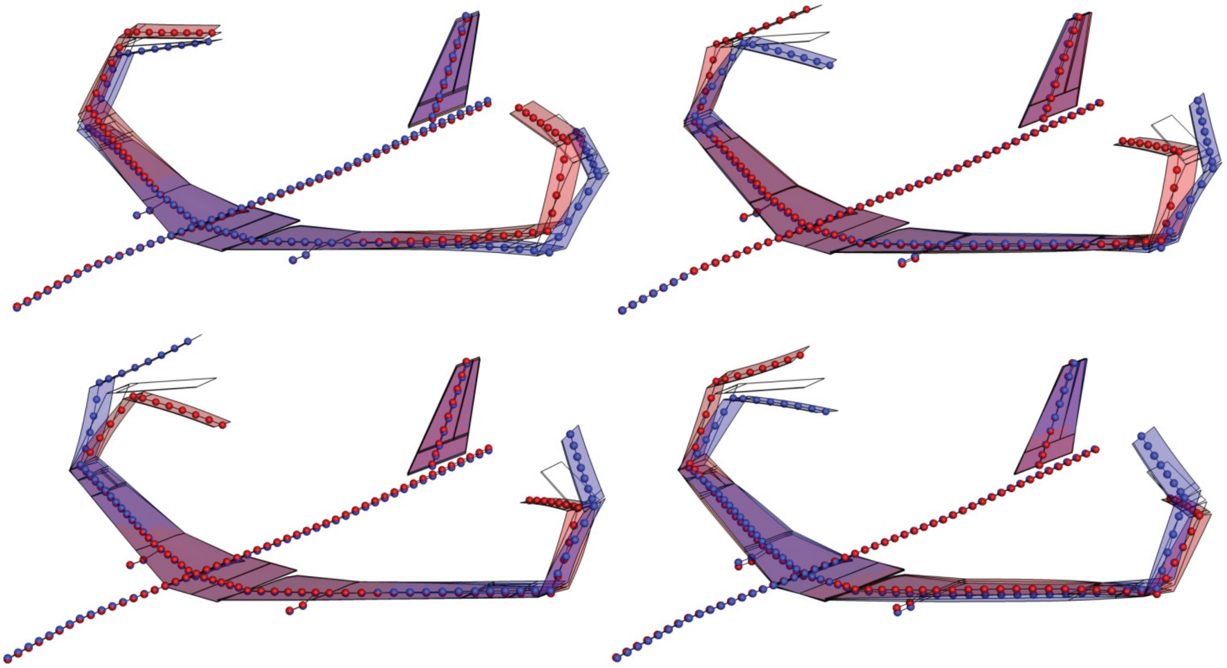

Figure 3.9. – Characteristic Modeshapes of the C-Wing

Table 3.3. – Basic Aircraft Data: C-Wing Configuration

Parameter	Value	Unit
service altitude	11000	m
PAX	150	
Fuel Capacity	20	t
OWE	58	t
MTOW	81t	t

The modeshapes and frequencies were computed as well as the flutter speed considering different fueling cases. The eigenfrequencies of the lowest frequency modes are shown in Table 3.4. Figure 3.9 shows the four lowest eigenmodes of the C-wing.

Table 3.4. – Eigenmode Frequencies of C-Wing Aircraft

Mode	Fuel Empty	Fuel Full	symmetry
1	1.09Hz	0.91Hz	symmetric
2	1.10Hz	1.07Hz	antisymmetic
3	1.11Hz	1.11Hz	symmetric
4	1.2Hz	1.15Hz	antisymmetic
5	1.9Hz	1.57Hz	symmetric

3.3.3. Stability and Response Analysis

In this section basic stability criteria are analyzed with respect to certification. Furthermore basic response properties of both aircraft are analyzed, in order to understand the impact on handling qualities detailed in the next chapter.

3.3.3.1. Longitudinal Trim and Stability

An aircraft needs to fulfill longitudinal trimmability [37, 1-B-19] (EASA CS-25.161) and stability [37, 1-B-20] (EASA CS-25.173) over the entire flight envelope, including all possible center of gravity and mass configurations. The rigid and elastic aircraft are trimmed for the entire defined flight envelope to check if the requirement is met.

Evaluation Figure 3.10 shows the required trim deflections for both configurations introduced in Section 3.3. It can be seen that as expected, a larger range of trim deflections is required for the UCC due to the shorter leverarm from the CG to the trim control surface, hence the smaller impact on the pitching moment. It can be seen that the aircraft is not trimmable for all CG and mass configurations, while the CC can be trimmed for all masses and CGs given the deflection limits. With respect to stability, for the Classical Configuration (CC) all trimmed conditions are stable while for the

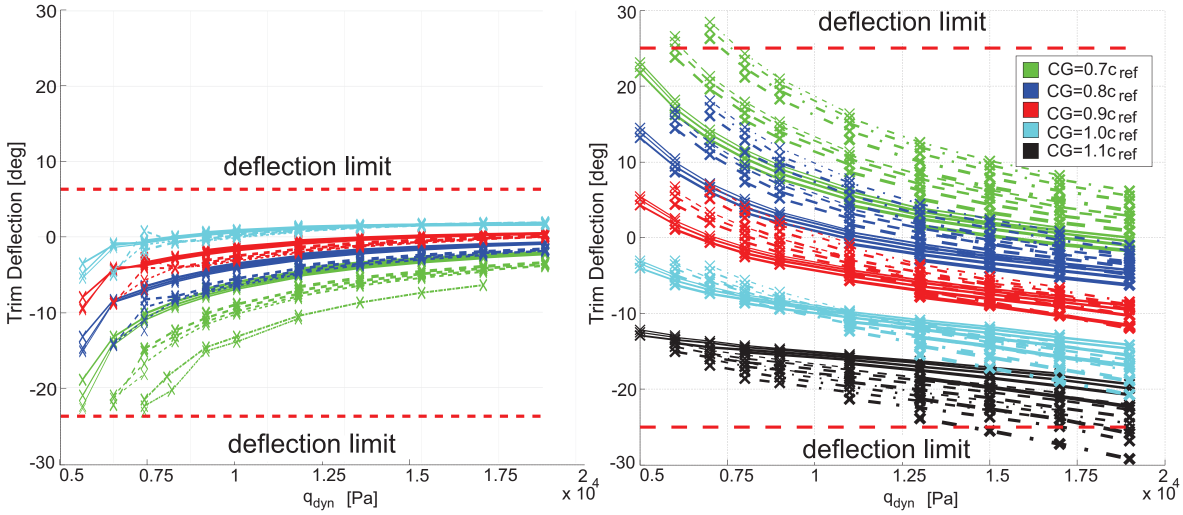

Figure 3.10. – Trim Envelope for the Classical and the C-Wing Configuration

Unconventional Configuration (UCC) trim conditions with the two most rearward CG positions are not statically stable. Furthermore a significant impact of the required trim deflections was observed for the UCC while there were only small changes in the trim angles for the CC due to elasticity.

3.3.3.2. Longitudinal Response

The impact of aeroelasticity on the longitudinal response differs for both configurations and is presented in the following.

Time Domain Response Figure 3.11 shows the pitch response following an elevator singlet input for both configurations for the rigid and elastic case. It can be seen that elasticity does not significantly impact the response of the classic configuration while a severe loss of longitudinal control authority can be seen for the unconventional configuration. The reason for this is that the longitudinal control surfaces impact the wing bending, which severely reduces their effectiveness.

Frequency Domain Response The bode diagrams for both configurations are shown in Figure 3.12 and Figure 3.13 for the transfer function from the stick input to the pitch attitude angle. It can be seen that the classic configuration shows a clear frequency separation, whereas for the unconventional configuration the structural modal frequencies are very close to the short period mode. This leads to a significant change in the transfer function, and shows a severe phase dropoff at the resonance frequency of the structural modes.

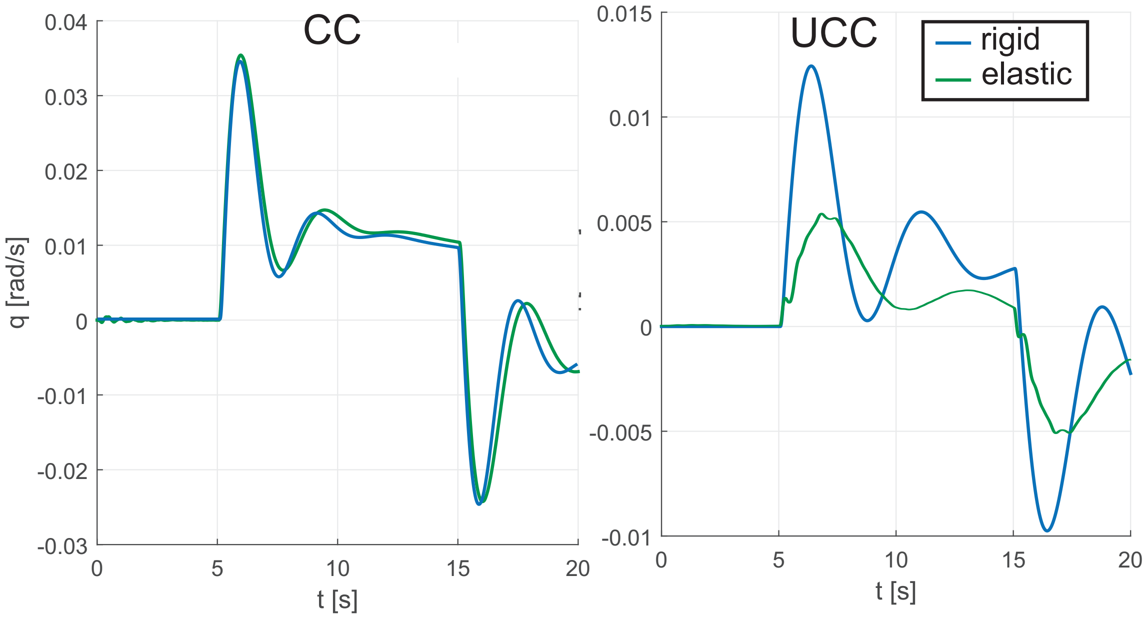

Figure 3.11. – Comparison of Response to a Elevator Singlet Input

3.3.3.3. Static Directional Stability

Static directional stability means that the aircraft after a disturbance in sideslip β naturally returns to a state with zero sideslip. Both configuration are statically directionally stable for all investigated flight conditions.

3.3.3.4. Roll Response

In the roll response similar observations to pitch response can be made. The roll control effectiveness is not significantly impacted due to aeroelasticity for the classical configuration whereas significant impact can be seen for the unconventional configuration as shown in Figure 3.14.

3.3.4. Controller Robustness

The robustness of the controller must be proven for certification. Nichols diagrams are a common method for showing the robustness of the controller. The requirements are defined in the Military Standards [129] by means of so-called Nichols diamonds. Figure 3.15, 3.16 and 3.17 show examples for Nichols plots [12] for the longitudinal and lateral controller for the rigid classic aircraft configuration including different envelope points. The diagrams show the transfer function for different cuts in the control loop over a range of frequencies from 0 to ∞. Along the transfer function the phygoid frequency and the lowest wing bending frequency are marked by a circle an a diamond. The transfer function for frequencies lower than the phygoid frequency should remain outside of the smallest

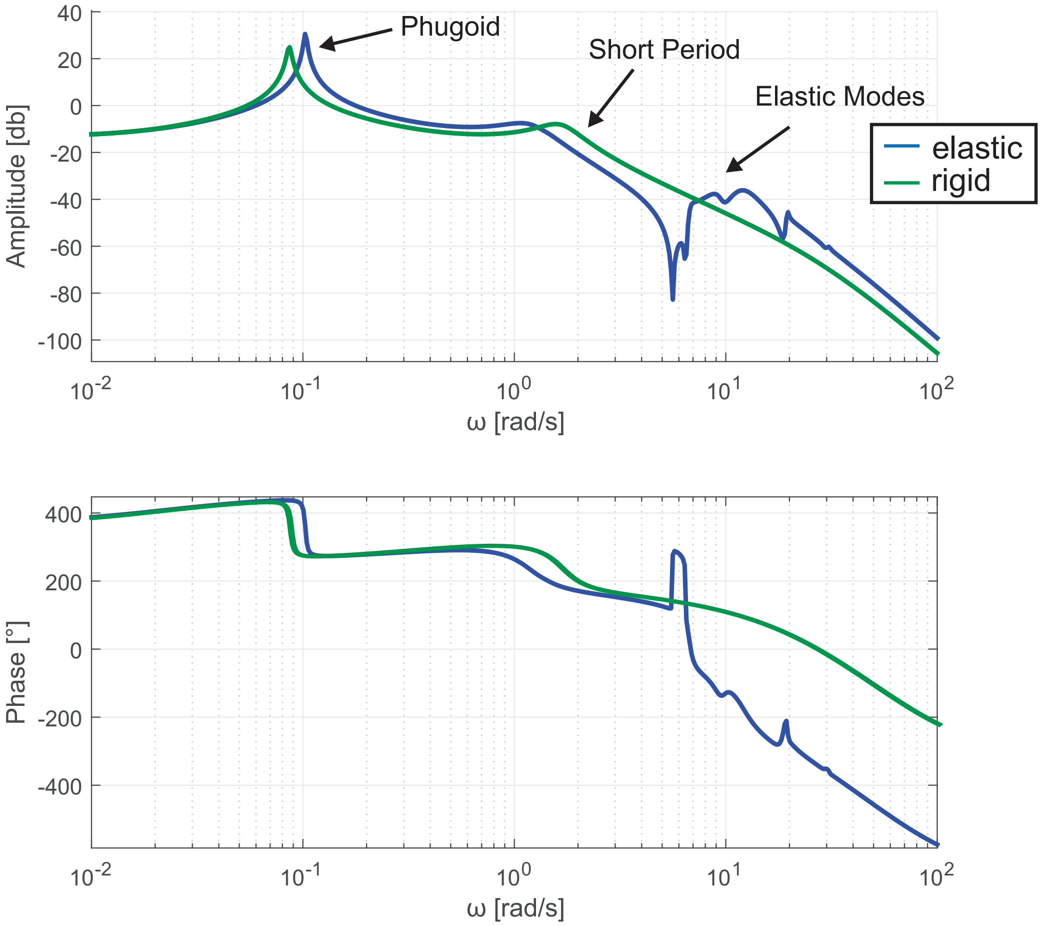

Figure 3.12. – Stick to Θ Transfer Function for Rigid and Elastic UCC

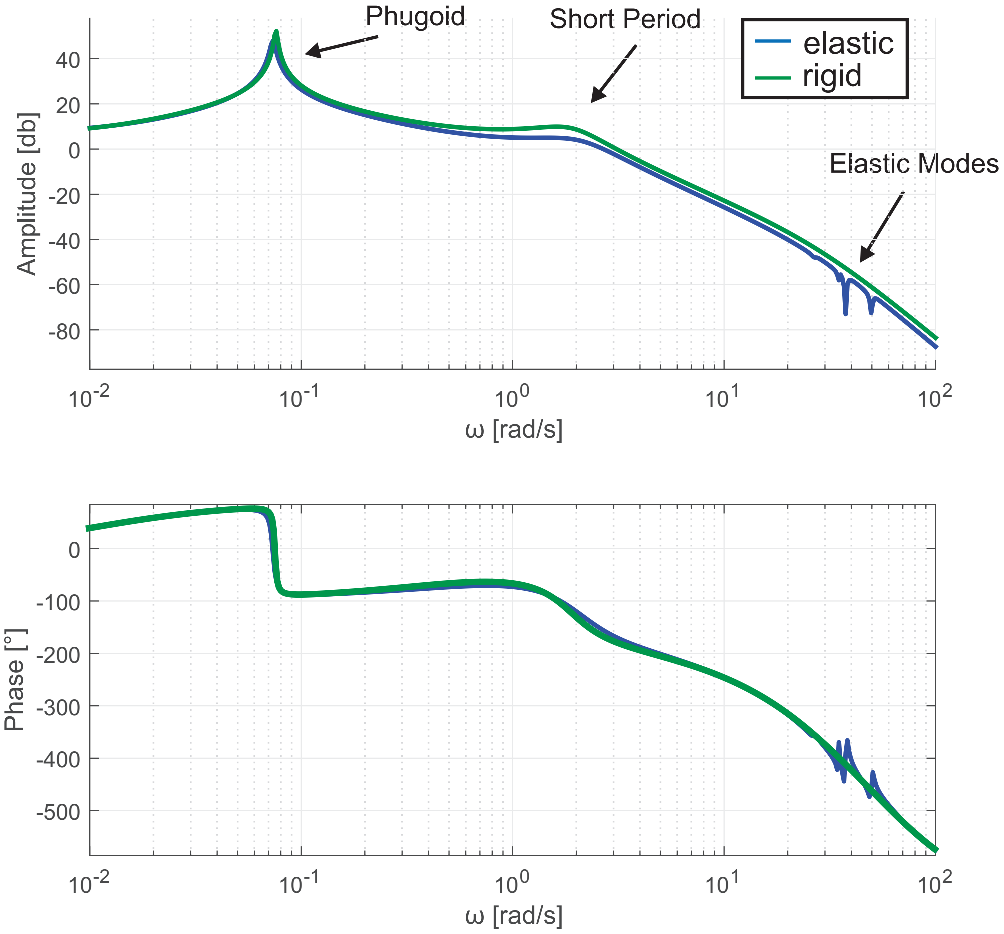

Figure 3.13. – Stick to Θ Transfer Function for Rigid and Elastic CC

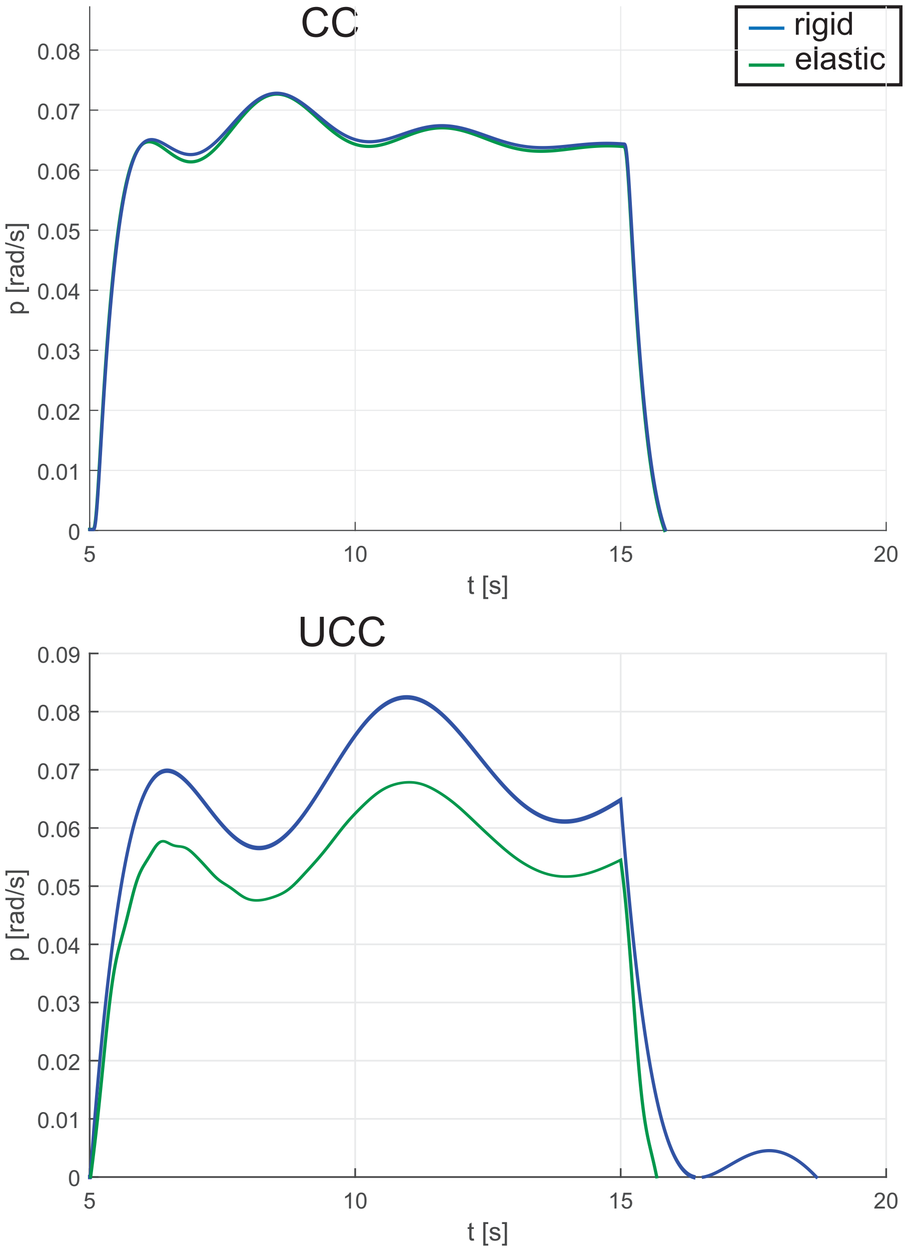

Figure 3.14. – Comparison of Response to a Roll Singlet Input

diamond, the transfer function between the phygoid frequency and the lowest wing bending mode should remain outside of the middle Nichols diamond and all frequencies higher than the first wing bending frequency must remain outside of the largest diamond. This accounts for the decreasing accuracy of the model with increasing frequencies. Observing these criteria in the plots it can be observed that the stability requirements are fulfilled. The Nichols diagrams are presented for the quasi-steady aeroelastic model as e.g. also done by Berger [13], but for a full certification however one would require the diagrams for the dynamic aeroelastic model. The remaining plots for the UCC are shown in Appendix B.1. All investigated flight meet the robustness requirements both for the CC and the UCC.

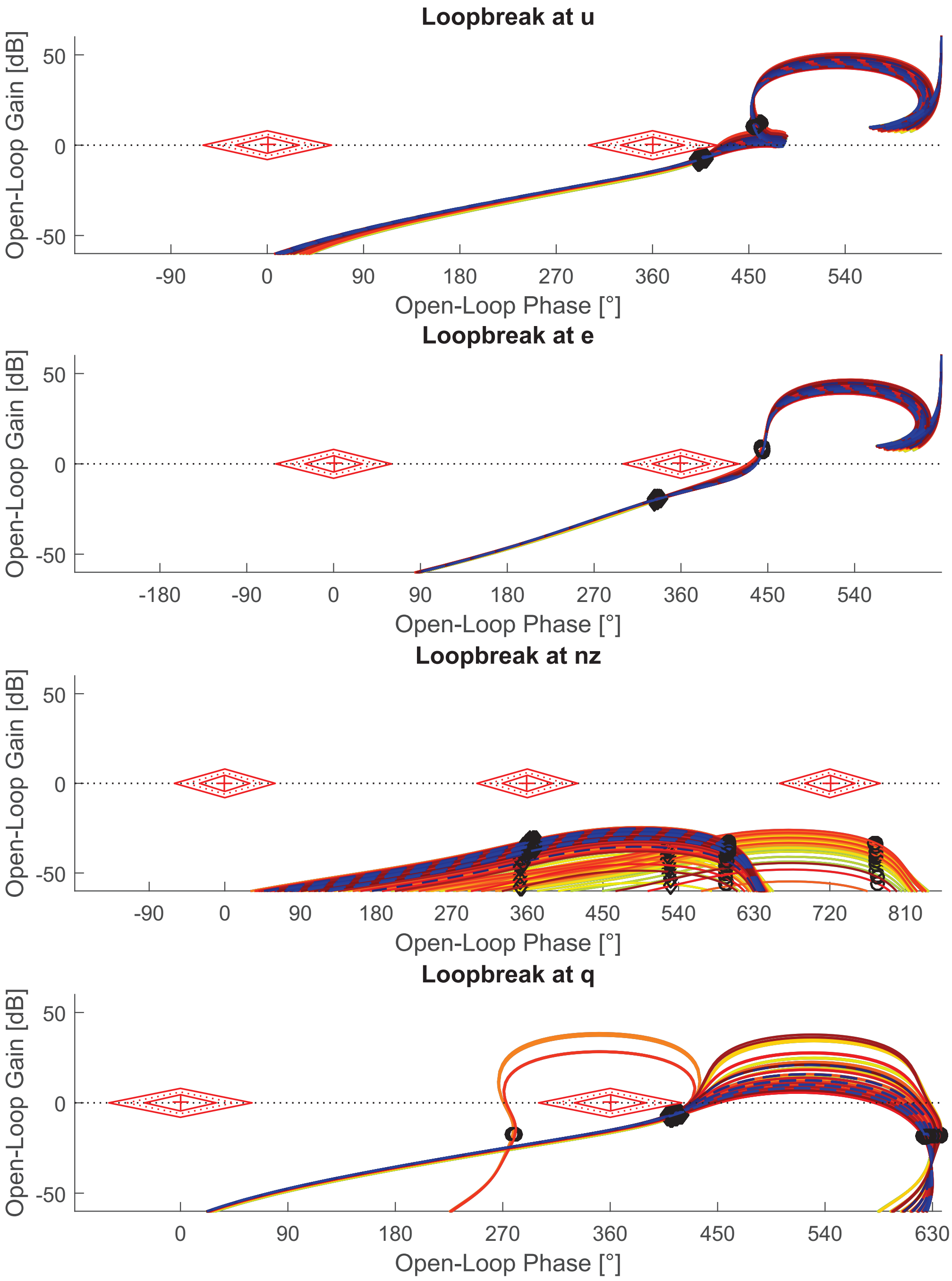

Figure 3.15. – Nichols Diagram for Longitudinal Controller, CC Rigid

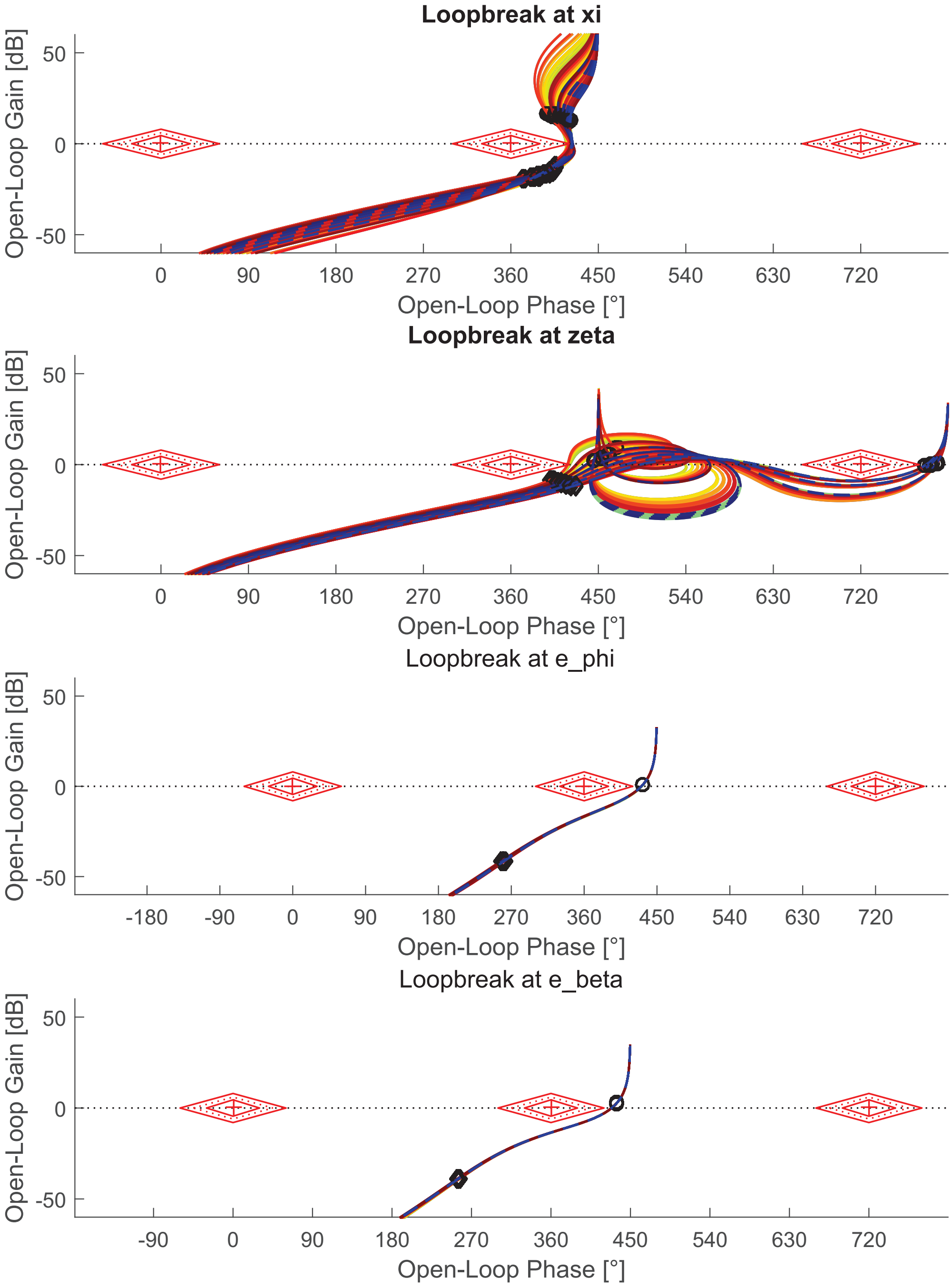
Loopbreak at xi

Loopbreak at zeta

Loopbreak at e_phi

Loopbreak at e_beta

Figure 3.16. – Nichols Diagram for Lateral Controller, CC Rigid

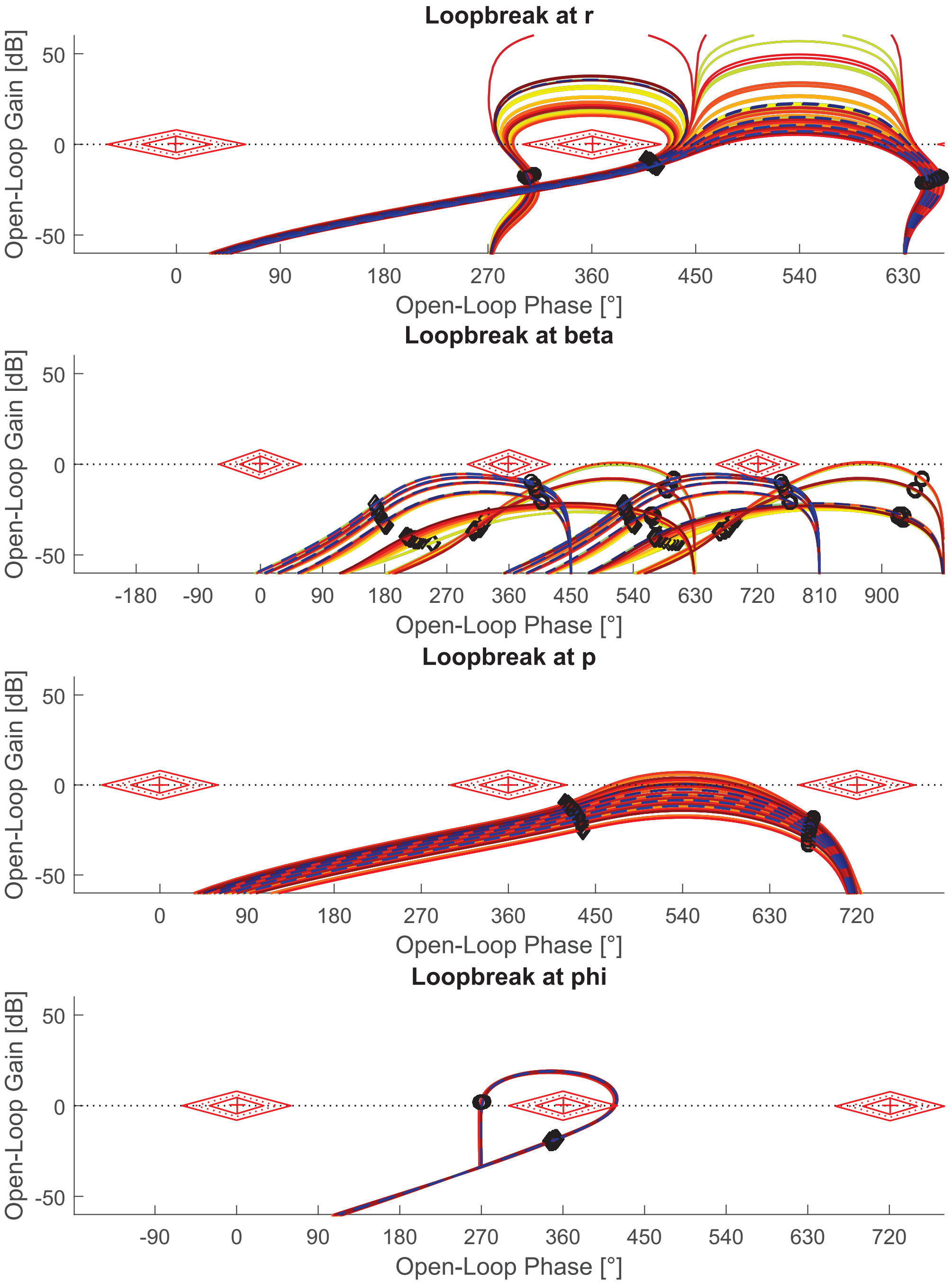
Loopbreak at r

Loopbreak at beta

Loopbreak at p

Loopbreak at phi

Figure 3.17. – Nichols Diagram for Lateral Controller, CC Rigid

4. Handling Quality and Certification Requirements with Configuration Assessment

This chapter introduces the handling quality and certification criteria applied in the presented assessment process for unconventional configurations. Additionally all criteria are evaluated for the two aircraft configurations introduced in Section 3.3, showing on the one hand the challenges for unconventional configurations with respect to handling qualities and on the other hand the impact of aeroelasticity on the handling qualities. Handling Qualities are defined as "...those qualities or characteristics of an aircraft that govern the ease and precision with which a pilot is able to perform the tasks required in support of an aircraft role" [28]. These Handling Qualities are determined by the pilots opinion of how well the aircraft flies. One way commonly applied, is to rate the aircraft behavior using the so called Cooper-Harper Rating, a numerical rating scale introduced by Cooper and Harper in 1966. The US Military Specifications for flying qualities MIL-HDBK-1797 [128] used for aircraft certification also refer to the Cooper Harper rating scale, distinguishing three levels of flying qualities: satisfactory (Level 1), acceptable (Level 2) and controllable (Level 3). These specifications are widely accepted and used for aircraft handling quality evaluation and hence are the major reference in this work as well. For aircraft certification Level 1 handling qualities are required in the operational flight envelope including likely failures. The required flying qualities in [128] are distinguished for different aircraft types. The criteria from the US Military Specifications [128] applicable for this work are large, heavy, low-to-medium maneuverability aircraft categorized as Class 3 aircraft. Furthermore the requirements are distinguished between three flight phases, Category A (CAT A), Category B (CAT B) and Category C (CAT C). Category A include non-terminal flight phases requiring high precision maneuvering such as aerial refueling, air combat and terrain following. Category B include non-terminal flight phases that require a gradual maneuvering such as cruise, climb, descent and hold. Category C include terminal fight phases such as take-off and landing. The flight phase most applicable for this investigation is is Category C, as the quantitative requirements are generally higher compared to Category B, while Category A is not applicable at all for a civil aviation aircraft. Additionally to [129] criteria from the EASA CS-25 [37] are investigated. All general criteria are investigated in direct and normal law. During normal operation the control system is active and will usually ensure good handling qualities. However during a failure condition the aircraft may return to direct law, in which case the pilot will still be required to appropriately control the aircraft. Otherwise, if the open-loop handling qualities are insufficient to safely land the aircraft, the probability of a control system failure must be proven to be lower than 10^{-9} according to EASA CS-25 regulations [37]. Both configurations are assessed with the assumption of a rigid airframe and with the elastic airframe model, in order to demonstrate the impact of the airframe elasticity on handling qualities. Furthermore criteria for the evaluation of pilot induced oscillations, a problem gaining importance for highly augmented aircraft, are applied such as the Bandwidth Criterion or the Neal-Smith Criterion [52]. The evaluation of handling qualities is typically separated into longitudinal motion and lateral motion.

4.1. Low Order Equivalent Systems

An aircraft in free flight is subject to natural rigid body modes. These free body modes of an aircraft are classically the short-peroid mode and the phygoid mode in the longitudinal motion, and the dutch roll, the roll mode and the spiral mode in the lateral motion. In special cases there may also be a roll-spiral oscillation. It was found early in the research of handling qualities, that an aircraft's natural modes are strongly linked to an aircraft's flying qualities. Thus, knowledge of the natural modes allows the prediction of the aircraft flying behavior and pilot perception. During a large number of flight tests and experiments boundaries were established for the frequency and damping of these modes which relate to certain Levels of Handling Qualities. Theses boundaries are now a part of the Military Specifications for Flying Qualities of Piloted Aircraft MIL-F-8785C [129] and its replacement the MIL-HDBK-1797 [128] and have become a standard for certification. These modal criteria are however only valid for a simple rigid aircraft. The application of feedback control, and also airframe elasticity introduce higher order effects into the aircraft dynamics. Thus the classical natural modes do not allow the full representation of the responses for these complex systems [52]. However DiFranco [32] showed that the response behavior of these systems can still be well represented using a second order system and an equivalent time delay capturing higher order effects. These equivalent systems which attempt to represent the aircraft dynamics using a low order system are called LOES and have been introduced for the analysis of aircraft dynamics for higher order systems. LOES generally provide a better approximation of the modes than only using the dominant pole of the system transfer function. The application LOES has become a standard and has already been included in the Military Specifications MIL-HDBK-1797-B [128]. In order to obtain a LOES transfer function representing the desired aircraft dynamics with classical modes, a suitable low order transfer function is matched with the respective High Order System (HOS) transfer function in the band of a certain frequency range, which is of interest. This range of frequencies which is of interest is mostly in the range from $\omega = 0.1 rad/s$ to $\omega = 10 rad/s$, which is most significant for the perception of a pilot [38]. The parameters of the LOES system are then found through an optimization, where the cost function is defined as

$$Err = \sum \left(20 log_{10} \mid G_{HOS} \mid - 20 log_{10} \mid G_{LOES} \mid\right)^2 + k_{\angle} \left(\angle G_{HOS} - \angle G_{LOES}\right)^2 , \qquad (4.1)$$

where $k_\angle = 0.0175$ [109] in order to put an equal weight on the amplitude and the phase portion of the transfer function. The error between the original HOS and the LOES should remain within the so-called Maximum Unnoticable Additional Dynamics (MUAD) boundaries given e.g. in [52] or [128]. These boundaries define the allowable error of the system approximation for which the pilot most likely will not notice a change of aircraft dynamics. Especially for HOS where the bandwidth of interest is within the bandwidth of aeroelastic modes a different weighting algorithm using the MUAD boundaries improved the results in some cases. Examples for the generation of LOES for longitudinal and lateral dynamics are shown in Sections 4.2.1.1 and 4.3.1.1.

4.2. Longitudinal Criteria

Longitudinal handling qualities have been the subject of the majority of handling qualities research in recent years [52], as these present many challenges to the piloting requirements. New increasingly efficient and more unconventional aircraft configurations require advanced control laws to ensure the stability and control of the aircraft. This increasing application of fly-by-wire technology and control laws which significantly alter the aircraft dynamics has lead to the phenomenon of pilot in the loop oscillations, where the pilot as part of the control loop may cause instabilities. In order to prevent and predict Pilot Induced Oscillations (PIO) a number of criteria were developed on top to the classical requirements. In this work both classical criteria and criteria for the assessment of PIOs are evaluated in the process. The investigated criteria for the longitudinal motion are summarized in Table 4.1 and are detailed in the following. The table indicates whether handling qualities and PIOs can be assessed and furthermore if the assessment is performed using time domain analysis, frequency domain analysis or a LOES.

Table 4.1. – Longitudinal HQs

Criterion	*HQ*	*PIO*	*T*	*F*	*L*	*Source*
Control Anticipation Parameter (CAP)	✓				✓	MIL-STD-1797B
Short Period Frequency and Damping	✓				✓	MIL-STD-1797B
C* Criterion	✓		✓	✓		[42]
Bandwidth Criterion	✓	✓		✓		MIL-STD-1797B
Neal Smith Criterion	✓	✓		✓		AFFDL-TR-70-74
Dropback Criterion	✓		✓			MIL-STD-1797B
Updated Dropback Criterion		✓	✓			[90]
Transient Peak Ratio Criterion	✓		✓			MIL-HDBK 1797
Gibson Phase Rate Criterion		✓		✓		AGARD-CP-508

T= Time Domain Specification, F=Frequency Domain Specification, L=LOES specification

4.2.1. Low Order Equivalent System Specifications

The classical modal criteria are assessed by means of LOES specifications rather than using the dominant pole, as already discussed in Section 4.1. The longitudinal modes are the short period and the phugoid mode, where especially the short period motion is critical for handling qualities. The phygoid mode is a long period mode which involves a large variation in airspeed, pitch attitude and altitude, but almost no angle-of-attack variation. Due to the large period of typically 20-60 seconds the phygoid is generally no problem for handling qualities and does not interact with the elastic airframe, and is therefore left out of consideration here.

4.2.1.1. Short Period Oscillation Criteria

The short-period mode is a usually well damped high frequency pitching of the aircraft about the center of gravity and occurs at frequencies between $\omega_{SP} = 1 rad/s$ and $\omega_{SP} = 5 rad/s$ [52]. The motion is so rapid that the aircraft speed does not have time to change, so the oscillation is essentially an angle-of-attack variation. The certification requirements [129] prescribe limits for the damping and frequency of this mode. The frequency of the short period for large aircraft may be close to low frequency structural modes, which can cause an interaction between aeroelasticity and flight dynamics detrimental to handling qualities. Large and heavy transport aircraft are especially vulnerable for this interaction as these large and heavy structures have very low frequency eigenmodes. The LOES best representing the short period dynamics depends on the investigated HOS transfer function. Using the transfer function $G_{\mathbf{q}\eta}$ from stick input η to pitch rate $\mathbf{q}$ the dynamics can be represented by

$$G_{\mathbf{q}\eta} = \frac{\mathbf{q}}{\eta} = k_{\mathbf{q}} e^{-\tau s} \frac{T_{\Theta 2} s + 1}{1 + 2\zeta_{SP}\omega_{SP} s + s^2 \omega_{SP}^2}, \tag{4.2}$$

as e.g. shown in [52] and [109], where ω_{SP} and ζ_{SP} are the short period frequency and damping, $T_{\Theta 2}$ is the time delay between the pitch attitude angle and the flight path angle, τ is an equivalent time delay and $k_{\mathbf{q}}$ is a gain. The parameters of Eq 4.11 are chosen in order to match $G_{\mathbf{q}\eta}$ with the high order response of the full aircraft model, including actuators and sensors both for the aircraft in normal law and direct law. Figure 4.1 and Figure 4.2 show the example of a matched low order system. Generally an excellent match could be obtained for all rigid configurations. Good matches were also obtained for the elastic version of the classical configuration, but the LOES match was poor for the unconventional aircraft in the elastic case. The boundaries for the short period frequency and damping for large aircraft (Class 3) and Category C flight phases according to [128] are shown in Figure 4.3 for direct law and normal law.

4.2.1.2. CAP Factor

The Control Anticipation Parameter (CAP) was defined by [15], and indicates an aircrafts ability to precisely track a desired flight path. It was found that for the tracking of a flight path the initial maneuver pitching acceleration $\dot{\mathbf{q}}$ and the obtained vertical acceleration n_z

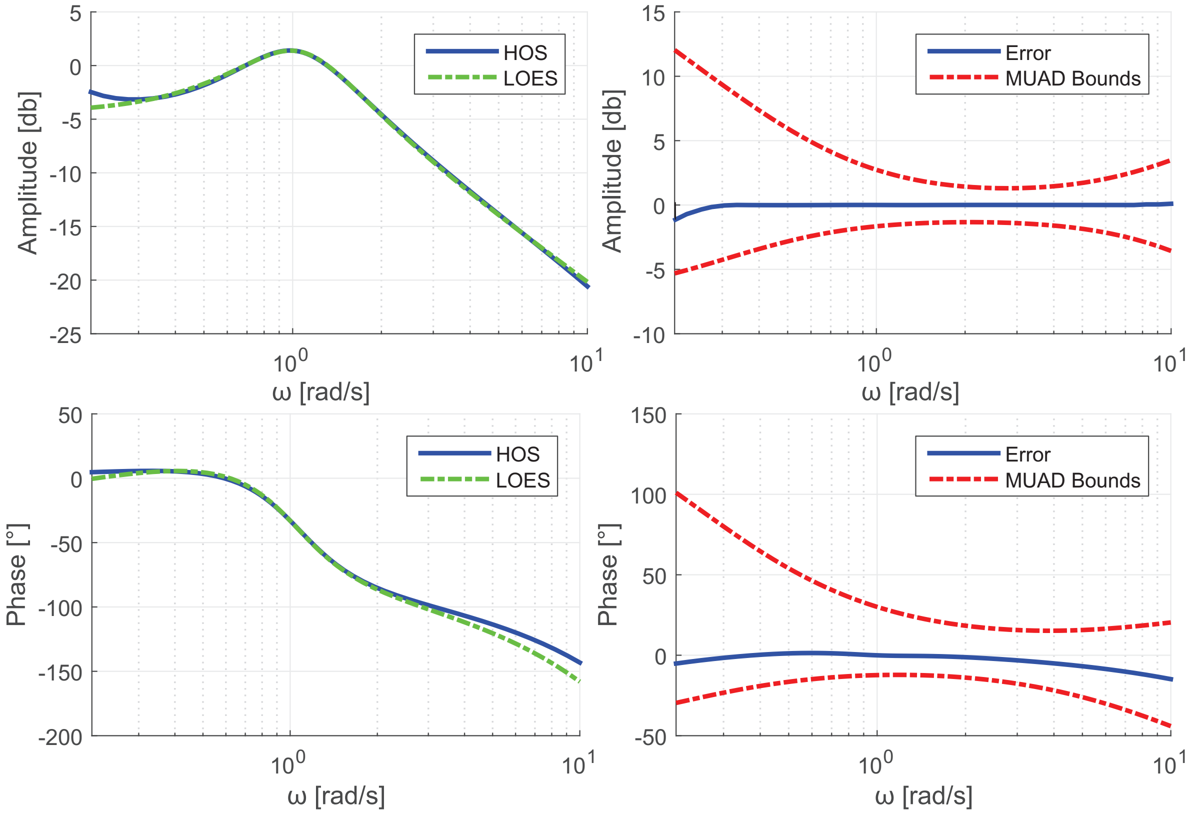

Figure 4.1. – Open Loop LOES for Classical Configuration

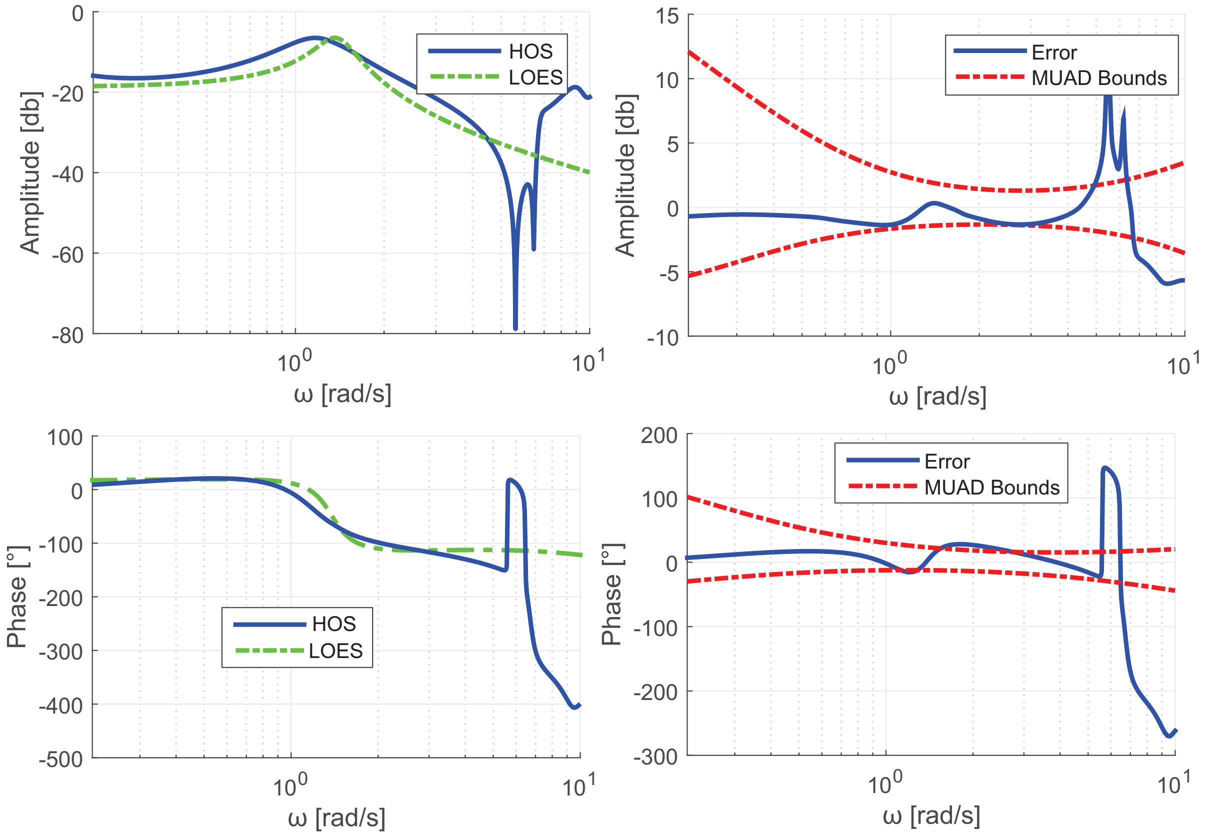

Figure 4.2. – Open Loop LOES for C-Wing Configuration

play a major role for the pilots ability to anticipate the aircraft's longitudinal flight path. The CAP was defined as the ratio between initial pitching acceleration and the steady-state normal acceleration, where all accelerations are measured about the instantaneous center of gravity

$$CAP = \frac{\dot{\mathbf{q}}(t=0)}{\lim_{t->\infty} n_z(t)} = \frac{\dot{\mathbf{q}}_0}{n_{z,\infty}}. \tag{4.3}$$

Given Eq. 4.3 the CAP can also be expressed in terms of the short period frequency, shown e.g. in [52]

$$CAP = \frac{\omega_{SP}^2}{n_z\alpha}. \tag{4.4}$$

The boundaries for the CAP for large aircraft (Class 3) and Category C flight phases according to [128] are shown Figure 4.3.

Evaluation Figure 4.3 shows the CAP and short period requirements for both aircraft configurations introduced in Section 3.3. The plotted values are obtained from the LOES system. The matches for the LOES system were excellent for the rigid aircraft configurations, and fairly good for the elastic classic configuration, however poor for the elastic C-Wing configuration. It can clearly be seen that the benchmark aircraft fulfills Level 1 HQs for the CAP and short period requirement, both in direct and normal law. The control laws further improve the handling qualities and shift them more to the center of the boundaries. The UCC shows Level 2 handling qualities in direct law for the rigid case. The control law manages to shift the dynamics accordingly so Level 1 is obtained in normal law. Looking at the elastic aircraft it can be seen that the handling qualities are Level 3, however since the LOES fit is relatively poor and the elastic interaction is significant, the applicability of this criterion is questionable for this configuration. It can further be seen that the applied control law design algorithm outlined in Section 3.2.3, which uses eigenstructure assignment to achieve desired CAP and short period values required for good handling quality characteristics, is working very well for the rigid aircraft.

4.2.2. Frequency Domain Criteria

In this section criteria requiring a frequency domain analysis are presented and evaluated. These criteria used the full order transfer-function obtained from linearization about the respective envelope point.

4.2.2.1. Bandwidth Criterion

The bandwidth criterion was developed by Hoh et. al. [54]. The goal was to create a criterion, which is applicable to new fly-by-wire technology, new command systems and aircraft response dynamics with higher order behavior. Some higher order dynamics cannot be captured by the classical modal criteria and respective LOES fits covered in Section

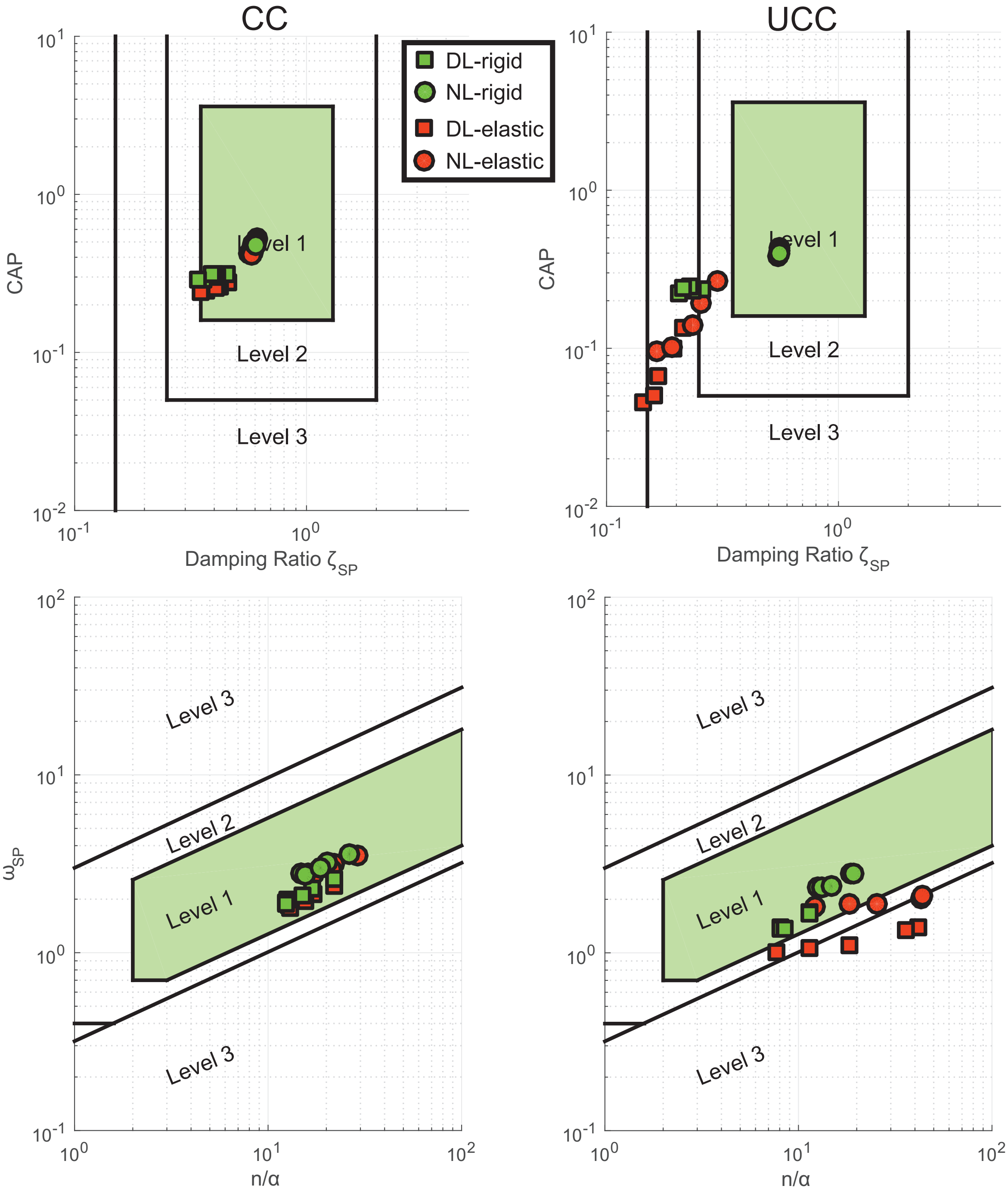

Figure 4.3. – Short Period and CAP Assessment

4.2.1, as e.g. for the given elastic UCC example aircraft. In order to capture these effects pilot models are introduced and the closed-loop pilot-aircraft system is investigated. The bandwidth criterion is a method for which the pilot is modeled by means of a gain alone [51]. The main idea of this criterion is that the pilot will try to adapt his gain in such a way that a good stability margin is obtained in the closed loop pilot-aircraft system. This means described in quantitative terms that at least a $6dB$ gain margin and a 45° phase margin is maintained in the closed-loop pilot-aircraft system. The advantage of this method is that the analysis is independent of the exact type of response behavior and order. The bandwidth frequency for the bandwidth criterion is defined different compared to classical control theory definitions. The bandwidth frequency is defined as the lowest of the two frequencies where either the $6dB$ margin or the 45° phase margin, as shown in Figure 4.4, is reached

$$\omega_{BW} = min\left\{\omega_{BW,A}, \omega_{BW,\angle}\right\}. \tag{4.5}$$

One second important aspect covered in the bandwidth criterion is the so-called high frequency phase rolloff, which is the rate of phase decay (gradient) above the bandwidth frequency. This high frequency phase rolloff can be interpreted as an equivalent time delay [109] and has been identified to be critical for pilot induced oscillations. This equivalent time delay is defined as

$$\tau_{BW,HRO} = \frac{\Delta\phi_{2\omega_{-180}}}{2\omega_{-180}180/\pi} \tag{4.6}$$

where $\Delta\phi_{2\omega_{-180}}$ is the phase angle between ω_{-180} and $2\omega_{-180}$ also shown in Figure 4.4. The longitudinal bandwidth criterion is applied on the transfer function $G_{\Theta\eta}$ from the stick input η to the pitch attitude angle Θ exemplary shown in Figure 4.4. The bounds to achieve Level 1 and Level 2 flying qualities in the landing case are defined in the MIL-1797B [128] and shown in Figure 4.5.

Evaluation The evaluation of the bandwidth criterion shown in Figure 4.5 shows that both the classical configuration and the UCC are on the verge between Level 1 and Level 2 handling qualities. Although a slight impact of elasticity can be observed the impact of elasticity on this criterion is minor.

4.2.2.2. Neal Smith Criterion

In the late 1960s Neal and Smith developed a method to assess aircraft handling qualities including a more complex pilot model. The pilot model was derived from fundamental considerations and flight test observations. It was found that a pilot will try to minimize the low frequency droop in the amplitude and at the same time will try to maintain a sufficient stability margin, equivalent to a phase margin of 60° to 110° in the transfer function from the stick input η to the pitch attitude angle Θ. Based on these observations a mathematical pilot model was derived, where the pilot is modeled including a component for amplitude compensation, a component for phase compensation and a time delay

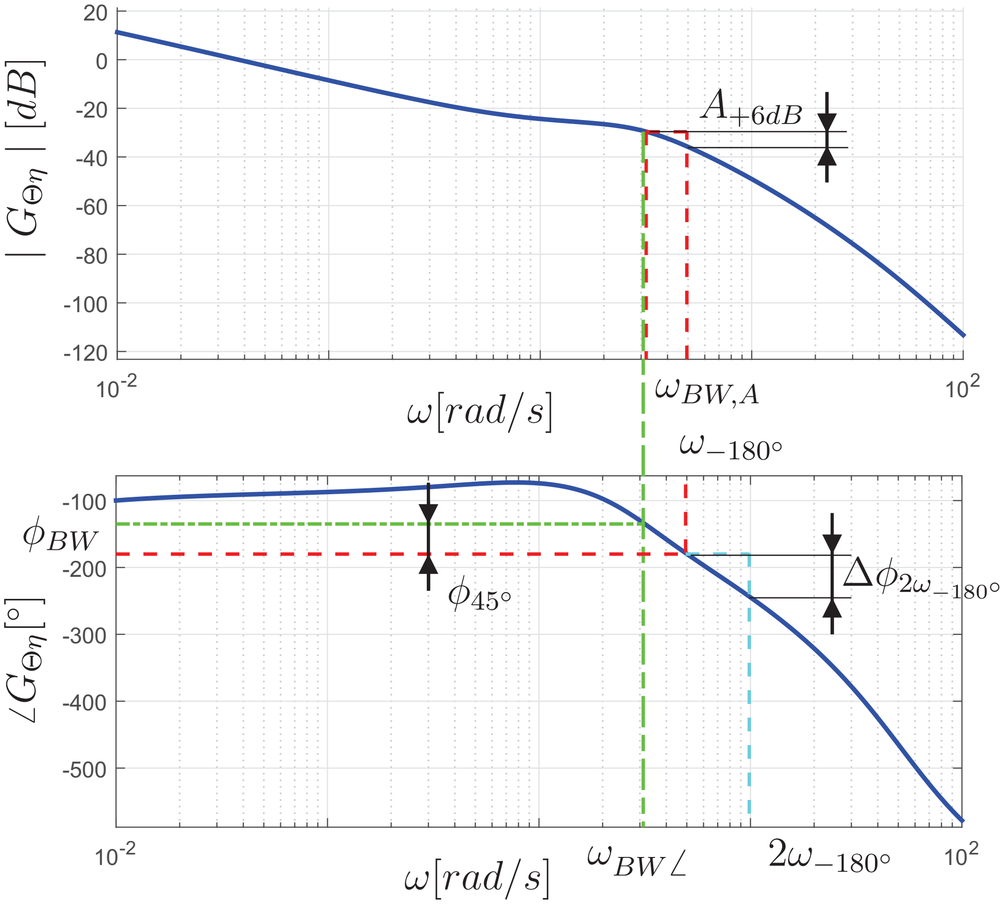

Figure 4.4. – Bode Plot for Bandwidth Criterion

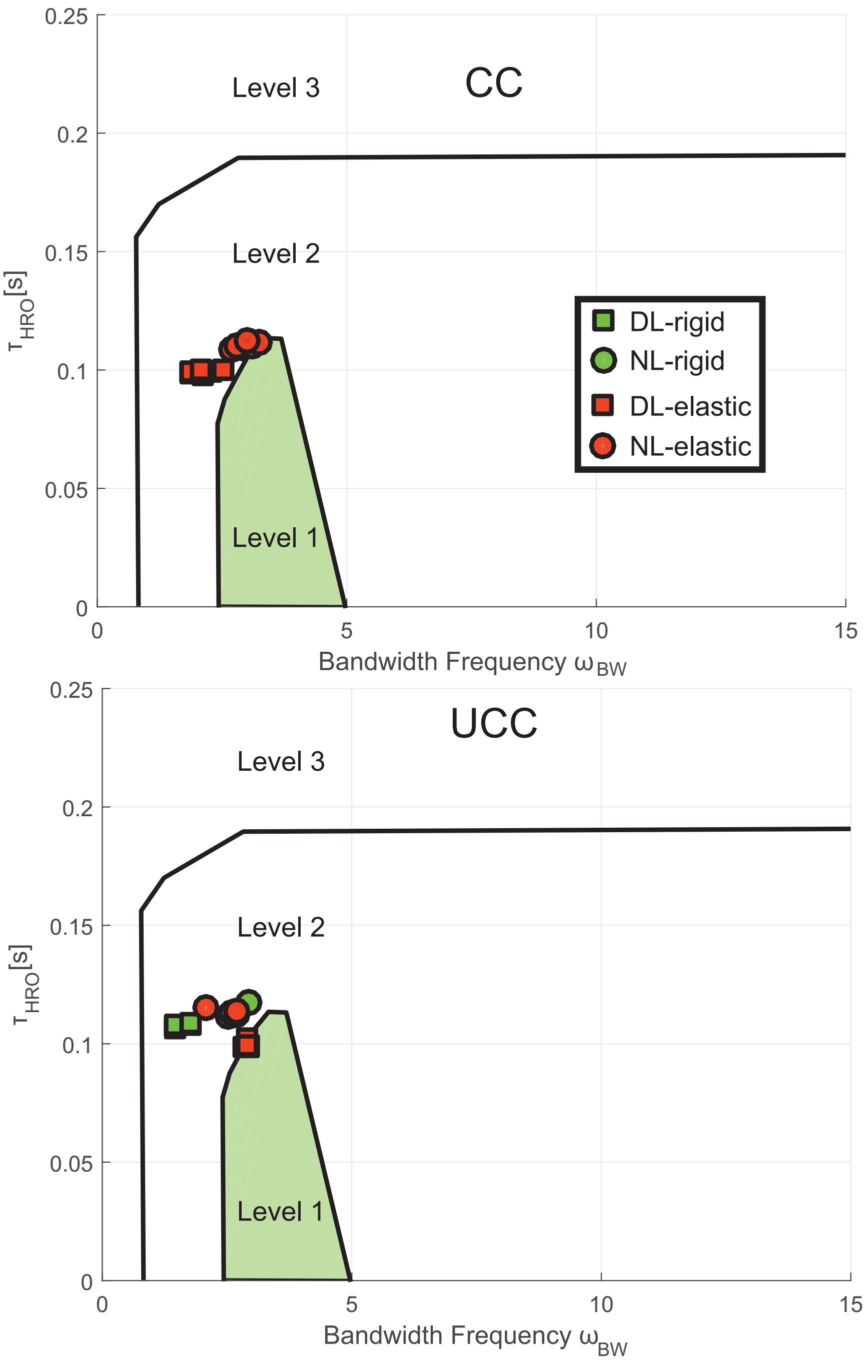

Figure 4.5. – Bandwidth Criterion for both Configurations in Direct Law and Normal Law

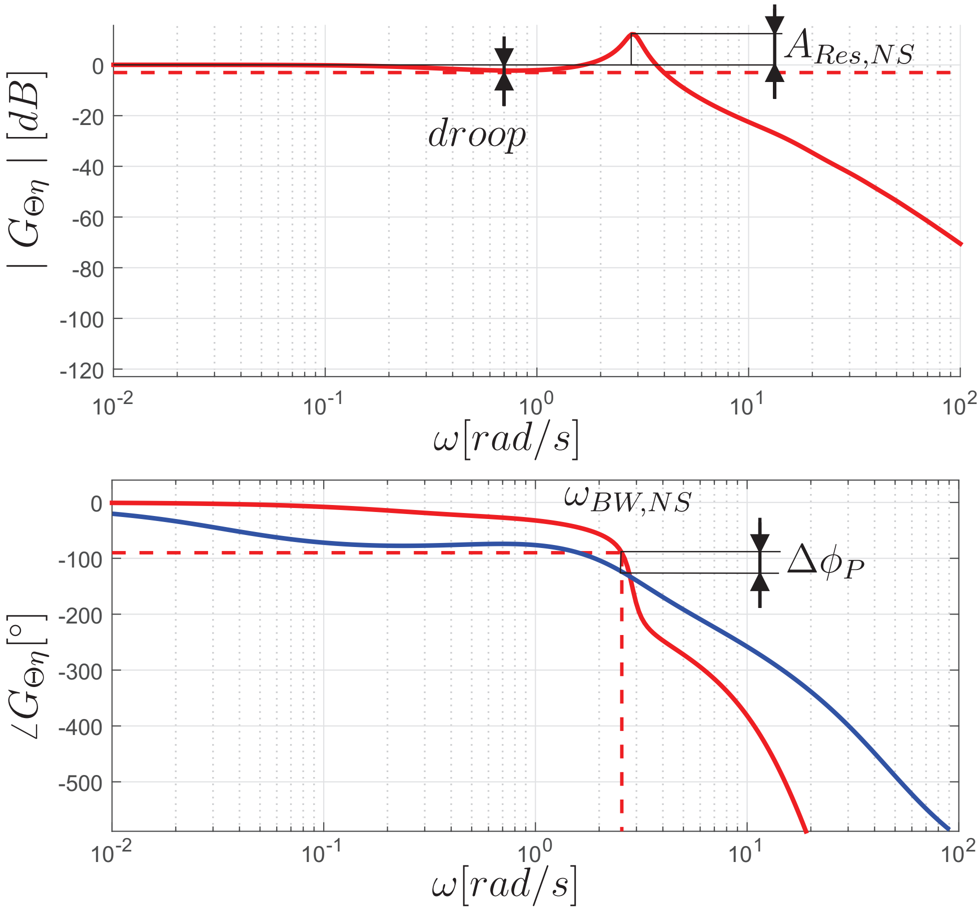

Figure 4.6. – Boundary Conditions for Neal-Smith Criterion

resulting from the neuromuscular delay of the pilot. This behavior is given by the transfer function

$$G_P = k_P e^{-s\tau} \frac{\tau_{P,1} s + 1}{\tau_{P2} s + 1} \tag{4.7}$$

where k_P is the pilot gain, $\tau_{P,2}$ and $\tau_{P,1}$ are the parameters for the pilot lead or lag and τ is the neuromuscular time delay given with $300ms$ as a widely used value. The phase changing filter for the pilot will only either show a Lag-Lead behavior or a Lead behavior. From this follows that if $\tau_{P,1} > \tau_{P,2}$ then $\tau_{P,2} = 0$. In order to determine the parameters for the pilot model it is assumed that at a defined bandwidth frequency ω_{BW} the phase of the closed pilot aircraft system must be $-90°$. This way it is possible for the pilot to generate fast input commands up to ω_{BW}. Furthermore the amplitude droop below the 0-dB line must not be more than 3dB. This limit value for the gain ensures that the pilot can adequately correct stationary errors. These boundary conditions are shown in Figure 4.6. The parameters for the pilot compensation are found using an optimization. The bandwidth frequency $\omega_{BW,NS}$ is found in the MIL-1797 [128], and is given with $\omega_{BW} = 1.5rad/s$ for the entire envelope of a civil transport aircraft, with the

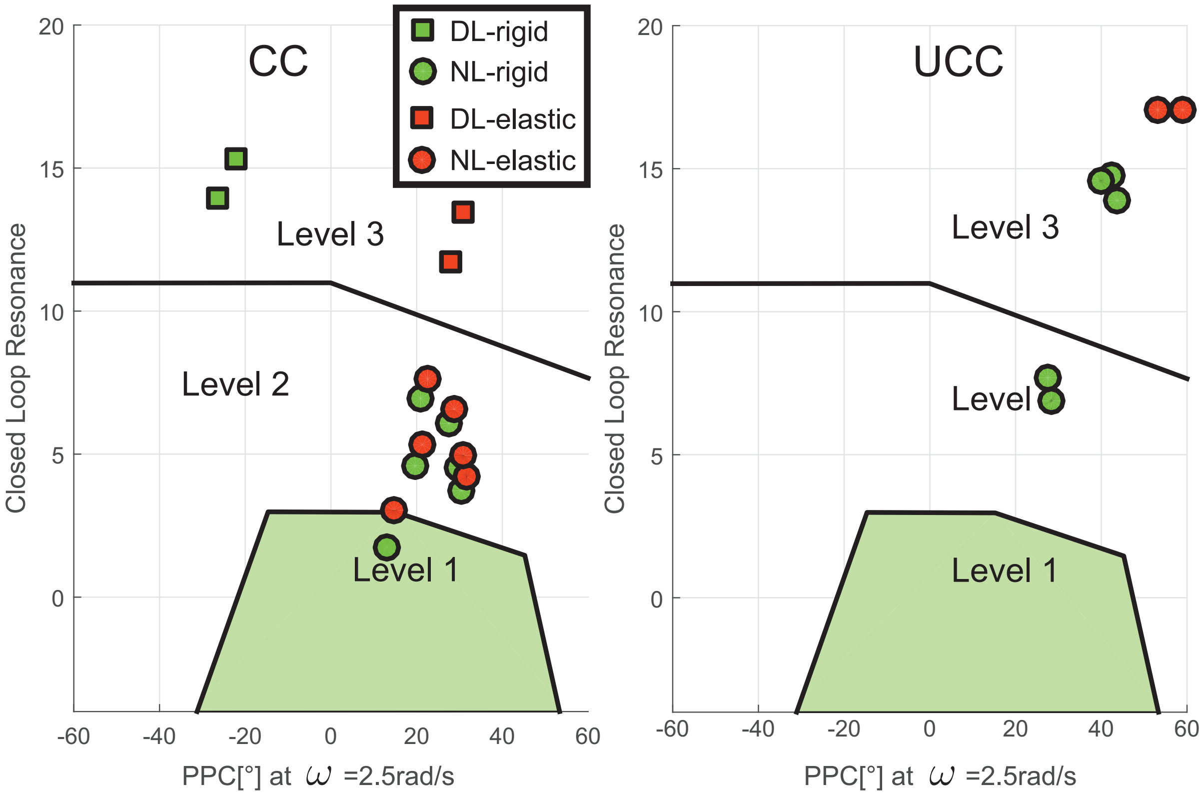

Figure 4.7. – Neal Smith Bounds for Landing

exception for landing where $\omega_{BW} = 2.5 rad/s$. The Neal-Smith criterion is evaluated using the pilot phase compensation (PPC) $\Delta\Phi_P$ and the value of the closed loop resonance amplitude $A_{Res,NS}$. The boundaries for these values to achieve respective handling quality levels are shown in Figure 4.7.

Evaluation The evaluation of the Neal-Smith criterion shows that for the benchmark configuration the direct law handling qualities are Level 3. The control law improves the HQs to Level 1 and 2. The UCC direct law are out of the given bounds, hence Level 3, the control law also improves the HQs but they still remain in the range between Level 2 and 3 depending on the flight state.

4.2.2.3. Gibson Phase Rate

The Gibson Phase Rate criterion was developed for the prediction of PIO tendencies of aircraft. Similar to the high frequency rolloff measure of the bandwidth criterion, the phase rate criterion is concerned with the open-loop pitch attitude frequency response in the region around $-180°$. The severity of the high order characteristics is related to the slope of the phase across the $-180°$ phase limit. The phase drop-off from the pitch

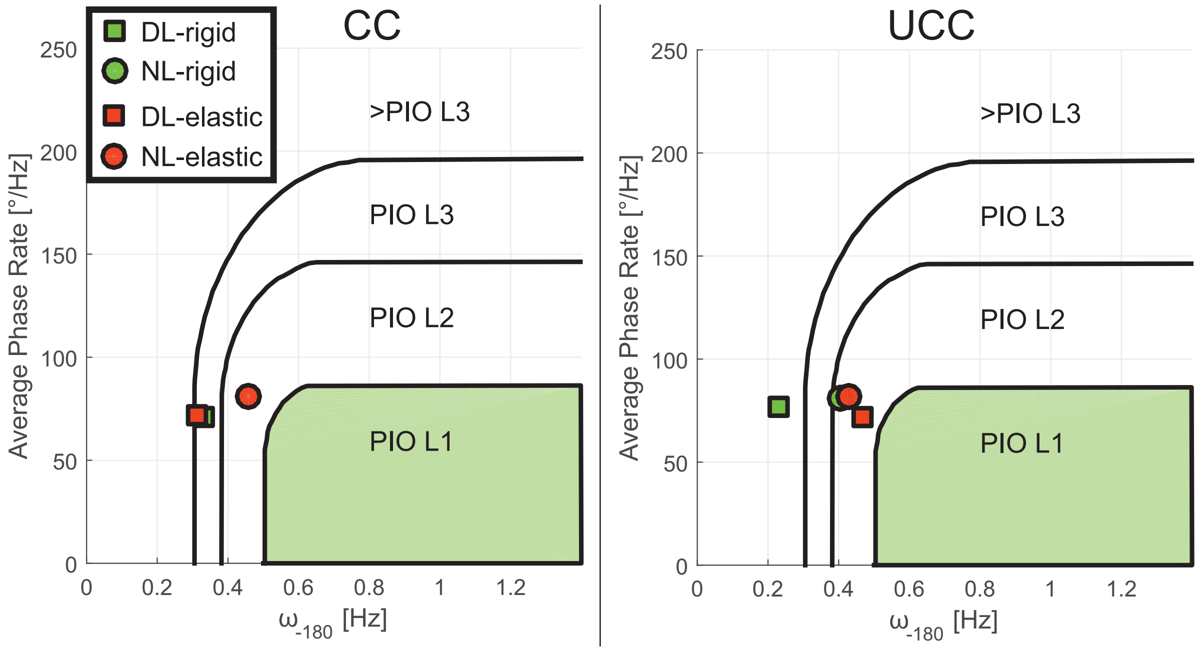

Figure 4.8. – Gibson Phase Rate

attitude transfer function is computed and related to the frequency at the phase limit of $-180°$, a measure defined as the average phase rate (APR)

$$APR = \frac{\Delta\phi}{\omega_{-180}} = \frac{-(\phi_{2\omega_{-180°}} + 180)}{\omega_{-180°}}, \tag{4.8}$$

where the values of $\phi_{2\omega_{-180°}}$ and $\omega_{-180°}$ are determined from the bode diagram as shown in Figure 4.4. The boundaries for the criterion are taken from [41] and are shown in Figure 4.8.

Evaluation The evaluation of the Gibson phase rate criterion is shown in Figure 4.8. The classical aircraft shows an APR which is sufficient to reach Level 1 HQs, meaning that the high frequency dropoff is not limiting the HQs. However the frequency where the phase-margin is reached is relatively low. It can be seen that the control law improves the phase margin and shifts the HQs from Level 3 to Level 2. Similar behavior can be seen for the C-Wing configuration.

4.2.3. Time Domain Criteria

This section presents and evaluates handling quality requirements defined as a time domain specification. The time domain histories can both be obtained and evaluated either from a linearized model about the respective envelope point or from the fully nonlinear model.

4.2.3.1. C* Criterion

Tobie et. al. [42] suggested a criterion based on the time history of the longitudinal dynamic response characteristics. The criterion is based on the concept of C*, which postulates that the pilot responds to a blend of pitch rate and normal acceleration. At low airspeeds, where the normal acceleration following a stick input is relatively small, the pitch rate is the more important reference parameter for the pilot. At high airspeeds when a small stick input leads to a significant change in normal acceleration, n_z is the more important reference for the pilot to anticipate pitch motion. C* combines these pilot reference parameters in a dimensionless variable

$$C^* = n_{z,P} + k\mathbf{q}, k = \frac{V_{CO}}{g}, \tag{4.9}$$

where V_{CO} is the so-called crossover velocity, which is the geometric mean of the minimum and maximum velocity of the respective aircraft. For transport aircraft $V_{CO} = 122m/s$ is a common value [22]. The bounds for the time history of a step input on the control for the landing approach are given in Figure 4.9. Additionally frequency domain bounds were defined for the amplitude transfer function $G_{C^*C^*_{cmd}}$ from C^*_{cmd} to C^* also shown in Figure 4.9.

Evaluation It can be seen that the classical configuration remains within the desired bounds both for the rigid and the elastic case. The UCC shows severe oscillations in the response of the elastic aircraft which result from the low frequency structural modes. It can be seen that the frequency is in the range of the first wing bending modes. The boundaries are exceeded for the C* criterion for the elastic UCC.

4.2.3.2. Gibson Dropback Criterion

The Dropback Criterion developed by Gibson [41] is a time domain criterion describing the aircraft's longitudinal response dynamics after releasing the controls following a step input, as shown in Figure 4.11. It can be seen that after a step input in the longitudinal control, in the response there is a time delay between the aircraft flight path angle γ and the aircraft attitude angle Θ. This time delay is defined as $T_{\Theta 2}$. The delay between the stick input until a constant $\dot{\gamma}$ is obtained is defined as T_γ. After releasing the stick, the attitude returns to a stationary value, this change in attitude is defined as dropback DB. The criterion relates the pitch rate overshoot $\mathbf{q}_{max}$ to the so called attitude dropback DB. Both values are divided by the stationary value of the pitch rate $\mathbf{q}_{\text{ss}}$ shown in Figure 4.11. Figure 4.12 shows the bounds required to achieve the respective levels of handling qualities

Evaluation The dropback characteristics of both aircraft configurations are within the Level 1 bounds for direct law. They are however slightly degraded by the control law for

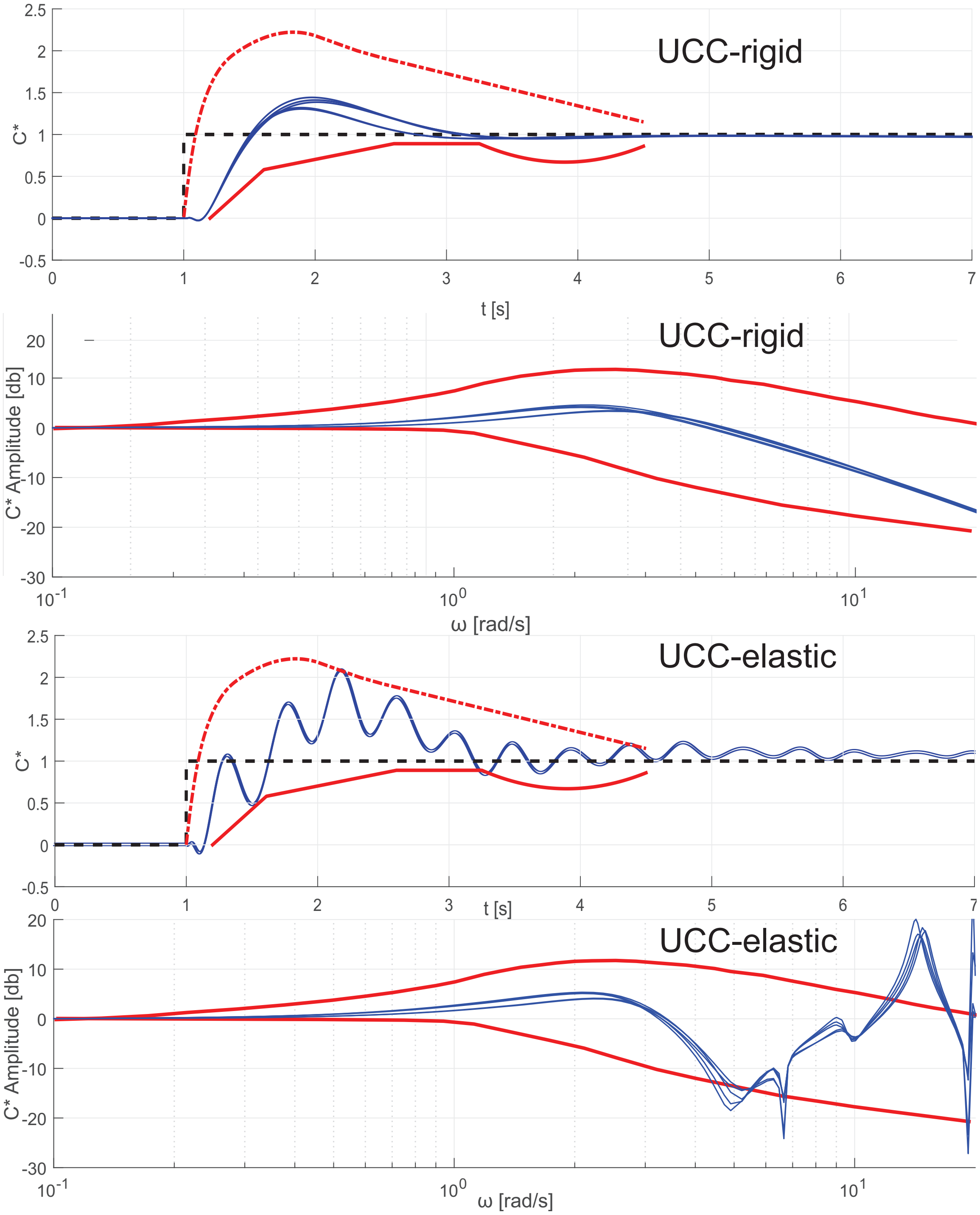

Figure 4.9. – C* Criterion for the Rigid and Elastic UCC for Normal Law

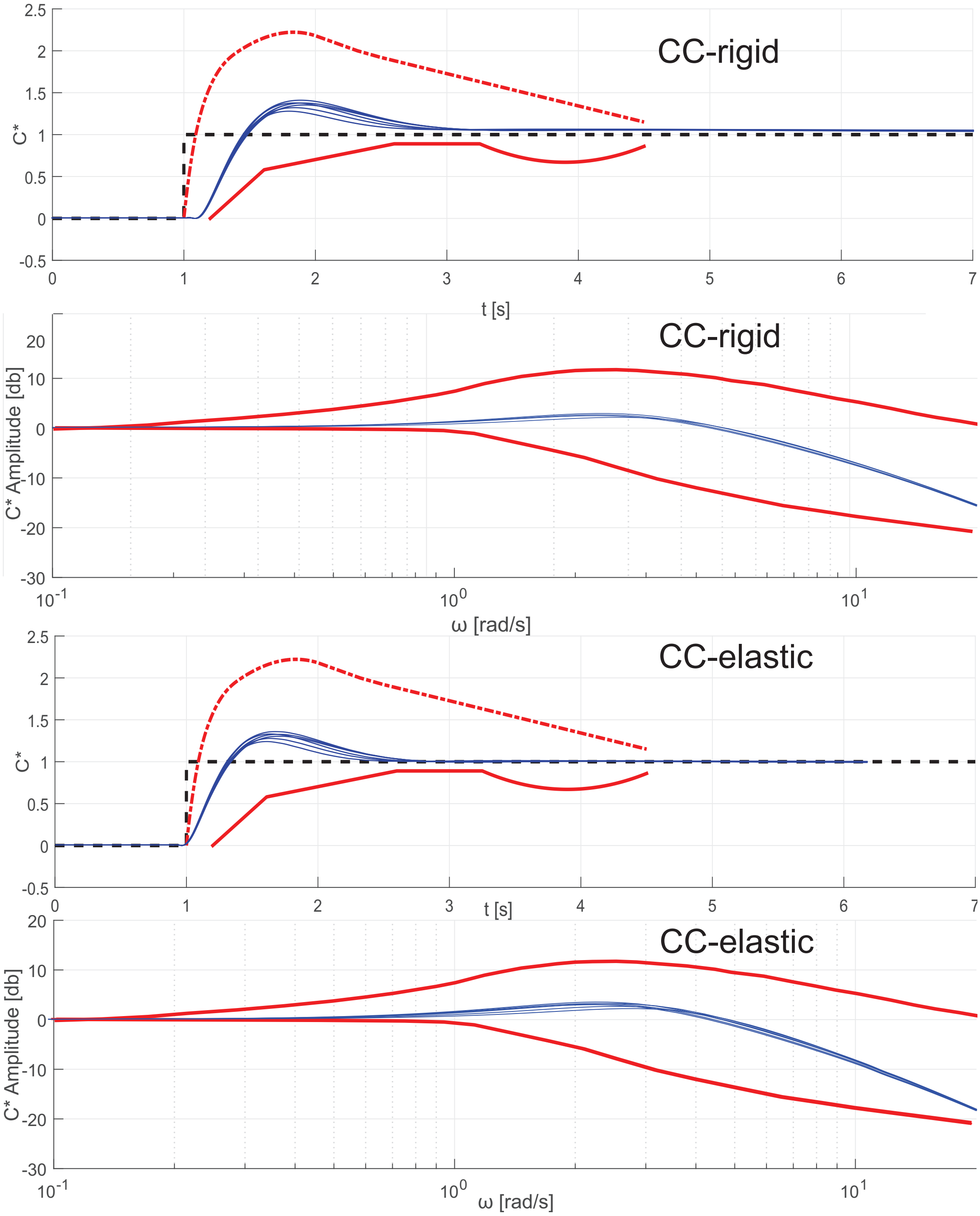

Figure 4.10. – C* Criterion for the Rigid and Elastic CC for Normal Law

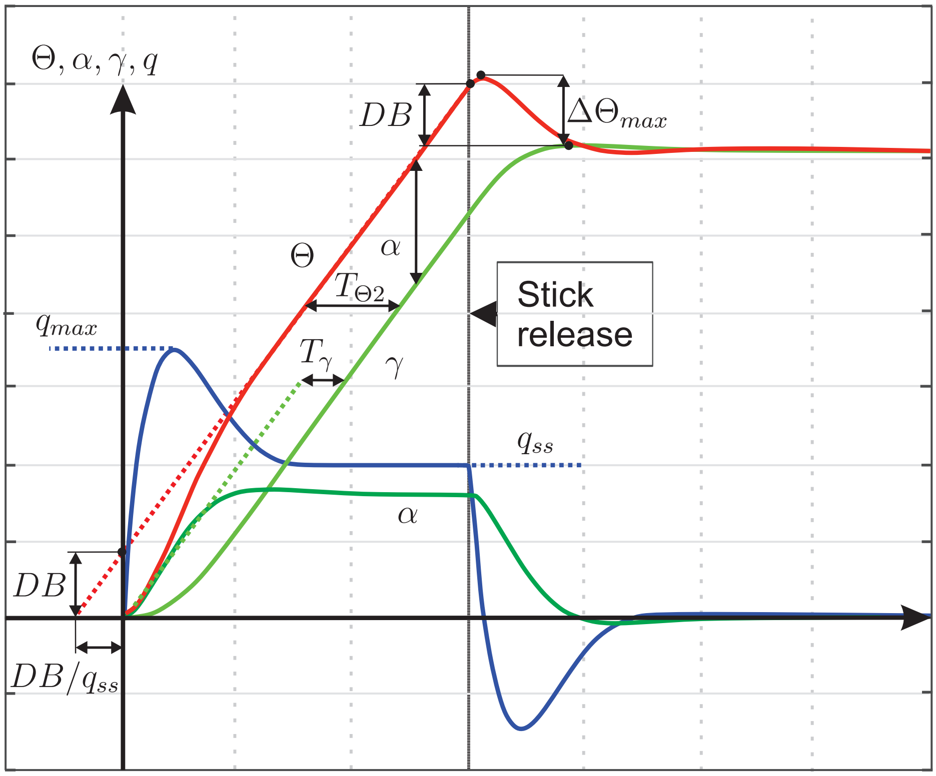

Figure 4.11. – Longitudinal Dynamics

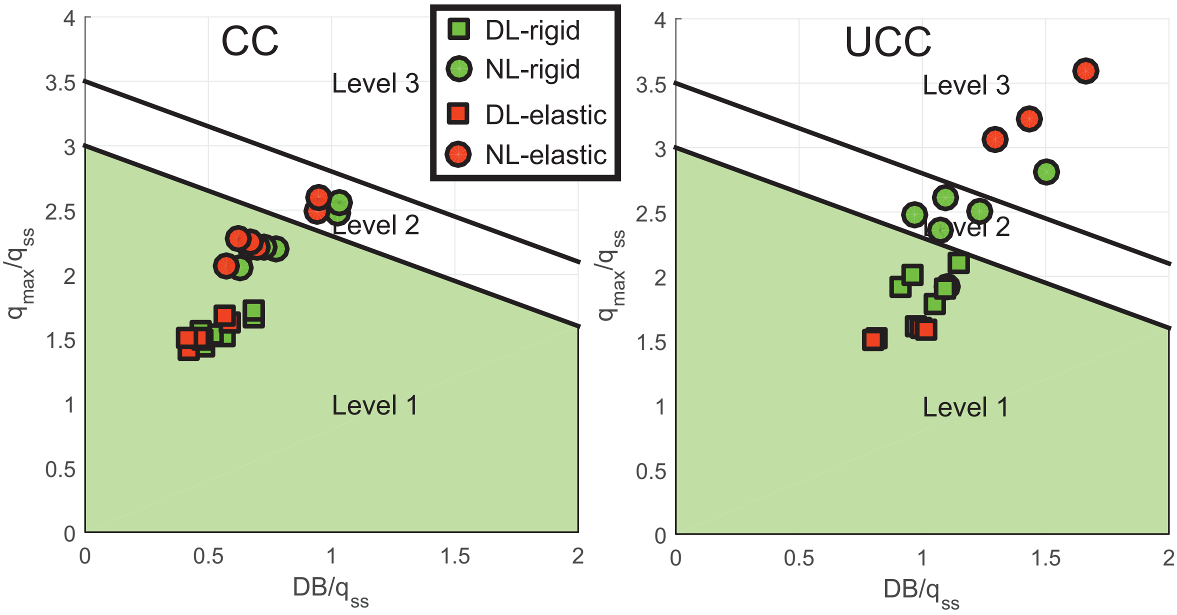

Figure 4.12. – Bounds for Gibson Dropback Criterion

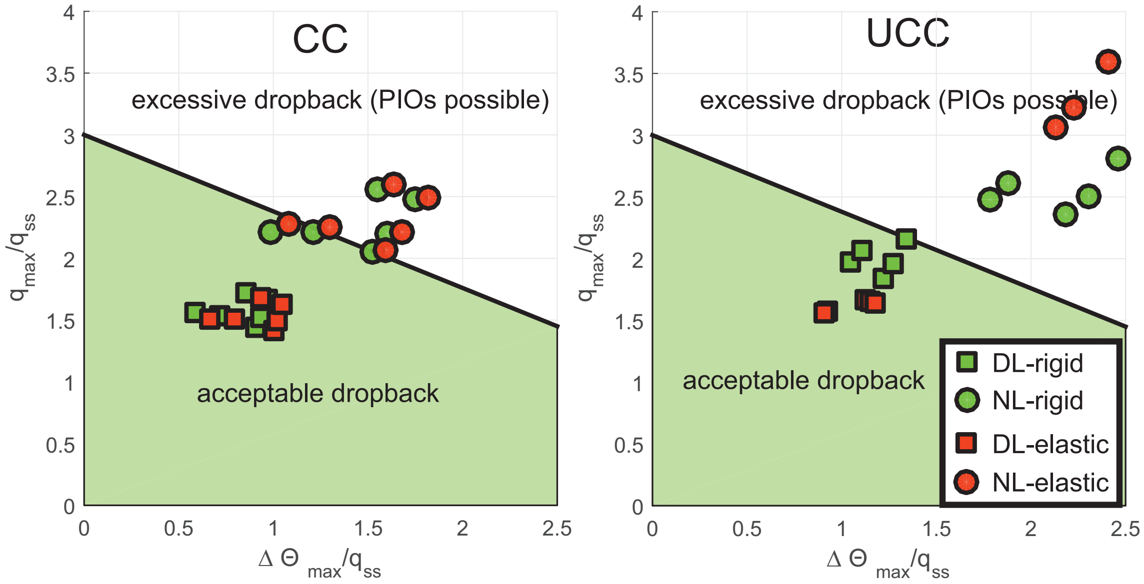

Figure 4.13. – Results for Updated Dropback Criterion

the classical configuration and more significantly degraded for the C-Wing configuration, specifically for the flexible C-Wing configuration.

4.2.3.3. Updated Dropback Criterion

The Gibson Dropback criterion was extended by Mitchel et. al. [90] to describe possible PIO risks of the aircraft, as an excessive dropback can lead to PIOs. This criterion uses the maximum difference in pitch attitude angle $\Delta\Theta_{max}$, as shown in Figure 4.11 instead of the dropback. The boundaries of the updated dropback criterion, as shown in Figure 4.13 only distinguish between two Levels of handling qualities. Acceptable dropback is considered safe whereas excessive dropback leads to possible risks for occurring PIOs.

Evaluation Similar observations as for the classical dropback criterion can be made for the updated dropback criterion. The direct law response behavior for both configurations is within the Level 1 bounds both for the rigid and the flexible aircraft model. The control law slightly deteriorates the dropback behavior for the CC and more significantly for the UCC.

4.2.3.4. Transient Peak Ratio

The Transient Peak Ratio (TPR) criterion characterizes the pitch rate behavior following a step input on the longitudinal control. The peaks of the pitch rate time response are related to an equivalent time delay. The equivalent time delay t_1 is found by constructing a tangent at the maximum of the derivative of the pitch rate, as shown in Figure 4.14.

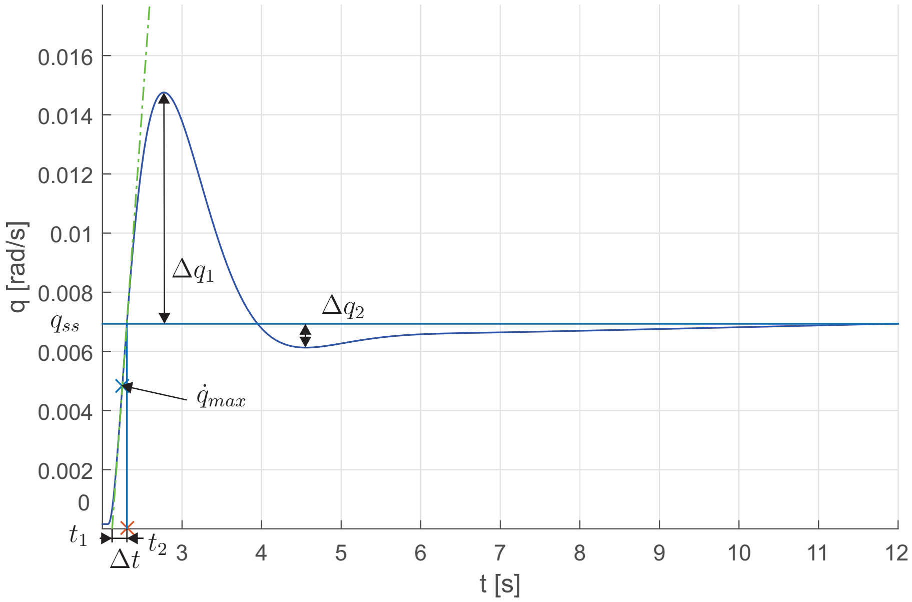

Figure 4.14. – Pitch Rate Response

The TPR is the ratio of the amplitude of the first two peaks $\mathbf{\Delta q}_1$ and $\mathbf{\Delta q}_2$ from the steady state value of $\mathbf{q}_{\text{ss}}$, as shown in Figure 4.14.

$$TPR = \frac{\Delta q_2}{\Delta q_1} \tag{4.10}$$

The boundaries for the TPR criterion are shown in Figure 4.15.

Evaluation The transient peak ratio criterion is met for the classical configuration in the rigid and in the elastic case. The unconventional configuration shows Level 2 behavior in some investigated flight states for the direct law system. Furthermore it can be seen that the equivalent time delay caused by the system delays and higher order behavior is at the limit between Level 1 and Level 2 for both configurations.

4.3. Lateral Criteria

The lateral handling of an aircraft is equally essential as the longitudinal handling to the safe operation of an aircraft and the execution of a mission. This section presents and evaluates criteria evaluating the lateral control characteristics and handling qualities of an aircraft ensuring that the pilot is able to perform the required mission tasks. The requirements investigated as part of this process are presented in Table 4.2 and are detailed in the following. The table indicates whether handling qualities and PIOs can be assessed and furthermore if the assessment is performed using time domain analysis, frequency domain analysis or a LOES.

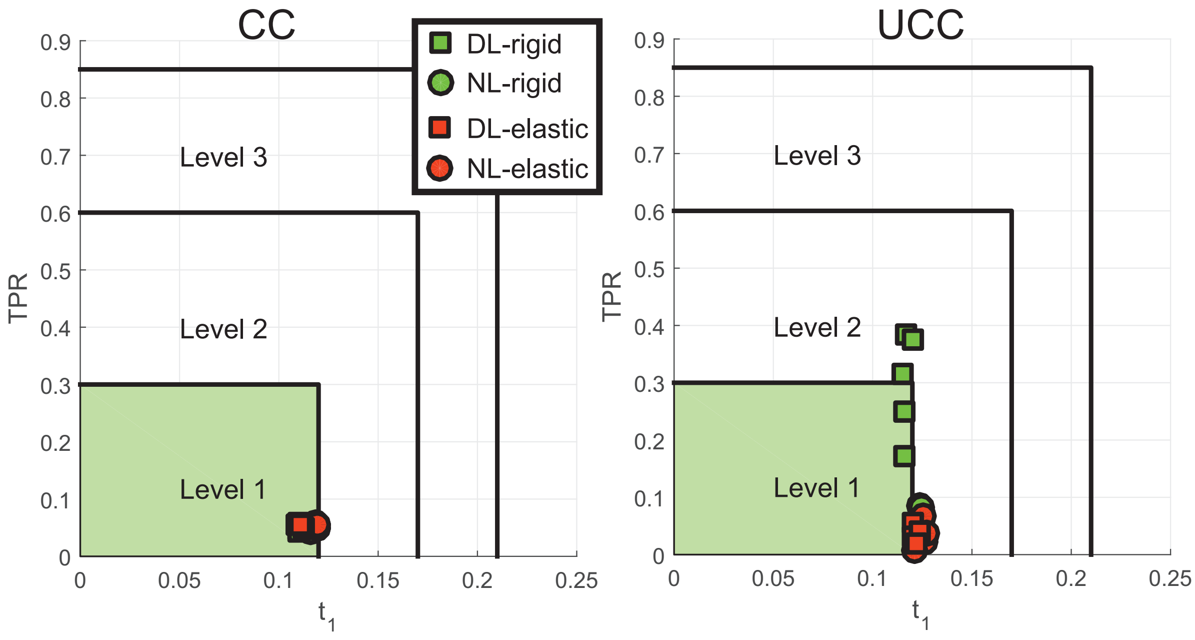

Figure 4.15. – Transient Peak Ratio Bounds

4.3.1. Modal Criteria

Similarly as for the longitudinal motion, the aircraft is classically characterized by a set of lateral modes in free flight. These modes are the dutch roll, the spiral mode and the roll mode. The frequencies and damping values of these modes are related to certain pilot perceptions of flying quality levels. The boundaries to obtain a certain level of handling qualities are given in the Military Standards 8785, Subpart C [129]. The lateral response transfer function also has to be matched by a LOES to represent the lateral dynamics in order to allow the application of the classical modal criteria. The transfer function of the classical aircraft lateral dynamics LOES is given by

$$\frac{\phi}{\xi} = e^{-ts}\frac{K_\phi(1+2\zeta_{DR}\omega_{DR}+s^2\omega_{DR}^2)(\tau_R s+1)}{(1+2\zeta_{DR}\omega_{DR}+s^2\omega_{DR}^2)(\tau_R s+1)(\tau_S s+1)}, \tag{4.11}$$

according to [52], where the typical lateral modes are represented in the denominator.

4.3.1.1. Dutch Roll Oscillation

The dutch roll, is a coupled oscillation about the yaw and roll axis with a relatively short period. The dutch roll typically appears at similar frequencies as the longitudinal short period, i.e. of the order of $1-5rad/s$ [52]. An insufficiently damped dutch roll mode leads to undesired handling behavior and poor flying qualities. The required frequencies and damping values in order to achieve good handling qualities are defined in the MIL-STD-1797-B [128] and shown in Figure 4.19.

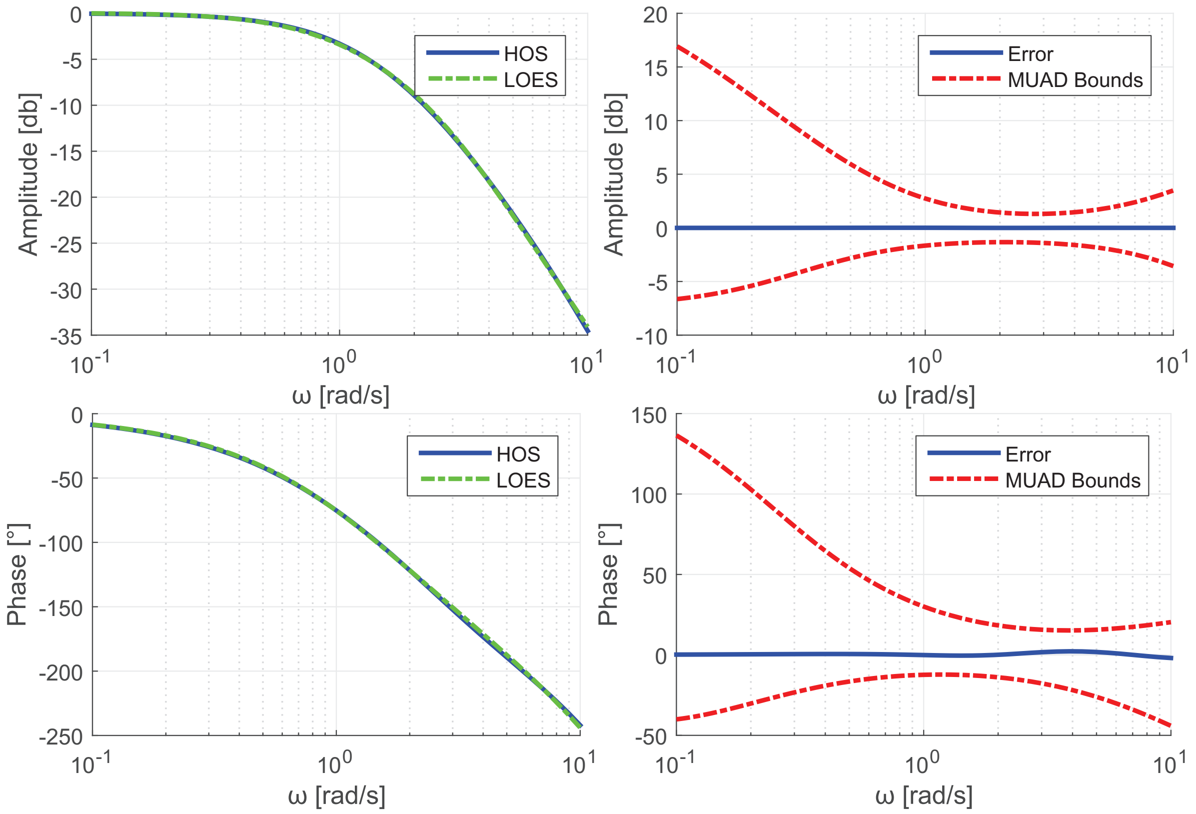

Figure 4.16. – LOES representation of rigid Lateral Dynamics, Conventional Configuration

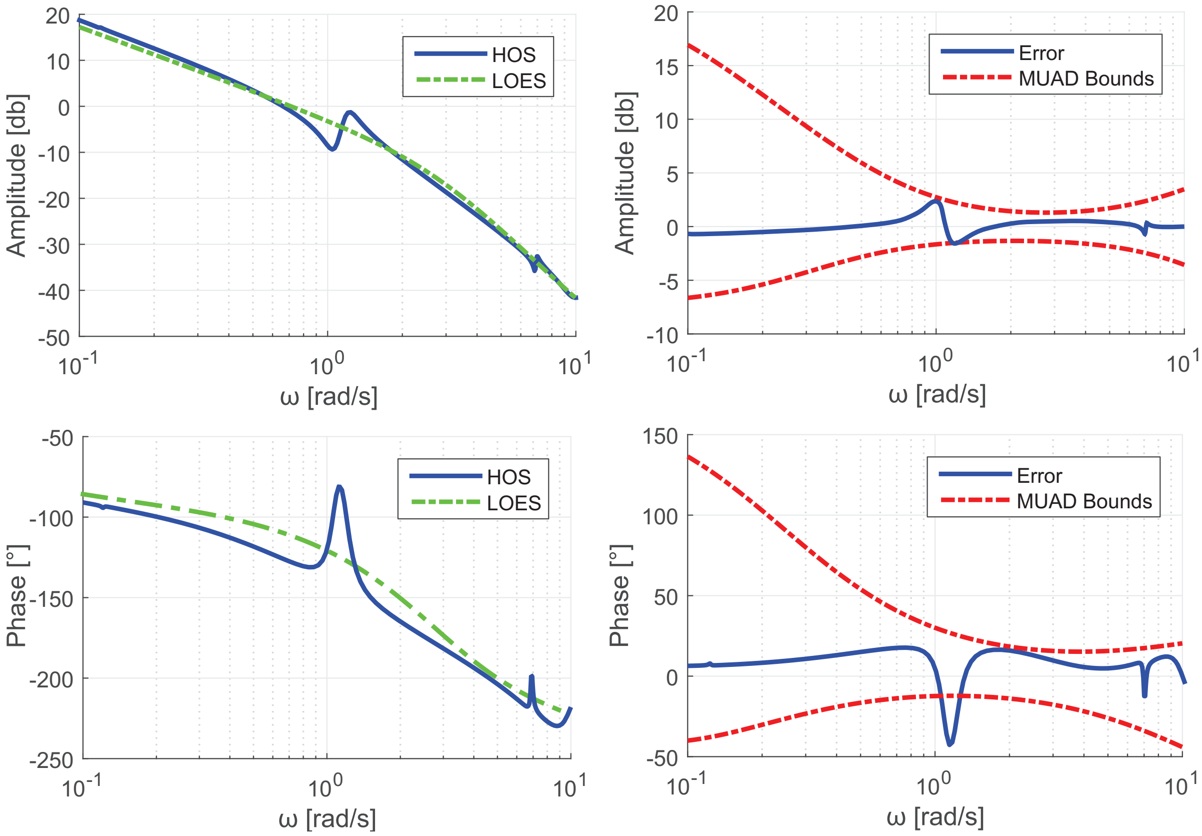

Figure 4.17. – LOES representation of elastic Lateral Dynamics, Unconventional Configuration

Table 4.2. – Lateral HQs

Criterion	*HQ*	*PIO*	*T*	*F*	*L*	*Source*
Dutch Roll Frequency	✓				✓	MIL-STD-1797B
Dutch Roll Damping	✓				✓	MIL-STD-1797B
Roll Mode Time Constant	✓				✓	MIL-STD-1797B
Roll Axis Equivalent Time Delay	✓		✓			MIL-STD-1797B
Roll Yaw Coupling	✓		✓			MIL-STD-1797B
Roll Oscillations	✓		✓			MIL-STD-1797B
Roll Performance	✓		✓			EASA CS-25
Lateral Bandwidth Criterion	✓	✓		✓		[90]

T=Time Domain Specification, F=Frequency Domain Specification, L=LOES specification

Evaluation Figure 4.19 presents the evaluation of the dutch roll criterion. Both configurations show Level 1 handling quality behavior in normal law. The direct law behavior is between Level 1 and Level 2 for the classical configuration and slightly worse for the C-Wing configuration, where the direct law handling qualities are on Level 2 or already on the verge to Level 3 depending on the respective flight state. No significant impact of the aircraft flexibility can be seen on the dutch roll for the investigated configurations.

4.3.1.2. Roll Mode

The roll mode time constant for Class 3 aircraft in Category C flight phases must be lower than $\tau_R < 1.4$ according to MIL-STD 1797-B [128].

4.3.1.3. Spiral Mode

The spiral mode is a slow recovery or divergence from a bank angle disturbance. The spiral mode may be stable or unstable, where only in the unstable case handling qualities may be impacted negatively. All stable cases are Level 1. The limits are given in terms of time to double, which can be computed from the location of the root of the spiral pole

$$T_{2s} = \frac{ln(2)}{\sigma_S} \tag{4.12}$$

The minimum time to double T_{2s} is 12 seconds for category C flight phases. Using this information boundaries in Figure 4.19 are computed.

Evaluation The roll mode and spiral mode time constant boundaries are depicted combined in Figure 4.19. Both configurations are within Level 1 bounds for the investigated flight states in normal and direct law.

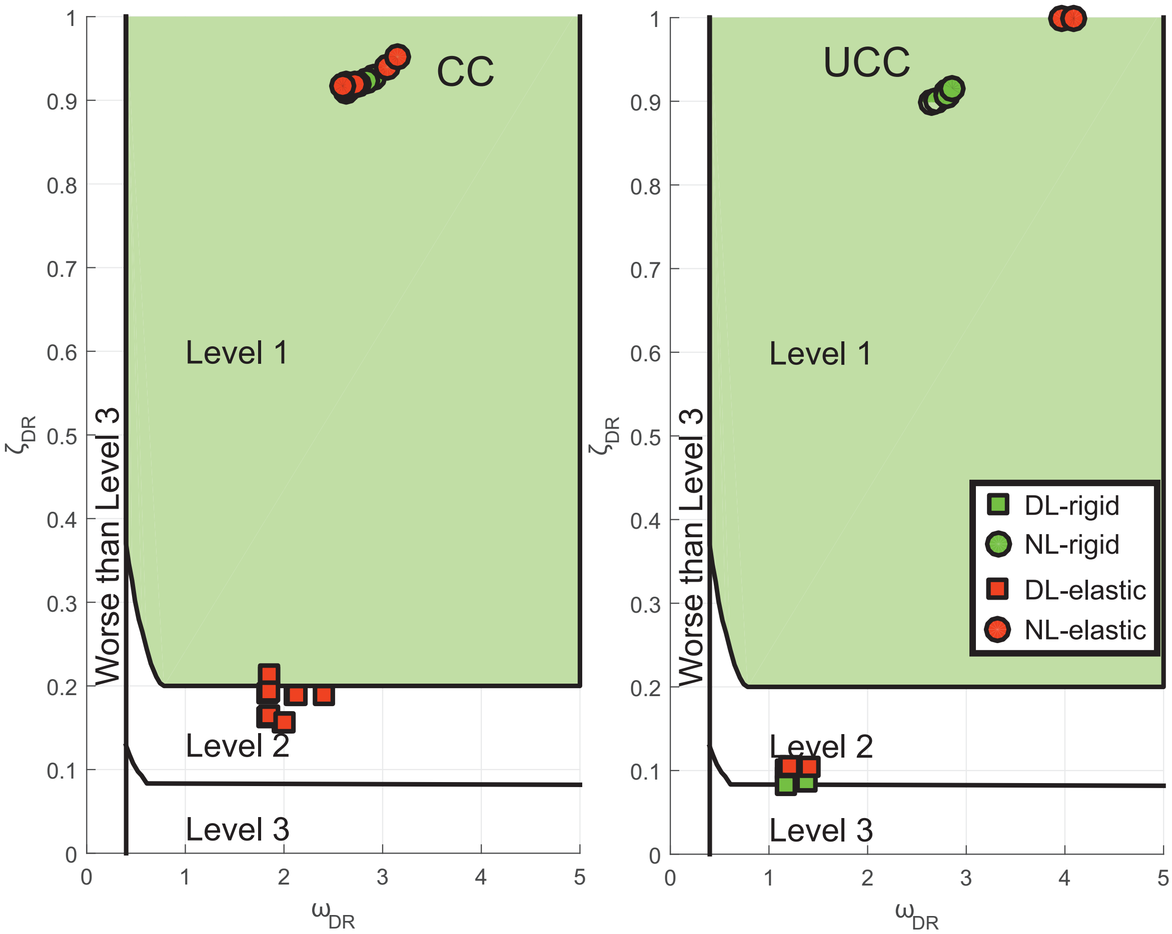

Figure 4.18. – Dutch Roll Evaluation

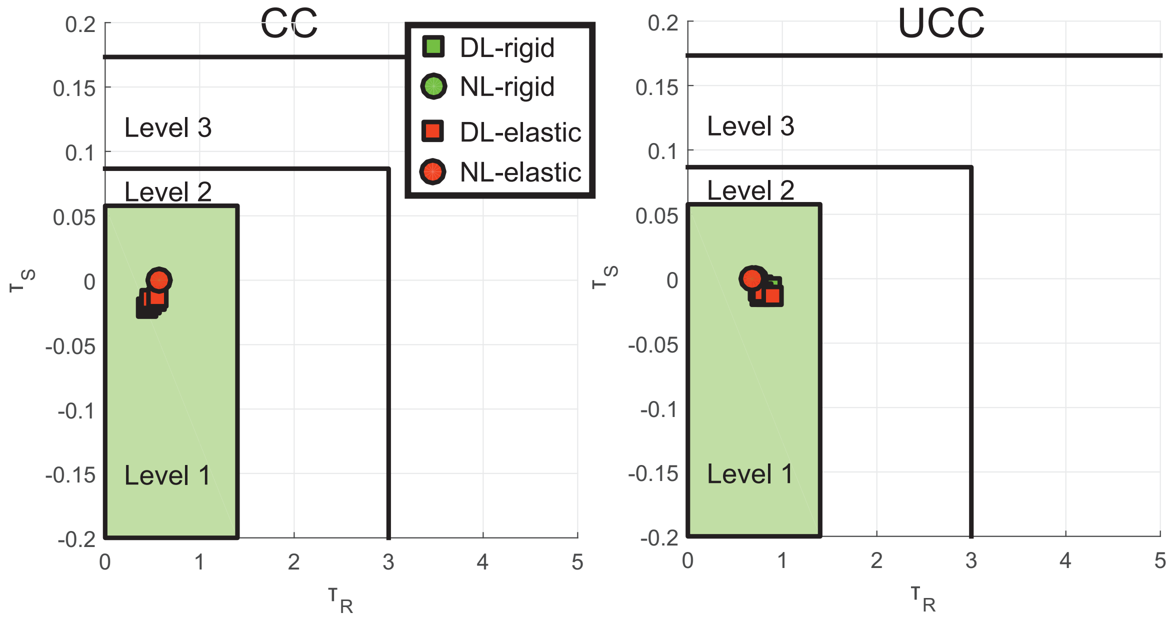

Figure 4.19. – Roll and Spiral Time Constant Boundaries

4.3.2. Time Domain Criteria

This subsection presents lateral criteria evaluated in the time domain.

4.3.2.1. Roll Time Delay

The roll time delay T_R is the equivalent time delay in the roll transfer function. This requirement is intended to ensure that the combined delay of prefilters, stability augmentation and actuators does not degrade the pilot's roll tracking capability. The roll time delay can be approximated from the roll rate response following a step shaped roll command input ξ. It is found by intersecting the tangent at the maximum slope of the roll rate $\dot{p}_{max}$ with the time axis, as shown in Figure 4.20. The limits for the roll time delay are stated in MIL-HDBK-1797A, 4.5.1.5, p.423 and are given by 0.1s for Level 1, 0.2 for Level 2 and 0.25 for Level 3.

Evaluation Figure 4.21 shows the evaluation of the roll time delay for multiple flight states. It can be seen that the values are at the limit between Level 1 and Level 2 handling qualities.

4.3.2.2. Roll Yaw Coupling

The roll yaw coupling evaluates the strength of the coupling between the roll and the yaw motion. An excessive coupling of the roll and yaw motion yield in bad handing qualities. Furthermore the phase is an important factor as the proverse/adverse yaw behavior is an

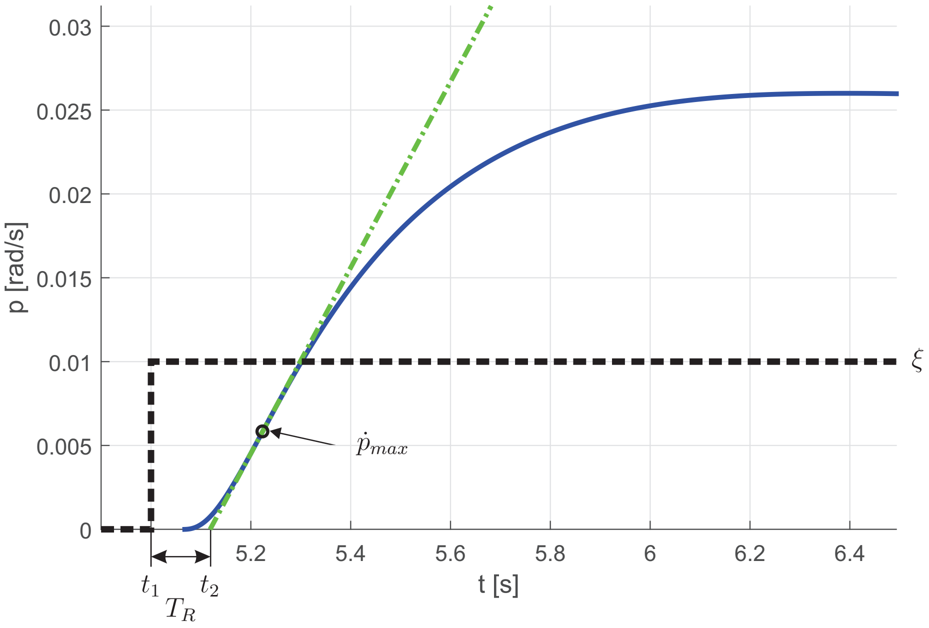

Figure 4.20. – Roll Time Delay Definition

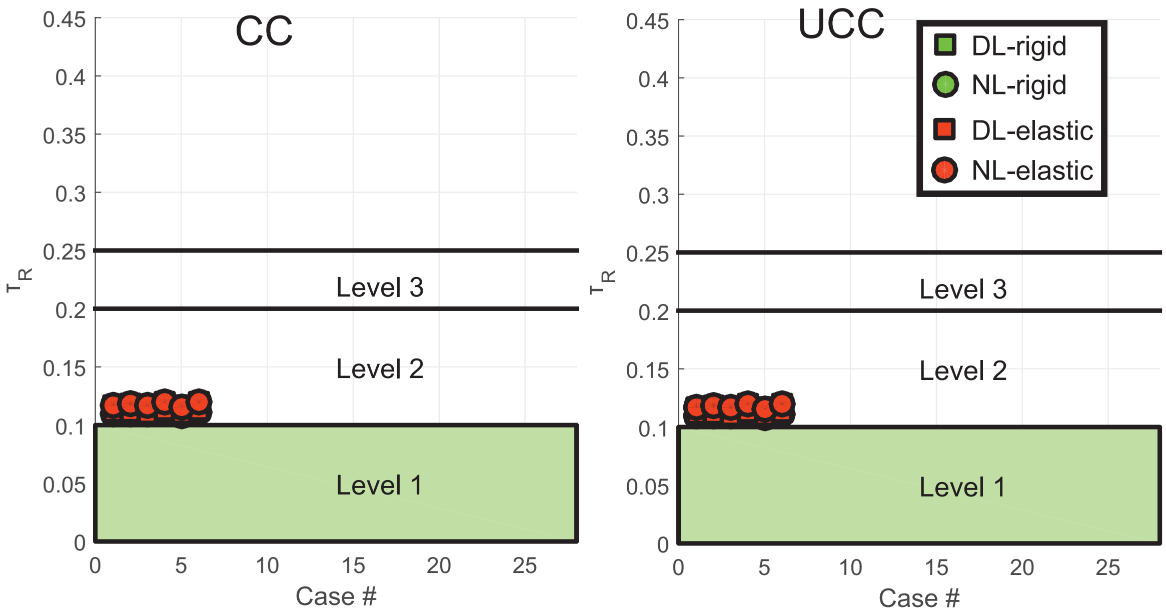

Figure 4.21. – Roll Time Delay Boundaries and Evaluation

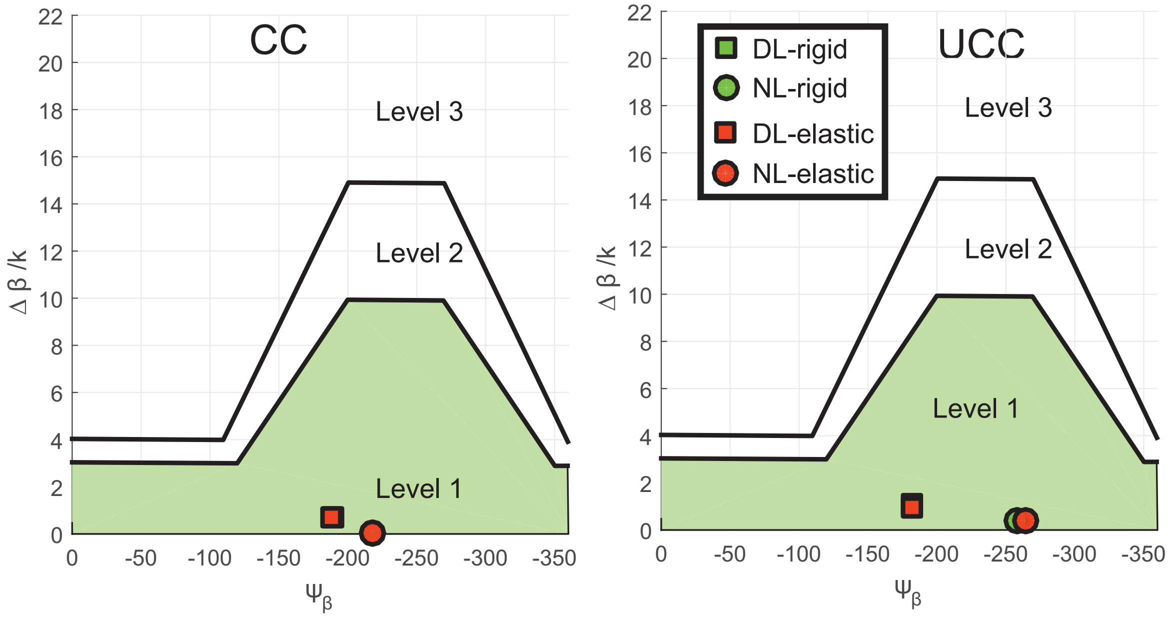

Figure 4.22. – Roll Yaw Coupling

important factor for the pilot perception of lateral handling qualities. The value ψ_β is the phase delay of the first peak in the sideslip angle after an aileron step input [52]. The value β/k evaluates the amplitude of the sideslip angle due to an aileron input.

Evaluation Figure 4.22 shows the evaluation of the Roll-Yaw coupling criterion for both configurations given the boundaries from [128]. It can be seen that Level 1 handling qualities are achieved without problems, hence it can be concluded that the investigated configurations do not have an undesired coupling of the roll and yaw motion.

4.3.2.3. Roll Oscillation Criterion

The roll oscillation criterion evaluates the oscillation following a step input on the roll command ξ. Figure 4.23 shows the response of the roll rate $\mathbf{p}$ following a roll command ξ singlet input. The oscillations can be seen clearly. The parameters used for the evaluation of the roll oscillation criterion are the mean roll rate $\mathbf{p}_{\mathrm{avg}}$ and a measure for the oscillatory component, $\mathbf{p}_{\mathrm{osc}}$, defining the ratio

$$\frac{\mathbf{p}_{\mathrm{osc}}}{\mathbf{p}_{\mathrm{avg}}} = \frac{\mathbf{p}_{pk,1} + \mathbf{p}_{pk,3} + 2\mathbf{p}_{pk,2}}{\mathbf{p}_{pk,1} + \mathbf{p}_{pk,3} + 2\mathbf{p}_{pk,2}} \tag{4.13}$$

if three peaks can be detected. Otherwise the ratio is defined by

$$\frac{\mathbf{p}_{\mathrm{osc}}}{\mathbf{p}_{\mathrm{avg}}} = \frac{\mathbf{p}_{pk,1} - \mathbf{p}_{pk,2}}{\mathbf{p}_{pk,1} + \mathbf{p}_{pk,2}} \tag{4.14}$$

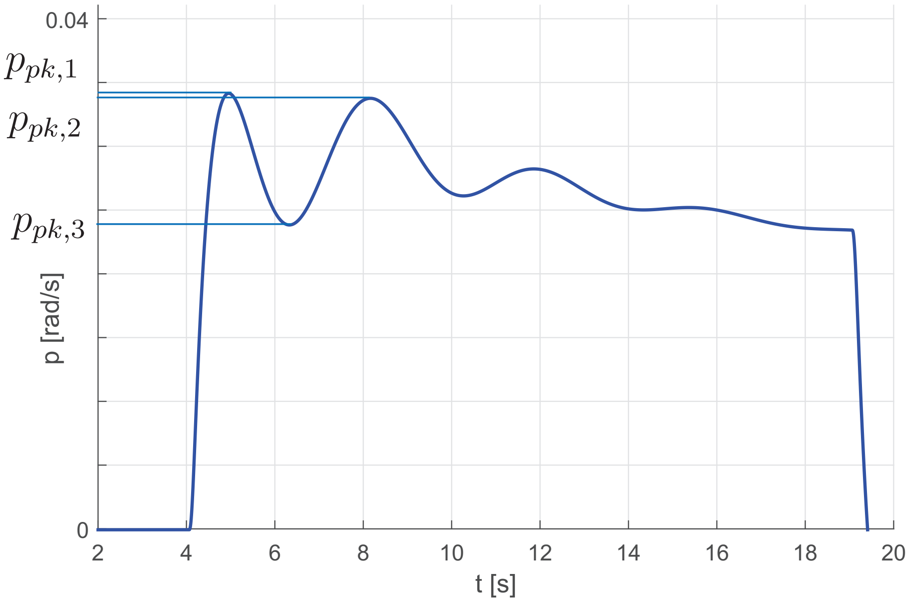

Figure 4.23. – Roll Rate Oscillations in Direct Law

according to [52]. Figure 4.24 shows the boundaries for the roll rate requirements.

Evaluation Figure 4.24 shows the evaluation of the roll oscillation criterion for both configurations. It can be seen that Level 1 handling qualities are achieved without problems, hence it can be concluded that the investigated configurations do not have an undesired excessive oscillation of the roll rate. It can also be seen that the controller almost completely removes the roll rate oscillations and thus even improves the handling qualities with respect to this criterion

4.3.2.4. Roll Control Performance

The roll performance criterion is one of the most important criteria governing the ability of the aircraft to respond to lateral control inputs [52]. This ensures the aircraft is able to perform cruise heading corrections as well as takeoff, landing or holding patterns for example. The roll performance is especially critical for large wingspans and heavy aircraft, as elasticity and the large inertia may make the aircraft less agile. EASA CS-25.147 [37, 1-B-17] defines requirements for lateral controllability. Sufficient lateral control is shown by rolling from $\Phi = -30\,\text{deg}$ to $\Phi = 30\,\text{deg}$ within $7s$ [37, 2-B-52].

4.3.2.5. Turn Performance with Engine Failure

Sufficient roll control must also be achieved in the case of OEI, the requirement for roll performance is however relaxed to $11s$.

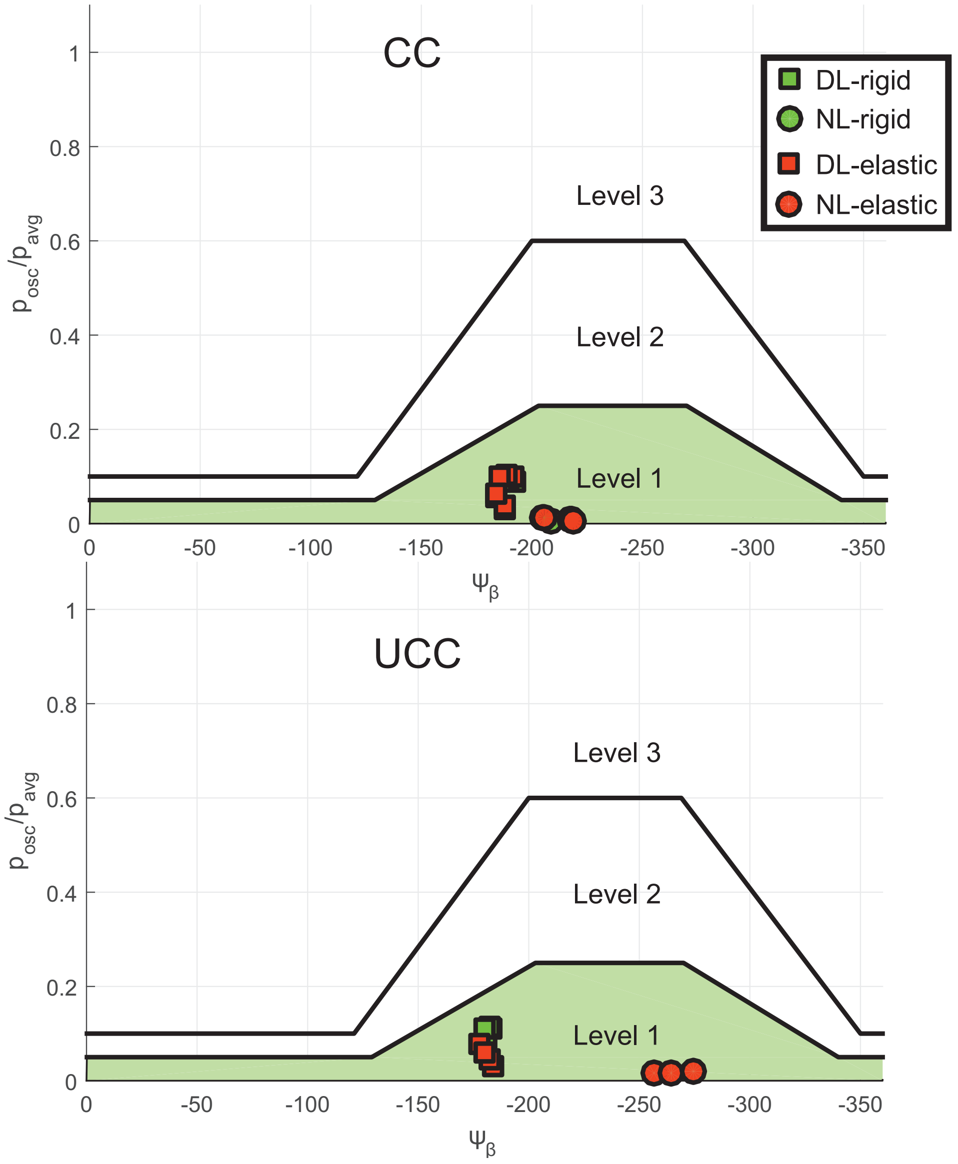

Figure 4.24. – Roll Rate Boundaries

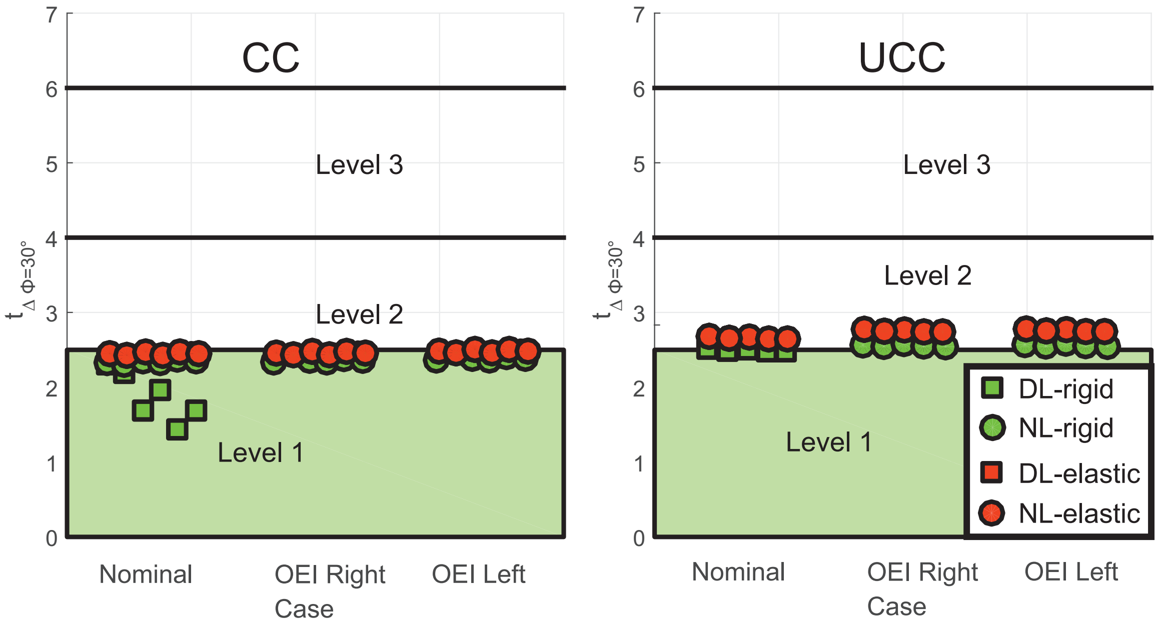

Figure 4.25. – Roll Control

Evaluation The roll control performance with and without engine failure can be seen in Figure 4.25. Although as found in the previous section, aeroelastic effects reduce the aileron efficiency for the UCC, with a full aileron deflection the achievable roll rate is still sufficient to reach close to Level 1 requirements. It can be seen that in both cases the roll performance is slightly better for the rigid models which represents the expected behavior.

4.3.3. Lateral Bandwidth Criterion

Equivalent to the longitudinal bandwidth criterion the lateral bandwidth criterion can be evaluated using the transfer function from the stick input ξ to the bank angle Φ, $G_{\Phi\xi}$.

Evaluation Figure 4.26 shows the evaluation of the lateral bandwidth criterion for both configurations, which are both very close to achieve Level 1 handling qualities. No significant impact of elasticity or the control system can be observed.

4.4. Performance Criteria

An aircraft has to be able to takeoff within a certain field length and has to be able to obtain a certain rate of climb for certification. This section shortly presents the takeoff and landing simulations performed during the investigations. Only the C-Wing simulations are shown as no problems occured for the CC.

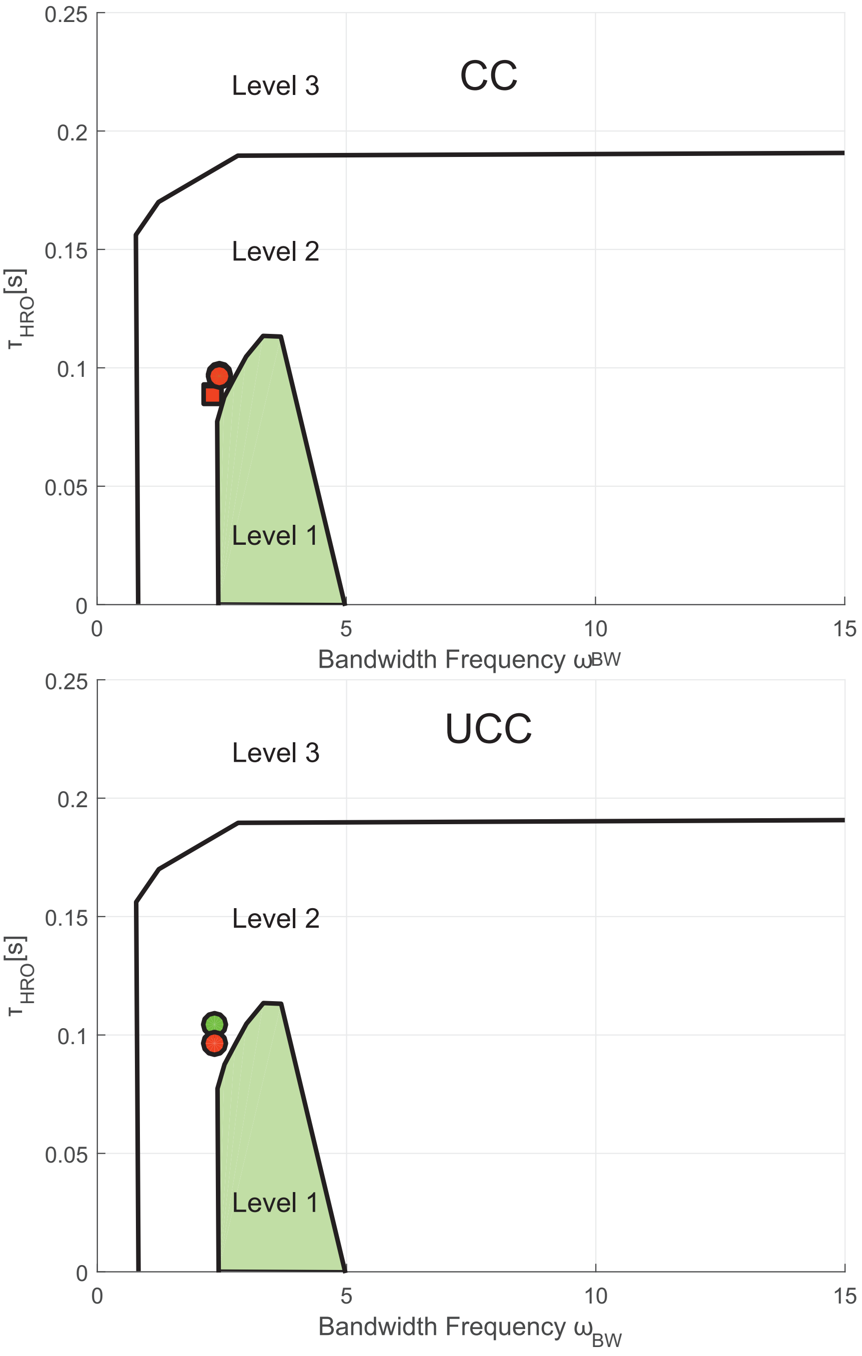

Figure 4.26. – Evaluation of the Lateral Bandwidth Criterion

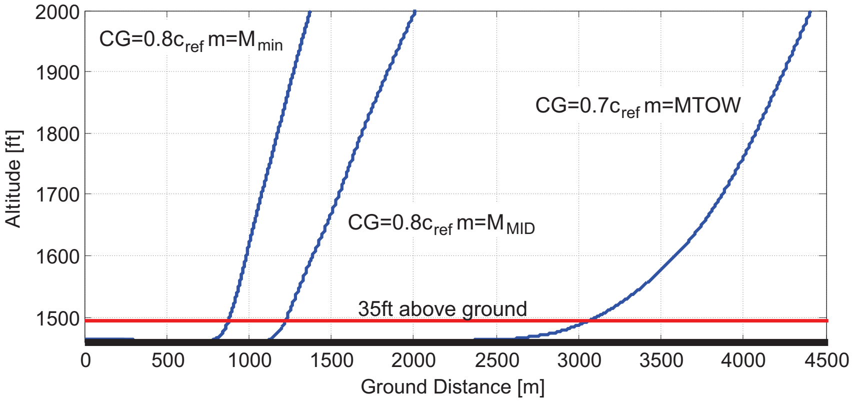

Figure 4.27. – Takeoff Trajectories for different CGs, C-Wing

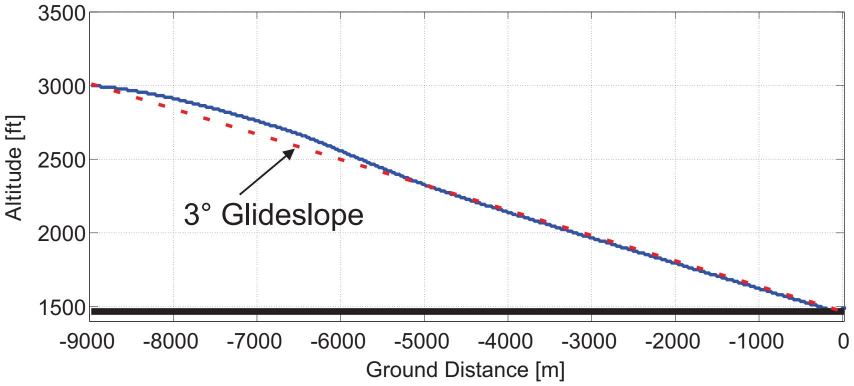

Figure 4.28. – Landing Trajectories for different CGs, C-Wing

4.4.1. Takeoff

Take-off and landing characteristics are investigated using the fast time flight simulation model and considering high lift system aerodynamics. Takeoff simulations were performed under ISA standard conditions and an airport field height of 1487ft (MUC). A rotation speed of VR = 150kts was attempted, however a speed of VR = 205kts was required for the case with the most forward CG and MTOW. The respective takeoff trajectories are visualized in Figure 4.27. It can be seen that for the latter case the transition to the climb angle is too slow to ensure a save takeoff. Furthermore the takeoff field length is exceeded by far compared to in-service aircraft with similar MTOW.

4.4.2. Landing

Landing simulations showed similar problems due to longitudinal control authority issues. An excessive landing speed of over 200kts at maximum landing weight was required in order to perform a safe landing flare. Figure 4.28 shows a typical landing trajectory.

5. Conclusion and Outlook

In this thesis an automated toolchain for the aeroelastic flight dynamics modeling, simulation, and assessment of handling qualities for novel aircraft configurations in the conceptual design phase was successfully implemented, validated and tested. The tool enables the parametrized modeling of arbitrary unconventional concepts (with few limits), and performs an automated structural sizing, based on standard or user defined loadcases, in order to estimate structural mass and stiffness. For the computation of loads, a direct time domain aeroelastic approach is used, while for the purpose of fast time flight simulation and handling quality assessment, a reduced order indirect simulation model is used. The different implemented simulation methods for the free-flying flexible aircraft ranging from a complex inertially coupled direct time domain model to more simplified indirect simulation approaches applying mean-axis, allow to check the validity of simplifications for each specific aircraft configuration, as these may vary depending on the investigated configuration. Furthermore the RFA approach may introduce uncertainties due to the approximation of the unsteady aerodynamic forces, which can be investigated by comparing simulations to the direct time domain approach.

Two different aircraft concepts were investigated with the toolchain, showing that handling qualities may be a significant issue for unconventional concepts. Furthermore it was shown that the aeroelastic impact on handling qualities may be severe for unconventional concepts, not only for large and heavy aircraft as for classical configurations but also for small, short medium haul aircraft, and therefore must be considered as early in the design as possible. The toolchain gives a first indication in the conceptual design phase, whether a concept will be likely to have a chance for certification and how complex and costly a control system will be. This allows to assess potential risks and drawbacks of new configurations in the early design process. The relatively fast turn around time allows to quickly assess the impact of design changes on handling qualities.

The generated simulation model for the flexible aircraft can be continuously used and updated for later design phases, as the tabulated aerodata may be replaced with windtunnel or flight-test data.

Regarding the handling qualities evaluation it can be said that the application of LOES is limited to airframes with frequency separation, or only slight impact of elasticity. If the rigid body modes and the elastic modes are close, different methods for the evaluation of handling qualities must be applied, to fully capture complex higher order system behavior. For this purpose the Bandwidth Criterion and the Neal-Smith criterion were utilized.

5.1. Contribution

The depth of the aircraft concept investigation in the conceptual design phase was significantly refined by the presented approach. The coupling of aeroleasticity and flight dynamics is not subject of conceptual design investigations in state-of-the-art methods and was introduced in this work. The proposed method is therefore unique with regards to the following aspects:

- The fully integrated aeroelastic sizing and simulation approach, allowing the automated sizing and generation of a flight simulation model only based on a basic geometry definition and a few other input parameters.
- The in depth flight dynamics and HQs evaluation in conceptual design for unconventional concepts, additionally enabling the consideration of aeroelasticity in the flight dynamic equations of motion.
- The implementation of multiple simulation approaches enabling the validation of simplifications, based on the fully coupled equations of motion, for each individual investigated configuration.
- The flight dynamics assessment of C-wing configuration considering aeroelasticity.

5.2. Outlook and Perspective

The implemented toolchain applies basic models, which may all be subject to extensions to achieve an increased accuracy. A number of extensions are proposed, which will likely be implemented in further projects. The tool can also be extended to allow multi-fidelity simulation. The object oriented design of the code allows an easy extension and integration of new methods.

- *Nonlinear Structural Elements:*
  The increasing elasticity of wings may lead to deflections which exceed the range of geometrically linear structural models. The implementation of nonlinear structural elements would allow the consideration of vehicles with very large wing bending deflections and extend the applicability of the presented toolchain.
- *Carbon Fiber Materials:*
  The implemented structural sizing model only allows the consideration of isotropic materials. Carbon fiber materials can only be considered by means of an equivalent isentropic material. Future concepts apply more advanced structural concepts, which show anisotropic behavior. This behavior can also be exploited for aerelastic design purposes. The properties of such structures can also be modeled by means of equivalent beam elements, as e.g. shown by [30] implementing a 3D beam model for a carbon fiber wind turbine blade. The condensation of more complex finite

element models to beam elements may also be a potential solution to be investigated in future research activities.

- *Proposed Aerodynamic Model Extensions:*
  The aerodynamic methods can be extended by correction methods to improve the accuracy and range of validity of the results. Mauermann [81] presented a method for correcting the UVLM results with CFD data. The UVLM also allows to skip the standard RFA approach, and to directly generate a linear state space model for the aeroelastic simulation as e.g. shown by [50] and [81], which should be investigated in the future.
  The compressibility correction applied for the UVLM is only an approximation with a limited validity. The feasibility of a fully compressible UVLM method for the three dimensional case, as already derived for the two dimensional case by [97] should be investigated.
  Generalized aerodynamic forces may also be computed with higher fidelity methods and can be used for the generation of the indirect aeroelastic flight simulation model. Furthermore the aerodynamic model may be coupled to a higher fidelity structural code.

- *Extended Control System Considerations:*
  This work also sets the basis for the inclusion of active maneuver load alleviation and active gust load alleviation systems in the conceptual design and sizing process. This would allow to directly the assess and consider the impact of these systems on the aircraft design already in the conceptual design phase.
  As shown in this work, standard control approaches may run into difficulties for significantly elastic configurations. Therefore more more complex control techniques allowing to control elastic modes have to be implemented for elastic aircraft configurations, where there is no clear frequency separation between the rigid body modes and the elastic modes. The generated models may be used for the development of control laws for the elastic aircraft to improve handling qualities.

Bibliography

[1] *Aeronautical Vestpocket Handbook*. United Technologies Pratt & Whitney, August 1986.

[2] *Luftfahrttechnisches Handbuch Masseanalyse - MA 508 52-01*. LTH, 1998.

[3] *Luftfahrttechnisches Handbuch Masseanalyse - MA 508 22-07*. LTH, 2013.

[4] H. Abbasi, P. Grant, and N. Li. Real-time simulation of flexible aircraft: a comparison of two methods. In *Guidance, Navigation, and Control and Co-located Conferences*. American Institute of Aeronautics and Astronautics, Aug. 2009.

[5] J. M. Abzug and E. E. Larrabee. *Airplane Stability and Control: A History of the Technologies that Made Aviation Possible*. Cambridge Aerospace Series, 2002.

[6] Advisory Council for Aviation Research and Innovation in Europe (ACARE). Strategic Research and Innovation Agenda (SRIA). September 2012.

[7] R. M. Ajaj, D. Smith, and A. T. Isikveren. A conceptual wing-box weight estimation model for transport aircraft. *Aeronautical Journal*, 2013.

[8] P. S. Andrews. *Modelling and simulation of flexible aircraft: handling qualities with active load control*. PhD thesis, Cranfield University, 2011.

[9] M. D. Ardema, M. C. Chambers, A. P. Patron, A. S. Hahn, H. Miura, and M. D. Moore. Analytical Fuselage and Wing Weight Estimation of Transport Aircraft. *NASA Technical Memorandum 110392*, 1996.

[10] D. H. Baldelli and P. Chen. Unified aeroelastic and flight dynamic formulation via rational function approximations. *Journal of Aircraft*, 43(3), May-June 2006.

[11] G. K. Batchelor. *An introduction to fluid dynamics*. Cambridge University Press, 1967.

[12] D. Bates and I. Postlethwaite. Robust multivariable control of aerospace systems. *Delft, Netherlands: DUP Science*, 2002.

[13] T. Berger, M. Tischler, S. Hagerott, D. Gangsaas, and N. Saeed. Lateral/directional control law design and handling qualities optimization for a business jet flight control system. In *AIAA Atmospheric Flight Mechanics Conference*, 2013.

[14] T. Berger, M. B. Tischler, S. G. Hagerott, D. Gangsaas, and N. Saeed. Longitudinal control law design and handling qualities optimization for a business jet flight control system. *AIAA Atmospheric Flight Mechanics Conference Proceedings, Minneapolis, MN*, pages 13–16, 2012.

[15] W. Bihrle. A Handling Qualities Theory for Precise Flight Path Control. Technical report, Wright Patterson Air Force Base, Ohio : Air Force Wright Aeronautical Laboratories, 1966.

[16] S. Binder. Generation of Aerodynamic and Aeroelastic Datasets for Flight Simulation on the Example of a C-Wing. Master's thesis, Technische Universität München, 2013.

[17] G. Bindolino, G. Ghiringhelli, S. Ricci, and M. Terraneo. Multilevel structural optimization for preliminary wing-box weight estimation. *Journal of Aircraft*, 47(2):475–489, Mar. 2010.

[18] R. Bisplinghoff, H. Ashley, and R. Halfman. *Aeroelasticity.* Dover Publications, 1996.

[19] F. Bocola, V. Muscarello, G. Quaranta, and P. Masarati. Pilot in the loop aeroservoelastic simulation in support to the conceptual design of a fly by wire airplane. *AIAA Atmospheric Flight Mechanics Conference*, 2015.

[20] E. M. Botero, A. Wendorff, T. MacDonald, A. Variyar, J. M. Vegh, T. W. Lukaczyk, J. J. Alonso, T. H. Orra, and C. I. da Silva. Suave: An open-source environment for conceptual vehicle design and optimization. In *AIAA SciTech.* American Institute of Aeronautics and Astronautics, Jan. 2016.

[21] A. Boucke. *Kopplungswerkzeuge für aeroelastische Simulationen.* PhD thesis, RWTH Aachen, 2003.

[22] R. Brockhaus. *Flugregelung.* Springer Berlin, Berlin, 2010.

[23] T. R. Brooks, G. Kennedy, and J. Martins. High-fidelity aerostructural optimization of a high aspect ratio tow-steered wing. In *AIAA SciTech.* American Institute of Aeronautics and Astronautics, Jan. 2016.

[24] D. A. Burdette, G. K. Kenway, and J. Martins. Performance evaluation of a morphing trailing edge using multipoint aerostructural design optimization. In *AIAA SciTech.* American Institute of Aeronautics and Astronautics, Jan. 2016.

[25] L. Cavagna, S. Ricci, and L. Riccobene. Structural sizing, aeroelastic analysis, and optimization in aircraft conceptual design. *Journal of Aircraft*, 48(6):1840–1855, Nov. 2011.

[26] L. Cavagna, S. Ricci, and L. Travaglini. Neocass: an integrated tool for structural sizing, aeroelastic analysis and mdo at conceptual design level. Technical report, AIAA Conference, 2010.

[27] I. Chakraborty, T. Nam, J. R. Gross, D. N. Mavris, J. A. Schetz, and R. K. Kapania. Comparative assessment of strut-braced and truss-braced wing configurations using multidisciplinary design optimization. *Journal of Aircraft*, pages 1–12, Apr. 2015.

[28] G. E. Cooper and R. P. Harper Jr. The use of pilot rating in the evaluation of aircraft handling qualities. Technical report, Neuilly-sur-Seine: Advisory Group for Aerospace Research and Development (AGARD), Agard Report 567, 1969.

[29] H. J. Damveld. *A Cybernetic Approach to Assess the Longitudinal Handling Qualities of Aeroelastic Aircraft.* PhD thesis, Technical Univeristy of Delft, 2009.

[30] R. de Frias Lopez. A 3D Finite Beam Element for the Modelling of Composite Wind Turbine Wings. Master's thesis, Royal Institute of Technology, 2013.

[31] Y. Denieul. Control allocation for multicontrol surfaces applied to unconventional aircraft configurations. *Final Year Project Report, Supaero, Airbus*, 2012.

[32] D. A. DiFranco. In-Flight Investigation of the Effects of Higher-Order Control System Dynamics on Longitudinal Handling Qualities. Technical report, Air Force Flight Dynamics Lab., AFFDL-TR-68-90, Wright-Patterson AFB, OH, Aug. 1968.

[33] F. Dorbath, B. Nagel, and V. Gollnick. Comparison of beam and shell theory for mass estimation in preliminary wing design. *Aircraft Structural Design Conference*, 2010.

[34] M. Drela. Integrated simulation model for preliminary aerodynamic structural, and control-law design of aircraft. *AIAA*, pages 1644–1656, 1999.

[35] M. Drela. Development of the D8 Transport Configuration. *29th AIAA Applied Aerodynamics Conference*, 2011.

[36] M. Drela. *Flight Vehicle Aerodynamics.* MIT Press, 2014.

[37] European Aviation Safety Agency. CS-25: Certification Specifications and Acceptable Means of Compliance for Large Aeroplanes, Amendment 14. December 2013.

[38] E. Field, J. Rossitto, F. Kenneth, and D. G. Mitchell. Landing approach flying qualities criteria for active control transport aircraft. Braunschweig : NATO Science and Technology Organization, 2000.

[39] I. Garrick. Propulsion of a flapping and oscillating airfoil. *NACA TR No. 567*, May 1936.

[40] M. Ghoreyshi, K. J. Badcock, and M. A. Woodgate. Accelerating the numerical generation of aerodynamic models for flight simulation. *Journal of Aircraft*, 46(3):972–980, May 2009.

[41] J. C. Gibson. Development of a methodology for excellence in handling qualities design for fly by wire aircraft. *TU Delft*, 1999.

[42] E. E. H. Tobie and L. Malcom. A new longitudinal handling qualities criterion. *Proceedings of the 18th National Aerospace Electronics Conference*, pages 93–97, 1966.

[43] F. Hamano. Derivative of rotation matrix: Direct matrix derivation of well-known formula. *Proceedings of Green Energy and Systems Conference*, 2013.

[44] M. Hanel. Integrated flight and aeroelastic control of a flexible transport aircraft. *AIAA*, pages 1002–1011, 1998.

[45] M. Hanel. *Robust Integrated Flight and Aeroelastic Control System Design for a large Transport Aircraft*. VDI-Verl., Düsseldorf, 2001.

[46] W. Heinze. Ein Beitrag zur quantitativen Analyse der technischen und wirtschaftlichen Auslegungsgrenzen verschiedener Flugzeugkonzepte für den Transport grosser Nutzlasten. *ZLR-Forschungsbericht 94-01*, Braunschweig 1994.

[47] F. Hellmundt. Entwurf von Regelgesetzen mit Gain Scheduling für die Robustheitsanalyse von Konfigurationsmodifikationen eines Flugzeugs unter Berücksichtigung der erreichbaren Handling Qualities. Master's thesis, Technische Universität München, 2013.

[48] F. Hellmundt, J. Dodenhoeft, and F. Holzapfel. L1 adaptive control with eigenstructure assignment for pole placement considering actuator dynamics and delays. *AIAA Scitech Conference*, 2016.

[49] H. Hesse and R. Palacios. Consistent structural linearization in flexible aircraft dynamics with large rigid-body motion. *AIAA*, 2013.

[50] H. Hesse and R. Palacios. Model reduction in flexible-aircraft dynamics with large rigid-body motion. In *Structures, Structural Dynamics, and Materials and Co-located Conferences*. American Institute of Aeronautics and Astronautics, Apr. 2013.

[51] J. Hodgkinson. *Aircraft Handling Qualities*. Blackwell Science Ltd, 1999.

[52] J. Hodgkinson. History of low-order equivalent systems for aircraft flying qualities. *Journal of Guidance, Control, and Dynamics*, 28(4):577–583, July 2005.

[53] J. Hofstee, T. Kier, C. Cerulli, and G. Looye. A variable, fully flexible dynamic response tool for special investigations (varloads). *International Forum for Aeroelasticity and Structural Dynamics*, 2003.

[54] R. H. Hoh, D. G. Mitchell, and J. Hodgkinson. Bandwidth - A Criterion for Highly Augmented Airplanes. In *Criteria for Handling Qualities of Military Aircraft*, number AGARD-CP-333, pages 9–1 – 9–11, apr 1982.

[55] F. Holzapfel, M. Heller, M. Weingartner, G. Sachs, and O. da Costa. Development of control laws for the simulation of a new transport aircraft. *Proceedings of the Institution of Mechanical Engineers, Part G: Journal of Aerospace Engineering*, (223):141, 2009.

[56] F. Hürlimann. *Mass Estimation of Transport Aircraft Wingbox Structures with a CAD/CAE-Based Multidisciplinary Process.* PhD thesis, ETH Zurich, 2010.

[57] International Organization for Standardization. Standard atmosphere. *ISO 2533:1975*, 1975.

[58] A. Isikveren, A. Seitz, P. Vratny, C. Pornet, K. Plötner, and M. Hornung. Conceptual studies of universally-electric systems architectures suitable for transport aircraft. *Deutscher Luft- und Raumfahrtkongress*, 2012.

[59] P. W. Jansen, R. E. Perez, and J. R. R. A. Martins. Aerostructural optimization of nonplanar lifting surfaces. *Journal of Aircraft*, 47(5):1490–1503, 2010.

[60] M. Karpel. Design for active and passive flutter suppression and gust alleviation. Technical report, NASA, 1981.

[61] M. Karpel. Time-domain aeroservoelastic modeling using weighted unsteady aerodynamic forces. *Journal of Guidance, Control, and Dynamics*, 13(1):30–37, Jan. 1990.

[62] M. Karpel and E. Strul. Minimum-state unsteady aerodynamic approximations with flexible constraints. *Journal of Aircraft*, 33(6):1190–1196, November-December 1996.

[63] J. Katz and A. Plotkin. *Low-Speed Aerodynamics.* Cambridge University Press, second edition edition, 2001.

[64] R. Kelm, M. Grabietz, and M. Läpple. *Wing Primary Structure Weight Estimation of Transport Aircrafts in the Pre-development Phase: For Presentation at the 54th Annual Conference of Society of Allied Weight Engineers, Inc., Huntsville, Alabama, 22-24 May 1995.* Society of Allied Weight Engineers, 1995.

[65] G. J. Kennedy and G. W. Kenway. High aspect ratio wing design: Optimal aerostructural tradeoffs for the next generation of materials. *SciTech Conference*, 2014.

[66] T. Kier and C. Reschke. An integrated model for aeroelastic simulation of large flexible aircraft using msc.nastran. 2004-11-22 - 2004-11-24, München. 2004. Proceedings of Virtual Product Development Conference and MSC. Software User Meeting 2004.

[67] T. M. Kier. Varloads: eine simulationsumgebung zur lastenberechnung eines voll flexiblen, freifliegenden flugzeugs. *German Congress of Aeronautical Sciences*, 2004.

[68] T. Klimmek. Parametric Set-Up of a Structural Model for FERMAT Configuration for Aeroelastic Loads Analysis. *ASD Journal*, 2014.

[69] U. Kling, C. Gologan, A. T. Isikveren, and M. Hornung. Aeroelastic investigations of a self trimming non-planar wing. *German Congress of Aeronautical Sciences*, 2013.

[70] K. König and J. Schuler. Integral control of large flexible aircraft. *RTO AVD Specialists Meeting on Structural Aspects of Flexible Aircraft Control, Ottawa 18-20 October 1999, number RTO MP-36. RTO, October 1999.*

[71] I. Kroo. Nonplanar wing concepts for increased aircraft efficiency. *VKI lecture series on Innovative Configurations and Advanced Concepts for Future Civil Aircraft*, 2005.

[72] I. Kroo. *Aircraft Design: Synthesis and Analysis*. Dept. of Aero/Astro, 2010.

[73] N. Li, P. Grant, and H. Abbasi. A comparison of the fixed-axes and the mean-axes modeling methods for flexible aircraft simulation. In *Guidance, Navigation, and Control and Co-located Conferences*. American Institute of Aeronautics and Astronautics, Aug. 2010.

[74] N. X. Li. Modeling of Flexible Aircraft for 3D Motion-Based Flight Simulators. Master's thesis, Universtiy of Toronto, 2010.

[75] R. H. Liebeck. Design of the blended wing body subsonic transport. *Journal of Aircraft*, 41(1):10–25, Jan. 2004.

[76] Lockheed Martin ERA Team. *NASA Environmentally Responsible Aviation, ASM Public Brief.* AIAA, 2012.

[77] G. Looye. Integrated flight mechanics and aeroelastic aircraft modeling using object-oriented modeling techniques. In *Guidance, Navigation, and Control and Co-located Conferences*. American Institute of Aeronautics and Astronautics, Aug. 1999.

[78] G. H. Looye. *An Integrated Approach to Aircraft Modelling and Flight Control Law Design*. PhD thesis, Technische Universiteit Delft, 2008.

[79] T. W. Lukaczyk, A. D. Wendorff, M. Colonno, T. D. Economon, J. J. Alonso, T. H. Orra, and C. Ilario. Suave: An open-source environment for multi-fidelity conceptual vehicle design. In *AIAA Aviation*. American Institute of Aeronautics and Astronautics, June 2015.

[80] R. Maier. ACFA 2020 an FP 7 Project on Active Control of Flexible Fuel Efficient Aircraft Configurations. *4th European Conference for Aerospace Sciences*, 2011.

[81] T. Mauermann. *Flexible Aircraft Modelling for Flight Loads Analysis of Wake Vortex Encounters*. PhD thesis, Technische Universität Carolo-Wilhelmina zu Braunschweig, 2010.

[82] J. McMasters and I. Kroo. Advanced configurations for very large transport airplanes. In *Aerospace Sciences Meetings*. American Institute of Aeronautics and Astronautics, Jan. 1998.

[83] T. Megson. *Aircraft Structures for Engineering Students*. Elsevier Aerospace Engineering, Oxford, United Kingdom, 2007.

[84] L. Meirovitch and I. Tuzcu. The lure of the mean axes. *Journal of Applied Mechanics*, 74(3):497–504, 2006.

[85] L. Meirovitch, I. Tuzcu, L. R. Center, V. P. Institute, and S. University. *Integrated Approach to the Dynamics and Control of Maneuvering Flexible Aircraft*. National Aeronautics and Space Administration, Langley Research Center, 2003.

[86] T. Melin. A vortex lattice matlab implementation for linear aerodynamic wing applications. Master's thesis, Royal Institute of Technology, 2000.

[87] B. Mialon, A. Khrabrov, S. B. Khelil, A. Huebner, A. D. Ronch, K. Badcock, L. Cavagna, P. Eliasson, M. Zhang, S. Ricci, J.-C. Jouhaud, G. Rog. Hitzel, and M. Lahuta. Validation of numerical prediction of dynamic derivatives: The DLR-F12 and the Transcruiser test cases. *Progress in Aerospace Sciences*, 47(8):674 – 694, 2011. Special Issue - Modeling and Simulating Aircraft Stability and Control Special Issue - Modeling and Simulating Aircraft Stability and Control.

[88] R. D. Milne. Dynamics of the Deformable Aeroplane, Parts I and II. *Her Majesty's Stationery Office, Reports and Memoranda No. 3345, London*, 1962.

[89] D. G. Mitchell, D. B. Doman, D. L. Key, D. H. Klyde, D. B. Leggett, D. J. Moorhouse, D. H. Mason, D. L. Raney, and D. K. Schmidt. Evolution, revolution, and challenges of handling qualities. *Journal of Guidance, Control, and Dynamics*, 27(1):12–28, Jan 2004.

[90] D. G. Mitchell, R. H. Hoh, B. L. Aponso, and D. H. Klyde. Proposed Incorporation of Mission-Oriented Flying Qualities into MIL-STD-1797A. *WL-TR-94-3162*, 1994.

[91] J. Murua, R. Palacios, and J. M. R. Graham. Applications of the unsteady vortex-lattice method in aircraft aeroelasticity and flight dynamics. *Progress in Aerospace Sciences*, 2012.

[92] N. M. Newmark. A method of computation for structural dynamics. *Journal of Engineering Mechanics*, 1959.

[93] N. Nguyen and I. Tuzcu. Flight dynamics of flexible aircraft with aeroelastic and inertial force interactions. *American Institute of Aeronautics and Astronautics*, 2009.

[94] P. E. Nikravesh. Understanding mean-axis conditions as floating reference frames. *Advances in Computational Multibody Systems*, 2:185–203, 2005.

[95] A. Ning and I. Kroo. Tip extensions, winglets, and c-wings: Conceptual design and optimization. In *Guidance, Navigation, and Control and Co-located Conferences*. American Institute of Aeronautics and Astronautics, Aug. 2008.

[96] K. I. Ning A. Multidisciplinary considerations in the design of wings and wing tip devices. *Journal of Aircraft*, 47(2):534–543, 2010.

[97] P. A. O. Soviero and F. Hernandes. Compressible unsteady vortex lattice method for arbitrary two-dimensional motion of thin profiles. *Journal of Aircraft*, 44(5):1494–1498, Sept. 2007.

[98] R. Palacios and C. Cesnik. Static nonlinear aeroelasticity of flexible slender wings in compressible flow. In *Structures, Structural Dynamics, and Materials and Co-located Conferences*. American Institute of Aeronautics and Astronautics, Apr. 2005.

[99] R. Palacios and B. Epureanu. An intrinsic description of the nonlinear aeroelasticity of very flexible wings. In *Structures, Structural Dynamics, and Materials and Co-located Conferences*. American Institute of Aeronautics and Astronautics, Apr. 2011.

[100] G. Pinho Chiozzotto. Conceptual design method for the wing weight estimation of strut-braced wing aircraft. In *5th CEAS Air & Space Conference, Delft, The Netherlands*, 2015.

[101] D. P. Raymer. *Aircraft Design: A Conceptual Approach*. AIAA - American Institute Of Aeronautics And Astronautics, 1999.

[102] Report of the High Level Group on Aviation and Aeronautical Research. Flightpath 2050 Europe's Vision for Aviation. 2011.

[103] C. Reschke. Flight loads analysis with inertially coupled equations of motion. In *AIAA Atmospheric Flight Mechanics Conference*, 2005.

[104] C. Reschke. *Integrated Flight Loads Modeling and Analysis for Flexible Transport Aircraft*. PhD thesis, Universitat Stuttgart, 2006.

[105] C. Reschke and G. Looye. Comparison of model integration approaches for flexible aircraft flight dynamics modelling. In *International Forum on Aeroelasticity and Structural Dynamics, Munich*, 2005.

[106] M. Ritter. Nonlinear Numerical Flight Dynamics of Flexible Aircraft in the Time Domain by Coupling of CFD, Flight Mechanics, and Structural Mechanics. In *Notes on Numerical Fluid Mechanics and Multidisciplinary Design*, volume 121, pages 339–347. Springer Berlin Heidelberg, 2013.

[107] K. Roger. Airplane math modelling methods for active control design. *Structural Aspects of Control, AGARD Conference Proceeding*, 9:4.1–4.11, 1977.

[108] J. Schirra and J. Watmuff. Euler based induced drag estimation for highly nonplanar lifting systems during conceptual design. *Deutscher Luft-und Raumfahrtkongress*, 2013.

[109] F. Schuck. *Ein integriertes Auslegungskonzept zur Sicherstellung exzellenter Handling Qualities für Kleinflugzeuge.* Dissertation, Technische Universität München, Mnchen, 2014.

[110] J. Schuler. *Flugregelung und aktive Schwingungsdämpfung für flexible Groaumflugzeuge.* VDI-Verl., Düsseldorf, 1998.

[111] R. C. Schwanz. Formulation of the equations of motion of an elastic aircraft for stability and control and flight control applications. *National Technical Information Service*, 1972.

[112] R. C. Scott, T. J. Allen, C. J. Funk, M. A. Castelluccio, B. W. Sexton, S. Claggett, J. Dykman, D. A. Coulson, and R. E. Bartels. Aeroservoelastic wind-tunnel test of the sugar truss braced wing wind-tunnel model. *American Institute of Aeronautics and Astronautics*, 2015.

[113] A. Seitz, M. Kruse, T. Wunderlich, J. Bold, and L. Heinrich. The DLR Project LamAiR: Design of a NLF Forward Swept Wing for Short and Medium Range Transport Application. *29th AIAA Applied Aerodynamics Conference*, 2011.

[114] K. Seywald. Wingbox mass prediction considering quasi steady aeroelasticity. Master's thesis, Technical University of Munich, 2011.

[115] K. Seywald, N. G. de Paula, A. Wildschek, F. Holzapfel, C. Breitsamter, and M. Förster. Validation of an Aeroelastic Analysis and Simulation Tool for the Assessment of Innovative, Highly Elastic Aircraft Configurations. *Deutscher Luft- und Raumfahrtkongress*, 2014.

[116] K. Seywald, F. Hellmundt., A. Wildschek, and F. Holzapfel. Airworthiness investigation of a highly nonplanar flexible wing concept. *ICAS Conference*, 2014.

[117] K. Seywald, A. Wildschek, and F. Holzapfel. A comparison of modeling methods for the simulation of free flying elastic aircraft. *International Forum on Aeroelasticity and Structural Dynamics*, 2015.

[118] F. J. Silvestre. *Methodology for Modelling the Dynamics of Flexible, High-Aspect-Ratio Aircraft in the Time Domain for Aeroservoelastic Investigations.* PhD thesis, Technische Universität Berlin, 2012.

[119] R. J. Simpson and R. Palacios. Numerical aspects of nonlinear flexible aircraft flight dynamics modeling. In *Structures, Structural Dynamics, and Materials and Co-located Conferences*. American Institute of Aeronautics and Astronautics, Apr. 2013.

[120] R. J. S. Simpson, R. Palacios, and J. Murua. Induced-drag calculations in the unsteady vortex lattice method. *AIAA Journal*, 51(7):1775–1779, May 2013.

[121] T. Theodorsen. General theory of aerodynamic instability and the mechanism of flutter. *NACA TR No. 496*, May 1934.

[122] S. H. Tiffany and W. M. J. Adams. Nonlinear programming extensions to rational function approximations of unsteady aerodynamics. *Proceedings of the AIAA/ASME/ASCE/AHS 28th Structures, Structural Dynamics, and Materials Conference, AIAA, New York*, pages 406–420, 1987.

[123] E. Torenbeek. *Synthesis of Subsonic Airplane Design.* Delf University Press and Kluwer Academic Publishers, 1982.

[124] E. Torenbeek. *Advanced Aircraft Design : Conceptual Design, Technology and Optimization of Subsonic Civil Airplanes.* Wiley, Somerset, 2013.

[125] E. Torenbeek and H. Wittenberg. *Flight Physics: Essentials of Aeronautical Disciplines and Technology, with Historical Notes.* Springer, 2009.

[126] M. Trapani, M. Pleissner, A. Isikveren, and V. Wieczorek, K. Preliminary investigation of a self-trimming non-planar wing using adaptive utilities. *Deutscher Luft- und Raumfahrtkongress*, 2012.

[127] I. Tuzcu. *Dynamics and Control of Flexible Aircraft.* PhD thesis, Virginia Polytechnic Institute and State University, 2001.

[128] U.S. Department of Defense. *Flying Qualities of Piloted Aircraft (MIL-HDBK-1797).*

[129] U.S. Department of Defense. *Military Specification for Flying Qualities of Piloted Airplanes (MIL-F-8785C).*

[130] A. Van der Velden, R. Kelm, D. Kokan, and J. Mertens. Application of MDO to a large subsonic transport aircraft. *38th Aerospace Science Meeting & Exhibit, AIAA 2000-0844*, 2000.

[131] M. R. Waszak, C. S. Buttrill, and D. K. Schmidt. Modeling and model simplification of aeroelastic vehicles. Technical report, NASA, 1992.

[132] M. R. Waszak, J. R. Davidson, and D. K. Schmidt. A simulation study of the flight dynamics of elastic aircraft. *NASA CR-4102*, 1 and 2, December 1987.

[133] M. R. Waszak and D. K. Schmidt. Flight dynamics of aeroelastic vehicles. *Journal of Aircraft*, 25(6):563–571, June 1988.

[134] G. F. P. Wellmer. *A Modular Method for the Direct Coupled Aeroelastic Simulation of Free-Flying Aircraft.* PhD thesis, RWTH Aachen, 2014.

[135] B. A. Winther, P. J. Goggin, and J. R. Dykman. Reduced-order dynamic aeroelastic model development and integration with nonlinear simulation. *Journal of Aircraft*, 37(5):833–839, Sept. 2000.

[136] C. Woernle. *Mehrkörpersysteme: eine Einführung in die Kinematik und Dynamik von Systemen starrer Körper.* Springer-Verlag, 2011.

[137] D. Zenkert. *Lecture Notes: Lightweight Structures and FEM.* Royal Institute of Technology, Stockholm, Sweden., 2009.

A. Derivations

A.1. Finite Beam Element Governing Equations

This section details the structural finite element model as also presented in [114]. For the wing beam model a fully three-dimensional beam element is selected, which results in six degrees of freedom (DOFs) per node, three translational DOFs and three rotational DOFs. Bending about the x and z-axis is assumed to be uncoupled, since coupled bending only occurs for asymmetric cross-sections whereas the considered cross-section model is fully symmetric. For a possible asymmetric extension of the cross-section model this fact should be kept in mind. For swept wings however the effect due to sweep is expected to outrange the effect of skew bending due to asymmetric cross-sections. The displacement vector for an element is

$$\underline{u}_e = (\delta_{x1}, \delta_{y1}, \delta_{z1}, \delta_{\epsilon x1}, \delta_{\epsilon y1}, \delta_{\epsilon z1}, \delta_{x2}, \delta_{y2}, \delta_{z2}, \delta_{\epsilon x2}, \delta_{\epsilon y2}, \delta_{\epsilon z2}) \tag{A.1}$$

where the indices 1 and 2 denote the two element nodes, δ denotes displacements, δ_ϵ denotes rotational displacements. The force vector for one element is

$$\underline{f}_e = (Q_{x1}, N_{y1}, Q_{z1}, M_{x1}, M_{T1}, M_{z1}, Q_{x2}, N_{y2}, Q_{z2}, M_{x2}, M_{T2}, M_{z2}) \tag{A.2}$$

where Q denotes transverse forces, N denotes the normal forces and M denotes moments. The structural analysis is implemented as a classical stiffness method. This implies that for the entire structure the nodal forces and nodal displacements are related through a stiffness matrix $\underline{K}$ [137]. The global system is determined by the relationship

$$\underline{f} = \underline{K} \cdot \underline{u} \tag{A.3}$$

where $\underline{f}$ is the global force vector and $\underline{u}$ is the global displacement vector. The global stiffness matrix $\underline{K}$ is obtained by assembly of single element stiffness matrices $\underline{K}_e$ in the following scheme

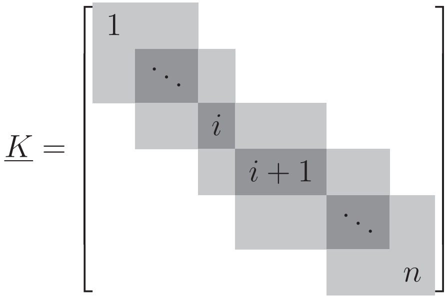

(A.4)

where one block represents a 12x12 element stiffness matrix for the element in between node i and node $i+1$.
The element stiffness matrix can be derived by discretization of the weak form of the differential equations. The stiffness matrix $\underline{K}_e^{loc}$ for the local beam element then becomes:

$$\underline{K}_e^{loc} = \begin{bmatrix} \frac{12EI_z}{l^3} & 0 & 0 & 0 & 0 & -\frac{6EI_z}{l^2} & -\frac{12EI_z}{l^3} & 0 & 0 & 0 & 0 & -\frac{6EI_z}{l^2} \\ 0 & \frac{EA}{l} & 0 & 0 & 0 & 0 & 0 & -\frac{EA}{l} & 0 & 0 & 0 & 0 \\ 0 & 0 & \frac{12EI_x}{l^3} & -\frac{6EI_x}{l^2} & 0 & 0 & 0 & 0 & -\frac{12EI_x}{l^3} & -\frac{6EI_x}{l^2} & 0 & 0 \\ 0 & 0 & -\frac{6EI_x}{l^2} & \frac{4EI_x}{l} & 0 & 0 & 0 & 0 & \frac{6EI_x}{l^2} & \frac{2EI_x}{l} & 0 & 0 \\ 0 & 0 & 0 & 0 & \frac{GJ}{l} & 0 & 0 & 0 & 0 & 0 & -\frac{GJ}{l} & 0 \\ -\frac{6EI_z}{l^2} & 0 & 0 & 0 & 0 & \frac{4EI_z}{l} & \frac{6EI_z}{l^2} & 0 & 0 & 0 & 0 & \frac{2EI_z}{l} \\ -\frac{12EI_z}{l^3} & 0 & 0 & 0 & 0 & \frac{6EI_z}{l^2} & \frac{12EI_z}{l^3} & 0 & 0 & 0 & 0 & \frac{6EI_z}{l^2} \\ 0 & -\frac{EA}{l} & 0 & 0 & 0 & 0 & 0 & \frac{EA}{l} & 0 & 0 & 0 & 0 \\ 0 & 0 & -\frac{12EI_x}{l^3} & \frac{6EI_x}{l^2} & 0 & 0 & 0 & 0 & \frac{12EI_x}{l^3} & \frac{6EI_x}{l^2} & 0 & 0 \\ 0 & 0 & -\frac{6EI_x}{l^2} & \frac{2EI_x}{l} & 0 & 0 & 0 & 0 & \frac{6EI_x}{l^2} & \frac{4EI_x}{l} & 0 & 0 \\ 0 & 0 & 0 & 0 & -\frac{GJ}{l} & 0 & 0 & 0 & 0 & 0 & \frac{GJ}{l} & 0 \\ -\frac{6EI_z}{l^2} & 0 & 0 & 0 & 0 & \frac{2EI_z}{l} & \frac{6EI_z}{l^2} & 0 & 0 & 0 & 0 & \frac{4EI_z}{l} \end{bmatrix} \tag{A.5}$$

The element stiffness matrix is given in element local coordinates, hence if the local element coordinates deviate from the global system coordinates a transformation has to be performed. Before $\underline{K}$ and $\underline{f}$ can be assembled all matrices and forces must be transformed into one global coordinate system. The rotation matrix $\underline{T}$ transforms the element stiffness matrix into global coordinates.

$$\underline{K}_e^{glob} = \underline{T}^T \underline{K}_e^{loc} \underline{T} \tag{A.6}$$

The same transformation matrix is valid for the transformation from the local element force vector into the global element force vector.

$$\underline{f}_e^{glob} = \underline{T}^T \underline{f}_e^{loc} \tag{A.7}$$

Before the assembled system can be solved all desired boundary conditions need to be incorporated. For simple boundary conditions the nodal deflection $\underline{u}_i$ is set to zero. This is done by deleting the respective row i and column i from $\underline{K}$ to obtain the structural stiffness matrix $\underline{K}_f$ and deleting row i from $\underline{f}$ to get $\underline{f}_f$. The linear system for the free nodes is then solved by matrix inversion of $\underline{K}_f$:

$$\underline{u}_f = \underline{K}_f^{-1} \underline{f}_f \tag{A.8}$$

For dynamic analysis further the mass matrix is required which is given either by

$$\underline{M}^{loc}_{e,\text{lumped}} = \frac{m}{2} \begin{bmatrix} 1 & 0 & 0 & 0 & 0 & 0 & 0 & 0 & 0 & 0 & 0 & 0 \\ 0 & 1 & 0 & 0 & 0 & 0 & 0 & 0 & 0 & 0 & 0 & 0 \\ 0 & 0 & 1 & 0 & 0 & 0 & 0 & 0 & 0 & 0 & 0 & 0 \\ 0 & 0 & 0 & 0 & 0 & 0 & 0 & 0 & 0 & 0 & 0 & 0 \\ 0 & 0 & 0 & 0 & \frac{\rho J l_e}{m} & 0 & 0 & 0 & 0 & 0 & 0 & 0 \\ 0 & 0 & 0 & 0 & 0 & 0 & 0 & 0 & 0 & 0 & 0 & 0 \\ 0 & 0 & 0 & 0 & 0 & 0 & 1 & 0 & 0 & 0 & 0 & 0 \\ 0 & 0 & 0 & 0 & 0 & 0 & 0 & 1 & 0 & 0 & 0 & 0 \\ 0 & 0 & 0 & 0 & 0 & 0 & 0 & 0 & 1 & 0 & 0 & 0 \\ 0 & 0 & 0 & 0 & 0 & 0 & 0 & 0 & 0 & 0 & 0 & 0 \\ 0 & 0 & 0 & 0 & 0 & 0 & 0 & 0 & 0 & 0 & \frac{\rho J l_e}{m} & 0 \\ 0 & 0 & 0 & 0 & 0 & 0 & 0 & 0 & 0 & 0 & 0 & 0 \end{bmatrix} \tag{A.9}$$

or by

$$\underline{M}^{loc}_{e,\text{consitent}} = \frac{m}{420} \begin{bmatrix} 156 & 0 & 0 & 0 & 0 & -22l_e & 54 & 0 & 0 & 0 & 0 & 13l_e \\ 0 & 140 & 0 & 0 & 0 & 0 & 0 & 70 & 0 & 0 & 0 & 0 \\ 0 & 0 & 156 & 22l_e & 0 & 0 & 0 & 0 & 54 & -13l_e & 0 & 0 \\ 0 & 0 & 22l_e & 4{l_e}^2 & 0 & 0 & 0 & 0 & 13l_e & -3{l_e}^2 & 0 & 0 \\ 0 & 0 & 0 & 0 & \frac{\rho J l_e 420}{3m} & 0 & 0 & 0 & 0 & 0 & \frac{\rho J l_e 420}{6m} & 0 \\ -22l_e & 0 & 0 & 0 & 0 & 4{l_e}^2 & -13l_e & 0 & 0 & 0 & 0 & -3{l_e}^2 \\ 54 & 0 & 0 & 0 & 0 & -13l_e & 156 & 0 & 0 & 0 & 0 & 22l_e \\ 0 & 70 & 0 & 0 & 0 & 0 & 0 & 140 & 0 & 0 & 0 & 0 \\ 0 & 0 & 54 & 13l_e & 0 & 0 & 0 & 0 & 156 & -22l_e & 0 & 0 \\ 0 & 0 & -13l_e & -3{l_e}^2 & 0 & 0 & 0 & 0 & -22l_e & 4{l_e}^2 & 0 & 0 \\ 0 & 0 & 0 & 0 & \frac{\rho J l_e 420}{6m} & 0 & 0 & 0 & 0 & 0 & \frac{\rho J l_e 420}{3m} & 0 \\ 13l_e & 0 & 0 & 0 & 0 & -3{l_e}^2 & 22l_e & 0 & 0 & 0 & 0 & 4{l_e}^2 \end{bmatrix} \tag{A.10}$$

using a formulation consistent to the stiffness matrix.

B. Additional Graphs

B.1. Nichols Diagrams

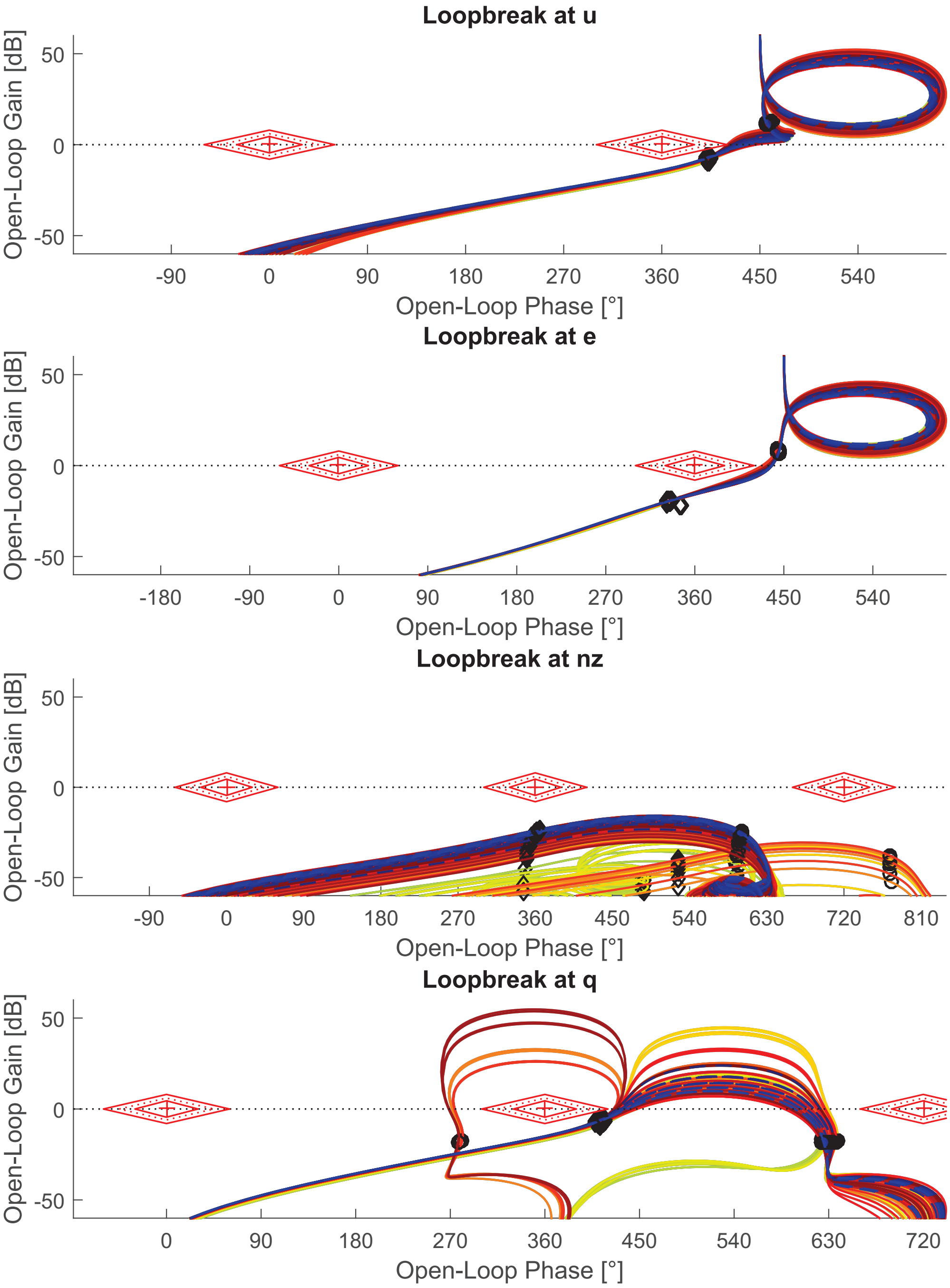

Figure B.1. – Nichols Diagram for Longitudinal Controller

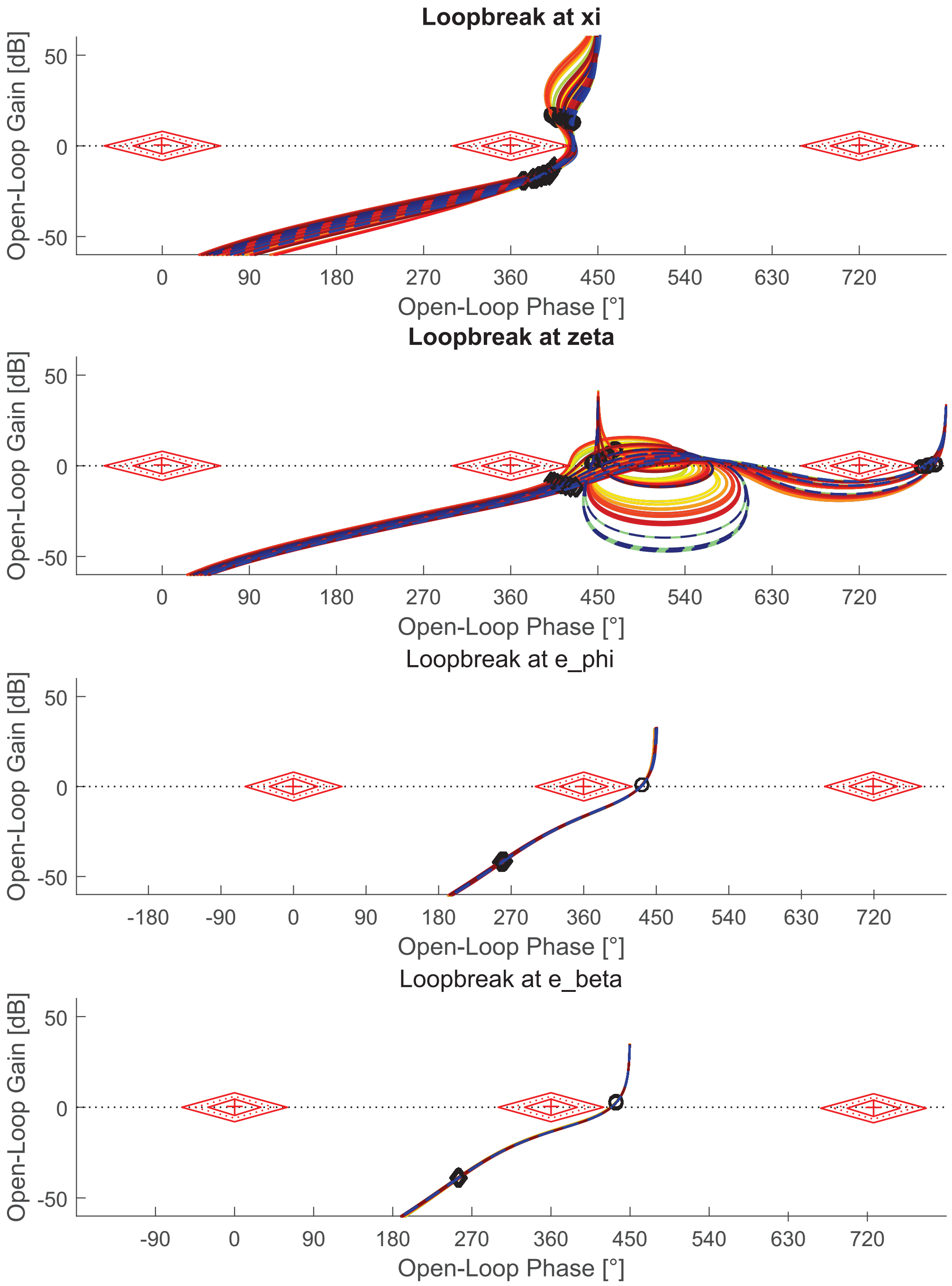

Figure B.2. – Nichols Diagram for Lateral Controller

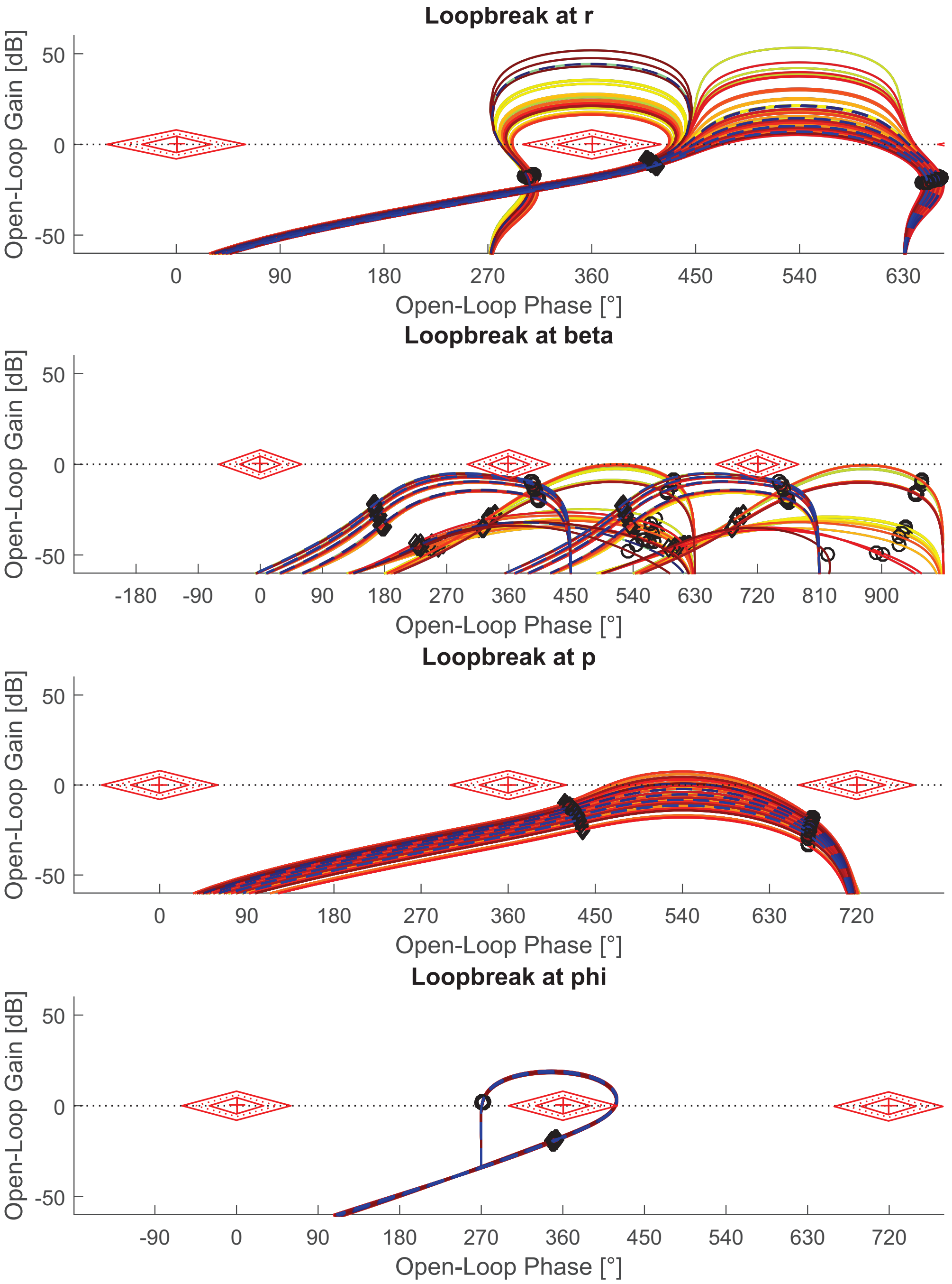

Figure B.3. – Nichols Diagram for Lateral Controller

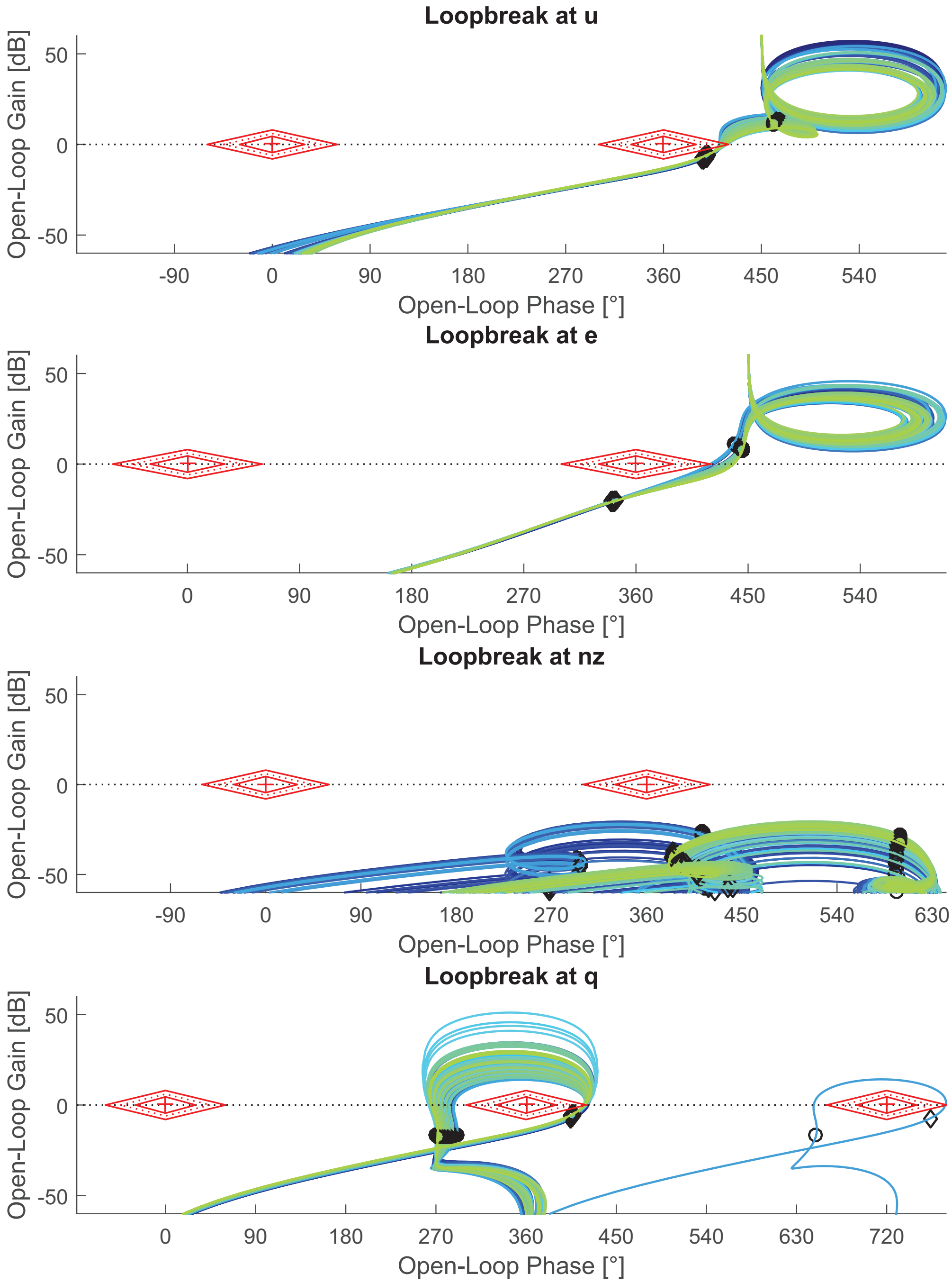

Figure B.4. – Nichols Diagram for Longitudinal Controller

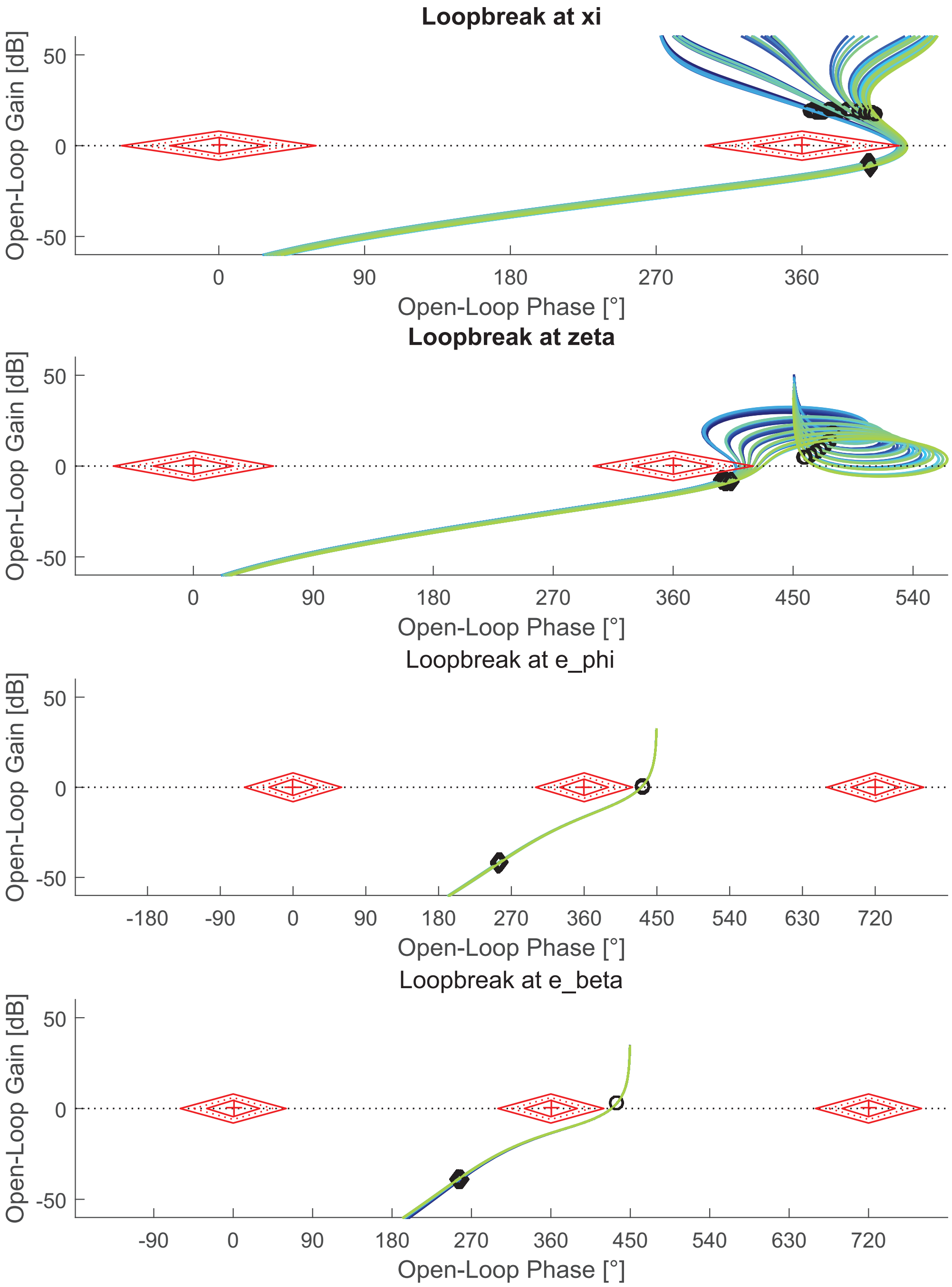

Loopbreak at xi

Loopbreak at zeta

Loopbreak at e_phi

Loopbreak at e_beta

Figure B.5. – Nichols Diagram for Lateral Controller

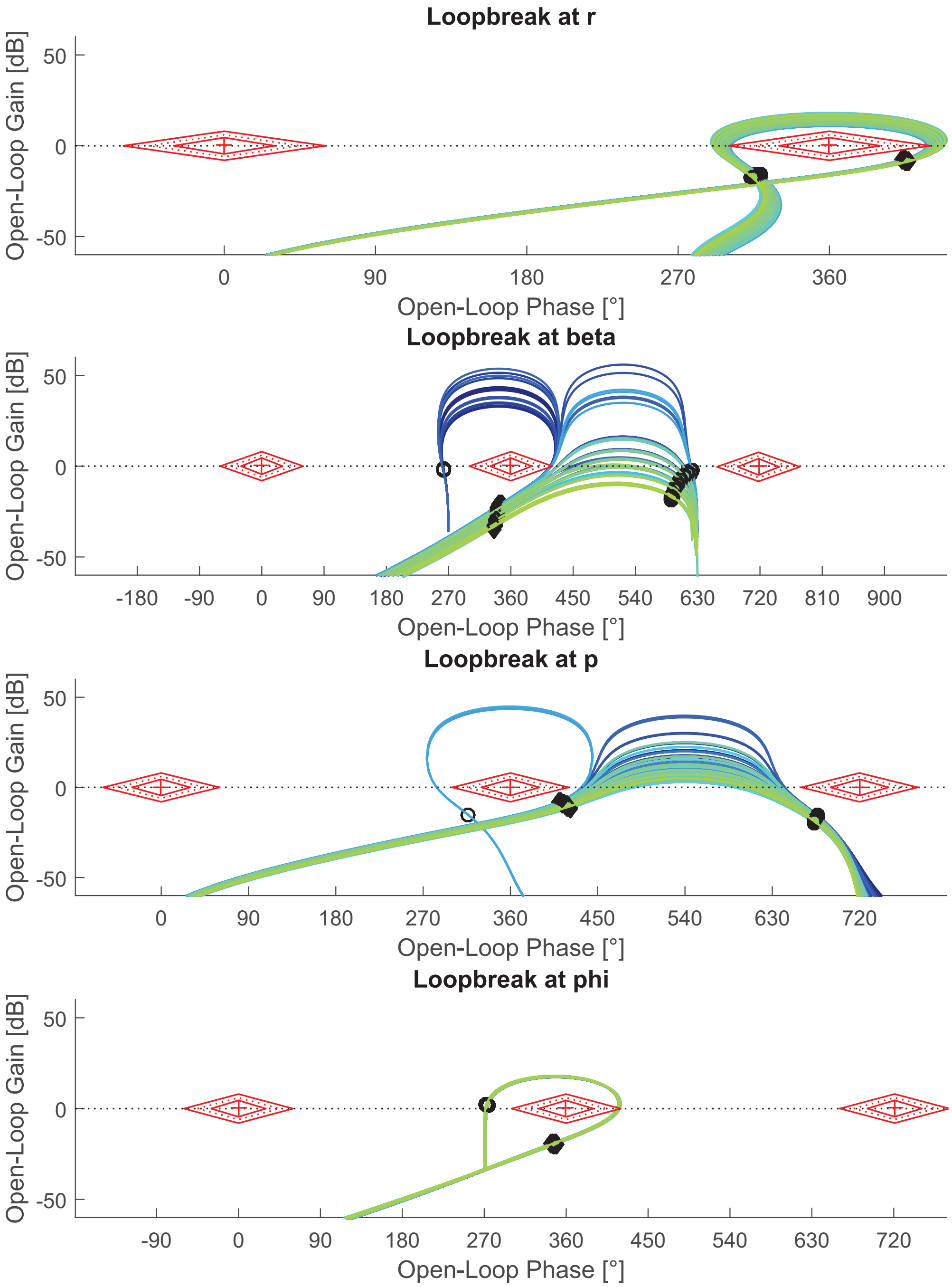

Figure B.6. – Nichols Diagram for Lateral Controller

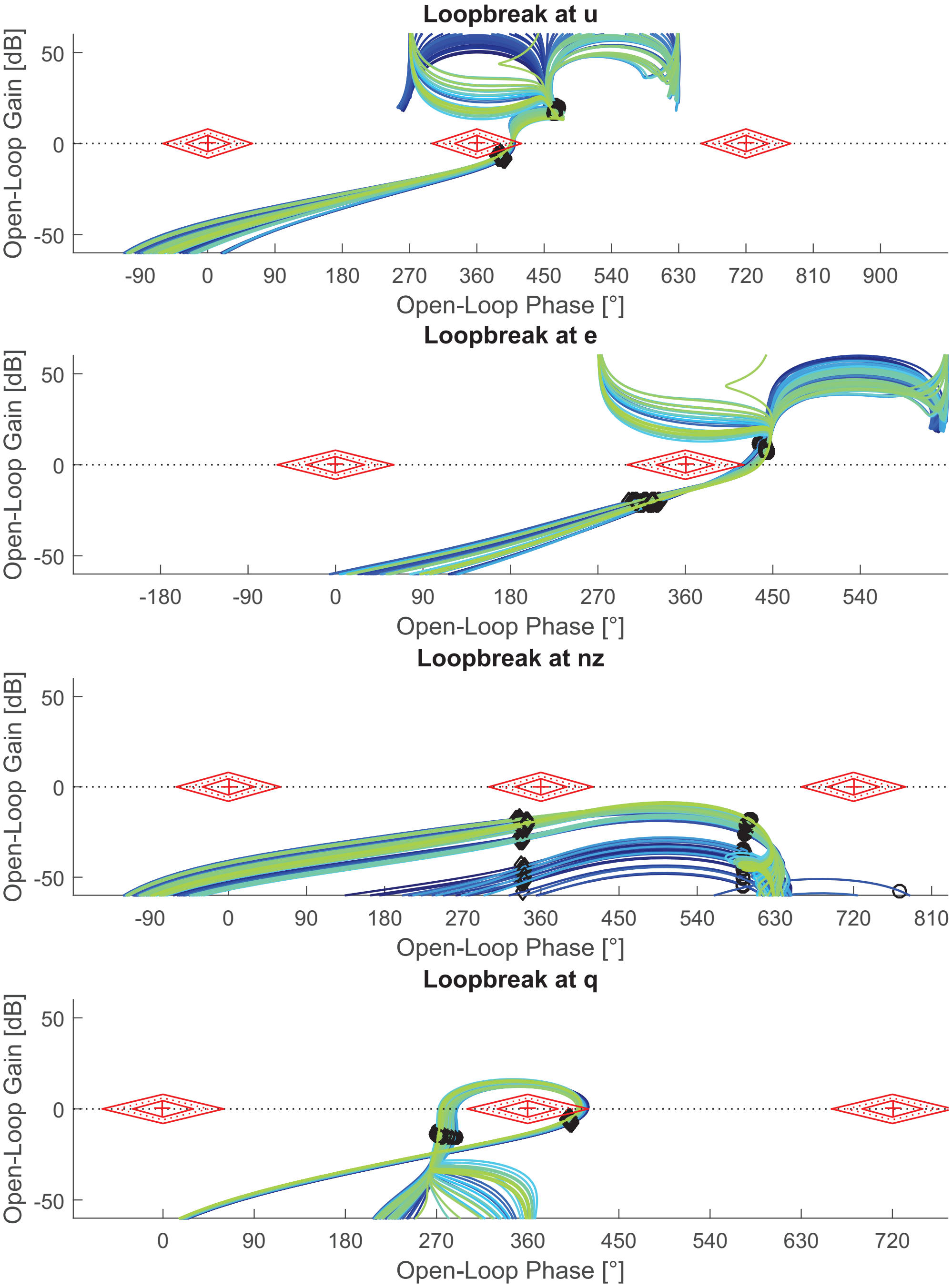

Figure B.7. – Nichols Diagram for Longitudinal Controller

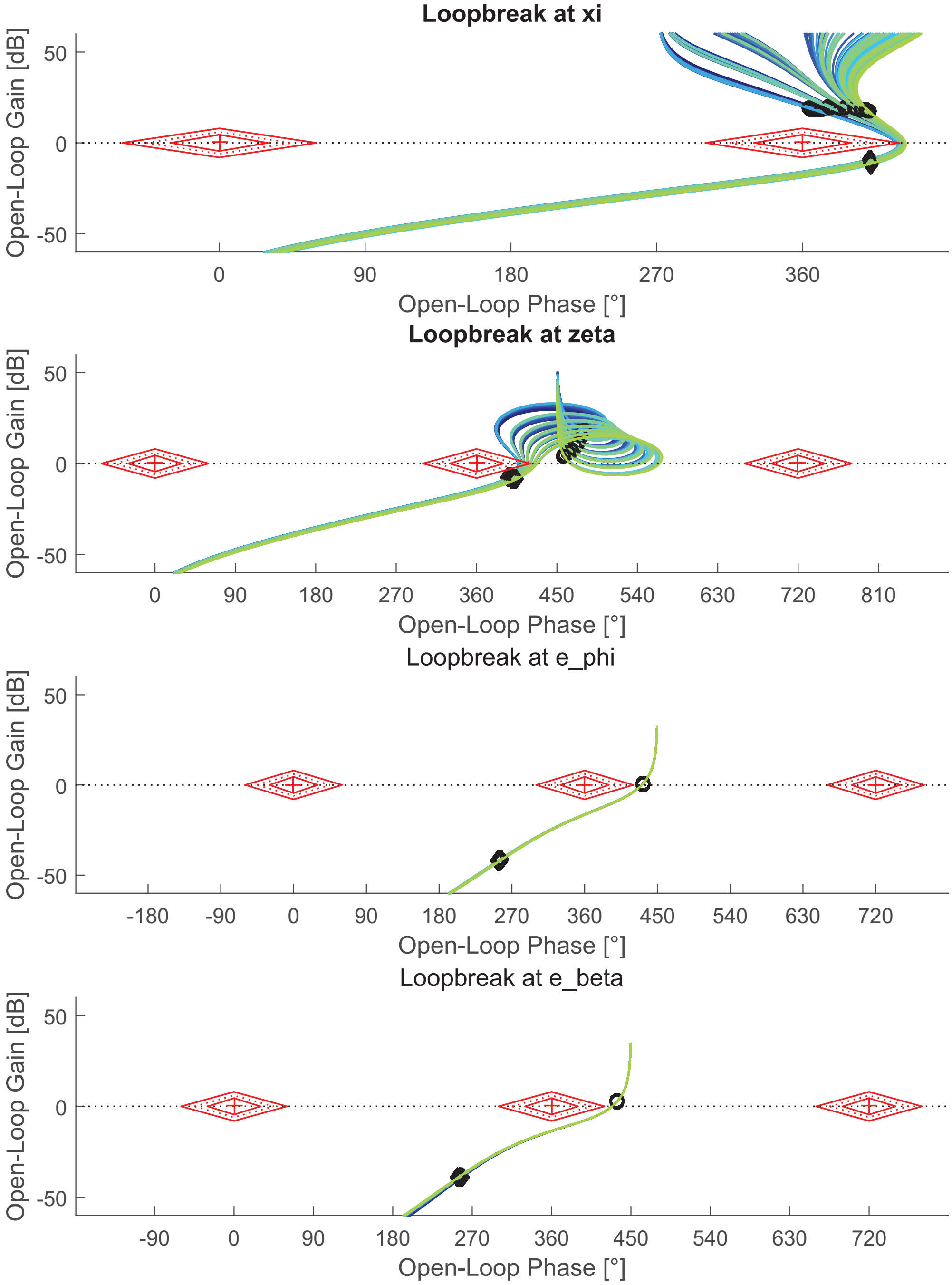

Figure B.8. – Nichols Diagram for Lateral Controller

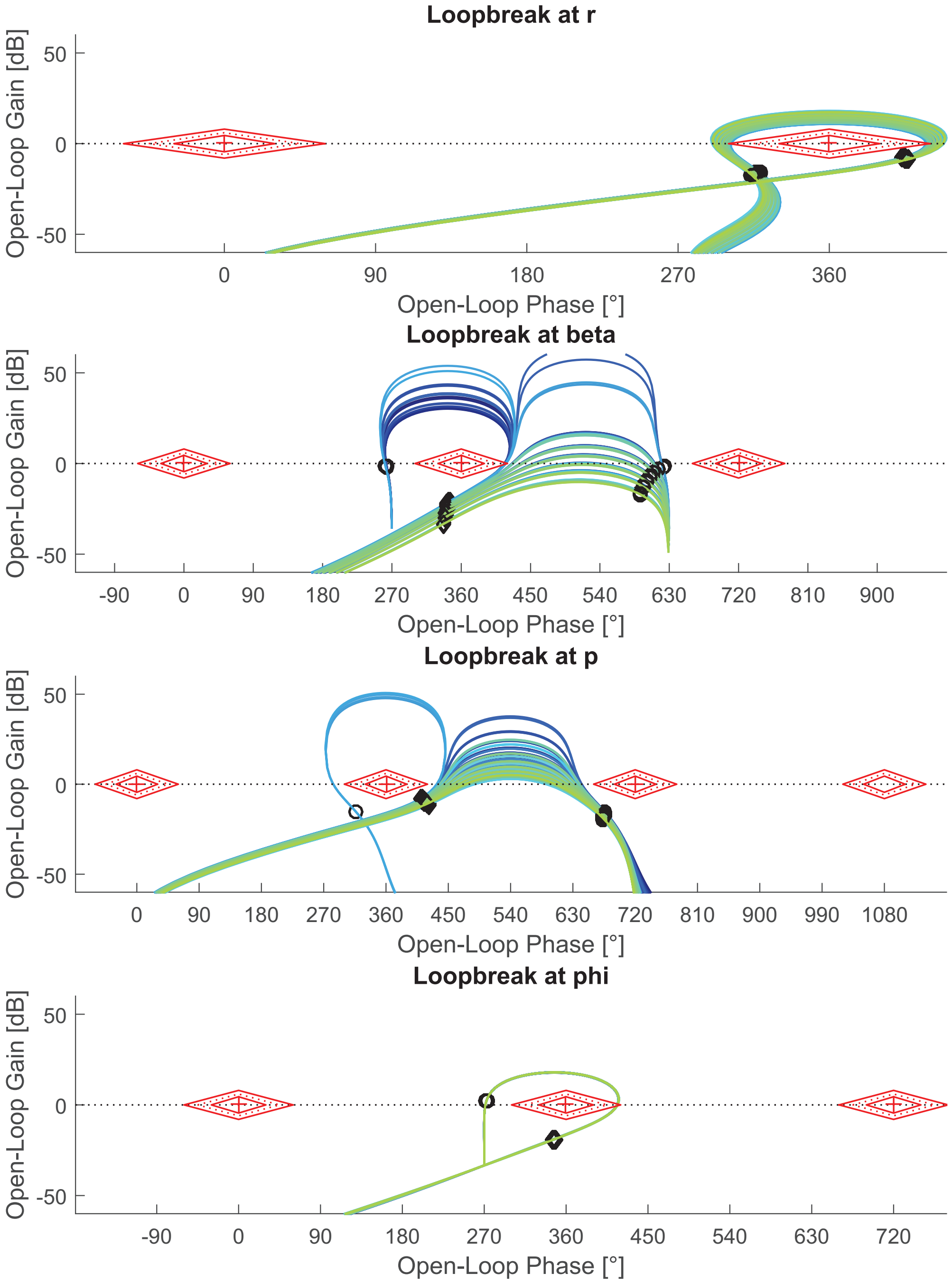

Figure B.9. – Nichols Diagram for Lateral Controller

C. Model Validation and Verification

This section shows the validation and verification of the implemented models. At first the different reference geometries are described and then the different parts of the code are validated. At first the structural and the aerodynamic models are validated separately to ensure the correct implementation of the respective equations. Finally the coupled aeroelastic model is validated.

C.1. Reference Geometries

C.1.1. 2D Airfoil

The most basic geometry used for validation is a two dimensional flat airfoil. The pitching axis is placed at 30% of the chord and the hinge axis of the control surface is placed at 70% of the chord as depicted in Figure C.1

Figure C.1. – 2D Aerofoil Validation Case

C.1.2. FlexOP Aircraft

The next validation geometry comprises a simplified aircraft including a high aspect ratio wing and a V-tail as shown in C.2.

C.2. Validation of the Structural Finite Element Code

In this section the validation of the applied structural finite element code is presented.

C.2.1. Structural Modes

The modal frequencies and shapes are computed with the implemented method and with the commercial finite element code MSC.Nastran for the wing model of the geometry

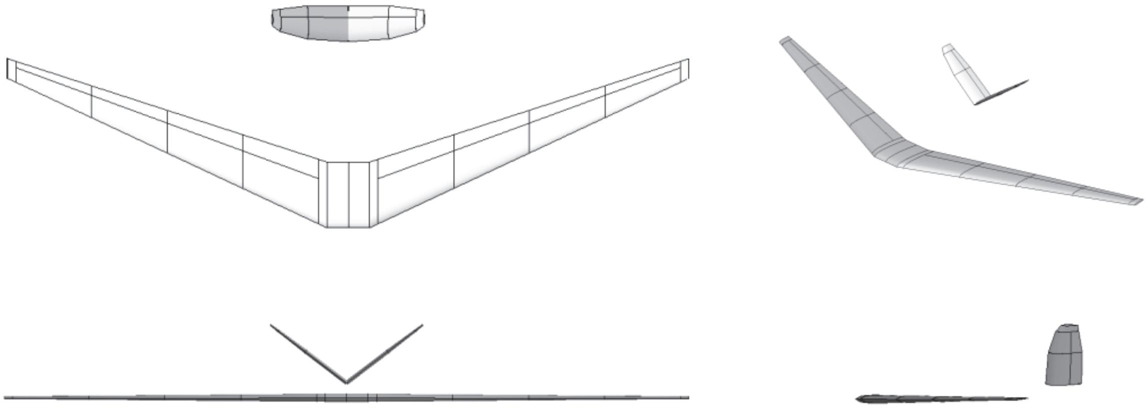

Figure C.2. – Validation Geometry (FLEXOP UAV Demonstrator)

shown in Section C.1.2. Table C.1 shows the computed modal frequencies for the lumped and consistent mass matrix shown in Section A.1. The modes match almost exactly with the modes obtained from Nastran, which proves the correctness of the implemented code. Particularly it can be concluded that both the mass matrix and the stiffness matrix are correct, why a separate validation of the deformations is not shown here.

Table C.1. – Validation of the Modal Frequencies

	dAEDalusNXT		*Nastran*		*Difference*	
Mass Matrix	*consistent*	*lumped*	*consistent*	*lumped*	*consistent*	*lumped*
Unit	*Hz*	*Hz*	*Hz*	*Hz*	*%*	*%*
1	4.7183	4.7168	4.7196	4.7182	-0.03	-0.03
2	6.4201	6.4182	6.4217	6.4198	-0.03	-0.03
3	14.1174	14.1129	14.1180	14.1135	0.00	0.00
4	20.3158	20.3076	20.3178	20.3097	-0.01	-0.01
5	30.9183	30.9220	30.9275	30.9312	-0.03	-0.03
6	45.3032	45.2997	45.2961	45.2926	0.02	0.02
7	52.7709	52.7343	52.8087	52.7719	-0.07	-0.07
8	78.7312	78.6536	78.7846	78.7069	-0.07	-0.07
9	82.3297	82.3508	82.3386	82.3598	-0.01	-0.01
10	123.1641	123.1612	123.3066	123.3028	-0.12	-0.11

C.2.2. Validation of Free Flying Structure

C.3. Aerodynamic Model Validation

This section presents validation results for the aerodynamic models. The VLM and the UVLM were validated separately.

C.3.1. Vortex Lattice Method

The results of the implemented vortex lattice code were compared to the results of NeoCass [26] for the same geometry using an equivalent discretization in both codes shown in Figure C.3. The case is compute for $Ma = 0.55$ and $\alpha = 5°$ using a Prandtl-Glauert correction. It can be seen that the results match well and the difference is smaller than 2.5% for all aerodynamic derivatives except for derivatives with respect to the yawing rate $\mathbf{r}$. The error may result from the different implementation of the wing twist in both codes.

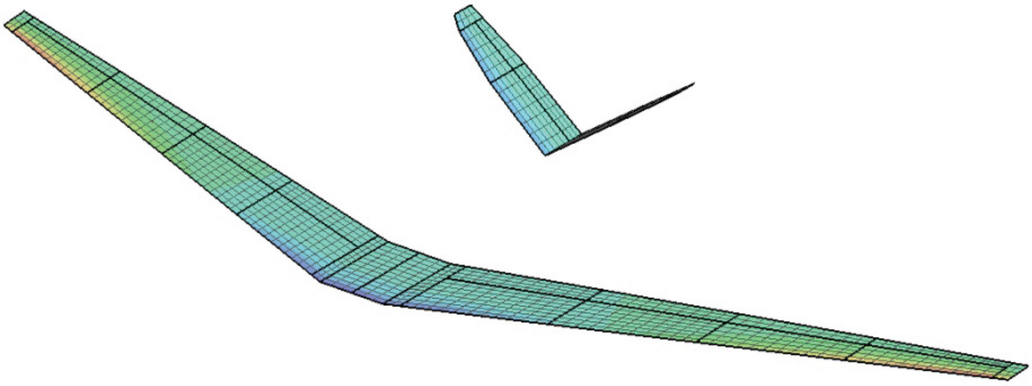

Figure C.3. – Pressure Distribution for Validation Case

C.3.2. Unsteady Vortex Lattice Method

The next step of the validation is the unsteady aerodynamic method, which at first is validated independently of the structure. Generalized aerodynamic forces were computed applying the UVLM, computing the time marching solution of the respective harmonic excitation for a range of reduced frequencies. The time transient generalized aerodynamic forces are then Fourier transformed. It was found that the wake rollup procedure commonly applied for the UVLM has little effect on the results, why this procedure was omitted for all presented computations.

Table C.2. – Validation of the VLM

Derivative	*NeoCass*	*dAEDalusNXT*	*% error*
C_Z	0.3954	0.3961	-0.177
C_m	-0.0249	-0.0244	2.01
$C_{Z\alpha}$	5.7902	5.8563	-1.142
$C_{m\alpha}$	-0.6077	-0.5931	2.402
$C_{Y\beta}$	-0.1969	-0.194	1.47
$C_{N\beta}$	-0.067	-0.0668	0.299
$C_{L\mathbf{p}}$	-1.9976	-2.0001	-0.125
$C_{Z\mathbf{q}}$	3.958	4.0036	-1.152
$C_{m\mathbf{q}}$	-3.1759	-3.2	-0.765
$C_{y\mathbf{r}}$	-0.1668	-0.1591	4.616
$C_{N\mathbf{r}}$	-0.0619	-0.0585	5.492

C.3.2.1. 2D Aerofoils

At first the results of the UVLM are benchmarked against the analytical solutions of Theodorsen [121] for the unsteady lift and pitching moment, and the analytical solution of Garrick [39] for the induced drag. In order to apply the 3D implementation of the UVLM to a 2D problem a rectangular wing with a large aspect ratio was modeled.

Plunging and Pitching Motion The results of the lift and pitching moment coefficient are shown in Figure C.4over a range of reduced frequencies from $k = 0$ to $k = 2$. The results agree well but the difference tends to increase with increasing k. A reason for this can be the assumed fixed wake in the derivation of the Theodorsen function.

Control Surface The results of the lift and pitching moment coefficient due to an oscillating control surface are shown in Figure C.5 over a range of reduced frequencies from k=0 to k=2. The results again agree well with the analytical solutions.

Induced Drag This section show the validation of the unsteady induced drag. Figure C.6 shows unsteady induced drag for a heave and pitch motion for two different reduced frequencies. It can be seen that a good match could be obtained compared to the analytical solution of Garrick [39].

C.3.2.2. 3D Geometry

Next the results of the UVLM are benchmarked for a three dimensional geometry. The results of the GAFs for the first two elastic modes of the FLEXOP configuration are shown in Figure C.7 over a range of reduced frequencies from k=0 to k=2 and compared to the commercial code MSC.Nastran and the open source tool NeoCASS which both implement a DLM method. It can be seen that a good match for the GAFs could be obtained for Ma = 0.15 over all reduced frequencies. Figure C.8 shows the same GAFs for Ma=0.5. It can be seen that the approximation of the Mach number correction applied for the UVLM works relatively well for low reduced frequencies but that the absolute error increases with increasing reduced frequencies.

C.4. Validation of the Coupled Aeroelastic Model

This section presents the validation of the coupled aeroelastic model. First the conservative force transfer is validated, next static aeroelastic trim computations are validated and finally the dynamic model is validated by gust response simulations and dynamic response simulations.

C.4.1. Validation of Conservative force transfer

The conservative force transfer is validated by simulating pitch maneuvers. First a simple 6DoF standard flight simulation for the rigid aircraft is performed using a aerodynamic data table generated from the VLM method presented in this work. Then the same simulation is performed with the full DoF flexible aircraft direct time domain model implementing the fixed-axis equations. The structure is artificially stiffened by setting the moments of inertia to sufficiently large values. Figure C.9 presents the simulation results. The pitch response following an elevator doublet shows a an excellent match comparing the simple 6DoF model based on VLM aerodynamic coefficients and the artificially stiffened flexible model using the force transformation matrix from Section 2.2.2. The fixed axis simulation was performed twice, choosing two different nodes, one located at the front fuselage and one located at the wingtip. The simulation results should be independent of the choice of the fixed node. This validates the force transformation matrix and the implementation of the fixed-axis equations of motion.

C.4.2. Steady Aeroelastic Coupling

The steady aeroelastic model is validated by computing the same cases with MSC.Nastran and dAEDalusNXT. The structural sizing is performed with dAEDalusNXT and then the obtained structure and aerodynamic grid is written into respective Nastran and NeoCass input cards [16]. All tools are able to perform aeroelastic trimming of the model. For the following computations the fuselage was assumed rigid, in order to reduce the complexity. For the validation a trim solution is performed in applying the same structural model and aerodynamic grid in all tools. Figure C.10 and Figure C.11 show the resulting vertical and torsional displacements in all tools for a cruise flight case for the CC.

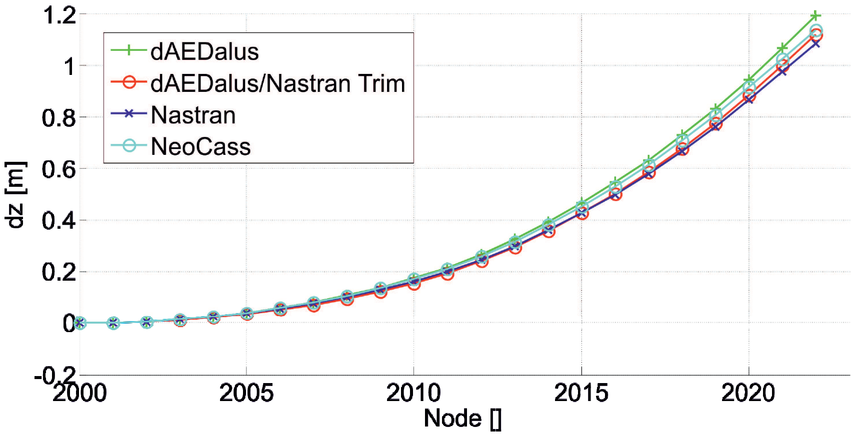

Figure C.10. – Trim Solution, z Displacement Ma=0.76, h=8000m

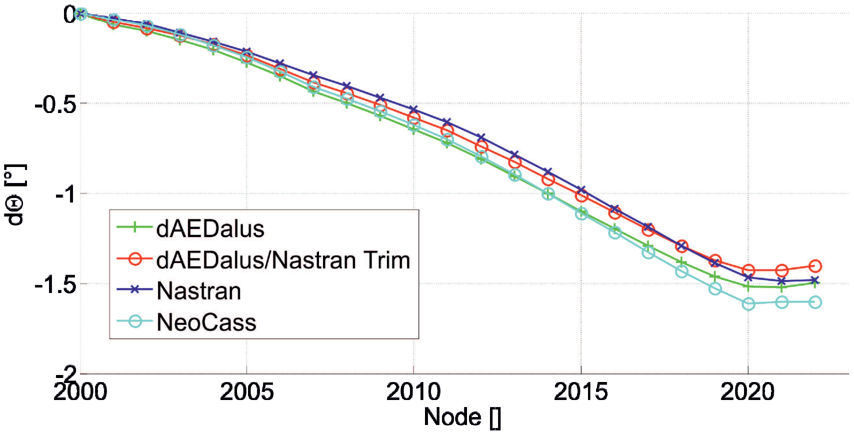

Figure C.11. – Trim Solution, Torsional Displacement Ma=0.76, h=8000m

A difference can be noticed in between the tools, which result from differences in the applied methods and implementation:

- MSC.Nastran performs trimming, based on the derivatives determined at the reference point at zero angle of attack. Further twist, camber and control surface deflections are not considered in the mesh, which remains flat, and therefore do not influence the derivatives [16]. Named effects can only be considered by additional downwash velocities at the collocation points. This shortcoming of MSC.Nastran was also noted in [26], p. 24 when comparing aerodynamic derivatives. NeoCass considers the named effects and therefore is closer to the dAEDalusNXT trim result. dAEDalusNXT recomputes and updates the deformations, control surface deflections and derivatives after every trim iteration, resulting in a more accurate trim solution. dAEDalusNXT and NeoCass VLM also adjust the wake to the free stream velocity, the Nastran DLM does not model the wake.

- Based on the derivatives, which differ due to named reasons the acceleration and following the inertial relief is computed. This further increases the difference in loads and deflections. The named inertial relief effect was removed in dAEDalusNXT by using the MSC.Nastran trim results instead of the originally obtained ones. It can be seen in Figure C.10 and Figure C.11 that the result moves significantly closer to the Nastran solution, now showing a much better match of the deflections.

- Remaining differences can be explained by different aeroelastic coupling and splining approaches in all tools.

C.4.3. Dynamic Aeroelasticity

C.4.3.1. Gust Response

Finally the gust response is compared between MSC.Nastran and dAEDalusNXT. This validates the dynamic aerostructural coupling, since both the unsteady structural model and the unsteady aerodynamic model are involved. Furthermore the Newmark-Beta time integration scheme is validated by the following computations. The UVLM computes the steady and unsteady part of the aerodynamic forces, hence to allow the comparison with MSC.Nastran the steady part of the signal was removed from the solution. The presented values are deviations from a trimmed cruise case, since the DLM only allows the computation of deviations. Additionally reduced order models (ROM) of the aeroelastic model were generated using the generalized aerodynamic forces, stiffness and mass matrix determined in dAEDalusNXT. Applying Rogers approximation and Karpels minimum state method (MSA) reduced order state space models (SSM) of the elastic vehicle are computed. The presented ROMs include ten and twenty structural modes, while all higher frequency modes are truncated. The computations were performed for four different 1-cos gusts from taken EASA CS-25 definitions [37] which are shown in Figure C.12. The obtained results are shown in Figure C.13. Generally a good agreement can be seen between the MSC.Nastran solution and the loosely coupled FE-UVLM time domain approach. Furthermore the reduced order state space models appear to agree very good with the full order model. The worse matching results for the shortest gust length for the ROMs results from the low number of modes, hence a higher frequency excitation can't be modeled fully due to the missing modes.

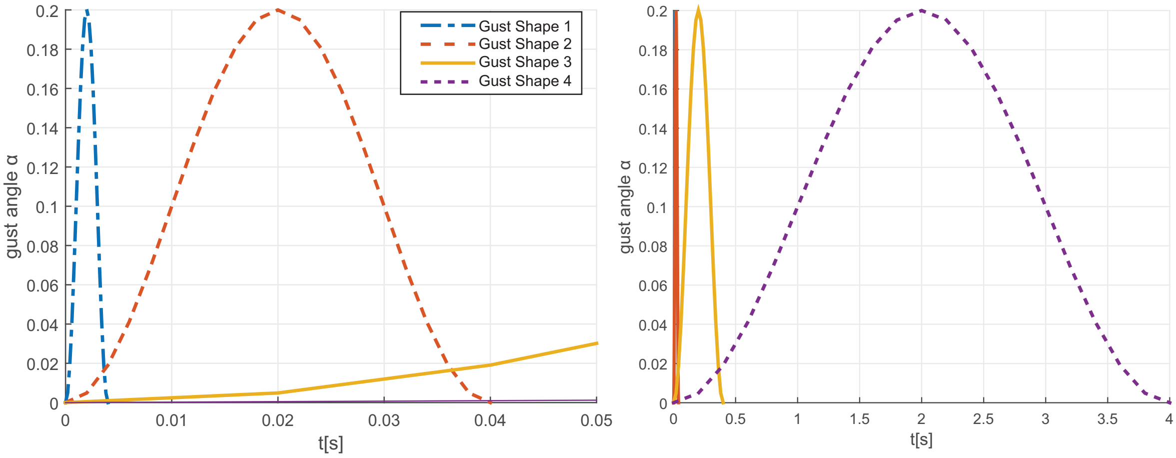

Figure C.12. – Gust Shapes

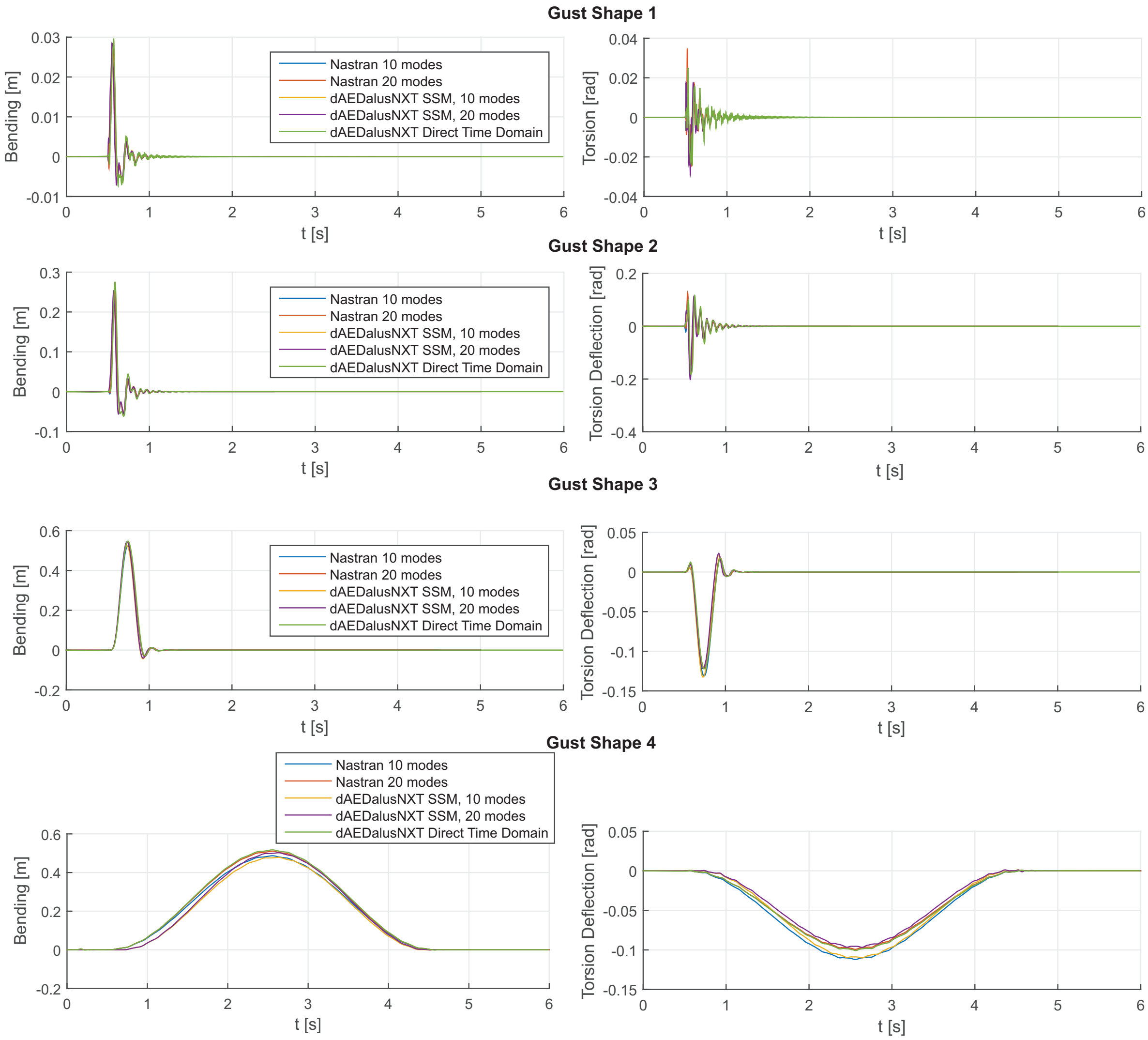

Figure C.13. – Wing Bending and Torsion Deflections due to different Gust Shapes

C.4.4. Validation of the Modal Reduction

The validation of the modal reduction can be seen in Figure C.14 and Figure C.15 where the aircraft response, of the configuration shown in Figure 2.1, is shown for a pitch and a roll doublet input. The responses are presented for the full DoF model (DTM, fixed axis), for 24 modes using a standard truncation (DTM, mean-axis 24 modes, standard-truncation) and for 24 modes using the load case sensitive (LS) truncation (DTM, mean-axis 24 modes, LS-truncation). It can be seen that the LS-truncation matches the full order system slightly better. Furthermore it can be seen that using the fast time model and the thereby introduced approximations result in an additional error in the response (FTM - LS-truncation).

C.4.5. Validation of the Aeroelastic State Space Model

The aeroelastic state space model for a restrained structure is already validated in Section C.4.3.1, where gust responses of the dAEDalusNXT generated state space models were compared to the dAEDalusNXT direct time marching scheme and MSC.Nastran gust simulation results. In addition the aeroelastic State Space Model (SSM) was validated in the free-flying fast time simulation. Figure C.16 shows a simulation using a pitch doublet excitation of the flexible aircraft for the direct time domain method (DTM, cp. Section 2.5) and the fast time simulation model (FTM ,cp. Section 2.6). It can be seen that the modal deformations for both simulations are very similar. The differences can be explained by the approximation of the Generalized Aerodynamic Forces (GAF)s using rational functions which introduces an error. Figure C.17 shows the trim shape obtained by the nonlinear model and the linearized state space model for the CC. Figure C.17 shows the trim shape of the nonlinear model compared to the aeroelastic model if the quasi-steady component of the state-space model is used.

C.5. Verification of the Structural Sizing Model

The structural sizing model was verified in [16] by comparing the resulting dAEDalusNXT model deflections in bending and torsion for a cruise case with actual aircraft flight test data. The results showed a very good match considering the simplicity of the dAEDalusNXT model.

C.6. Acknowledgments

In order to validate different parts of the dAEDalusNXT code the FLEXOP aircraft was used as a reference geometry. The FLEXOP project has received funding from the European Union’s Horizon 2020 research and innovation programme under grant agreement No 636307.

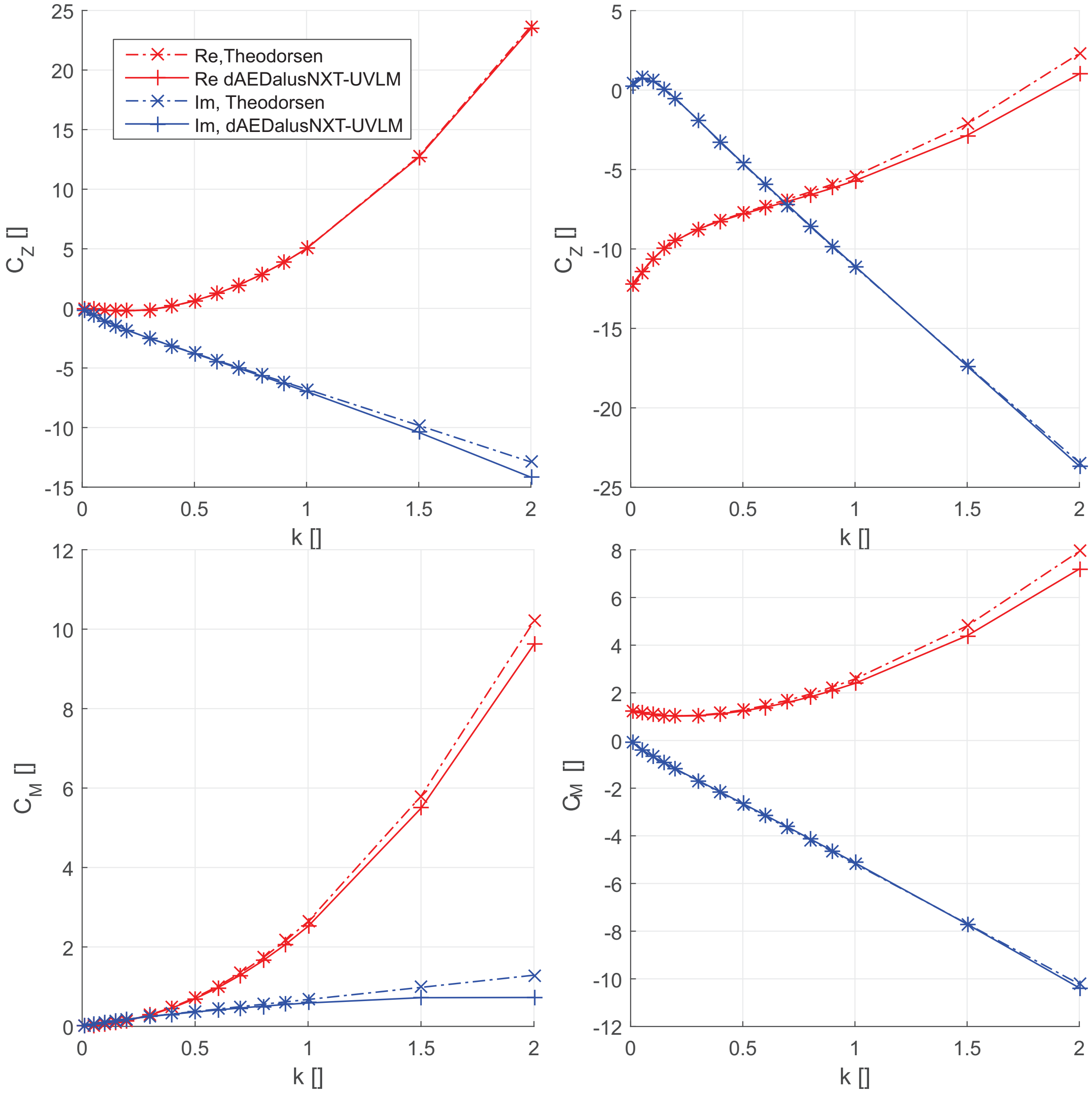

Figure C.4. – Generalized Aerodynamic Forces for Heave and Pitch

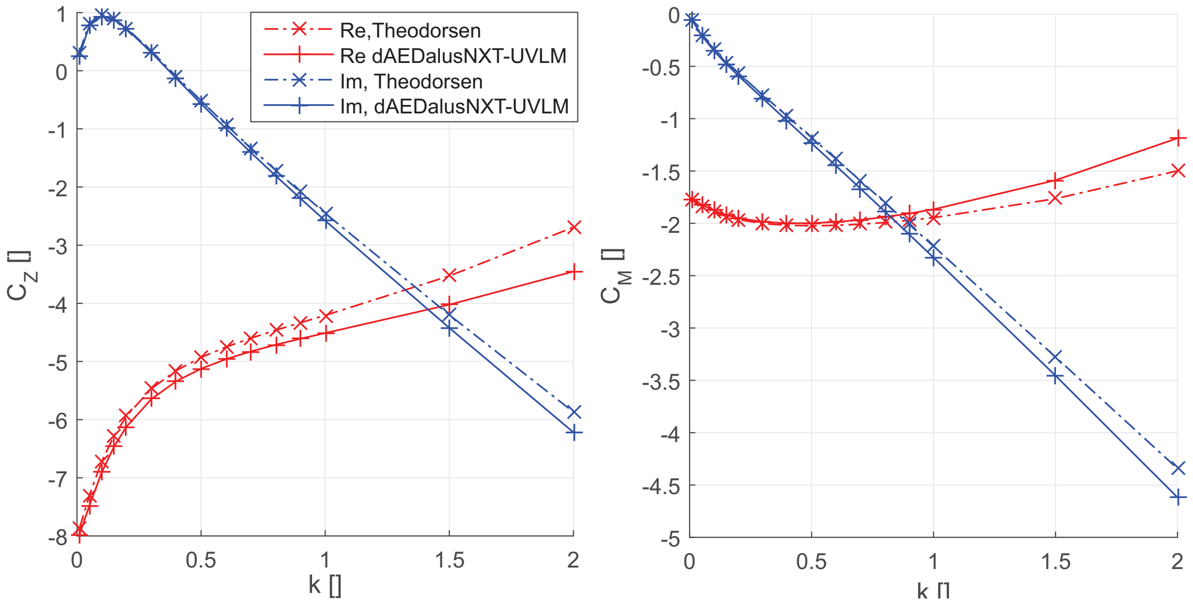

Figure C.5. – Generalized Aerodynamic Forces for Oscillating Control Surface

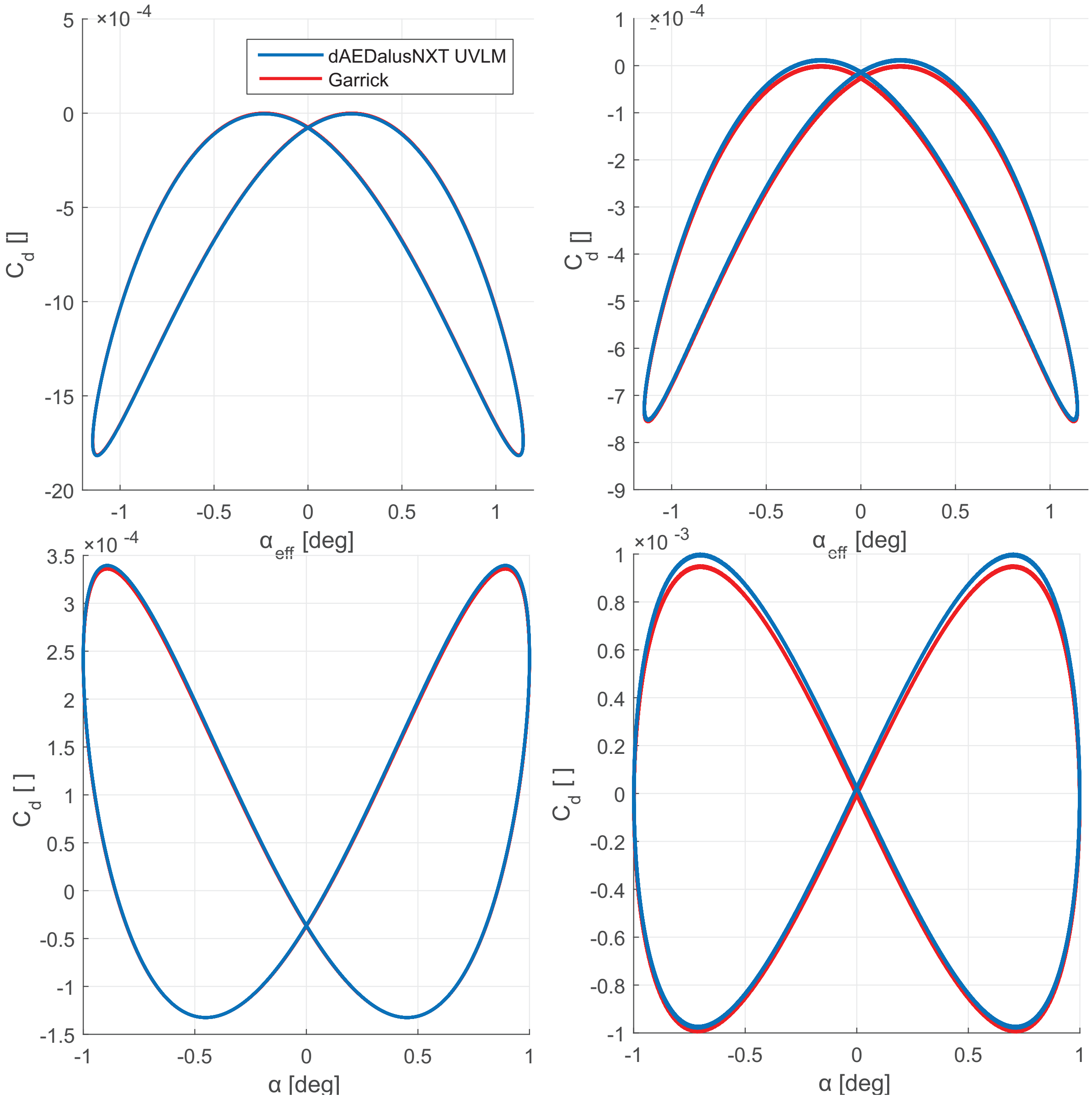

Figure C.6. – Unsteady Induced Drag for Heave and Pitch

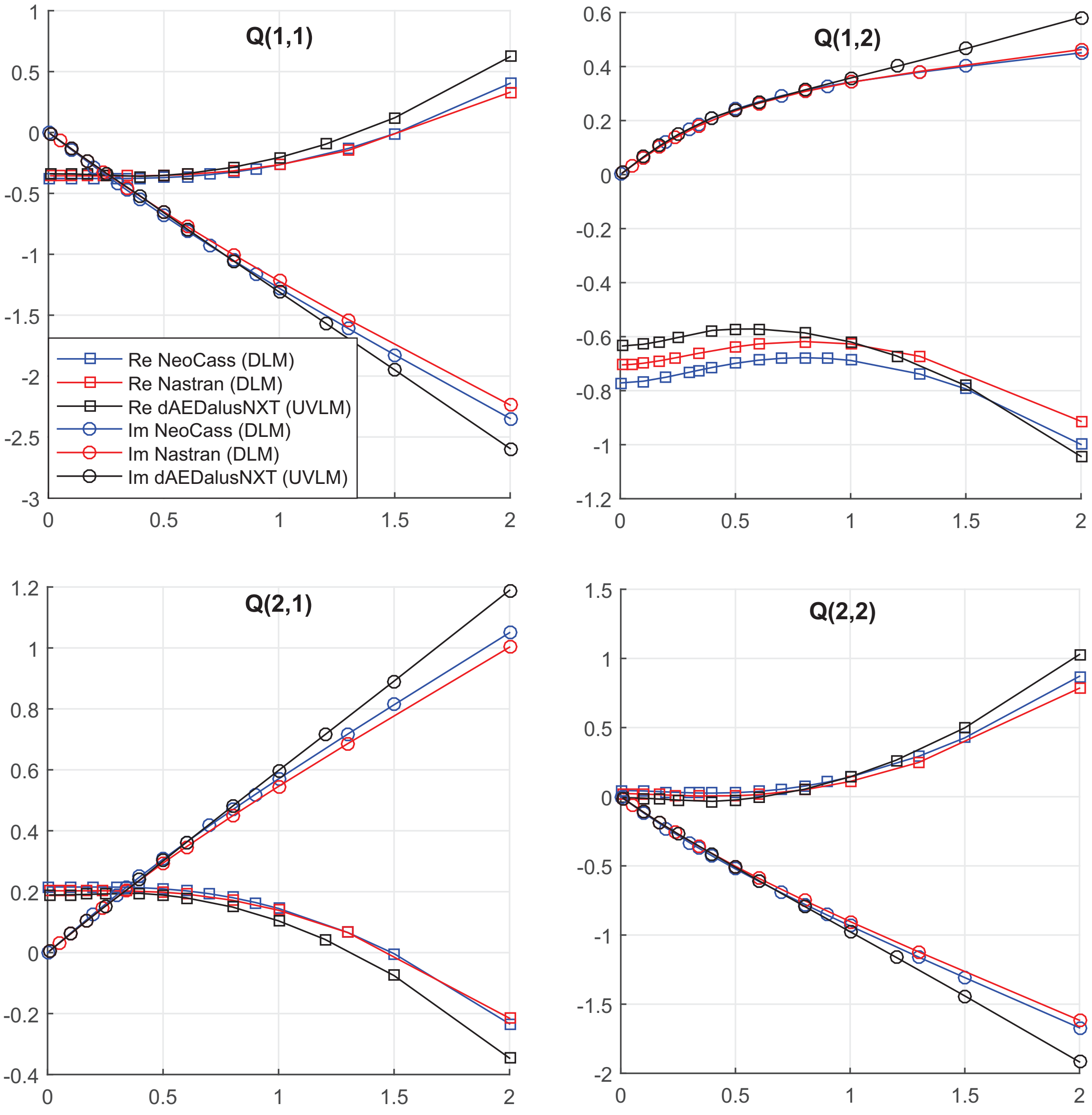

Figure C.7. – Comparison of GAFs for FlexOp Reference Geometry, Ma=0.15

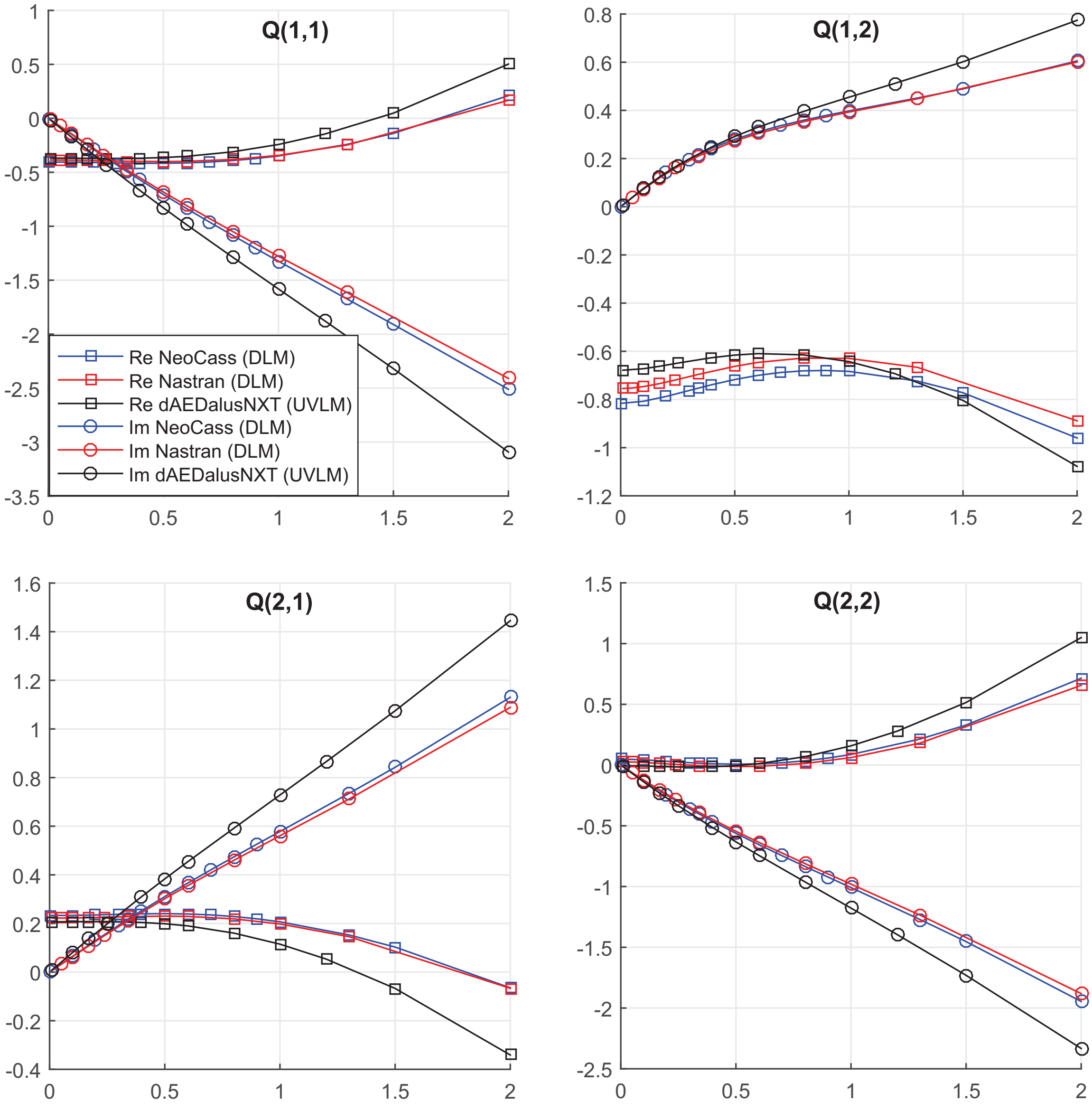

Figure C.8. – Comparison of GAFs for FlexOp Reference Geometry, Ma=0.5

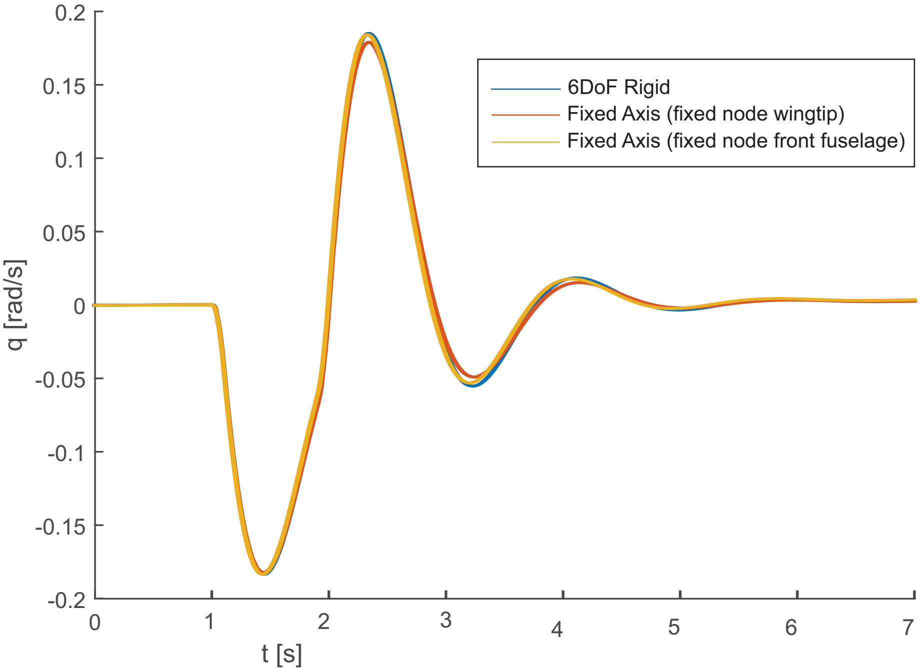

Figure C.9. – Comparison for Rigid Model

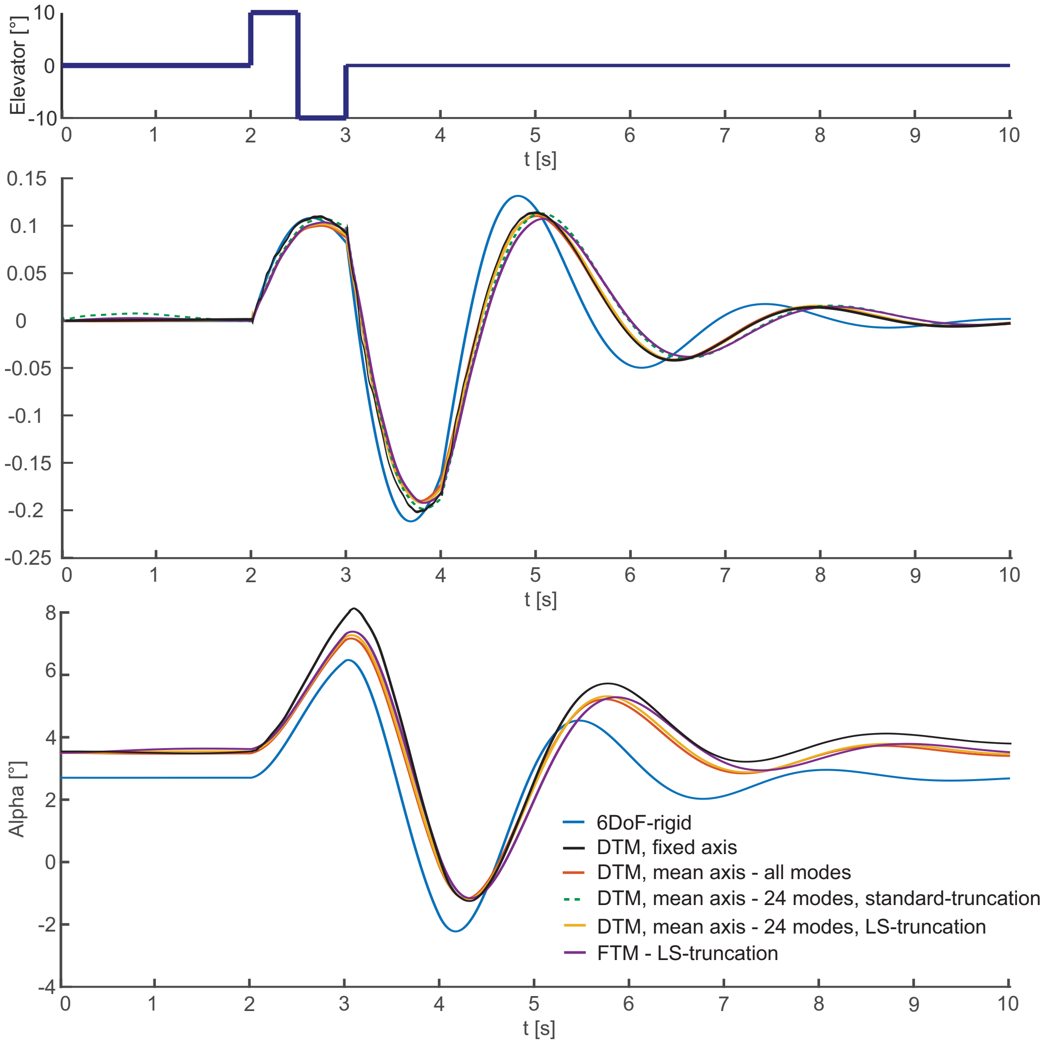

Figure C.14. – Deformation during a Short Period Excitation

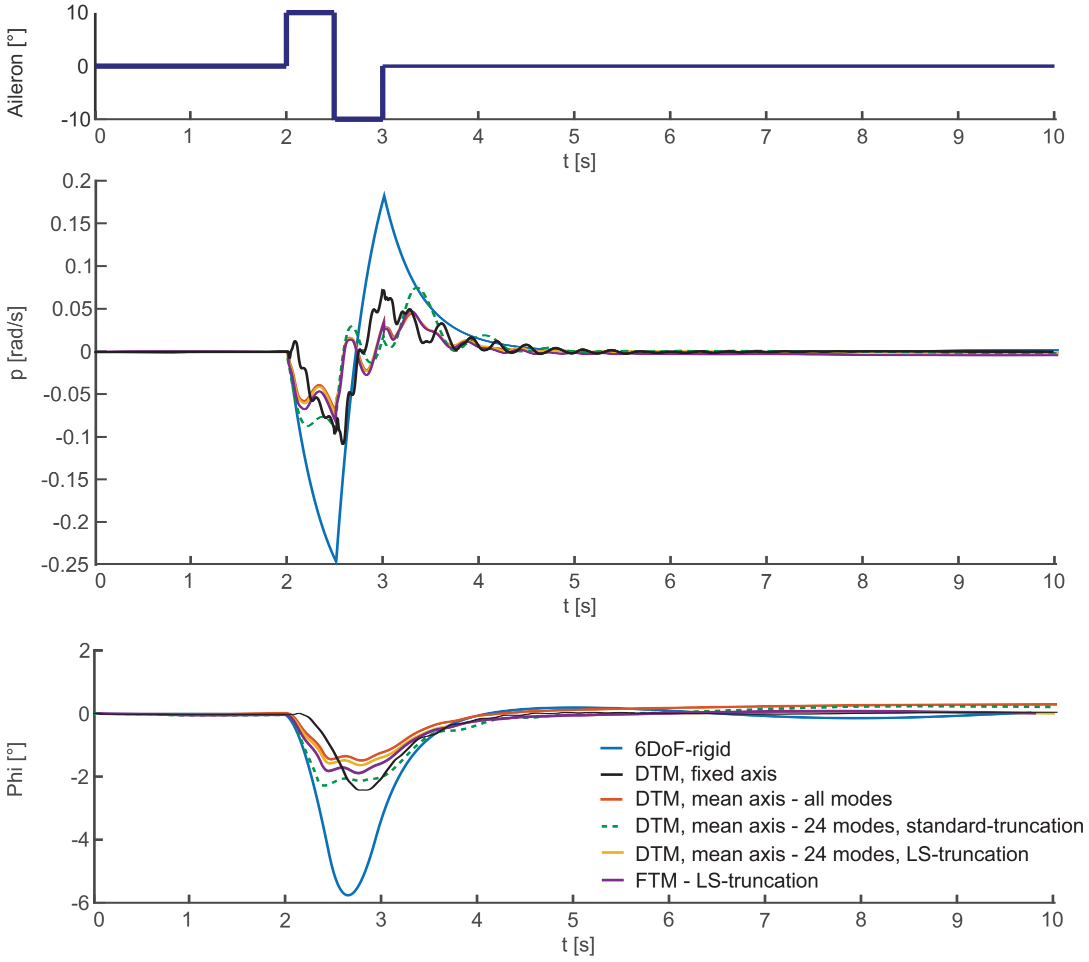

Figure C.15. – Response due to Aileron Doublet

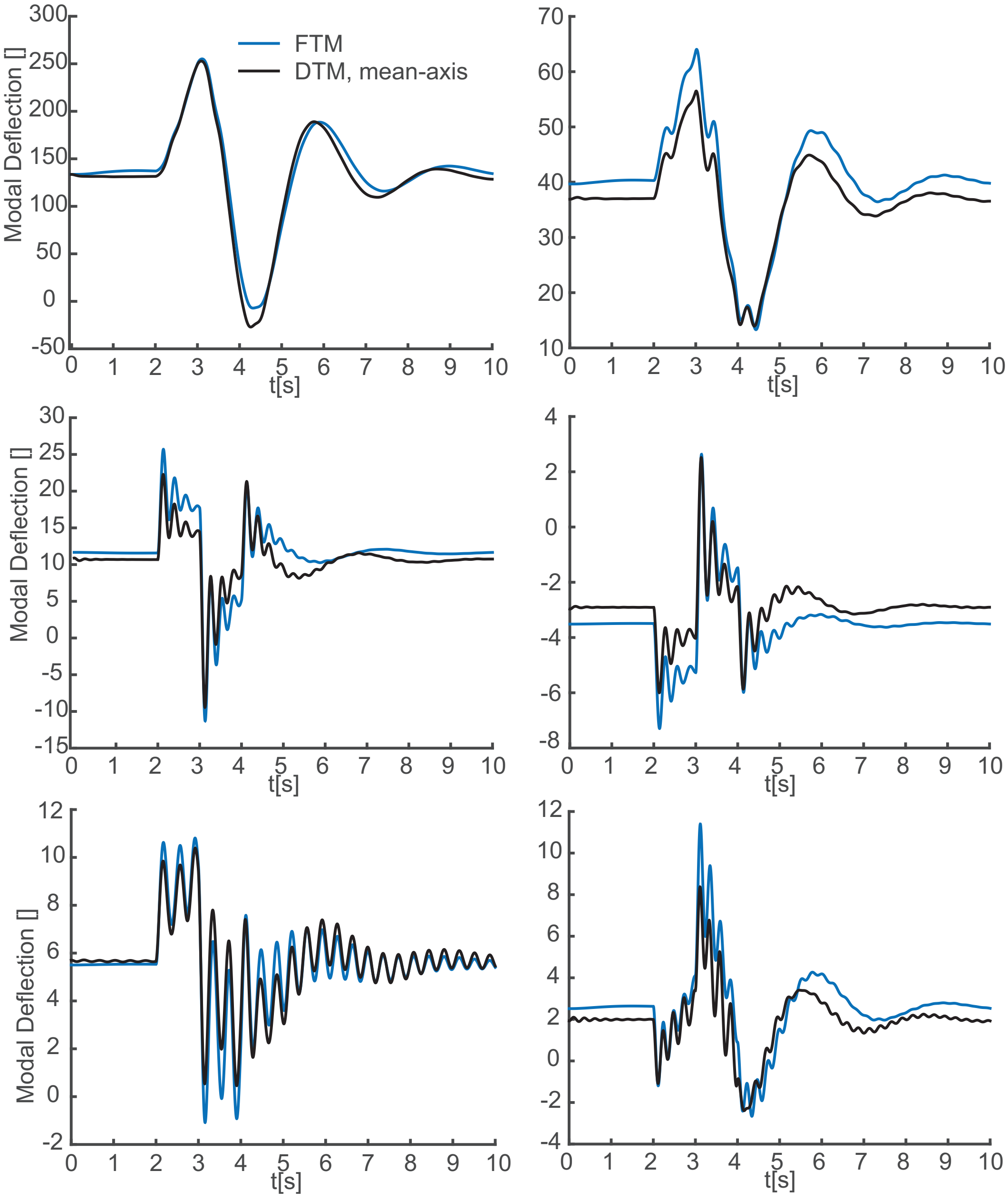

Figure C.16. – Validation of the Free-Flying Fast Time Simulation Model

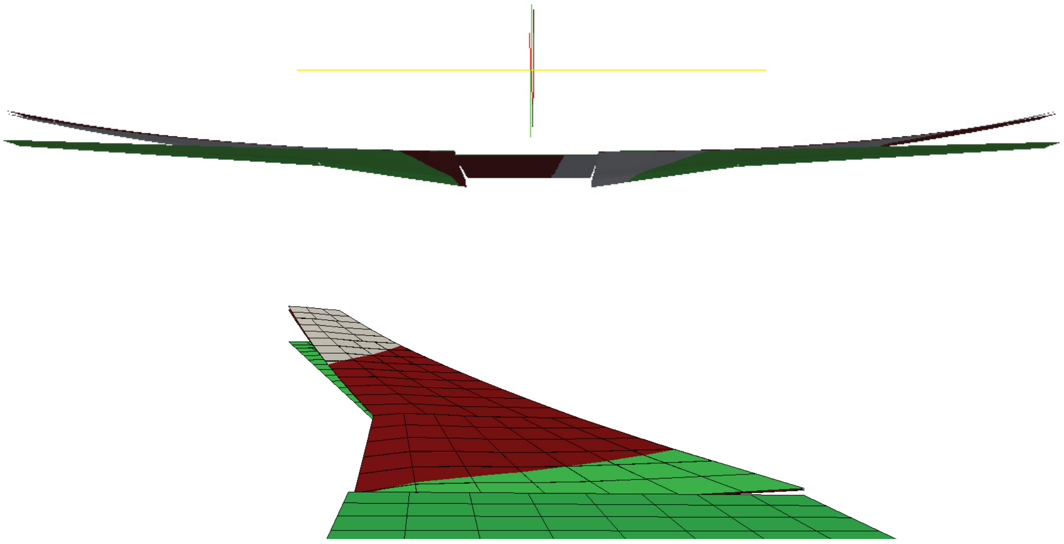

Figure C.17. – Comparison of Trimshape between State Space Model and Nonlinear Model

D. Illustration Credits

- http://www.aviationcv.com/aviation-blog/wp-content/uploads/2015/06/PSC0512_JT_116.jpg
- https://www.aiaa.org/uploadedFiles/About-AIAA/Press-Room/Key_Speeches-Reports-and-Presentations/2012/Martin-Lockheed-AVC-AIAA-GEPC2.pdf
- http://www.bauhaus-luftfahrt.net/presse-medien/ila-2012/08-der-ce-liner/BHL_Ce-Liner_In-flight1.jpg
- http://www.nasa.gov/sites/default/files/d8_vertical.jpg
- http://www.dlr.de/as/Portaldata/5/Resources/images/aktuelles/2013_06-leb/2013_06_21_Messe_Paris_%2836%29.JPG
- https://www.nasa.gov/sites/default/files/images/619090main_avc_boeing_concept_original_4x3_full.jpg
- http://aviationweek.com/site-files/aviationweek.com/files/archive/sitelife.aviationweek.com/ver1.0/Content/images/store/6/6/16d9434b-599a-4647-9646-fe160b948948.Full.jpg
- http://cdn.ientry.com/sites/webpronews/article_pics/futuristic_700.jpg
- http://events.airbus.com/fileadmin/media_gallery/photos/aircraft/future_aircraft_and_concepts/Airbus-Concept_plane_-side_back_view_left.jpg

E. Tool Input File

This appendix presents how to define an aircraft in the XML format readable by dAEDalus-NXT by means of a simple example aircraft.

E.1. XML

An aircraft can be composed from a set of predefined objects, which have basic properties that have to be defined. The basic objects are the wing object, the fuselage object, the nacelle object and the engine object. All aerodynamic surfaces like wings, canards or tail surfaces can be defined using the wing object.

E.1.1. Wing Object

The basic setup of a wing object is shown in Figure E.1. A wing is composed of multiple wing segments.

```
        <wings>
                <wing name="MainWing" symmetric="1">
                        <segment ID="1">
                                .....
                        </segment>
                        <segment ID="2">
                                .....
                        </segment>
                </wing>
        </wings>
```

The tool is able to take user inputs, such as sectional span profiles, wing twist, sweep, dihedral, etc. to automatically produce the geometries required for the aerodynamic and structural methods. Differences in such values along the span are possible, with automate interpolation between changes. If the user desires to perform an aeroelastic simulation, the wingbox outer dimensions, as well as the wingbox type has to be defined. Currently only a standard wingbox with a front and rear spar and a top and bottom skin is implemented. Additionally the material has to be defined. The definition of a wing segment is demonstrated in the following listing.

```
<segment ID="1">
        <location>
```

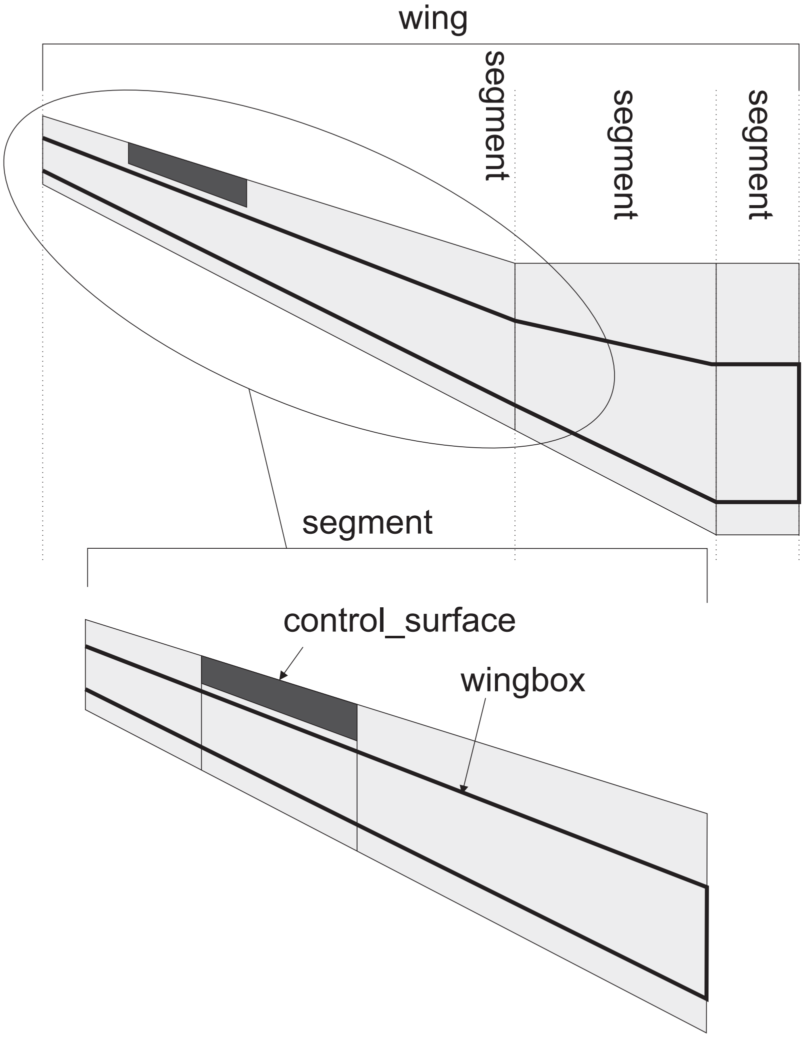

Figure E.1. – XML Definition of a Wing in dAEDalusNXT

```
        <x>20.439</x>
        <y>0</y>
        <z>-1.044</z>
    </location>
    <dihedral>0</dihedral>
    <le_sweep>0</le_sweep>
    <span>9</span>
    <root_chord>7.743</root_chord>
    <tip_chord>7.743</tip_chord>
    <root_twist>3.58</root_twist>
    <tip_twist>2.27</tip_twist>
    <root_profile>NACA0012</root_profile>
    <tip_profile>NACA0012</tip_profile>
    <wingbox type="StandardWingbox">
        <root_frontspar> 0.165 </root_frontspar>
        <tip_frontspar> 0.165 </tip_frontspar>
        <root_rearspar> 0.638 </root_rearspar>
        <tip_rearspar> 0.638 </tip_rearspar>
        <is_fueled> 1 </is_fueled>
        <material type="aluminum" > </material>
    </wingbox>
</segment>
```

E.1.1.1. Control Surface Definition

A control surface for each wing segment can be defined by the following syntax.

```
<control_surface name="elevator" location="trailing_edge">
    <hingeline type="tapered">0.33</hingeline>
    <starts>0.1</starts>
    <ends>0.89</ends>
</control_surface>
```

where the location of the control surface can be defined at the leading or at the trailing edge, the hingeline can be defined to be tapered with the segment or constant in chord.

E.1.2. Fuselage Definition

Similarly to a wing a fuselage is composed of different segments as shown in Figure E.2 and defined the following way:

```
<fuselages>
    <fuselage name="Fuselage">
        <segment name="Nose">
            ....
```

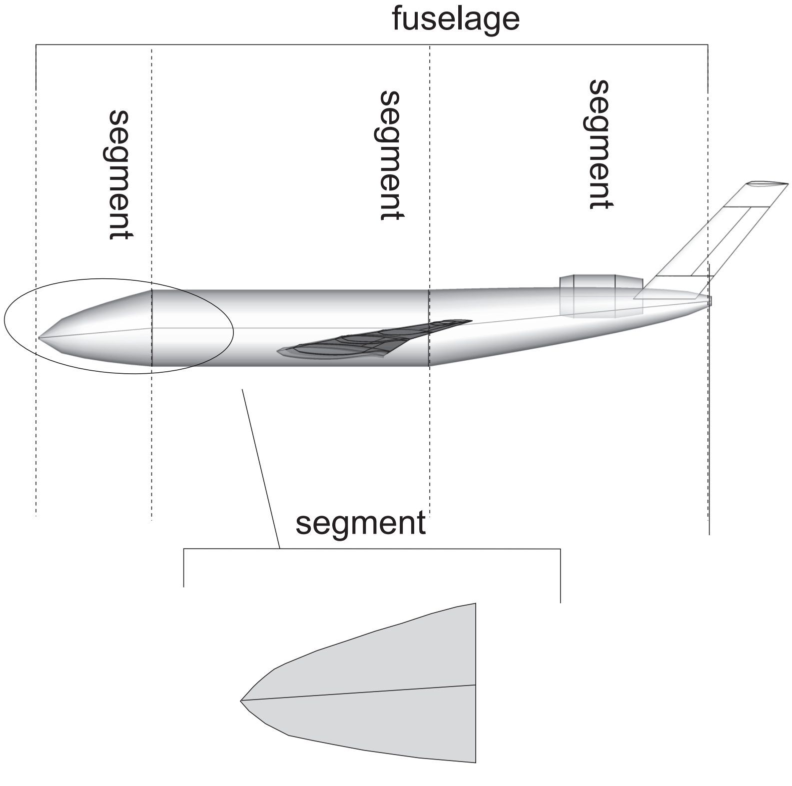

Figure E.2. – XML Definition of a Fuselage in dAEDalusNXT

```
        </segment>
        <segment name="Cabin">
            ....
        </segment>
        <segment name="Tail">
            ....
        </segment>
    </fuselage>
</fuselages>
```

A segment is defined the following way

```
<segment name="Cabin">
    <location>
        <attach_to> previous </attach_to>
    </location>
    <length>33.96</length>
    <front_width>3</front_width>
    <rear_width>3</rear_width>
    <front_height>3</front_height>
    <rear_height>3</rear_height>
    <sweep>0</sweep>
</segment>
```

E.1.3. Engine Definition

An engine is defined the following way

```
<engine name="left" mounting="MainWing">
    <cg_pos>
        <x> 24.5263 </x>
        <y> -9.294 </y>
        <z> -2.3061</z>
    </cg_pos>
        <mass_engine> 8694.93 </mass_engine>
        <mass_pylon>  1688.5  </mass_pylon>
        <max_thrust>  287000 </max_thrust>
</engine>
```

where the the variable mounting defines the object the engine is attached to, which may be a wing or a fuselage object.

E.1.4. Coupling Conditions

In order to connect the different objects coupling conditions have to be defined as demonstrated in the following listing

```
<boundary_conditions>
        <connection>
                <beam name="MainWing"> </beam>
                <beam name="Fuselage"> </beam>
        </connection>
        <connection>
                <beam name="HorizontalTail"> </beam>
                <beam name="Fuselage"> </beam>
        </connection>
        <restraining>
                <beam name="Fuselage">
                        <x> 25 </x>
                        <y>     0</y>
                        <z>     0</z>
                </beam>
        </restraining>
</boundary_conditions>
```

If no type is defined a full coupling is assumed (all DoFs).

E.1.5. Control Allocation Definitions

Finally the control surfaces have to be assigned to their main function, whether they should be used for pitch, roll or yaw control or for trimming.

```
<control>
        <control_allocation>
                <trim_surface name="elevator"> </trim_surface>
                <pitch_cmd name="elevator">  </pitch_cmd>
                <roll_cmd name="aileron">  </roll_cmd>
                <yaw_cmd name="rudder">  </yaw_cmd>
        </control_allocation>
</control>
```